TO MY MOTHER AND FATHER

MIXING IN LARGE SCALE STORAGE TANKS

(Studies on the boundary layer thickness at the base of storage tanks agitated with side-entry propellers)

by

Ghassan Hassan Al-Hassani

A thesis submitted to the University of Aston in Birmingham for the degree of Doctor of Philosophy

Department of Chemical Engineering
The University of Aston in Birmingham

November, 1977

SUMMARY

MIXING IN LARGE SCALE STORAGE TANKS

(Studies of the boundary layer thickness at the base of storage tanks agitated with side-entry propellor)

Ghassan Hassan Al-Hassani Ph.D. 1977

Studies of the thickness of the viscous sub-layer and its distribution around the base of a tank fitted with a side-entry propeller has been studied by simulating the process on a 1.2m diameter tank. An electro-chemical technique has been employed to study the thickness of the viscous sub-layer and the effect of impeller speed, impeller diameter, shaft angle, liquid depth, and physical properties of the solution on this thickness. Also a hot-film anemometer was used to check and compare the results obtained by the electro-chemical technique and it was found that both were in agreement. However, the results obtained by the electro-chemical technique gives an indication of the effect of the diffusivity and the thickness of the viscous sub-layer was related to both Reynolds number and Schmidt number.

A mathematical model has been developed to describe the velocity distribution along the impeller jet and to predict the thickness of the viscous sub-layer along the jet. The results obtained from this model agree with those obtained by experiment.

Studies on minimizing the thickness of the viscous sub-layer showed that the presence of one or more small baffles on the base of the tank help to lift the sediments into the bulk of the solution.

Finally, full-scale measurements were carried-out on 79m diameter tank to provide data for scale-up.

Key Words: Side-Entry Mixing

CONTENTS

ACKNOWLEDGEMENT

The author would like to thank Professor G.V. Jeffreys, the Head of the Chemical Engineering Department for his continual encouragment, assistance and supervision. Also my thanks to the academic and technical staff of the Department for their generous help, to Mrs. N. Armstrong for typing this thesis and Miss P. Hickton for assistance in checking the manuscript.

I would also like to thank the Iraqi Ministry of Oil for generously financing and sponsoring this work. My thanks is also due to the staff at Angle-bay terminal of British Petroleum Company for giving the opportunity to carry out some experiments at their establishment.

CHAPTER I

INTRODUCTION

Mixing operations in the petroleum industry pose many problems, one of which is the prevention of the sedimentation of sludge and waxes which exist in the crude oil while in storage. Such an operation is often performed in large tanks up to 88m diameter, fitted with from one to four side-entry propeller mixers mounted horizontally about 1m above the base. These are used to mix the materials in the tank and to obtain a uniform composition throughout the tank thereby ensuring continuity of refining operations.

Crude oil brought to the refinery usually contains a quantity of sludge and wax which, if left in the storage tank for an appreciable time before being pumped to the process, will sediment out and collect on the floor of the tank and therefore reduce its capacity. To avoid such a problem it is necessary to keep the whole content of the tank in a homogenous state by good mixing. The choice and the design of equipment to be used for mixing depends largely on experience and very little is known about the time necessary for these mixers to agitate the tank contents to achieve the desired effect, there-by preventing the waste of a considerable amount of power by overrunning these mixers.

The application of mechanical energy through a mixer imposes forced convection which results in either an increase in mass motion or in turbulence or in both. This turbulence is generated by liquid velocity discontinuities which leads to a turbulent entrainment of one liquid in another. When

two fluid streams adjacent to each other move at different velocities, a shear stress is established, and when this stress is sufficient to over-come the viscosity resistance, the flow line is deformed and eddy motion initiated. This motion spreads throughout the flowing stream causing turbulence and mixing. Therefore, it is necessary to bring large quantities of liquid into the turbulence area to completely mix the tank contents and this is accomplished by causing circulation of the liquid to all parts of the tank. All the liquid in the tank must be brought into contact with an eddy forming flow discontinuity. However, measurements of time-averaged velocities in a turbulent field over a solid boundary have shown a region close to the wall, known as the viscous sub-layer, in which the transfer of momentum by turbulent velocity fluctuations is negligible compared with transfer by molecular viscosity. Therefore, in large tanks, any particles of wax or sludge with a low velocity that approach the walls and pass through this layer, will decrease in velocity until it touches the wall. It will be impossible for these particles to get out of this layer again. So that in order to prevent sedimentation, mixing should be performed in such a way as to provide turbulence everywhere in the tank to minimize the thickness of this layer and to retain the particles in the main bulk of the fluid.

The parameters of the system and the physical properties of the fluid are factors which are important in studying this layer as they could affect its thickness. Therefore, the object of this work is to measure and identify the factors that affect the thickness of the viscous sub-layer. In addition ways to minimize the thickness of this layer have been investigated. The electrochemical technique as a direct method of measuring

the rate of mass transfer near the wall is one of the techniques employed here as an indirect but accurate method of measuring the thickness of the viscous sub-layer. Also the hot-film anemometer has been used for the measurements of the velocity. This method has some restrictions such as the probes used could cause disturbances inside the viscous sub-layer. The photographic work employed here was undertaken to support the electrochemical technique and to show the distribution of this layer over the base of the tank.

Water is used as a main fluid in the measurements because it is easy to handle and readily available and its physical data is well known.

CHAPTER II

2 MIXING AND MASS TRANSFER

2.1 INTRODUCTION

Mixing is an operation which tends to reduce non-uniformities or gradients in composition, temperature, or properties of material in bulk. Such an operation is performed by moving the material between various parts of the whole mass.

The aim of mixing is not only to produce more uniform mixtures of components, but sometimes to transfer material to or from surfaces of particles or phases, as in the case of distillation, leaching and liquid-liquid extraction, where fluid motion reduces the thickness of the resisting film.

Since mass transfer of fluids is a function of diffusion and fluid motion, the application of the principles of fluid mechanics is the most useful approach to understand mixing. Two principal actions of fluid motion exist in mixing operation:

1) The mass or macroscopic motion of material over large distances resulting in a major flow pattern.
2) The small scale or microscopic motion which associated with turbulence and translation of material over small distances.

In systems where the natural diffusion and convection currents are less than desired, forced convection may be imposed which results in either increased mass motion, or in turbulence, or in both. To produce forced convection, rotating impellers are usually used in most of the mixing

operations. These impellers cause the liquid to move and effect mass flow and turbulence. The physical properties of the fluid, as well as the geometry and position of the mixer play an important role in studying the flow and turbulence.

2.2 TYPES OF MIXERS

Manufacturers of agitation equipment have constructed a great variety of impeller types. These impellers may differ in physical form, action, or their speed. A special type may sometimes be necessary to perform an unusual mixing operation.

Different attempts have been made in the published literature to classify impeller types. One of these was to classify the impeller according to their use in a laminar or turbulent flow. Another attempt was to adjust the design of any impeller to vary the balance of flow and head. It is also possible to group impellers by peripheral speed since the three common types - propellers, turbine, and paddle - normally fall into distinct ranges.

Voncken (1) classified impellers into three groups with regard to their action - rotating, vibrating, and shearing impellers. In his classifications, Voncken had to sub-divide the first group into two classes according to the type of flow produced. He inserted most of the most commonly used impellers into the first group.

To have larger groups with clear differences it was suggested that impellers be classified on the basis of the physical form and on category of operation. This attempt has been made by UHL and GRAY (2). The multitude of impeller

configurations can be grouped into five distinct categories, of which only the first four are of Commercial importance.

2.2.1 PROPELLERS

This type of impeller has essentially high speed and produce axial-flow, where the discharge flow is parallel to the agitator shaft. They are usually used for low viscosity liquids without restrictions to the shape and size of the vessel. The circulating capacity is high and entrainment of surrounding liquid occurs. The Marine-type propeller is almost universally used in the three-blade type.

2.2.2 TURBINES

Turbines impellers are usually of the radial-flow type. Two basic physical forms of the turbine are, the flat-blade radial discharging type and the pitched blade axial thrust type. The blades may be curved or flat and their number is not important; and can be two or more. All others are modifications of these two basic types. The conventional turbines are, flat blade, disc flat blade, pitched vane, curved blade, tilted blade, shrouded, pitched blade, pitched curved blade, and arrowhead (2).

2.2.3 PADDLES

This type of impeller consists basically of two blades, with a high ratio of impeller to tank diameter. The paddle is similar to the turbine in that both have similar physical form and power condition, but the paddle could be used in the laminar range, or in the transition and turbulent range without baffles, while turbines are not normally considered

for either of these conditions. Apart from that, the paddle is not very effective for high viscosity operations. Different types of paddles are the basic paddle, reverse pitch, glassed steel, anchor, leaf, gate, finger, double motion, and Helix (2).

2.2.4 HIGH SHEAR IMPELLERS

This type of impeller with a high speed operates in the high Reynolds number range with a low ratio of impeller to tank diameter. The blade area is small. Such impellers can be classified as low-flow high-velocity impellers. Most of them are radial discharging type. Different types are the disk, modified disk, modified core, and modified turbine (2).

2.2.5 RECIPROCATING IMPELLERS

This type of impeller has little application and is not commercial. It has been applied in small autoclaves where solenoid-type integral drive can be adopted to eliminate a shaft seal.

2.3 MIXING TIME

In most of the mixing operations, the time necessary to reach homogeneity is important. Usually the mixing time is defined as the time needed for homogenization to the molecular scale. At this scale, measurements are difficult to achieve, and it is only the terminal mixing time that can be measured. It is defined as the time required to attain homogeneity at the scale of observation. The difference between the mixing time and the terminal mixing

time is very small.

There are many methods of measuring the mixing time, but most of them consist of the injection of a tracer fluid and recording of the time required to smooth out the fluctuations.

The conductivity method for the measurement of the mixing time consist of injecting a small amount of electrolyte into the solution in the vessel and recording the fluctuations in the conductivity at one or preferably more points in the vessel, until these fluctuations are smaller than a certain arbitrary deviation from the mean concentration . Probes made of platinum wire are usually needed to measure the conductivity. Fossett (3), used the conductivity method to measure the mixing time of tetra ethyl lead in petroleum oil. He used a tank made of a section of 1.5m diameter concrete pipe plugged at the bottom and fitted with two jets in the form of a Y to simulate a full scale tank 6m high and 35.4m diameter. He took samples at different levels as time progressed and continued mixing until all levels showed the same content of the tracer. The mixing time was obtained and he proposed this correlation:

$$\Theta = \frac{8T^2}{\sqrt{VQ_o}} \qquad (2.1)$$

He claimed that the mixing time is independent of the Reynolds number. He carried out some measurements on the full-scale tank and the results were in agreement with the model results. He claimed that the mixing time and the power consumption is less when using a jet than a propeller.

This has not been confirmed by Rushton (4) who investigated mixing in an 80,000 barrel gasoline storage and blending tank to measure the mixing time. The tank was fitted with a side-entry 71cm diameter propeller. He determined the time of the mixing of tetra ethyl lead with gasoline both for stratified start and for mixing during and after TEL addition. He found that, although the total time for filling and mixing is approximately equal in both cases, the energy consumed in the first case is much less than the second. He compared his results with Fossett's results (3) for a jet and found that both the mixing time and the energy consumed using a propeller is less than that for a jet. Kramers, Baars and Knoll (5), used the conductivity method to study the effect of the different parameters of the system on the mixing time, using two measuring cells made of platinum wires. They found that the mixing time was inversely proportional to the rotational speed and the product of (ΘN) is constant. This means that Θ decrease with the increase of Reynolds number. With eccentric location of the propeller shaft in a vertical unbaffled vessel, they found that mixing was improved as the intensity of the tangential swirl of the liquid was reduced. The tank size was found to have no effect on the mixing time as long as the tendency to form a vortex was small. They derived the following correlation to be used for scale-up:

$$P_i \Theta = \text{Const} \times \rho L^5 N^2 \qquad (2.2)$$

This means that for constant density, speed and power, the mixing time is proportional to the linear dimension of the

tank. The results obtained by Holmes, Voncken and Dekker (6) for circulation time in a turbine-stirred vessel agreed with the results of Kramers (5) in that the product of (ΘN) is constant in the turbulent region.

Biggs (7) compared the mixing time for different types of impellers. He found that the mixing time using a propeller is approximately 100% greater than for the turbine. His results were in agreement with the results obtained by Norwood and Metzner (8).

Yuge and O'Shima (9), studied the mixing characteristics of high viscosity liquids in a stirred tank using the conductivity method. They found that in the range of Reynold number greater than 20, paddle or turbine impellers were suitable and in the smaller range, helical ribbon and helical screw impellers were preferable. Also they noticed that the effect of diffusive mixing was significant, particularly in the case of paddle or turbine impellers in the range of Reynolds number less than 10. The time constant of diffusive mixing becomes greater than that of convective mixing and diffusive mixing controlled the overall rate of the mixing process. Doyle (10) also measured the mixing time by the conductivity method for a 1.2m tank fitted with a side-entry propeller. He found that:

$$N\Theta \frac{d^2}{T_2} = \text{Constant} \qquad (2.3)$$

and suggested this correlation for scale-up of geometrically similar tanks providing the impeller Reynolds number is less than some critical value. He suggested $\sim 10^5$, depending on the geometry.

The indicator method based on the visual technique consists of injecting a small amount of dissolved acid in water, containing the equivalent amount of base. By using an indicator of sufficient colour intensity in the proper pH range, the disappearance of the last wisp of colour marks the moment at which the terminal mixing time is reached. Fox and Gex (11), used the indicator method for measuring the mixing time. They used two cylindrical vessels of .3m and 1.5m diameter and two basic types of mixers were investigated. These were the jet mixer and the three-blade propeller. The results indicated two flow regimes, incipient laminar and turbulent. For a jet the mixing time found inversely proportional to $(Vd_o)^a$, where the exponent a is 5/6 for turbulent flow and 2 for laminar flow, while for a propeller Θ was inversely proportional to $(Nd^2)^b$ where the exponent b is 5/6 for turbulent and 10/6 for laminar flow. They confirmed Rushton's(4) proposal that jets require more power to perform the same work as a propeller.

Norwood and Metzner (8), used a baffled cylindrical flat-bottomed mixing vessel, with the fluid agitated with centrally positioned turbine impeller having six blades. They carried out their measurements for mixing time in this vessel. In comparing their results with those of Fox and Gex (11), they found that the mixing time factor for the agitation of Newtonian fluids by turbine impeller in baffled tank would be related to that by a jet, and a propeller, in an unbaffled tank by the square root of the ratio (T/d). The mixing time factors and power consumption data combined suggested that turbines are much more efficient at low Reynolds number than propellers.

Doyle (10), carried out experiments using the indicator method. He found that the mixing time, in a side-entry propeller tank, was a function of the molecular diffusivity of the materials employed, and suggested that scale-up was not suitable using this method. He explained the influenceof diffusivity on mixing time, measured by the indicator method, by a suitable model in which he assumed that the effect of large scale shearing was more important than those of small-scale turbulence.

Van de Vusse (12) applied the schlieren method to measure mixing time. In this method, the homogenization of two miscible liquids with different refractive indices was studied. Half of the vessel was filled with one liquid, then another liquid of about the same density and viscosity but with a different refractive index, was carefully poured on top of the first. The time which elapsed from the beginning of stirring and the disappearance of the last schlieren, was considered as the mixing time. Van de Vusse carried out his measurements in a mixing vessel fitted with a mixer placed vertically at about half the distance between the bottom of the vessel and the liquid level. He found that the size of the tank has no effect on the mixing time except for very large sizes, where dead corners were found to increase the mixing time. In studying the different type of stirrers he found that for the propeller the eccentricity and the inclination of the stirrer decreases the mixing time due to an increase in the relative velocity of the rotating stirrer and the liquid, while for radial flow impellers, the time was longer as the vicinity of the wall impeded the flow of liquid in a radial direction. He also

proved that in both axial and radial flow impellers, the baffles tend to reduce the mixing time.

The thermal impulse method consists of injecting a small amount of heated fluid or generation of a heat pulse by an electrical heating element in the agitated fluid and recording the fluctuations of the temperature at one or more points in the vessel. Gluz and Parluschenko (13), used this method with thermocouples to detect the temperature fluctuations resulting from the addition of a small quantity of warm liquid. The advantage of this method lay in the ability to introduce liquids of very high or very low conductivity and tends to reduce the possibility of contamination of the system.

2.4 PUMPING CAPACITY

The pumping capacity of a rotating impeller, defined as the volumetric flow rate leaving the impeller blades is of importance in studying the mixing process and the performance of the mixer. It is equal to the mean velocity of the liquid leaving the impeller blades multiplied by the area swept by the tip of the blades. Therefore, fluid velocity measurement is important in evaluating the pumping capacity.

From the definition of the pumping capacity, the following expression could be written for propeller and turbine type impellers respectively:

$$Q_{prop} = \bar{V}_z \quad \frac{\pi d^2}{4} \tag{2.4}$$

$$Q_{tur.} = \bar{V}_r \quad \pi d W \tag{2.5}$$

and are valid only if axial or radial flow is predominant, and cannot be used for the intermediate types of flow such as that caused by turbines with inclined blades. By assuming the average velocity of the liquid leaving the impeller blades to be proportional to the tip speed of the blades (πNd), the above equations become:

$$Q = KNd^3 \qquad (2.6)$$

where K is the constant (1) in the turbulent region for a given impeller geometry.

Rushton, Mack and Everett (14) measured the impeller pumping capacity by a direct measure of the volume of water pumped over a weir from the impeller, but as the shape is different from a stirred tank, the results cannot be regarded as valid for this situation. Using the "streak method" to photograph a small illuminated liquid tracer droplet moving in the liquid agitated by a flat-blade turbine operating in a cylindrical baffled tank, Sachs and Rushton (15) studied the volumetric discharge of the turbine and found that it was proportional to the turbine speed at various radial distances from the impeller. The discharge stream entrained surrounding fluid to an amount nearly equal to the volumetric discharge of the impeller. An extension of this work was carried out by Metzner and Taylor (16) who measured not only the velocity but also the magnitude of shear and power dissipation rates resulting from velocity gradients within the tank, in both Newtonian and non-Newtonian systems. They carried out their experiments using centrally positioned turbine impellers of 5 to 15cm

in diameter. They found that the fluid velocity in the horizontal plane of the impeller varied almost linearly with the rotational speed in the Newtonian systems, while the movement in pseudoplastic systems increased exponentially with the impeller speed because of the cumulative effects of local velocity and viscosity changes in these systems.

Based on the analogy between a turbine mixer and a centrifugal pump, Van de Vusse (12) found the following expression for the theoretical pumping capacity of a flat-blade turbine impeller:

$$q = \pi^2 N d^2 W (1-C^2)^{\frac{1}{2}} \qquad (2.7)$$

He assumed that the loss of energy due to drag on the impeller and entrainment of fluid by the jet stream from the impeller were both negligible. He agreed with Rushton (15) that:

$$q \propto N P_i d^z \qquad (2.8)$$

Nagata (17,18) used the pitot tube to measure the fluid velocity in a 60cm unbaffled tank with a radial flow type impellers, while Norwood and Metzner (8) used a thermistor probe connected to a Wheatston"s bridge to measure the fluid velocity in baffled tanks ranging from 14.5 to 40cm in diameter agitated by a flat-blade dimensionally similar turbines with diameters of 5, 10 and 15cm. They obtained the total flow rate by integrating the measured velocities over the entire moving stream of fluid. They found the following correlation for the

volumetric flow rate over Reynolds number range of 36 to 1.7×10^4:

$$q = 9. \times 10^4 \, N d^2 W \, (d^4 \rho / \mu)^{.5} \, (1 - C^2)^{.5} \qquad (2.9)$$

They agreed with Van de Vusse (12) that C is negligible for baffled systems, but they could not prove the applicability of this correlation for use on large-scale equipment .

2.5 FLOW PATTERN

The flow pattern produced by agitating a fluid inside a vessel depends on many factors such as the shape and size of the vessel, type and size of the impeller, presence of baffles and position of the impeller shaft. Many authors have researched on the effect of these parameters in studying the flow pattern.

For any type of impeller rotating liquid inside unbaffled cylindrical tanks, a vortex will be formed around which the liquid will swirl and poor mixing will result because there is little motion from top to bottom. This vortex becomes deeper as the impeller speed increases until it touches the impeller itself causing part of the impeller to rotate in the air. One way of avoiding this is to introduce baffles in the tank, but for a propeller this could be avoided by positioning the propeller shaft off the centre of the tank. When the propeller turns counter clockwise, the shaft is to be placed to the left of the centre line and at an angle to the vertical (19), but any change in location of the propeller will cause rotary flow and produce a vortex.

Side-entry mounting of the impeller shaft is normally

used with very large tanks. To avoid using baffles and to prevent swirl, the shaft is placed parallel to the bottom and at angle of 5^{o} to 10^{o} to the left of the centre (10). Again the position is critical.

Nagata (20) studied the flow pattern created by radial-flow type impeller in 60cm tank with baffles. In this system, he divided the circulation flow into four zones, two having a horizontal flow to discharge the fluid from the impeller and to return the fluid in the vicinity of the tank axis, while the other two had a vertical flow along the wall and along the axis of the impeller. The velocity rapidly decreases in the first section due to the divergence of the discharge jet. Holmes (21) found that the mean velocity of the recirculation loop was about equal to the velocity at the end of the discharge jet. He calculated the velocity on the assumption that the discharge rate is constant. This means that there is no entrainment along the jet.

Metzner and Taylor (16) used the photographic technique to study the flow pattern of highly viscous liquids in both Newtonian and non-Newtonian systems, while Norwood and Metzner (8) in their studies on the flow pattern suggested the use of a model that assumes nearly all the mixing occurs in a small "perfectly mixed" region near the impeller, with the flow throughout the remainder of the tank serving primarly to bring the fluid into this highly turbulent region of the impeller. On the basis of this model, they related the volumetric flow rates to the operating variables.

In studying the effect of baffles on mixing, Newitt, Shipp and Black (22) used a vertical baffle welded to the side of

a cylindrical container in which the flow pattern was symmetrical about the axis. They noticed that the liquid passing the edge of the baffle tended to form a vortex layer which curled round on itself to form a vortex roll which remained stationary and hence contributed little to the mixing process. When this baffle was fixed some distance from the wall of the container, they noticed two vortex layers which curled on themselves producing a double row of dissimilar vortices. Reavell (23) in his studies on the flow pattern suggested that the shape of the vessel had a pronounced effect on achieving a satisfactory flow. He explained that rectangular vessels of depth less than the width gave difficulties in ensuring a sufficient flow of liquid and turbulence in the corners, specially when using solids in the mixture. In improving the flow pattern inside cylincrical tanks agitated with propellers, he used a small baffle of cruciform shape placed in the bottom of the tank. The impeller was arranged to force the liquid downwards. Axial flow was encouraged when the liquid was close to the baffle, then radial flow preceeded from the centre towards the wall, travelling vertically to reach the liquid level, then turns downwards and back to the impeller.

CHAPTER III

3 THE ELECTROCHEMICAL TECHNIQUE AND THE APPLICATION TO THE MASS TRANSFER MEASUREMENTS

3.1 INTRODUCTION

The diffusion - controlled electrochemical technique has been applied successfully in a variety of convective heat and mass transfer investigations. In this technique the transfer surface under investigation is enclosed by an electrode embedded flush with the surface, called the cathode, and another electrode called the anode which is situated downstream. An external potential is applied between these two electrodes when an electrolyte solution is used as the flow medium. Under the condition of diffusion - controlled reaction, the mass transfer coefficient, which is obtained from the rate of transfer of the ions in the solution can be estimated directly from the measured current. The technique has many advantages over other techniques in mass transfer measurements as it enables the evaluation of, not only average values of the mass transfer coefficients, but also point values and it can also detect fluctuations in the local values because of its fast response. It is relatively simple to use and to construct, and can give high accuracy since the current is effectively the only measured variable. However, the use of this technique is limited to study transport phenomena associated with liquids which exhibit diffusion - controlled electrochemical reaction characteristics.

3.2 MECHANISM OF DIFFUSION - CONTROLLED ELECTROCHEMICAL REACTION

Electrode reactions involve the transfer of ions from

the bulk of the solution to the surface of the electrode, and depend on the chemical and physical changes taking place at the surface of the electrode. Concentration polarization developed when the transfer of the ions occurs from the bulk of the solution to the electrode surface is the rate controlling step in the electrode process. This is accompanied by a decrease in concentration of the electrolyte in the immediate vicinity of the electrode. Moveover, chemical polarization may take place whereby the process rate is controlled by the electrochemical reaction on the surface of the electrode. By neglecting the chemical polarization when the concentration is zero at the liquid-solid interface, the mass transfer coefficient could be found directly from the limiting current.

In the electrochemical reaction, the ions are transferred from the bulk of the solution to the surface of the electrode by:-

a) Migration due to the potential field

b) Diffusion due to the concentration gradient

c) Convection by the flow

Therefore, the rate of mass transfer of a reacting species can be expressed as:

$$N_A = (D + E_\Psi)C_A\,(n/R_{Te})\left(\frac{\delta\Psi}{\delta y}\right) - (D + E_D)\left(\frac{\delta C_A}{\delta y}\right) + VC_A \qquad (3.1)$$

and applied to a steady and unidirectional transfer in the direction perpendicualr to the surface of the electrode. In equation (3.1), the three terms on the right-hand side represent the migration, diffusion, and convection terms respectively

The convection term can be neglected in the redox process because there is no net bulk flow in the y-direction within the boundary layer. A further simplifications to equation (3.1) can be introduced by eliminating the migration term by adding a large excess of an indifferent electrolyte, which does not react at the electrode, to the electrochemical solution. Such an electrolyte of high concentration and conductivity will prevent any potential gradient $(\frac{\delta \Psi}{\delta y})$ near the wall and therefore the migration term becomes negligible so that the reaction is then controlled by the diffusion process. Hence equation (3.1) becomes:

$$N_A = -(D + E_D) \frac{\delta C_A}{\delta y} \qquad (3.2)$$

integrating equation (3.2) gives:

$$N_A = K (C_b - C_i) \qquad (3.3)$$

and since:

$$N_A = I/An F \qquad (3.4)$$

substituting equation (3.4) into equation (3.3) gives:

$$K = I/An F (C_b - C_i) \qquad (3.5)$$

In the absence of chemical polarization, the concentration of electrolyte at the electrode surface will be zero. This means that the reacting ions having diffused through the boundary layer are immediately removed from the surface of the electrode by the electrochemical reaction with the result

that equation (3.5) becomes:

$$K = I/An\ F\ C_b \qquad (3.6)$$

When a negative potential is applied to the cathode, the positive ions migrate from the bulk of the solution to the cathode surface and the accumulation of these ions is equivalent to the charging current. As the potential is increased, the current increases exponentially and thereafter approaches a constant value called the "limiting current". Under these conditions the ions tranferred to the electrode surface react quickly and the increase in potential will not result in increase in the rate of the reaction. Lin (24) found that the value of the limiting current was proportional to the bulk concentration of the ions reacted at the cathode. When the potential increased over the limiting current region, a steep increase in the current occurs, due to the discharge by a secondary reaction.

As the flow rate increases, the value of the limiting current is increased and finally the flat portion of the polarization curves terminates above a certain upper limit of the flowrate; the reaction becomes too slow to remove all ions reaching the electrode surface. The upper limit of the flow rate is called "the critical flowrate".

3.3 THE REDOX SYSTEM

The redox system used consisted of equal concentrations of potassium ferricyanide and potassium ferrocyanide with a large excess of sodium hydroxide as an indifferent electrolyte. This system was chosen for this work, where the cathodic

reduction of potassium ferricyanide takes place on nickel electrodes. The reaction is:

$$F_e(CN)_6^{-3} + e \longrightarrow Fe(CN)_6^{-4} \quad \text{at the cathode}$$

$$Fe(CN)_6^{-4} \longrightarrow Fe(CN)_6^{-3} + e \quad \text{at the anode}$$

The anode usually has a larger surface area than the cathode. This arrangement of electodes makes the current density at the anode smaller than that at the cathode and the process at the anode has no noticable effect on the current voltage curve. Using the redox system, the steady state electrode potentials are reached in a much shorter time than in the deposition reaction, and the electrochemical reactions are very rapid at high mass transfer rates so that the concentration at the electrode surface is zero and chemical polarization is negligable, while the bulk concentration of the reacting ions remain virtually constant. Polished nickel electrodes were used in this system because they have a low surface roughness and remain physically unchanged during the electrochemical process.

Analytical methods for the determination of the concentration of the ferri cyanide ions and the ferro cyanide ions are simple and accurate. The iodometric titration with thio sulphate was used to determine the concentration of the ferri cyanide ions while the concentration of the ferrocyanide ions was determied by simple titration with permanganate under acidic conditions (25).

3.4 PRE-TREATMENT OF ELECTRODES

Chemical polarization has been one of the problems in applying the electrochemical technique. Most of the workers who have used this technique, found it necessary to treat the electrode surfaces before operation. Eisenberg (26) suggested a pre-treatment process of first polishing the nickel surface with a fine emery cloth, followed by washing with carbon tetrachloride to remove any grease left on the surface, and then activating these electrodes cathodically by the treatment with 5% sodium hydroxide solution by passing a current density of $20mA/cm^2$ for 15 minutes where hydrogen was evolved.

Mackley (27) followed a similar method of pre-treatment except that he did not degrease the electode and suggested that sodium hydroxide treatment was sufficient to clean the electrodes.

3.5 STABILITY OF THE ELECTROLYTE SOLUTION

3.5.1 EFFECT OF SUNLIGHT

Both ferricyanide and ferrocyanide ions decompose when they are exposed to the sunlight. Kolthoff and Pearson (28) proposed that the decompostion of the ferrocyanide ion took the form:

$$Fe(CN)_6^{-4} + H_2O \underset{\text{dark}}{\overset{\text{light}}{\rightleftharpoons}} \left[Fe(CN)_5.H_2O\right]^{-3} + C\bar{N}$$

$$C\bar{N} + H_2O \rightleftharpoons HCN + O\bar{H}$$

they believed that the decomposition of the ferricyanide ion follows the same behaviour . The stability of the solutions in sunlight depends upon the concentration of alkali present

in the solution as indifferent electrolyte. This causes the equation to move to the left and thereby makes the solution more stable.

Mackley (27) found that exposing the solution to sunlight for 48 hours decreased the ferrocyanide ion concentration by 10% and gave a corresponding increase in the concentration of the ferricyanide ion over this period. He suggested that an oxidation process occurs whereby the ferrocyanide ion is converted to ferricyanide ions.

3.5.2 EFFECT OF DISSOLVED OXYGEN

The presence of dissolved oxygen in the redox system decreases the value of the limiting current. The effect of the oxygen is very complex. It decomposes the ferricyanide ion into iron oxide which contaminates the electrode surface and produces chemical polarization as the surface concentration of the reacting ions increase above zero.

Sutey and Kundsen (29) investigated the time dependence of the effect of dissolved oxygen. They found that if test solutions were first saturated with nitrogen, further exposure to air for short periods of time did not greatly affect the value of the limiting current. Moreover, for a solution with 70% oxygen saturation, the limiting current dropped by only 5% over an operating period of 275 minutes.

3.6 APPLICATION OF THE ELECTROCHEMICAL TECHNIQUE TO THE MASS TRANSFER MEASUREMENTS

The use of the electrochemical technique can be applied to the measurements of mass transfer rates. At the electrode used as the mass trasfer surface, a limiting current can be established quickly from the reaction of the electrolytic

solution which is a direct measure of the mass flux of a specific species of ion at the measuring surface. Knowing the concentration of this species of ion in the bulk of the solution, the mass transfer coefficient can be calculated from equation (3.6).

Many authors have used and developed the electrochemical technique for the measurements of the mass transfer rates of different flow systems and various conditions. Eisenberg, Wilke and Tobias (30, 31) used the electrochemical method to study mass transfer at a vertical plate. They measured the limiting current by the deposition of copper and silver. Their results for the Laminar region were correlated by this equation:

$$N_{sh} = 0.67 \, (N_{Gr} \, N_{Sc})^{0.25} \qquad (3.7)$$

and were found to be in agreement with Wagner (32) who estimated the limiting current during the deposition of copper from an acidic solution of copper sulphate. Ibl's measurements (33,34) covered the transition region in addition to the laminar region and his results were correlated by:-

$$N_{sh} = 0.31 \, (N_{Sc} \, N_{Gr})^{0.28} \qquad (3.8)$$

Fench and Tobias (35) studied the free convection mass transfer at a horizontal plate using the cathode reduction of copper ions from copper sulphate solution and their results were correlated by:-

$$N_{sh} = 0.19 \, (N_{Sc} \, N_{Gr})^{1/3} \qquad (3.9)$$

Schutz (36) studied the mass transfer at the surface of a cylinder and a sphere using the electrolysis of copper sulphate in sulphuric acid and his correlation agreed with the equation obtained for free convection heat transfer from horizontal cylinders. Bazan & Ariva (37, 38) in their studies of the mass transfer on inner cylindrical electrodes found that the limiting current density is linearly related to the concentration of the reacting ions.

In studies of turbulent mass transfer between a pipe wall and a fluid in turbulent flow under conditions of a fully developed concentration profile, many equations have been proposed. All correlations to predict the mass transfer coefficient confirm that K_{∞}^{+} is proportional to N_{Sc}^{n} for high N_{Sc}. Lin (39) proposed $N_{Sc}^{2/3}$ and Disseler (40) suggested $N_{Sc}^{3/4}$. Shaw and Hanratty (41) in their measurements of fully developed mass transfer rates confirmed that K_{∞}^{+} is independent of Reynolds number.

Hubbard and Lightfoot (42) used the reduction of ferricyanide to measure the mass transfer rate in a rectangular channel at different Reynolds numbers and Schmidt numbers, and their results were in agreement with Chilton and Colburn empirical equation (43). Ross and Wragg (44) studied the rates of mass transfer by measuring the limiting current for the deposition of copper from acidified solution of copper sulphate onto copper cathodes which formed part of the inner wall of an annular flow cell. They studied fully developed laminar and turbulent flow conditions. They found that the average mass transfer coefficient increased with N_{Re} and found a definite change in the gradient between turbulent and laminar flow regions. Their correlation for laminar flow agreed with both the Leveque equation for

annulus flow and with the results of Friend and Metzner (45), and they claimed that the results of Lin (24) for a tube, based on the Leveque equation, was lower than the theoretical solution. Their correlation for turbulent flow agreed with results of both Lin (24) and Shaw, Reiss and Hanratty (46) for a circular tube.

Mizushin (47) compared the results of Lin (24), who measured the mass transfer rate between flow in the annulus and between two tubes and the wall surface of the inner tube, with those of Shaw (41), Hubbard and Lightfoot (42), and Harriot and Hamilton (48) who applied the dissolving wall method, Son and Hanratty (49), Lin (39) and Mizushin (50). He claimed that the correlations of Hubbard and Lightfoot (42) and Harriot and Hamilton (48) represented data better than that of Son and Hanratty (49).

Measurements were made for fully developed turbulent flow and for the entry region of a pipe where the local value of the mass transfer coefficient decreases from infinity at the inlet to a minimum value down stream. Shaw, Reiss and Hanratty (46) used the reduction of ferricyanide to study the effect of the entry length on the mass transfer coefficient. They reported that N_{Sc} for laminar flow was proportional to $(L/d_e)^{-1/3}$ and their results for N_{Sc} agreed with those of Eisenberg (26). They also found that the range of (L/d_e) over which dependency holds decreases as Reynolds number was increased.

In developing the electrochemical technique, Shaw (41) estimated the fluctuations in the local mass transfer rate to the wall by measuring the fluctuations in the electrical

current passing through isolated cathodes surrounded by the active surface. These fluctuations reflect the unsteady nature of the viscous sub-layer, which plays an important part in determining the transfer rates. Shaw discussed the effects of the cathode on his results and showed that the fluctuations tended to be averaged over the cathode surface and larger cathodes give smaller signals. Dimpolous and Hanratty (51) studied the flow around a cylinder to measure the velocity gradients in the boundary layer and they determined both the average and local values of the mass transfer coefficient. The measured values of the mass transfer coefficient were in agreement with the calculated values from the velocity gradients.

Mizushin (52) measured fluctuations in the mass transfer coefficient at the wall of an agitated vessel in addition to the average and local values. The vessel used for the measurements contained paddle-type impellers and an aqueous solution of copper sulphate and sulphuric acid was used as the electrolytic solution. A large section of the wall of the vessel was a cathodefor measuring the average mass transfer coefficient and in addition there were small isolated cathodes for the measurement of the local mass transfer coefficient. He found that the transfer of mass, heat and momentum were caused mainly by tangential motion of the fluid and that these were due to the vertical motion of fluid and were very small. He also found that $(\acute{K}/\overline{K})$ had a peak value at the height of the impeller, which was explained by the jet flow from the impeller.

In addition to applying the electrochemical technique to measure the mass transfer coefficient, Mitchell and Hanratty (53) developed this technique to measure the shear

stress and the velocity fluctuations in fully developed turbulent flow by measuring the limiting current to embedded cathodes in the wall of a pipe. These cathodes were rectangular in shape and made of nickel sheets. Also Reiss and Hanratty (54) used different sized nickel circular wires to measure the longitudinal and circumferential shear stress and velocity fluctuations, and Mitchell reported that the velocity fluctuation intensity near the wall was independent of Reynolds number. This was in agreement with measurements made by other authors (55, 56, 57) using the hot-film anemometer.

In measuring the velocity gradient in the viscous sublayer, Mizushina (47) reported that he used two special types of small probes, constructed at the University of Kyo to to measure the velocity in a tube using the redox system. These probes were called the hot-wire type probe and the blunt-nose type probe. The results of these measurements were calimed to be in agreement with the result of Klebanoff (58) for the measurements of flow along a flat plate with zero pressure gradient.

Sirkar and Hanratty (59) studied the relation between turbulent mass transfer to the wall and the velocity field at high N_{Sc}, in a fully developed turbulent flow in a pipe. From the measurements of the average mass transfer coefficient and the fluctuations in the mass transfer coefficient, they found that the value of the mass transfer intensity was 0.29 compared to 0.48 obtained by Shaw (41). Hanratty et al confirmed that the decrease in the intensity with increase of size was due to averaging over the electrode surface. Sirkar and Hanratty (60, 61) also studied the limiting

behaviour of the transverse turbulent velocity close to a wall. They found the root mean squared value of the component in the transverse direction was about 0.09 of the time averaged velocity gradient to the wall. This was in agreement with the photographic measurements of solid particles close to a wall. They concluded that close to the wall the transverse component was increased linearly with distance form the wall.

CHAPTER IV

4 STUDIES ON THE VISCOUS SUB-LAYER

4.1 INTRODUCTION

The laminar sub-layer, described as a quasi-laminar flow along a fluid-solid interface, has been the subject of numerous investigations for more than 75 years. In this layer, resistance to the transfer of mass between solid boundary and a turbulent field occurs. Prandtl (62), in his hypothesis for the boundary layer, suggested that the viscous effects are of great importance and influence the fluid motions adjacent to the wall.

General turbulent flow is usually divided into three regions:

1. Turbulent core,
2. Transition zone,
3. Sub-layer region

The sub-layer region is usually called the laminar sub-layer, but it is more appropriate to refer to it as the viscous sub-layer because of the unsteady nature of fluid motion in this layer. The wall region, which is often referred to the combination of the viscous sub-layer and the transition region, has a great importance in the control of transport phenomena and the generation and maintenance of turbulence. The relatively small amount of mixing within the sub-layer compared to that of the core cause transport in this region to proceed in-part by molecular mechanisms, and consequently, occurs more slowly here than elsewhere. Many workers have attempted to predict the rate of transport in this region and

to develop models of the phenomena. Some notable contributions were made by Von Karman (63), Li Moutlon and Putnam (39), Deissler (40), Higbie (64), Danckwerts (65), Harriott (66), Hanratty (77) and Toor and Merchells (67). Also, extensive experimental work has been carried out by many workers using different techniques. Most of the techniques applied have been satisfactory. Visually it is difficult to obtain accurate quantitative data. Measurements with hotwire, hotfilm, or pitot tube are limited by the size of the probe and the possibility of disturbing the flow field. However, promising results have been obtained by Reiss (54), Hanratty (77) and Mitchell (53) using the electrochemical technique.

4.2 VELOCITY DISTRIBUTION

In studying the nature of turbulent motion at Reynolds numbers greater than a critical value, turbulence eddies must be characterised by their velocities, and by the distance over which these velocities change significantly. These distances are known as the scale of motion. The most rapid eddy has the largest scale of motion (ℓ). Such large eddies contain the main part of the kinetic energy of the turbulent motion but eddies of a smaller scale (λ), exist in addition to the large scale eddy and although these eddies are large in number, they represent only a small portion of the kinetic energy of the stream. They are created by the superposition of large scale eddies on each other and therefore the Reynolds number decreases rapidly with decreasing λ.

There is a continuous transfer of energy from large-scale eddies to small scale eddies and as the energy is dissipated there is

an increase in the number of the small scale eddies. The energy loss occuring in the flow can be expressed by the eddy viscosity as:

$$\varepsilon = \mu_{turb} \left(\frac{\Delta V}{\ell}\right)^2 \qquad (4.1)$$

Near the solid surface, these turbulent eddies of small scale do not suddenly disappear, but are gradually damped, due to the effect of viscosity.

Studies of turbulent flow confined within pipes and channels or bounded on one side by a wall have shown that the power laws are useful in providing an approximation of the mean velocity distribution over a limited Reynolds number range. These laws are empirical. For smooth straight pipes of circular cross-section, the power law, based on Blassius resistance formula, was found to be applicable to two-dimensional channels with parallel smooth walls and two-dimensional layers (68). In deriving these laws, the pressure gradient was neglected or made to change slowly in the stream direction so that its effect was minor compared to the effect of the wall shear stress. The following formula (68) was obtained by assuming the local friction coefficient to depend on the Reynolds number:

$$\frac{\bar{V}}{U^*} = C \left(\frac{U^* y}{\gamma}\right)^{\frac{m}{2-m}} \qquad (4.2)$$

and for pipes the formula takes this special form:

$$\frac{V}{V_{max}} = \left(\frac{y}{\delta}\right)^{1/2} \qquad (4.3)$$

Prandtl (62) derived the "law of the wall" which covers the region close to the wall where the effect of viscosity is directly felt. He based his hypothesis on the assumption that the tangential stream at the wall must depend on the velocity U at the distance y from the wall, on the viscosity μ, and the dènsity ρ. He developed the following general expre ssion:

$$\frac{V}{U^*} = f\left(\frac{U^* y}{\gamma}\right) \qquad (4.4)$$

and for the laminar sub-layer, the law takes this special form:

$$\frac{V}{U^*} = \frac{U^* y}{\gamma} \qquad (4.5)$$

or:
$$V^+ = y^+ \qquad (4.6)$$

This arises from the circumstances that the sub-layer is so thin that the shear stress (τ) there-in is constant and equal to (τ_w). Prandtl, suggested that the range of (y) over which the law of the wall is valid must be established by experiment, but found it to be valid even when there is a pressure gradient, until conditions of near "separated flow" were reached.

Von Karman (63) introduced the "velocity-defect law" which covers the bulk of the shear layer where viscous forces

become negligible. The law is based on the argument that the reduction in velocity ($V_{max} - V$) at a distance y is the result of a tangential stress at the wall and is independent of how this stress arises, but dependent on the distance (δ) to which the effect has diffused from the wall. The following expression represents the general form of the velocity-defect law:

$$\frac{V_{max} - V}{U^*} = g(\frac{y}{\delta}) \qquad (4.7)$$

Unlike the law of the wall, this law is applied for rough as well as smooth walls, provided the roughness elements are not so large that (y) becomes indeterminate. The law is different for pipes and channels than for boundary layers, as it is affected by the pressure gradient and the free stream turbulence. Von Karman, in his hypothesis for turbulent flow past a solid plate, divided the flow into three regions:

1. Region of turbulent flow
2. Region of "Buffer" layer
3. Laminar sub-layer

and assumed that the turbulent flow in the buffer layer is damped as it approaches the solid wall and that the same law for the turbulent flow region is applicable here except that the viscosity effect becomes significant. While Prandtl (62) in his hypothesis, assumed that in the region $y < \delta$, the fluid motion is entirely laminar and called this region as the "laminar sub-layer".

Landau and Levich (69) stated that the turbulent motion in the viscous sub-layer does not suddenly disappear but is gradually damped as it approaches the wall, and that the quantities in the viscous sub-layer may be functions of viscosity. They added that although turbulent eddies do not originate in the viscous sub-layer, they enter it from the side $y > \delta$, and that the eddy velocities have the same magnitude as the average velocities in the sub-layer. They found the following expressions for the velocity distributions at different regions:

1. at $0 \leq y^+ \leq 5$

$$V^+ = y^+ \tag{4.8}$$

2. at $5 \leq y^+ \leq 30$

$$V^+ = 10 \text{ arctg } (0.1y^+) + 1.2 \tag{4.9}$$

3. at $y^+ > 30$

$$V^+ = 5.5 + 2.5 \ln y^+ \tag{4.10}$$

Belov et al, (70) studied the relationship between average and fluctuation characteristics in the boundary layer near the wall of a flat plate upon which a jet stream was impinging. They used the hot-film anemometer and a micro-pitot tube for the velocity measurements. Their results of the measurements of the distribution of the mean average velocity across the boundary layer near the plate showed that the field of average velocities in the region near the wall is similar to the field near the edge of the plate, and can be described by the well-known Blassius profile for a laminar boundary layer. They found that, as the critical Reynold's number increased, the velocity profile

becomes more inflated, which indicates the transition from laminar flow in the boundary layer to a turbulent form. They described the velocity profile in the laminar sub-layer by the following relationship:

$$\frac{V}{U^*} = yU^*/\gamma \qquad (4.11)$$

while in the completely turbulent region, the average velocity profile was:

$$\frac{V}{U^*} = 5.75 \log yU^*/\gamma + 5.5 \qquad (4.12)$$

They explained that the fluctuations of the velocity, when the jet penetrated deeply into the boundary layer near the plate, generated conditions for acceleration of the transition from a laminar form to a turbulent form of flow. They found that the maximum fluctuations occured in the immediate vicinity of the wall.

Taylor (71), Deissler (72) and Rannie (73) obtained similar expressions for the velocity profiles at different ranges of y^+. Reicherdt (74) found an expression for velocity profile which covers the whole range of y^+ but it was rather complex while Van Driests formula (75) for the whole range of y^+ involved a quadrature requiring numerical evaluations. However, Spalding (76) obtained a formula for the experimental velocity distribution in the laminar sub-layer and the turbulent core which was of the form:

$$y^+ = \overset{+}{V}^+ + 0.1108\left(e^{0.4V^+} - 1 - 0.4V^+ - \frac{(0.4V^+)^2}{2!} - \frac{(0.4V^+)^3}{3!} - \frac{(0.4V^+)^4}{4!}\right) \qquad (4.13)$$

4.3 NATURE OF THE VISCOUS SUB-LAYER

Hanratty (77) described the exchange of mass and heat between a turbulent fluid and a solid surface through a model formulated by Danckwerts (78) to explain mass transfer in two-phase system. According to this model, the fluid in the immediate vicinity of the wall is not a continuous laminar layer but is discontinuous. He assumed that when a mass of fluid comes in contact with the wall, there will be an equilibrium state, but the rate of exchange between fluid masses and the wall decrease with time until eventually all the masses were replaced and the whole process was then repeated. He found that the measured exchange rate with the wall increased with decrease of the average contact time. Velocity profile data derived from Hanratty's model were in good agreement with Deissler's date (72).

Einstein and Li (79) proposed a model which visualized a periodic growth and decay of the sub-layer. The magnitude of the life-period of the sub-layer was predicted theoretically and has been checked experimentally. They assumed that when turbulent flow with a finite main velocity exists at the boundary near the wall, there will be a high velocity gradient at the wall which results in a high viscous shear. This shear, which is not transmitted to the free fluid, will decelerate fluid adjacent to the boundary creating a viscosity controlled sub-layer growing in thickness

with time. Consequently, the boundary shear will be reduced and the growth becomes increasingly slower. Therefore, they assumed that the sub-layer was unsteady laminar flow bounded on one side by the rigid wall, and by turbulent flow in the other side. Under these circumstances, they found that the Reynolds number of the sub-layer increased continuously, indicating an over-growing tendency to become unstable. They added that under the effect of the disturbances from the turbulent flow outside, the flow in the sub-layer became unstable and turned into turbulent flow as soon as a critical value of Reynolds number has been exceeded. This will cause turbulent mixing between the previously turbulent flow and the newly created sub-layer turbulence, and when this mixing is more effective than viscosity, the fluid in the sub-layer will be accelerated by the turbulent fluid outside to about the bulk velocity in a time shorter than that required for the viscous sub-layer to build up. When this cycle terminated, a new cycle began. According to the above theory, it was assumed that the entire sub-layer becomes part of the turbulent flow during the decay period, but it was possible that only the outer part of the sub-layer becomes turbulent while the inner part of the sub-layer remains always at the boundary.

On the basis of this theory they presented a mathematical model for the period of growth of the sub-layer assuming uni-directional unsteady flow. They also assumed that the eddy-viscosity of the turbulent flow to be larger than the molecular viscosity of the fluid during the period of decay, resulting in a constant average velocity at all points of the turbulent flow. They found the following equations:

$$V = \frac{2V_B}{\sqrt{\pi}} \int_0^H e^{-h^2} dh \qquad (4.14)$$

where $$H = \frac{Z}{2\sqrt{\gamma t}} \qquad (4.15)$$

$$\delta_v = \frac{2}{\sqrt{\pi}} \sqrt{\gamma t} \qquad (4.16)$$

and $$T_p = \frac{4}{\pi} \frac{V_B^2 \gamma}{U*^4} \qquad (4.17)$$

Sackmann and Heltler (80) injected dye and observed that it is either mixed with the turbulent flow almost instantly or it is carried down stream for some time before mixing occurs. They stated that the dye injected into the laminar sub-layer will not mix with the turbulent flow if the injection pressure matches correctly the pressure in the following fluid; that is, if the laminar sub-layer is not disturbed. This approach differs from Einstein and Li (79) who explained that this depends on whether the laminar sub-layer is in the growth period or in the decay period.

In an attempt to modify the model proposed by Einsten and Li (79), Meek and Baer (81) carried out measurements in steel and pyrex tubes, for air and liquid, systems using a thermo-system boundary layer probe to measure velocity fluctuations very close to the wall. They determined the mean period of growth and decay of the sub-layer and the maximum and minimum values of the sub-layer thickness in the direction normal and parallel to the flow direction and found that:

$$T_p^+ = \frac{2V_B^+}{\sqrt{\pi}} \qquad (4.18)$$

and $$\delta^+ = 3.64T_p^+ \qquad (4.19)$$

These equations are in good agreement with Schlichting (82). The computed velocity profiles were compared with the experimental data of Hummel (83) and were in agreement, except near the outer edge of the sub-layer where a discrepancy in slope exists because of the semi-infinite boundary condition. They also carried out some measurements on the effect of polymer on the system and found that it reduced the pressure drop and increased the thickness of the layer because of the elastic effects which stabilize the sub-layer. However, this effect is instantaneous when the polymer is injected in the region of the sub-layer, while if the polymer is injected in the main flow, it would take time before it affected the sub-layer.

Kline and Runstadler (84) used the flow-visualization technique to study the flow in the wall layer of the turbulent boundary layer. They injected a line of dye in a two-dimensional water channel across the entire flow on a wall, using a needle attached to a standard medical syringe. They found that when the dye was introduced very close to the wall, in a turbulent boundary layer, the wall layer was not two-dimensional but instead it consisted of a repeated three-dimensional pattern. They did not give complete details, but they described the pattern to consist of arrays of " islands of hesitation" and longitudinal vortices which impart a wispy appearance to the flow. These islands of hesitation were found as long stretched filaments

in the direction of flow which move down stream more slowly than the surrounding fluid. It was believed that the vortex originated as a break-down or roll-up along the edge of the islands of hesitation and orientated in the direction of flow, but stand at a slight angle to the wall so that its distance from the wall increases as it moves down-stream. When they reached a certain critical distance from the wall they broke-up into a typical turbulent eddy, by a process which is too rapid for the eye to follow. They failed however, to give a quantitative value of this distance. When comparing their results with the results of Townend (85), Laufer (86), Shigemiton (87), Einstin and LI (88), Coles (89), and Clausser(90), they found that all these results support their model.

Black (91) developed a theory based on the hypothesis that the primary role of random turbulence in the wall shear layer is not to transfer mean momentum locally, but to excite a violent repetitive instability in the sub-layer flow. According to this theory, Black explained that energy is transferred from the basic linear motion to a rotational mode at each point of break-down, and this break-down was regarded as a moving vortex generator, located near the edge of the sub-layer. Each break-down is accompanied by a strong jet like eruption of fluid across the layer which carries the generated vorticity outwards to form a continuous vortex sheet at some angle to the wall. He found that, since the turbulence does not contribute to the local momentum transfer, the time-dependent motion between successive break-down will be governed only by viscous stress and by the stream-wise pressure gradient, if it exists. Therefore,

turbulent wall shear flow is a time-dependent viscous motion which strives continuously to return to its original laminar state but which is continually thwarted by repetitive breakdown due to an instability excited by the turbulence within the layer. Instead of dividing the layer into a viscous sub-layer and a fully trubulent flow, Black divided it into a temporal regime of slow viscous development and rapid inviscid breakdown. During the development period, the sub-layer regions suffer an increasing momentum deficit as a result of viscous deceleration of the wall layer, while during the short breakdown period, this momentum deficit is transferred to the outer region by the strong outflowing jet of fluid associated with the breakdown.

Corino and Brodkey (92) made an investigation of the fluid motion very close to a solid boundary. They developed a technique that involved suspending solid particles of colloidal size in a liquid and photographing their motion with a high-speed camera moving with the flow to give detailed observations of the region close to the wall of a pipe They observed a change in the character of the fluid motions with distance from the wall. The sub-layer was continuously distrubed by small-scale velocity fluctuations of low magnitude and periodically distrubed by fluid elements which penetrated into the region from positions further removed from the wall. From a thin region adjacent to the sub-layer, fluid elements were periodically ejected outwards towards the centre. These events were found to produce a zone of high shear and when the ejected elements entered this shear zone, it interacted with the mean flow and created intensive, chaotic velocity fluctuations which

are believed to play an important role in the wall region. They observed an increase in size of the scale of disturbance with increasing distance from wall, which agreed quantitatively with the visual studies of Kline et al (93) and Nedderman (94), and qualitatively with hot-film measurements of Laufer (86), and with the indirect measurements of Mitchell and Hanratty (53) using the electro-chemical technique.

Kim et al (95) made extensive visual and quantitative studies of the turbulent boundary layer using the hot-wire anemometer to measure the mean velocity in a water channel and the visualisation method by generating time-lines and forming streaks to find the instantaneous velocity distribution. They revealed the presence of well-organised and temporarily dependent motions within the viscous sub-layer which lead to the formation of flow-speed streaks in the region very close to the wall. These streaks interact with the outer portions of the flow through a process of gradual "lift-up", then sudden oscillation, bursting and ejection. They believed that the process helps in the production of new turbulence and transport of turbulence within the boundary layer on smooth walls. Kim et al (95) examined the structure of the boundary layer of a smooth flat plate in a low-speed water flow using the hot-wire anemometer and the visualisation method and their results supported the theory of Kline et al (93). They believed that all the turbulence production occurs during intermittent "bursting periods", and explained this process in three stages.

1. Lifting of the low-speed streaks from the inner layer which form unstable instantaneous velocity profile.

2. Growth of an oscillatory motion in the region of flow; flowing from the instable zone.

3. Break up of the oscillatory, but well-defined, motion into more random or chaotic motions accompanied by a return to the wall of the low-speed streak.

4.4 WALL TURBULENCE

Fage and Townend (96) used the ultra-microscope to study the micro-turbulence near the boundary of the fluid in pipes. They found that near the centre of the pipe the ratios v'_z/V v'_ϕ/V and v'_r/V are approximately equal, but as the wall was approached, the ratio v'_ϕ/V obtained from the velocity disturbance normal to the wall decreased to zero, whilst the other ratios increased. They also found that in the region near the wall, there were no particles moving in a rectilinear path. This contradicts the concept of the viscous sub-layer. Taylor (97) derived an expression for the unstable disturbance which forms in a viscous fluid contained between two cylinders and compared his results with the experimental results of Fage and Townend (96). He found that the disturbance between two rotating cylinders exhibits all the characteristic features which were observed in the neighbourhood of the wall of a pipe through which fluid is flowing under pressure. He explained that the reason for the rapid increase in v'_r/V compared to v'_z/V as the surface is approached was that the transverse component of the pressure gradient at the surface is large compared with the longitudinal component. In studying the region near the wall, Lin et al (39), measured the concentration distribution near the surfaces of concentration-polarized electrodes

in turbulent fluid streams using the deposition of Cadmium metal from Cadmium sulphate solution. He also confirmed the concentration changes by means of light interference. The change in the concentration of the fluid was followed by a change in the refractive index, causing the displacement of interference fringes which consequently give the local concentration at any point in the fluid. Since the Schmidt number was high, the concentration of Cadmium ions was essentially constant throughout the fluid and dropped to zero at the wall, and the concentration profile therefore, was greatly dependent on conditions in the region of the sub-layer. They assumed that turbulence existed in the laminar sub-layer and claimed that there is no definite laminar film of pure molecular diffusion near the wall. Also that the concept of different fluid layers is not correct and can be eliminated. Hanratty (77) confirmed that these results and the results of Fage and Townend (96) both contradict the concept of the viscous sub-layer.

Popovich and Hummel (98) applied the flash photolysis method to study conditions in the viscous sub-layer in a square section smooth pipe. The technique consisted of introducing a coloured tracer in the form of a parallelpiped into a photo-sensitive fluid by focusing the image from a Xenon flash tube onto the test section of a pipe. They compared their results of the mean velocity distribution in the viscous sub-layer with the results Reichardt (99), obtained by the hot-film anemometer, Nikuradse (98) using the pitot tube and Hetler (100) using the particle method. All these results agreed well up to a distance about $y^+ = 17$ from the wall, while between $y^+ = 17$ and $y^+ = 56$,

the results obtained by the particle method were lower than those obtained by other methods and were in agreement with their results. Popovich and Hummel's results were also in good agreement with the theory of Hanratty (77). Echelmann and Reichardt's results (101) obtained from the measurements in a turbulent channel flow using the hot-film anemometer showed that in the vicinity of the wall, $y^+ < 0.1$, the ú fluctuations were proportional to the wall distance y^+; and the distribution of this fluctuation normalised with the local mean velocity in this region showed a maximum intensity of 0.37 at a distance of $y^+ \simeq 4$ and a minimum value of 0.24 at the wall. These values were confirmed by Laufer (86) and Bakewell (102) who also found that within the sub-layer both signals of the hot-film probe and the wall probe were very similar, but the probe signal precedes the wall signal. This similarity was also found by Gupta (103), and the lead in the probe signal was also observed by the visual studies of both Corino and Brodkey (92), and Kline and Runstadler (84). Thomas and Greene (104) also used the hot-film anemometer to study the characteristics of the viscous sub-layer for both Newtonian and drag reducing solution in turbulent tube flow. They suggested that the effect of the mean axial pressure gradient on the viscous sub-layer becomes important for the deeper molecular penetration associated with low Reynolds number, and this was valid until the value of Reynolds number exceeded a critical value where transition from laminar to turbulent flow occurs. Their results were in basic agreement with the data of Meek and Baer (81).

Sternburg (105) carried out measurements near the wall for a boundary layer and a pipe flow to determine the

variation of the velocity fluctuations and the turbulent shear stress. He calculated the variation of the shear stress using the measured mean velocity profile and the fact that the total shear stress is constant near the wall. He found that the turbulent shear stress and the fluctuations in the region outside the wall vary slowly compared to the wall region. Inside the wall region, he found that ú fluctuation first increases to a maximum value well inside the wall region and at the point where it starts to rise, the shear stress starts to decrease. He suggested that the viscous sub-layer is the entire region between the wall and the fully turbulent part of the flow and gave no indication to the presence of a transition zone between those two layers.

Nagata et al (106) used the hot-film anemometer to measure and analyse the turbulent motion in an unbaffled cylindrical mixing vessel with a 6-blade turbine. Their measurements of the tangential velocity by the hot-film anemometer were in good agreement with their previous measurements using the pitot tube and showed that the value of the radial velocity is rather high at the impeller height but is only one-fourth of the tangential velocity. They confirmed that the radial and axial mixing is much slower than tangential mixing. They compared their results with the results of baffled agitation (106) and found that the fluctuation velocity in the unbaffled agitation vessel is smaller at the impeller height, but is larger in parts remote from the impeller.

Armistead and Keyes (107) used flush-mounted hot-film sensors to study local turbulence-induced fluctuations in the rate of heat transfer in a pipe through which water

flowed. In their studies of the relationship between the heat transfer fluctuations in the vicinity of the wall, they found a significant correlation which decreased as the anemometer was moved from moderate distance upstream to moderate distances downstream of the wall sensor. They also observed a periodic component in the correlation curves of velocity fluctuations in the vicinity of the wall and it was of the same order of magnitude as that predicted by Einstein and Li (88), and Black (91) for sub-layer flow models.

CHAPTER V

5 THEORETICAL ANALYSIS OF FLOW CHARACTERISTICS

5.1 INTRODUCTION

In fluid motions for which the measured pressure distribution nearly agrees with the perfect fluid theory, the influence of viscosity at high Reynolds numbers in confined to a very thin layer in the immediate vicinity of the solid wall (82). In that layer the velocity of the fluid increases from zero at the wall (no slip) to its full value corresponding to the external frictionless flow. This layer is the boundary layer and in this layer the velocity gradient normal to the wall is very large and the viscosity of the fluid exerts a large influence so that the shearing stress may assume large values.

The efflux of a jet from an orifice or a propeller affords an example of motion in the absence of solid boundaries to which it is possible to apply the boundary layer theory. The characteristics of jet flow from propeller mixers may be analysed to show how the mixing process can be accomplished in large tanks. The stream emerging from the impeller behaves like a circular submerged jet where the high velocity fluid causes entrainment, and turbulence spreads the entrained fluid throughout the jet.

The amount of fluid discharged from a rotating impeller is of significance because of its volume rate and the area through which it flows. For a propeller, the flow is that which emerges at the face of the impeller at a cross-sectional area based on the propeller diameter. It has been shown that:

$$Q = KNd^3 \qquad (5.1)$$

The flow of liquid initiated by a propeller has more turbulent energy than that of a nozzle jet. The rate at which liqiud is entrained per unit power expended is a good index to mixing in large tanks fitted with side-entry propellers. The direction of flow of a nozzle jet is axial, while, due to the torque exerted on the propeller blades, there is a rotary flow in addition to the axial flow in the propeller jet.

5.2 ENTRAINMENT

In the mixing process of turbulence where masses and materials are transported in all directions, not only the rapid-moving liquid moves into slow moving zones, but also slow moving liquids will be entrained into more rapid zones. The phenomena of entrainment is well illustrated by the flow of a submerged fluid jet (4):

Figure (1) is a schematic diagram of the spread of a circular jet in a quiet fluid, in the x - y plane. The velocity gradients near the boundary of the jet, where high velocity flow is adjacent to low velocity flow, is sufficient to create instability and initiate turbulence. The turbulence spreads towards the centre of the stream and into the quiet fluid. At the boundary of the jet where the velocity gradient is sufficiently high, materials are accelerated by momentum transfer and become a part of the flowing jet. The velocity profiles across the jet will vary with distance from the jet entrance and decrease to such a value that there will no longer be a sufficiently large value of velocity

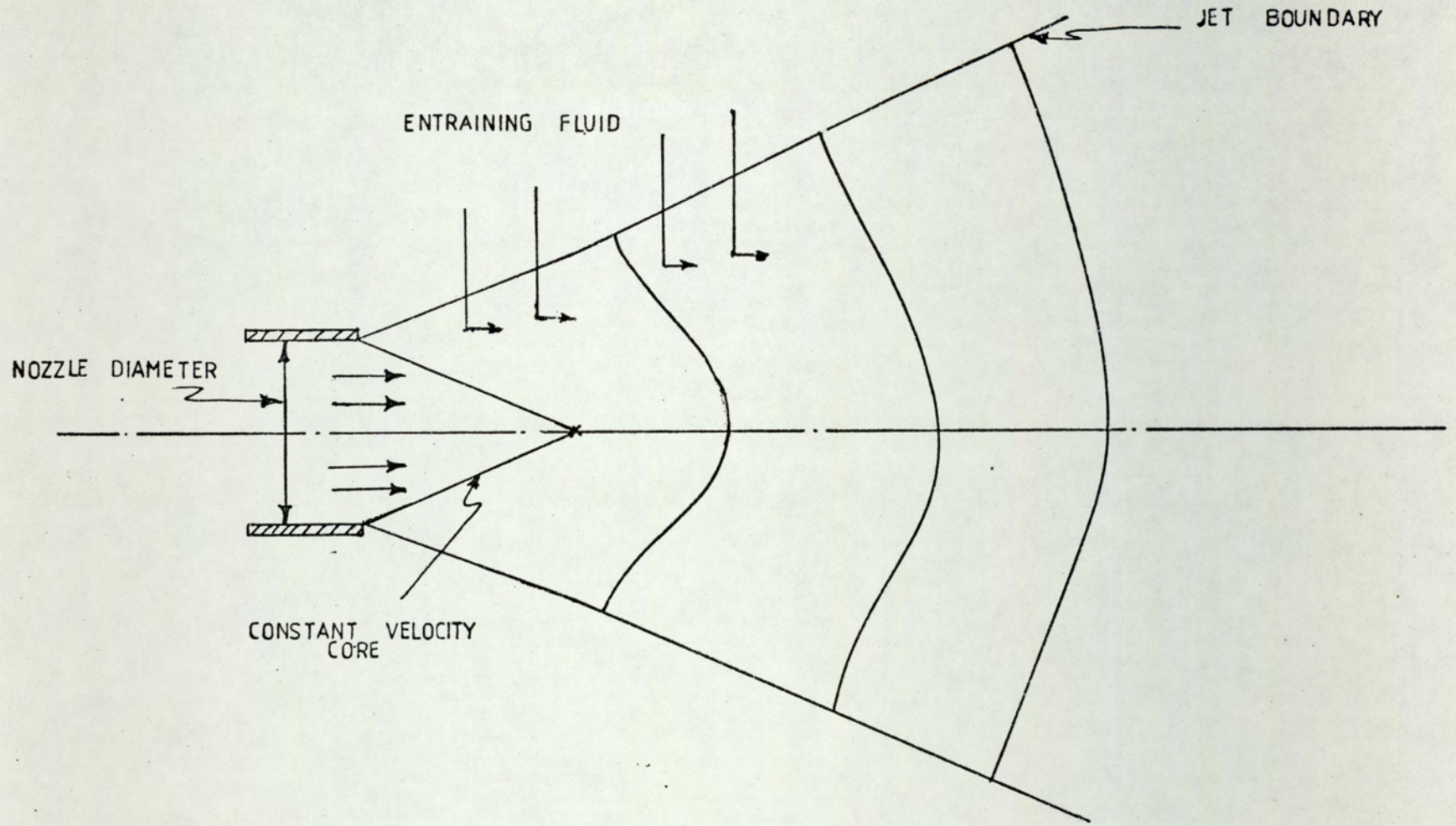

FIGURE_ 1 _ FREE TURBULENT JET EMERGING FROM ANOZZLE

gradient to cause more entrainment.. Mixing will proceed between the surrounding fluid and the jet, and within the jet, during the entire process.

Mixing of fluids in a large tank fitted with a side-entry propeller could be simulated to an axially symmetric jet injected into a fluid at rest. The zone between the jet boundary and the base of the tank where the boundary layer lies, can be characterized by the velocity profiles of the jet at its boundaries. To find the velocity distributions on the jet boundaries, in all directions, it is necessary to take a volume element in the jet and study the mass and momentum balance over this element.

Taking cylindrical polar cordinates (z, ϕ, r), as shown in figure (2), and denoting the velocity components V_z, V_ϕ, V_r respectively, the overall mass balance is:

$$\frac{\delta\rho}{\delta t}(r\delta\phi\delta r\delta z) = -\left[\frac{\delta}{\delta z}(\rho V_z \delta\phi r\delta r)\delta z + \frac{\delta}{\delta\phi}(\rho V\phi \delta z\delta r)\delta\phi + \frac{\delta}{\delta r}(\rho V_r \delta z\delta\phi)\delta r\right] \qquad (5.2)$$

where the left-hand side of the equation represents the rate of accumulation and the right-hand side represents the net mass perpendicular to face z, ϕ and r respectively.

For an incompressible fluid, the density of the fluid is constant and for a steady state:

$$\frac{\delta V_r}{\delta r} + \frac{V_r}{r} + \frac{1}{r}\frac{\delta V\phi}{\delta\phi} + \frac{\delta V_z}{\delta z} = 0 \qquad (5.3)$$

The momentum balance on a volume element is:

$$\begin{pmatrix}\text{Rate of momentum}\\ \text{accumulation}\end{pmatrix} = \begin{pmatrix}\text{Rate of}\\ \text{momentum}\\ \text{in}\end{pmatrix} - \begin{pmatrix}\text{Rate of}\\ \text{momentum}\\ \text{out}\end{pmatrix} + \begin{pmatrix}\text{sum of pressure}\\ \text{and gravity}\\ \text{effect}\end{pmatrix}$$

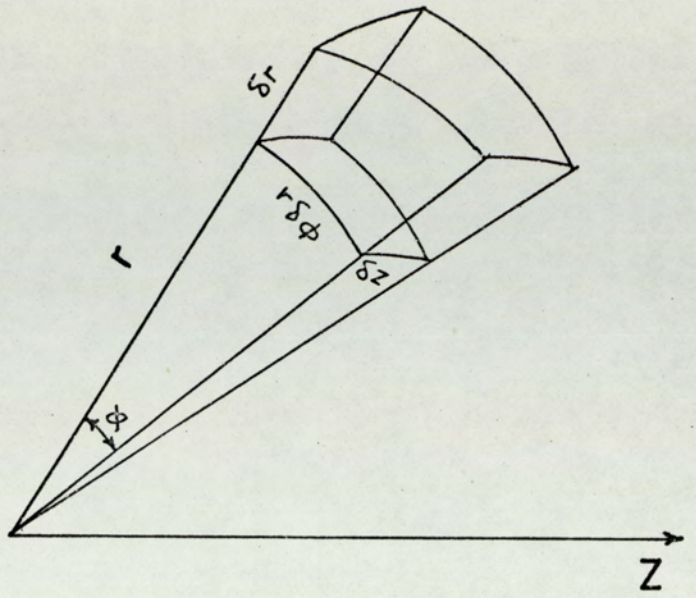

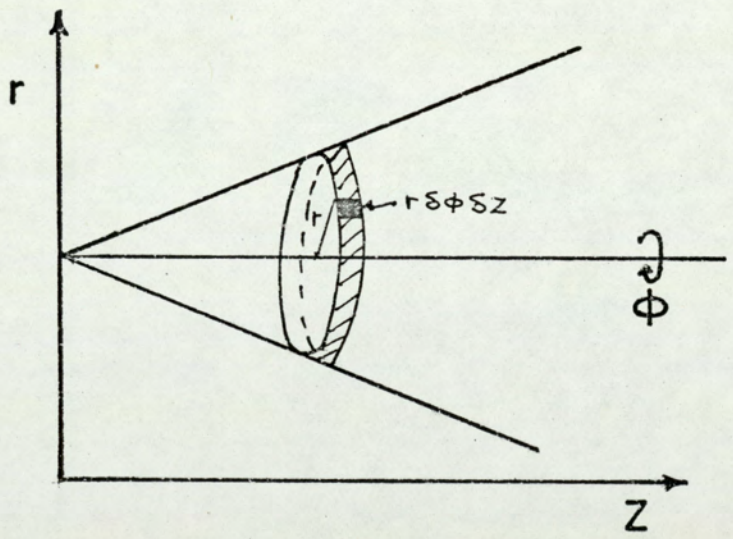

FIGURE_2_REPRESENTATION OF THE AREA OF AN ELEMENT IN THE JET

For the component z, the overall momentum balance is:

$$\frac{\delta \rho V_z}{\delta t} = -\rho\left[\frac{\delta}{\delta z}(V_z V_z) + \frac{1}{r}\frac{\delta}{\delta \phi}(V_\phi V_z) + \frac{1}{r}\frac{\delta}{\delta r}(rV_r V_z)\right] - \left[\frac{\delta \tau_{zz}}{\delta z} + \frac{1}{r}\frac{\delta \tau_{\phi z}}{\delta \phi} + \frac{1}{r}\frac{\delta}{\delta r}(r\tau_{rz})\right] - \frac{\delta P_z}{\delta z} + \rho g_z \qquad (5.4)$$

Similarly, the momentum balance for component ϕ and r, give the following two equations respectively:

$$\frac{\delta \rho V_\phi}{\delta t} = -\rho\left[\frac{\delta}{\delta z}(V_z V_\phi) + \frac{1}{r}\frac{\delta}{\delta \phi}(V_\phi V_\phi) + \frac{1}{r}\frac{\delta}{\delta r}(rV_r V_\phi)\right] - \left[\frac{\delta T_{z\phi}}{\delta z} + \frac{1}{r}\frac{\delta T_{\phi\phi}}{\delta \phi} + \frac{1}{r}\frac{\delta}{\delta r}(rT_{r\phi})\right] - \frac{1}{r}\frac{\delta P_\phi}{\delta \phi} + \rho g_\phi \qquad (5.5)$$

and:

$$\frac{\delta \rho V_r}{\delta t} = -\rho\left[\frac{\delta}{\delta z}(V_z V_r) + \frac{1}{r}\frac{\delta}{\delta \phi}(V_\phi V_r) + \frac{1}{r}\frac{\delta}{\delta r}(rV_r V_r)\right] - \left[\frac{\delta}{\delta z}\tau_{zr} + \frac{1}{r}\frac{\delta \tau_{\phi r}}{\delta \phi} + \frac{1}{r}\frac{(r\tau_{rr})}{\delta r}\right] - \frac{\delta P_r}{\delta r} + \rho g_r \qquad (5.6)$$

by subsituting the values of the shear stress (82) in equations (5.4), (5.5) and (5.6), the following is obtained:

$$\rho\left(V_r\frac{\delta V_z}{\delta r} + \frac{V_\phi}{r}\frac{\delta V_z}{\delta \phi} + V_z\frac{\delta V_z}{\delta z}\right) = -\frac{\delta p}{\delta z} + \mu\left(\frac{\delta 2V_z}{\delta r^2} + \frac{1}{r}\frac{\delta V_z}{\delta r} + \frac{1}{r^2}\frac{\delta 2V_z}{\delta \phi^2} + \frac{\delta 2V_z}{\delta z^2}\right) \qquad (5.7)$$

$$\rho\left(V_r \frac{\delta V_\phi}{\delta r} + \frac{V_\phi}{r} \frac{\delta V_\phi}{\delta \phi} + \frac{V_r V_\phi}{r} + V_z \frac{\delta V_\phi}{\delta z}\right) = -\frac{1}{r} \frac{\delta p}{\delta \phi} + \mu\left(\frac{\delta 2V_\phi}{\delta r^2} + \frac{1}{r} \frac{\delta V_\phi}{\delta r}\right.$$

$$\left. -\frac{V_\phi}{r^2} + \frac{1}{r^2} \frac{\delta 2V_\phi}{\delta \phi^2} + \frac{2}{r^2} \frac{\delta V_r}{\delta \phi} + \frac{\delta_2 V_\phi}{\delta z^2}\right) \qquad (5.8)$$

and

$$\rho\left(V_r \frac{\delta V_r}{\delta r} + \frac{V_\phi}{r} \frac{\delta V_r}{\delta \phi} - \frac{V_\phi^2}{r} + V_z \frac{\delta V_r}{\delta z}\right) = -\frac{\delta p}{\delta r} + \mu\left(\frac{\delta_2 V_r}{\delta r^2} + \frac{1}{r} \frac{\delta V_r}{\delta r}\right.$$

$$\left. -\frac{V_r}{r^2} + \frac{1}{r} \frac{\delta_2 V_r}{\delta \phi^2} - \frac{2}{r^2} \frac{\delta V_\phi}{\delta \phi} + \frac{\delta_2 V_r}{\delta z^2}\right) \qquad (5.9)$$

Equations (5.7), (5.8), and (5.9) are called the equations of motion. These three equations together with equation (5.3) constitute the Navier-Stokes equations.

In the system considered, there are:

1. No external forces acting on the system.
2. The density and the viscosity are constant (incompressible fluid).
3. Steady State.
4. The pressure gradient is small and negligble; because the liquid is in contact with the atmosphere and the momentum is constant across the jet.
5. Having an axial symmetry, all the derivatives with respect to ϕ are zero.

Therefore the Navier-Stokes equations become:

$$V_r \frac{\delta V_z}{\delta r} + V_z \frac{\delta V_z}{\delta z} = \gamma\left(\frac{\delta_2 V_z}{\delta r^2} + \frac{1}{r} \frac{\delta V_z}{\delta r} + \frac{\delta_2 V_z}{\delta z^2}\right) \qquad (5.10)$$

$$V_r \frac{\delta V_\phi}{\delta r} + \frac{V_r V_\phi}{r} + V_z \frac{\delta V_\phi}{\delta z} = \gamma\left(\frac{\delta_2 V_\phi}{\delta r^2} + \frac{1}{r} \frac{\delta \phi}{\delta r} - \frac{V_\phi}{r^2} + \frac{\delta_2 V_\phi}{\delta z^2}\right) \qquad (5.11)$$

$$V_r \frac{\delta V_r}{\delta r} - \frac{V_\phi^2}{r} + V_z \frac{\delta V_r}{\delta z} = -\frac{1}{\rho}\frac{\delta p}{\delta r} + \gamma\left(\frac{\delta_2 V_r}{\delta r^2} + \frac{1}{r}\frac{\delta V_r}{\delta r} - \frac{V_r}{r^2} + \frac{\delta_2 V_r}{\delta z^2}\right) \quad (5.12)$$

$$\frac{\delta V_r}{\delta r} + \frac{V_r}{r} + \frac{\delta V_z}{\delta z} = 0 \quad (5.13)$$

Using the standard properties of the jet that the velocity normal to the jet axis (V_r) is small and that derivatives normal to the jet axis are much larger than derivatives parallel to the jet axis leads to the simplification of the above equations to these forms:

$$V_r \frac{\delta V_z}{\delta r} + V_z \frac{\delta V_z}{\delta z} = \gamma\left(\frac{\delta_2 V_z}{\delta r^2} + \frac{1}{r}\frac{\delta V_z}{\delta r}\right) \quad (5.14)$$

$$V_r \frac{\delta V_\phi}{\delta r} + \frac{V_r V_\phi}{r} + V_z \frac{\delta V_\phi}{\delta z} = \gamma\left(\frac{\delta_2 V_\phi}{\delta r^2} + \frac{1}{r}\frac{\delta V_\phi}{\delta r} - \frac{V_\phi}{r^2}\right) \quad (5.15)$$

$$V_r \frac{\delta V_r}{\delta r} - \frac{V_\phi^2}{r} + V_z \frac{\delta V_r}{\delta z} = -\frac{1}{\rho}\frac{\delta p}{\delta r} + \gamma\left(\frac{\delta_2 V_r}{\delta r^2} + \frac{1}{r}\frac{\delta V_r}{\delta r} - \frac{V_r}{r^2}\right) \quad (5.16)$$

$$\frac{\delta V_r}{\delta r} + \frac{V_r}{r} + \frac{\delta V_z}{\delta z} = 0 \quad (5.17)$$

equation (5.16) consists entirely of small terms, so that equations (5.14), (5.15), and (5.17) provide three equations for the three unknown velocity components. To solve these equations, each term should be converted into its momentum integral by integration over the thickness of the jet (82). As shown in Figure (2), the area of integration is:

$$(r + \delta r)\,(r + \delta r)\delta\phi - r^2\delta\phi = 2r\,\delta r\delta\phi$$

$$\therefore \int_0^{\pi} 2r\delta r\delta\phi = 2\pi r dr$$

Therefore integrating equation (5.17) gives:

$$\int_0^{\delta} 2\pi r \frac{\delta V_r}{\delta r} dr = -\int_0^{\delta} 2\pi r \frac{\delta V_z}{\delta z} dr - \int_0^{\delta} 2\pi r \frac{V_r}{r} dr$$

or

$$\int_0^{\delta} r \frac{\delta V_r}{\delta r} dr = -\int_0^{\delta} r \frac{\delta V_z}{\delta z} d_r - \int_0^{\delta} V_r\, d_r \qquad (5.18)$$

Similarly, integrating the terms of equations (5.14), (5.15), and (5.16) gives the following equations respectively:

$$rV_zV_r\Big|_0^{\delta} + \frac{\delta}{\delta z}\int_0^{\delta} r\,V_z{}^2 dr = \gamma\,\frac{\delta(V_z r)}{\delta r}\Big|_0^{\delta} - \gamma V_z\Big|_0^{\delta} \qquad (5.19)$$

$$rV_rV_\phi\Big|_{\delta} + \frac{\delta}{\delta z}\int_0^{\delta} rV_zV_\phi dr + \int_0^{\delta} V_rV_\phi dr = \gamma\left[\frac{r\delta V_\phi}{\delta r}\Big|_0^{\delta} - \int_0^{\delta} \frac{V_\phi}{r} dr\right] \qquad (5.20)$$

$$\frac{\delta}{\delta z}\int_0^{\delta} rV_rV_z dr - rV_rV_z\Big|_0^{\delta} - \int_0^{\delta} (V_r{}^2 + V_\phi{}^2) dr =$$

$$\gamma\left[r\,\frac{\delta V_r}{\delta r}\Big|_0^{\delta} - \int_0^{\delta} \frac{V_r}{r} dr\right] \qquad (5.21)$$

Velocity Profiles and Boundary Conditions: In this part of the analysis it is assumed that certain velocity profiles exist for the three velocity components at the jet boundary. These must represent the whole system and fit the boundary conditions.

Figure (3) shows the core $z_1 - z_c$ where, inside that core the velocity is constant and assumed to have the value of the fluid velocity at the tip of the impeller and equal to the quantity (KNd).

The velocity in the region $z_c - z_z$ decreases exponentially with the distance z from the impeller tip on the jet axis, also it changes with respect to the thickness of the jet in the r-direction. To correlate this, a dimensionless length is proposed which is represented by:

$$y = \frac{r}{\delta} \tag{5.22}$$

and for a certain value of δ:

$$\delta r = \delta \, \delta y \tag{5.23}$$

Velocity component $-V_z-$: The velocity in the z-direction decreases with distance from the impeller. Therefore:

$$V_z = V_z(2y^2 - y^3) + KNde^{-z} (1 - 2y^2 + y^3) \tag{5.24}$$

so that at:

$$r = 0, \qquad y = 0, \qquad z \geq z_c$$

$$V_z = KNDe^{-z}, \qquad \frac{\delta V_z}{\delta r} = 0$$

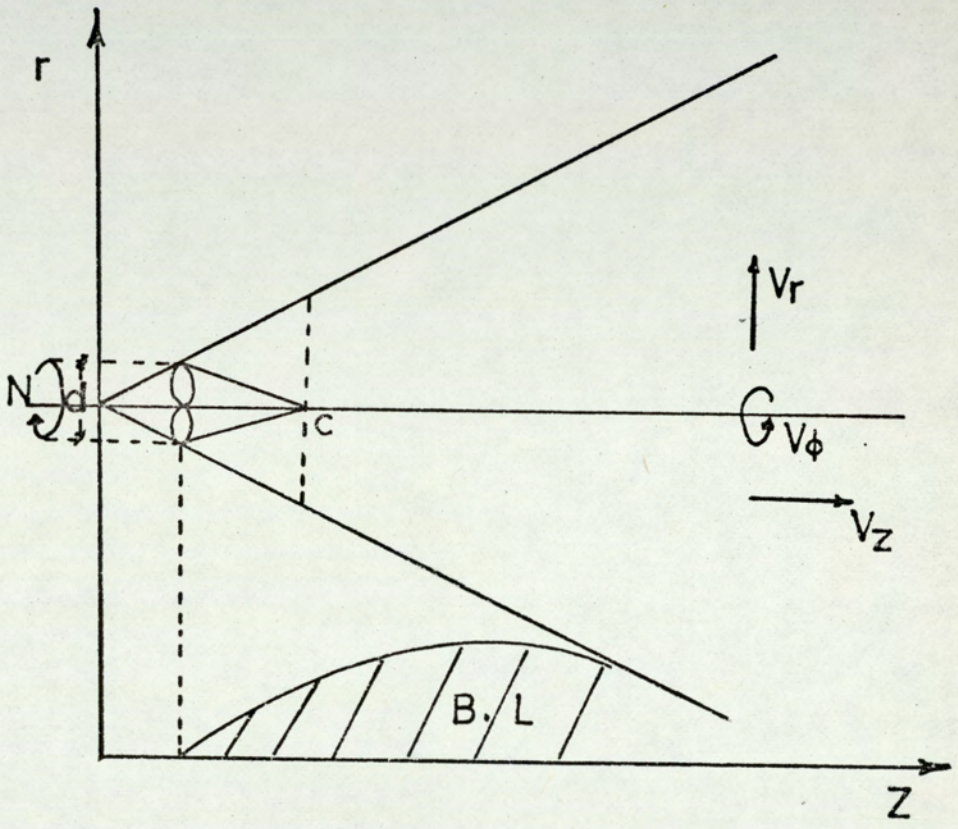

FIGURE_ 3 _ BOUNDARY LAYER BETWEEN THE JET LIMIT AND THE BASE OF THE TANK.

and at:

$$r = \delta, \qquad y = 1, \qquad z \geq z_c$$

$$v_z = V_z, \qquad \frac{\delta V_z}{\delta r} = (V_z - KNd)/\delta$$

where

$$K = K'/e^{-z_c}$$

Velocity Component $-V_\phi-$: This velocity behaves in the same way as V_z does, so that:

$$v_\phi = V_\phi\,(2y^2 - y^3) + K_1 Nde^{-z}\,(1 - 2y^2 + y^3) \qquad (5.25)$$

where

$$K_1 = K_1'/e^{-z}$$

Velocity Component $-V_r-$: The velocity in the r-direction is very small and could be assumed to be zero at the tip of the impeller, so that:

$$v_r = V_r\,(2y - y^2) \qquad (5.26)$$

Therefore:

$$\text{at} \qquad r = 0, \qquad y = 0, \qquad z \geq z_c$$

$$V_r = 0, \qquad \text{and} \quad \frac{dV_r}{dr} = \frac{2V_r}{\delta}$$

and at $r = \delta, \quad y = 1, \quad z \geq z_c$

$$v_r = V_r, \qquad \frac{dV_r}{dr} = 0$$

The distance $z_1 - z_c$ is usually about three times the impeller diameter:

$$z_c = 3d \tag{5.27}$$

The next step is to substitute the value of the velocity profiles into equations (5.18), (5.19), (5.20) and (5.21), then the various integrals required can be evaluated:

$$\int_0^{\delta} r\, V_z^2 dr = \int_0^1 \delta^2 y \left[V_z(2y^2 - y^3) + KNde^{-z}(1-2y^2+y^3) \right]^2 dy$$

or

$$\int_0^{\delta} r\, V_z^2 dr = \delta^2 \left[0.22V_z^2 + 0.16KNde^{-z}V_z + 0.12K^2N^2d^2e^{-2z} \right] \tag{5.28}$$

similarly:

$$\frac{\delta(V_z r)}{\delta r}\Bigg|_0^{\delta} = 2V_z - 2KNde^{-z} \tag{5.29}$$

$$\int_0^{\delta} rV_z dr = \delta^2 \left[0.3V_z + 0.2KNde^{-z} \right] \tag{5.30}$$

$$\int_0^{\delta} rV_r V_\phi dr = \delta^2 V_r \left[0.276V_\phi + 0.14\ K_1 N d e^{-z}\right] \tag{5.31}$$

$$\int_0^{\delta} V_r V_\phi dr = \delta\ V_r \left[0.366\ V_\phi + 0.3\ K_1 N d e^{-z}\right] \tag{5.32}$$

$$\int_0^{\delta} \frac{V_\phi}{r}\, dr = \left[0.66\ V_\phi + 3.66\ K_1 N d e^{-z}\right] \tag{5.33}$$

$$\int_0^{\delta} rV_z V_r dr = \delta^2 V_r \left[0.276\ V_z + 0.14\ K N d e^{-z}\right] \tag{5.34}$$

$$\frac{\delta(rV_\phi)}{\delta r}\Bigg|_0^{\delta} = 2V_\phi - 2K_1 N d e^{-z} \tag{5.35}$$

$$\int_0^{\delta} rV_\phi\ V_z dr = \delta^2 \left[0.22V_\phi V_z + 0.08V_z K_1 N d e^{-z} + 0.08V_\phi K N d e^{-z} + 0.12\ K K_1 N^2 d^2 e^{-2z}\right] \tag{5.36}$$

$$\int_0^{\delta} V_\phi{}^2 dr = \delta\left[0.276V_\phi{}^2 + 0.14V_\phi\ K_1 N d e^{-z} + 0.324K_1{}^2 N^2 d^2 e^{-2z}\right] \tag{5.37}$$

$$\int_0^{\delta} V_r{}^2 dr = 0.53\ \delta\ V_r{}^2 \tag{5.38}$$

$$\int_0^{\delta} \frac{V_r}{r}\, dr = 1.5V_r \tag{5.39}$$

$$\frac{\delta(r\ V_r)}{\delta r}\Bigg|_{o}^{\delta} = V_r \qquad (5.40)$$

Before substituting these integrals into the equations, a relationship between the thickness of the jet and the velocity at the jet boundary is required and such a relation can be obtained by evaluating the momentum at two points on the axis of the jet. Since the momentum is constant across any section of the jet (82), the momentum at Z_1 is equal to the momentum at any point z_z. That is:

$$M_1 = \pi(\acute{K}Nd)^2 \ \frac{d^2}{4}$$

$$M_z = \int_o^{\delta} 2\pi r\ V_z{}^2 dr$$

$$M_1 = M_z$$

$$\therefore \quad \pi\ \frac{\acute{K}^2N^2d^4}{4} = 2\pi \int_o^{\delta} r\ V_z{}^2 dr$$

$$\text{or} \quad \pi\ \frac{\acute{K}^2N^2d^4}{4} = 2\pi\delta^2\left[0.22V_z{}^2 + 0.16V_zKNde^{-z} + K^2N^2d^2e^{-2z}\right]$$

$$\therefore \quad \delta^2 = K^2N^2d^4e^{-2z}c/\mathcal{E}\left[0.22V_z{}^2 + 0.16V_zKNde^{-z} + 0.12K^2N^2d^2e^{-2z}\right] \qquad (5.41)$$

$$\text{and} \quad 2\delta d\delta = -\delta^2\left(\frac{(0.44V_z + 0.16KNde^{-z})\frac{dV_z}{dz} - (0.16V_zKNde^{-z} + 0.24K^2N^2d^2e^{-2z})}{(0.22V_z{}^2 + 0.16KNde^{-z}V_z + 0.12K^2N^2d^2e^{-2z})}\right) \qquad (5.42)$$

substituting the values of the integrals and equations (5.41) and (5.42) into equation (5.18) gives:

$$\int_0^{\delta} r \frac{\delta V_z}{\delta z} dr = -\int_0^{\delta} r \frac{\delta V_r}{\delta r} dr - \int_0^{\delta} V_r dr$$

$$\text{or} \quad \frac{\delta}{\delta z}\int_0^{\delta} r V_z dr = -\int_0^{\delta} \frac{\delta(V_r r)}{\delta r} dr$$

$$\frac{\delta}{\delta z}\int_0^{\delta} r V_z dr = -\delta V_r + C$$

where C is a constant of integration

$$\frac{\delta}{\delta z}(\delta^2(0.3V_z + 0.2KNde^{-z})) = -\delta V_r + C \qquad (5.43)$$

$$2\delta(0.3V_z + 0.2KNde^{-z})\frac{d\delta}{dz} + \delta^2\left(0.3\frac{dV_z}{dz} - 0.2KNde^{-z}\right) = -\delta V_r + C$$

substituting the value of δ and $\frac{d\delta}{dz}$ gives:

$$-\delta^2(0.3V_z+0.2KNde^{-z})\left(\frac{(0.44V_z+0.16KNde^{-z})\frac{dV_z}{dz}-(0.16V_zKNde^{-z}+0.24K^2N^2d^2e^{-2z})}{(0.22V_z^2+0.16V_zKNde^{-z}+0.12K\,N^2d^2e^{-2z})}\right)$$
$$+\delta^2(0.3\frac{dV_z}{dz} - 0.2KNde^{-z}) = -\delta V_r + C$$

or:

$$\left(\frac{(0.3V_z + 0.2KNde^{-z})\,(0.44V_z + 0.16KNde^{-z})}{(0.22V_z^2 + 0.16V_zKNde^{-z} + 0.12\,K^2N^2d^2e^{-2z})} - 0.3 \right) \frac{dV_z}{dz}$$

$$-\left(\frac{(0.3V_z + 0.2KNde^{-z})\,(0.16V_zKNde^{-z} + 0.24K^2N^2d^2e^{-2z})}{(0.22V_z^2 + 0.16V_zKNde^{-z} + 0.12\,K^2N^2d^2e^{-2z})} - 0.2KNde^{-z} \right)$$

$$= \frac{V_r}{\delta} - \frac{C}{\delta^2} \qquad (5.44)$$

For the boundary conditions:

$$\text{at } z = z_c \qquad V_r = 0 \qquad \frac{dV_z}{dz} = -KNde^{-z}c \qquad V_z = KNde^{-z}c$$

$$\therefore \qquad C = \frac{K^2N^2d^4e^{-2z}c}{8KNde^{-z}c} = \frac{1}{8}\,KNd^3e^{-z}c \qquad (5.45)$$

Similarly, equation (5.19) gives:

$$-V_z\left(\frac{\delta}{\delta z}\left[\delta^2(0.3V_z + 0.2KNde^{-z}) \right] \right) + V_zC$$

$$+ \frac{\delta}{\delta z}\left[\delta^2(0.22V_z^2 + 0.16V_zKNde^{-z} + 0.12K^2N^2d^2e^{-2z}) \right]$$

$$= \gamma(V_z - KNde^{-z})$$

By re-arranging the equation and substituting the values of δ, $\frac{d\delta}{dz}$ and the value of C, the following is obtained:

$$\frac{dV_z}{dz} = \left(\frac{1}{(0.66V_z^2 + 0.088V_z KNde^{-z} - 0.004K^2N^2d^2e^{-2z})} \right) \left[KNde^{-z} (0.004V_z^2 \right.$$

$$+ 0.072V_z KNde^{-z} + 0.024K^2N^2d^2e^{-2z})$$

$$\left. + \left(\frac{8\gamma(V_z - KNde^{-z})}{V_z KNd^3e^{-z}c} - \frac{4}{3} \right) \frac{(0.22V_z^2 + 0.16V_z KNde^{-z} + 0.12K^2N^2d^2e^{-2z})^2}{(KNde^{-z}c)} \right] \quad (5.46)$$

Also Equation (5.20) gives:

$$-2\delta(1.366V_\phi + 0.3K_1Nde^{-z})(0.3V_z + 0.2KNde^{-z}) \frac{d\delta}{dz}$$

$$-\delta^2(1.366V_\phi + 0.3K_1Nde^{-z})(0.3\frac{dV_z}{dz} - 0.2KNde^{-z})$$

$$+2\delta(0.22V_\phi V_z + 0.08K_1Nde^{-z}V_z + 0.08V_\phi KNde^{-z} + KK_1N^2d^2e^{-2z}) \frac{d\delta}{dz}$$

$$+\delta^2(0.22V\phi \frac{dV_z}{dz} + 0.22V_z \frac{dV_\phi}{dz} + 0.08K_1Nde^{-z} \frac{dV_z}{dz} - 0.08K_1Nde^{-z}V_z$$

$$+ 0.08KNde^{-z} \frac{dV_\phi}{dz} - 0.08KNde^{-z}V_\phi - 0.24KK_1N^2d^2e^{-2z})$$

$$+ (1.366V_\phi + 0.3K_1Nde^{-z})C = \gamma(0.33V_\phi - 2.83K_1Nde^{-z})$$

Again, substituting the values of C, δ, and $\frac{d\delta}{dz}$ and re-arranging the equation gives:

$$\frac{dV_\phi}{dz} = \frac{1}{(0.22V_z + 0.8KNde^{-z})}\left[\left((0.08K_1Nde^{-z}V_z - 0.096V_\phi KNde^{-z} + 0.18KK_1N^2d^2e^{-2z})\right.\right.$$

$$+ \frac{dV_z}{dz}\left(\frac{\begin{pmatrix}0.0176V_z^2K_1Nde^{-z} + 0.0308V_zK_1KN^2d^2e^{-2z} + 0.0216K_1K^2N^3d^3e^{-3z}\\ -0.1256V_\phi V_z^2 - 0.1334V_\phi V_zKNde^{-z} - 0.049V_\phi K^2N^2d^2e^{-2z}\end{pmatrix}}{(0.22V_z^2 + 0.16V_z KNde^{-z} + 0.12\,K^2N^2d^2e^{-2z})}\right)$$

$$+ \left\{\begin{matrix}(0.1898V_zV_\phi + 0.01V_zK_1Nde^{-z} + 0.1652V_\phi KNde^{-z} - 0.06KK_1N^2d^2e^{-2z})\ x\\ (0.16V_z\,KNde^{-z} + 0.24K^2N^2d^2e^{-2z})/(0.22V_z^2 + 0.16V_zKNde^{-z} + 0.12K^2N^2d^2e^{-2z})\end{matrix}\right\}$$

$$+\left[\left(\frac{8\gamma(0.33V_\phi - 2.833K_1Nde^{-z})}{KNd^3e^{-z}c} - (1.366V_\phi + 0.3K_1Nde^{-z})\right)\ x\right.$$

$$\left.\left.\left(\frac{(0.22V_z^2 + 0.16V_z\,KNde^{-z} + 0.12\,K^2N^2d^2e^{-2z})}{KNde^{-z}c}\right)\right] \qquad (5.47)$$

Equations (5.46), (5.47) must be solved numerically and the Runge-Kutta method of solving first order differential equations with initial values was selected A computer program has been written to evaluate the values of the velocity components as shown in Appendix (A5)

After the values of the velocity components have been found and their behaviour in the z and ϕ direction characterized, the thickness of the boundary layer between the jet boundary and the base of the tank is obtained by simulating the flow of fluid adjacent to a flat plate at zero incidence (82). The drag of a plate wetted on one side is expressed as:

$$D_r(x) = b\rho \int_{y=0}^{\infty} V\,(V_\infty - v)dy \qquad (5.48)$$

on the other hand, the drag can be expressed as an integral of the shearing stress τ_w at the wall, taken along the plate:

$$D_r(x) = b \int_o^x \tau_w(x)\, dx \qquad (5.49)$$

Therefore:

$$\tau_w(x) = \rho \frac{d}{dx} \int_{y=0}^{\infty} v.(V - v)\, dy \qquad (5.50)$$

This equation can be deduced in a purely formal way from the boundary layer equations by first integrating the equation of motion in the x - direction with respect to y from y = 0 to y = ∞. Equation (5.50) is finally obtained without difficulty if the velocity component V is eliminated with the aid of the equation of continuity and if it is noticed that:

$$\mu \left(\frac{\delta v}{\delta y}\right)_{y=0} = \tau_w$$

Introducing the momentum thickness δ_2, defined as:

$$\delta_2 V^2 = \int_{y=0}^{\infty} v(V - v)\, dy \qquad (5.51)$$

Substituting equation (5.51) into (5.50) gives:

$$V^2 \frac{d\delta_2}{dx} = \frac{\tau_w}{\rho} \qquad (5.52)$$

This equation means that the shearing stress at the wall is equal to the momentum loss in the boundary layer.

With reference to equation (5.50) and (5.52), an approximate relation of the boundary layer along a flat plate at zero incidence can be performed. This method consists of assuming a suitable expression for the velocity distribution U(y) in the boundary layer which satisfies the boundary conditions for U(y), so that:

$$\frac{v}{V} = (\frac{3}{2}y - \frac{1}{2}y^3) = f \qquad (5.53)$$

where $y = \frac{y}{\delta(x)}$

Therefore: $\int_o^\infty v(V-v)dy = V^2 \delta(x) \int_o^1 f\,(1-f)\,dy$

$$= V^2 \delta(x) \int_o^1 (\frac{3}{2}y - \frac{1}{2}y^3)(1-\frac{3}{2}y - \frac{1}{2}y^3)dy$$

$$= \frac{39}{280} V^2 \delta(x)$$

Also: $\int_o^\infty v(V-v)dy = V^2\delta_2 = \frac{39}{280} V^2 \delta(x)$

$$\therefore \quad \delta_2 = \frac{39}{280} \delta(x) \qquad (5.54)$$

The value of the displacement thickness δ_1 is:

$$\delta_1 V = \int_o^\infty (V-v)dy$$

or $$\delta_1 = \frac{3}{8}\delta(x) \qquad (5.55)$$

Furthermore, the viscous shearing stress at the wall is given by:

$$\frac{\tau_w}{\rho} = \gamma\left(\frac{\delta v}{\delta y}\right)_{y=0} = \frac{\gamma V}{\delta(x)} f'_{(\upsilon)} = \frac{3\gamma V}{2\delta(x)} \tag{5.56}$$

Substituting equation (5.56), (5.54) into equation (5.52) gives:

$$\delta(x)\frac{d\delta(x)}{dx} = \frac{140\gamma}{13V}$$

or
$$\delta(x)^2 = \frac{280}{13}\gamma\int_o^x \frac{dx}{V} \tag{5.57}$$

After obtaining the value of the thickness of the boundary layer, it is necessary to ascertain the thickness of the laminar sub-layer which lies inside the boundary layer. Thus from the definition of this layer (82):

$$\delta_v = \frac{5\gamma}{U^*} \tag{5.58}$$

and
$$U^* = \left(\frac{\tau_w}{\rho}\right)^{\frac{1}{2}} \tag{5.59}$$

Therefore:
$$\delta_v = 5\gamma\left(\frac{\tau_w}{\rho}\right)^{-\frac{1}{2}}$$

From equation (5.56)

$$\frac{\tau_w}{\rho} = \frac{3\gamma V}{2\delta(x)} \tag{5.60}$$

and $$\delta(x)^2 = \frac{280}{13}\gamma \int_o^x \frac{dx}{V}$$

$$\therefore \quad \delta(x) = \sqrt{\frac{280\gamma}{13}\int_o^x \frac{dx}{V}} \qquad (5.61)$$

Substituting equation (5.61) into equation (5.60) gives:

$$\frac{\tau_w}{\rho} = 2\sqrt{\frac{3\gamma V}{\frac{280}{13}\gamma \int_o^x \frac{dx}{V}}} \qquad (5.62)$$

and substituting equation (5.62) into equation (5.58) gives:

$$\delta_v = \frac{5\gamma}{\sqrt{\frac{3}{2}\gamma V}} \left(\frac{280\gamma}{13}\int_o^x \frac{dx}{V}\right)^{\frac{1}{4}}$$

or

$$\delta_v = 8.795 \left(\frac{\gamma^3}{V^2}\int_o^x \frac{dx}{V}\right)^{\frac{1}{4}} \qquad (5.63)$$

Equation (5.63) is the final equation which give the value of the thickness of the laminar sub-layer as a function of viscosity, velocity and distance. This equation has been tested in Chapter VII and VIII.

CHAPTER VI

6 EXPERIMENTAL WORK

6.1 INTRODUCTION

The electro-chemical technique has been chosen as the main method of measuring the thickness of the laminar sub-layer and the means of studying the flow behaviour in this layer. To apply this technique, a model tank 1.2m in diameter fitted with one side-entry impeller, was built to simulate a large oil storage tank. The effects of the various parameters were determined in the following experimental programme. The electro-chemical technique was first assessed in an open channel which was built with electrodes of different diameters fixed into the base of the channel. The results were consistent and reliable and confirmed that this method could be applied to the model tank. Although the hot-film anemmeter has some limitations and restrictions, it has been utilized as a second method to check the results obtained by the electro-chemical technique.

In addition, photographs of the model tank filled with agitated liquid were taken while sediment was added in order to show the flow pattern and the distribution of the sediment over the base of the tank. The qualitative results of these photographs provided some suggestions for minimizing the thickness of the laminer sub-layer.

Finally, full-scale measurements were made on an oil storage tank. The results would give a comparison with the model tank results and could suggest a method of scale-up

6.2 TEST CHANNEL

6.2.1 EQUIPMENT

A test channel was built to verify the use of the electrochemical technique before it was applied to the model tank. Numerous experiments were carried out to ascertain the existence of the limiting current and to choose the optimum electrode diameter. The channel was of 150cm long by 7.5cm wide made of 1cm acrylic sheet with an inlet and outlet openings of 2cm diameter as shown in figure (4). Three different sizes of nickel wires, each of 10cm length, were used as test electrodes and these were embeded-flush with the surface of the channel. Three holes were drilled through the base of the channel, with diameters slightly greater than the electrode, to allow the electrode to be inserted and embeded flush with the surface. The clearance between the electrode and the hole was filled with glue. After the glue had dried, the electrodes were cleaned and smoothed with fine emery paper to ensure they had the same shape of the channel surface. Some distance from the test electrode, a small nickel sheet of size 10cm by 7.5cm dimension was inserted in the base of the channel as a reference electrode. The area of this electrode was large so that under normal operating conditions it did not limit the electrode circuit current. Both the reference electrode and the test electrodes were connected to the circuit shown in figure (5). The inlet and outlet of the channel were connected to two 10-litre spherical aspirators by means of plastic tubes as shown in the diagram and electrolytic solution was circulated through the system by a stainless steel centrifugal pump. The upper aspirator which represented the feed tank was connected to a rotameter for flow rate

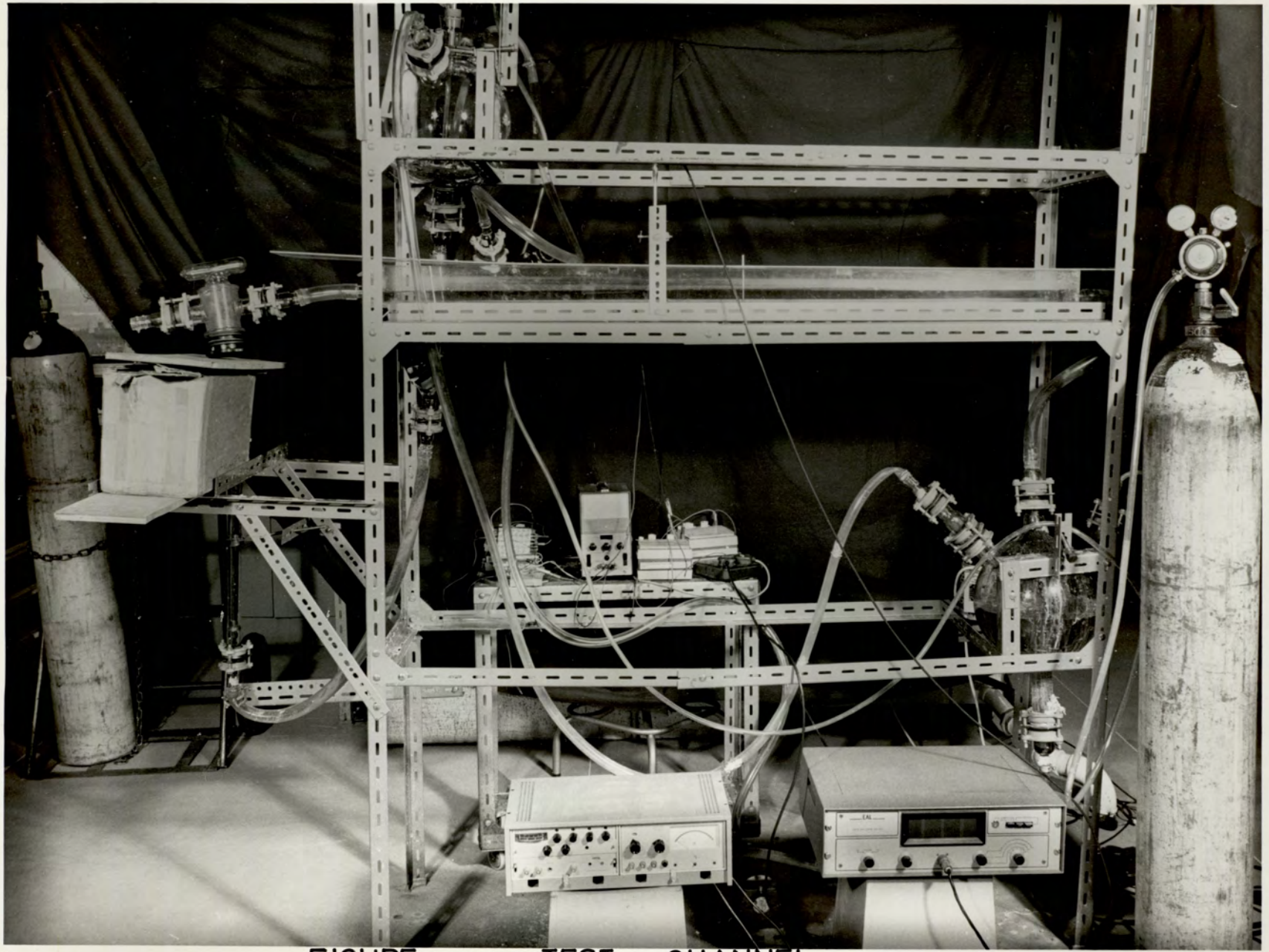

FIGURE - 4 - TEST CHANNEL

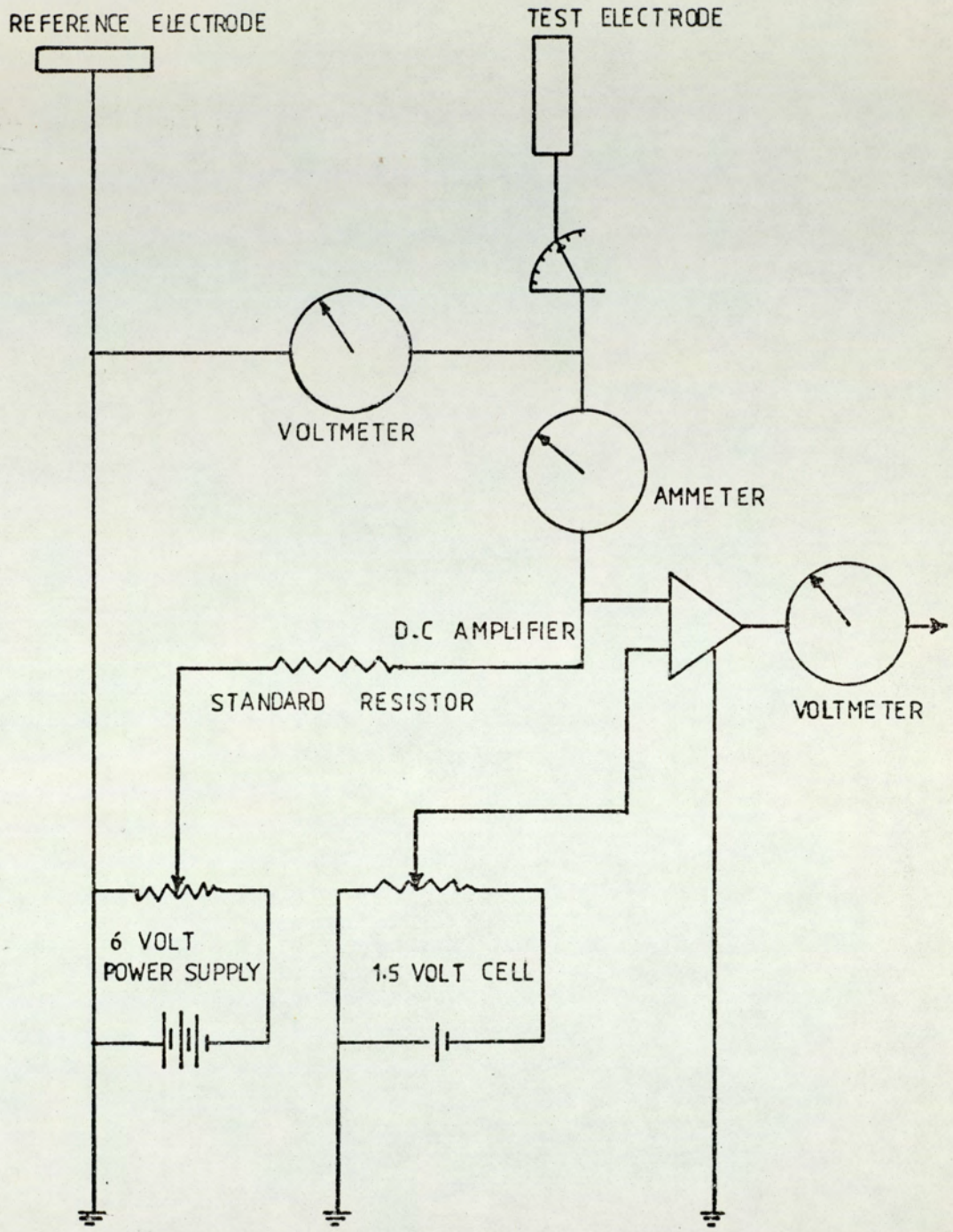

FIGURE _ 5 _ ELECTRICAL CIRCUITRY

measurements and the fluid overflowed through a pipe into the lower aspirator as shown in Figure (6). Nitrogen was purged continuously from a cylinder into the liquids in the the system to eliminate oxidation of the solution by dissolved oxygen. The whole apparatus was covered with a black cloth to prevent exposing the solution to the sunlight, as it was found that sunlight decomposed the ferrocyanide in the solution.

6.2.2 ELECTRO-CHEMICAL TECHNIQUE - USE AND VERIFICATION

Hanratty (54) used the electro-chemical technique for the measurements of instantaneous rates of mass transfer on a pipe wall. He developed this technique which had previously been used by Eisenburg (26) and Lin (24) for the measurement of the average rate of mass transfer from a rotating cylinder and an annulus respectively. The electro-chemical technique is used to study the unsteady flow in the immediate vicinity of a wall where the fluctuations in the flow can be measured indirectly through fluctuations in the concentration gradient at wall. The local rate of mass transfer is studied by measuring the average current and fluctuations in the current flowing to or from a small polarized electrode mounted flush with the solid boundary. As a potential is applied to the system, the overall process may be controlled by the rate of transfer of ions to the electrode surface to replace those that have been removed by the electrode reaction. This is called concentration polarization as it is associated with a decrease in concentration of the electrolyte in the immediate vicinity of the electrode.

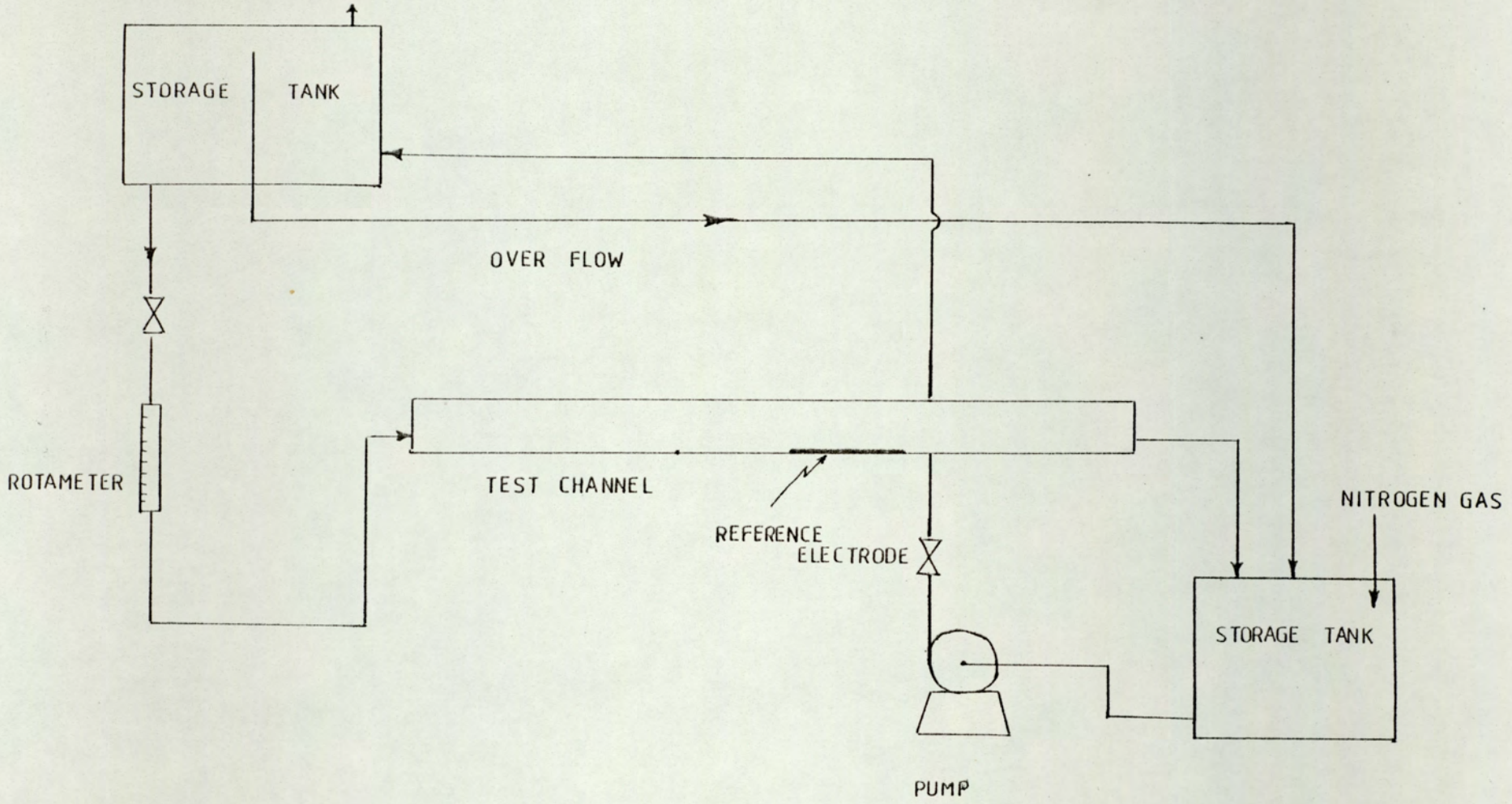

FIGURE - 6 - FLOW DIAGRAM OF THE TEST CHANNEL

The electro-chemical reaction rate increases with increase in applied potential until it equals the rate of diffusion of the reacting ions to the electrode surface. At the same time the surface concentration of the reacting ion gradually falls towards zero.

6.2.3 ELECTROLYTIC SOLUTION AND ELECTRICAL CIRCUIT

The electro-chemical system chosen for the present work was the cathodic reduction of potassium ferricyanide on nickel electrodes. The electrolyte solution consisted of equal molar concentrations of potassium ferricyanide and potassium ferrocyanide with a large excess of sodium hydroxide as the indifferent electrolyte. The electrolyte was maintained electrically neutral to prevent the electric field from affecting the migration of ferricynaide ions to the electrode. The electrochemical reaction of this Redox system is:

$$Fe(CN)_6^{-3} + e \longrightarrow Fe(CN)_6^{-4} \quad \text{at the Cathode}$$

$$Fe(CN)_6^{-4} \longrightarrow Fe(CN)_6^{-3} + e \quad \text{at the Anode}$$

Table 1 shows the various properties of the electrolyte solution.

Ferrocyanide Concentration	0.01	Molar
Ferricyanide Concentration	0.01	Molar
Sodium hydroxide Concentration	2.0	Molar
Density	1.09	gm/Cm^3
Viscosity	1.37	Centipoise
Diffusion Coefficient	5.2×10^{-6}	cm^2/Sec

Table 1 Properties of Electrolyte Solution

The electric circuit shown in figure (5) has been used for the estimation of the limiting current. The power was supplied by an electrical power supply and the voltage applied to the electrodes was controlled by a rheostat which could be varied from 0 to 1.6 volts. Both the applied voltage and the limiting current passing through the electrodes were measured with micro volt-ammeters. The three test electrodes were connected to the circuit through a flick-switch which enabled each electrode to be tested in turn.

The determination of the current was made by connecting a voltmeter across a standard resister and measuring the voltage drop across the resister. This voltage was amplified using a wide band differential input D.C amplifier.

6.2.4 METHOD

In most of the measurements carried out on the channel, the procedure was as follows:

1. The Rotameter was calibrated by pumping water through the system and at the same time the volume of water was collected

over a certain period of time. A curve was plotted showing the scale on the Rotameter in terms of volumetric flow rate.

2. The test electrodes were treated cathodically at -1.5 volts for 10 to 20 minutes with a 5% sodium hydroxide as electrolyte. and then rinsed with demineralized water and dried. This treatment was found to increase the reproducibility of the determinations (34).

3. The electric circuit was switched on and the voltmeter and anemometer were calibrated for zero position.

4. 12 litres of solution of .01 potassium ferricyanide, .01M of potassium ferrocyanide, and 2.M of sodium hydroxide, was prepared and brought to the room temperature ($20^{o}C$). A sample of this solution was taken for the estimation of physical properties (viscosity and density) and its concentration was confirmed.

5. The above solution was placed in the storage tank and nitrogen gas was sparged to keep the solution saturated and prevent oxidation by oxygen already dissolved in the system.

6. The Centrifugal pump was switched on to deliver about 6 litres of the solution to the head tank and then the control value of the rotameter was opened to let the solution flow to the channel passing through the rotameter. The pumping speed was controlled by a rheostat which balanced the pumping rate to the feed tank and the flow rate to the channel. The discharge from the channel passed to the storage tank.

7. After attaining a steady flow condition, the flow rate was determined by the rotameter.

8. Voltage was applied to the electrodes and slowly increased

from zero to 1.6 volts incrementally using a rheostat. The current passing through the circuit was observed and noted for each voltage increment. In the range of 0 to 0.3 volts, the current was increasing sharply while above that range it attained a constant value which represented the limiting current and indicated that the reaction was controlled by diffusion only. This limiting current started to increase again as the voltage exceeded about 1 volt, depending on the flow rate and the size of the electrode. This was due to the over-voltage applied to the system. 9. These measurements were made to different flow rates, and for the three different test electrodes. The voltage-current plateaus were plotted for different Reynolds numbers and different electrode diameters.

6.3 MODEL TANK

6.3.1 TANK DETAILS

After the electro-chemical technique had been verified on the test channel, a cylindrical model tank of 1.2m diameter and 60cm high was built of 0.65cm acrylic sheet and reinforced with bands of the same material as shown in figure (7). A self-adhesive scale was fixed to the tank height to indicate the depth of the liquid. The tank was mounted above a steel tank so as to prevent spillage of solution in case of leakage or overflow. The tank was supported by an angle framework and also contained the various auxiliary equipment. A mirror, mounted at an angle of 45^{o} above the tank, and supported by the framework as shown in Figure (7), was used for photographing the mixing process. The tank and its contents were illuminated by a set of four fluorescent

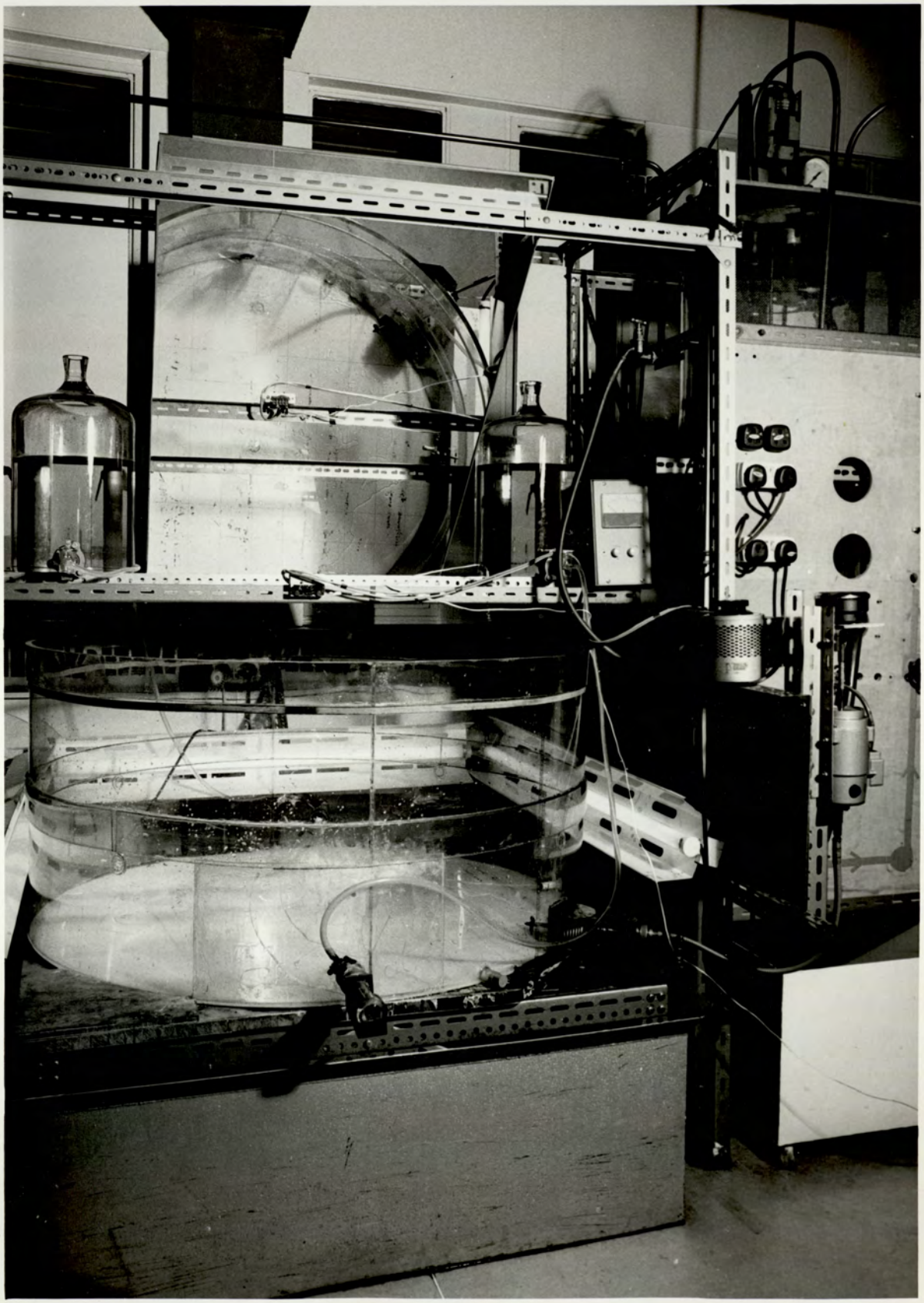

FIGURE _ 7 _1.2M DIAMETER TANK

tubes fixed around the tank wall.

The whole equipment was covered with black cloth when using the electro-chemical technique to ensure that the solution was not exposed to the sunlight. Also, when using this technique, the contents of the tank were purged by nitrogen from a pressurised nitrogen cylinder.

The impeller shaft was inserted into the side of the tank 5cm above the base as shown in figure (8). One end contained a screwed fitting to permit fitting impellers of different types and sizes, while the other end was slotted and connected to a 1/8HP D.C motor through a flexibile drive. A rheostat was connected across the power supply of the motor to enable adjustment of the impeller speed to any desired value. An electronic tachometer with a range of 0 - 10,000 RPM was mounted on to the framework to estimate the impeller speed and the photocell of this tachometer was fixed near to the motor shaft.

To enable the impeller shaft to be set at different angles with the axis, a special swivelling seal was made which prevented leakage of liquid from inside the tank. This mechanical shaft seal was mounted in a brass housing and pivoted to a brass plate secured to the tank and sealed by a rubber gasket. To measure the impeller shaft angle, a protractor shown in figure (8) was fitted to a plate which enabled the desired angle to be set by fixing it in a clamping screw.

A set of five geometrically similar impellers of different diameters shown in figure (9), made of nickel-plated brass, were used for the experiments. In addition to these, a plastic marine propeller was used in the experimental

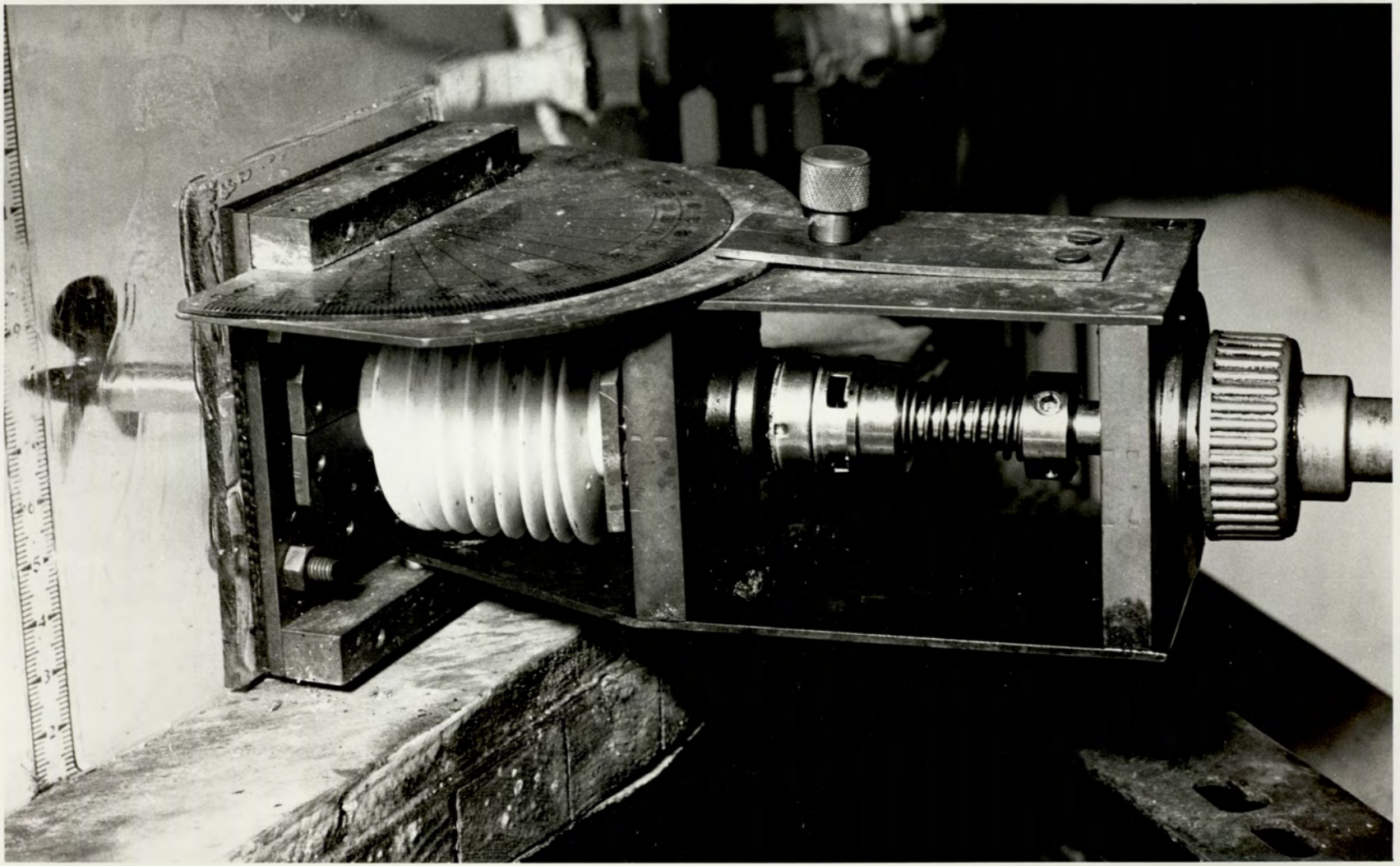

FIGURE_8_IMPELLER SHAFT SEAL

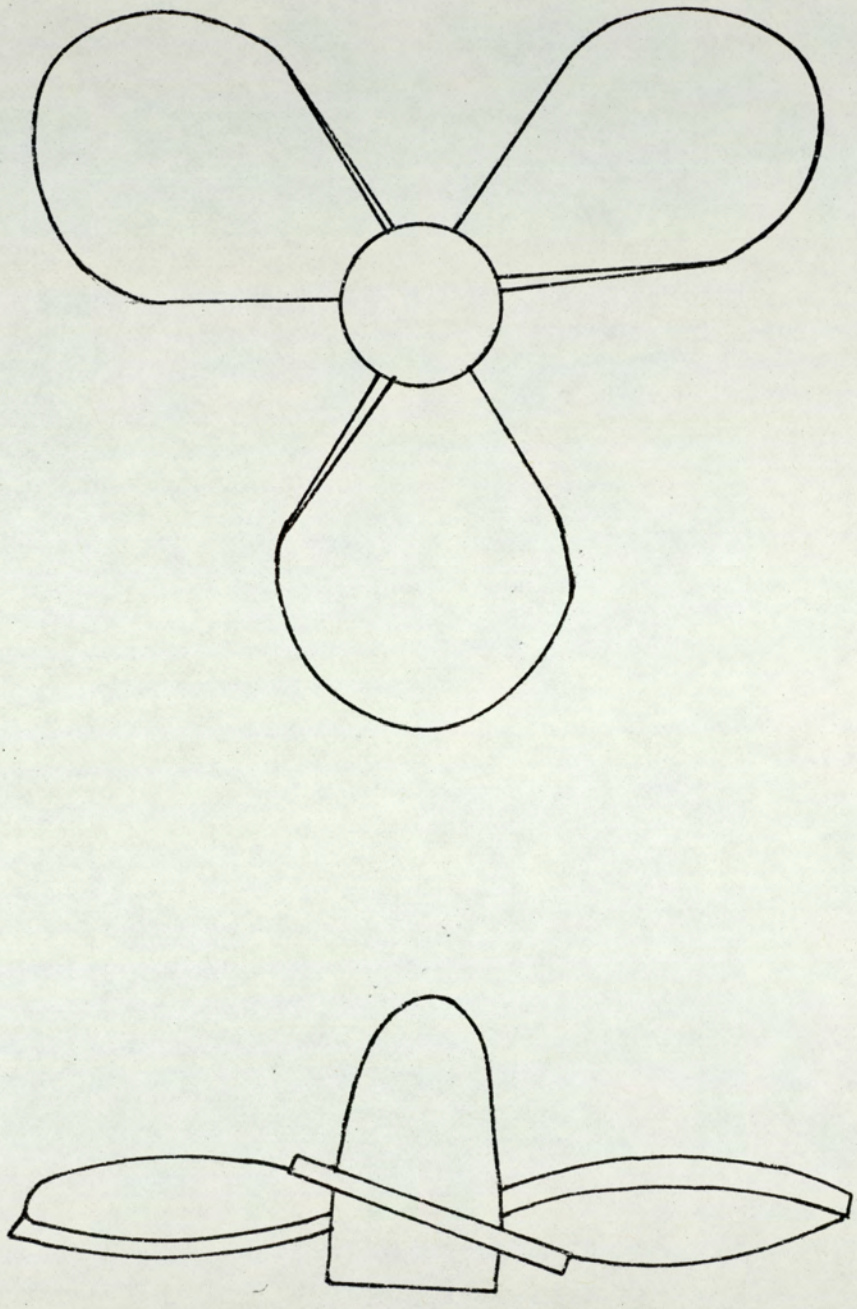

FIGURE_9_SCHEMATIC REPRESENTATION OF THE IMPELLER.

work. Those were the same impellers used for Doyle's study of mixing times (10). The base of the tank was secured on a piece of fibre having the same size as the tank base and was painted with white emulsion paint. Grids of 100mm were inscribed through the paint to provide a reference for positioning the hot-film probes and the electrodes. 22 test electrodes were distributed around the tank for the electro-chemical technique as shown in figure (10). These electrodes were 0.1mm diameter nickel wires each of 10cm length and embedded in the base of the tank, flush with the surface of the tank. The tank base was drilled in the positions where these electrodes had to be embedded and the diameter of these holes were made slightly larger than the electrodes diameters to give a clearance for inserting the glue as in figure (11). Also a groove having the area and depth of the reference electrode was prepared and two holes were drilled inside the groove to connect this electrode to the circuit. After placing the electrodes in their appropriate positions they were made flush with the tank surface and glue was inserted around the holes to seal them to the tank and the whole was left to dry. The electrodes were treated and smoothed with fine emery paper to ensure they were flat, clean and embedded flush with the surface. The other end of the electrodes was connected to the electrical circuit in the usual way.

6.3.2 DEGASSER

Although it was possible to avoid oxidation of the solution for the electro-chemical technique by saturating it with nitrogen gas, it was decided to degas the distilled

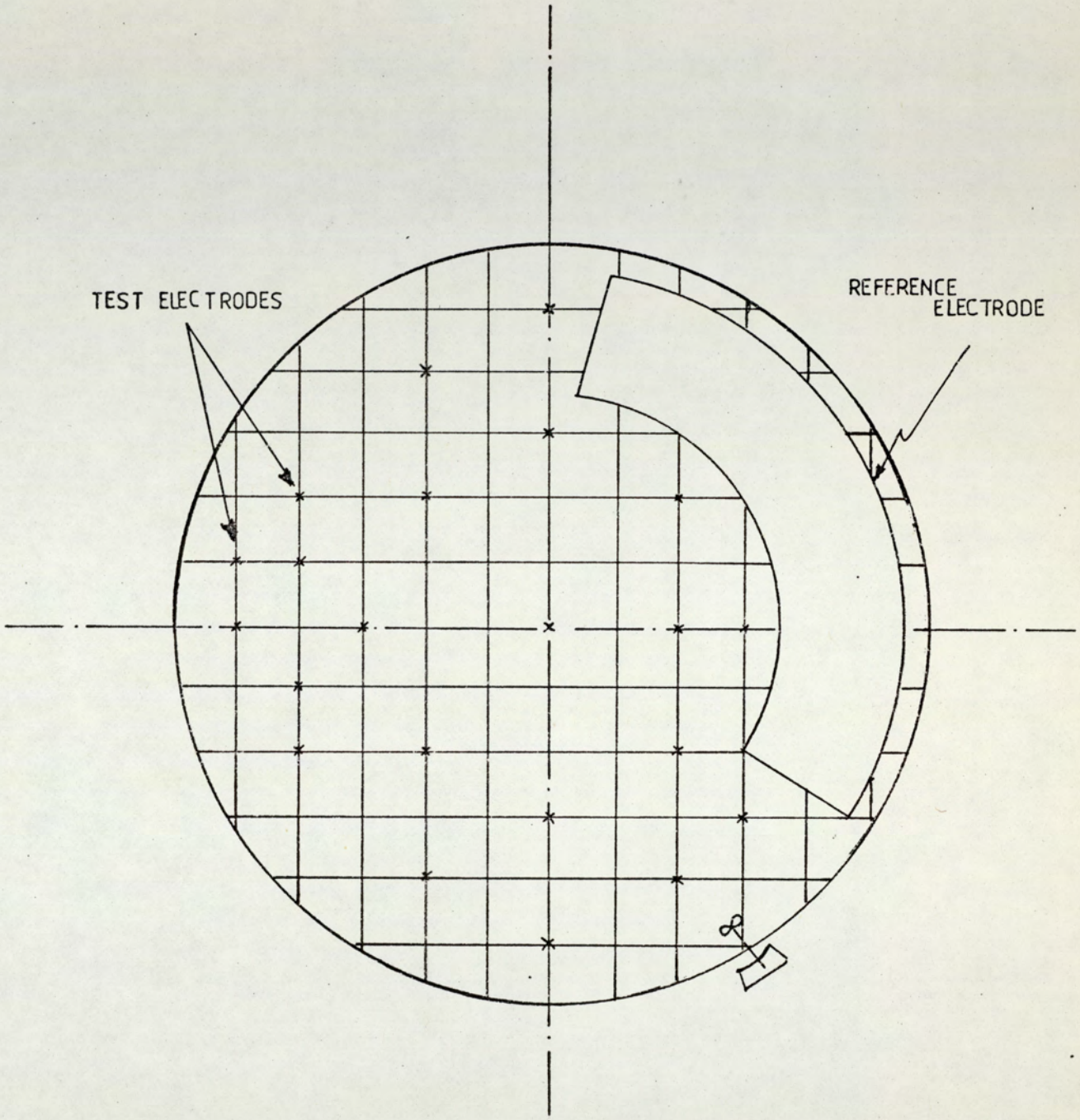

FIGURE_10 _DISTRIBUTION OF THE ELECTRODES AROUND THE BASE OF THE TANK.

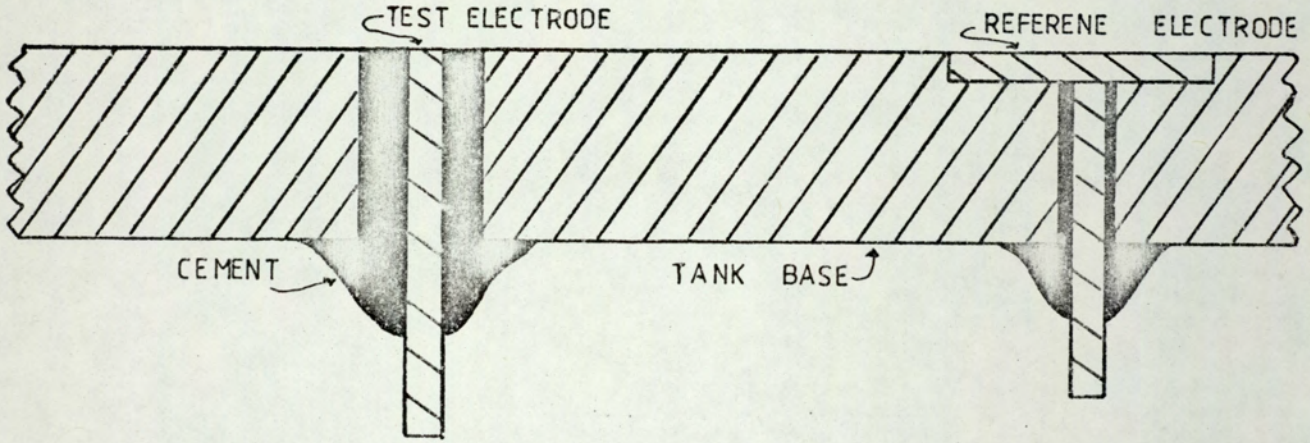

FIGURE_11_ SCHEMATIC REPRESENTATION OF THE ELECTRODES BUILT IN THE BASE OF THE TANK .

water used for making up the solution in addition to the use of nitrogen gas. The need for degassed water also arose when using the hot-film anemometer. If ordinary water was used, the hot probe will nucleate air bubbles and thereby invalidate the Calibration curve gives misleading results.

For these reasons, a degasser was constructed to remove dissolved air from the water and this is shown in figures (12, 13). This degasser produced 70 liters of degassed water per hour and consisted of 48.0cm diameter QVF pipe, a 48.0cm to 36.0cm reducing section and a 30.0cm to 2.5cm cone section. These sections were assembled as shown in the diagram. A three-way drain value was attached to the bottom chamber which allowed the degassed water to pass to the filter, or to waste, or it could isolate the degassing vessel. The agitator, vacuum gauge and pipe lines to and from the vessel were supported by a 1.25cm aluminium plate which was also used to cover the top of the vessel and seal the contents from the atmosphere. The vessel was mounted on an angle iron frame to support the various lines and valves and the whole was surrounded with wired pvc sheet.

Hot and cold water was supplied to the degassing chamber through a 1.25cm ball valve to adjust the water to the required temperature while the overflow line passed, via another valve, to the waste. The vacuum was produced by a vacuum pump, and at the top of the degasser, a line was provided, as shown in figure (14) that contained a valve by which the vacuum could be releaved at the end of the degassing operation. The 72.0mm diameter impeller used for agitating the water during degassing was connected to the 1/8HP motor

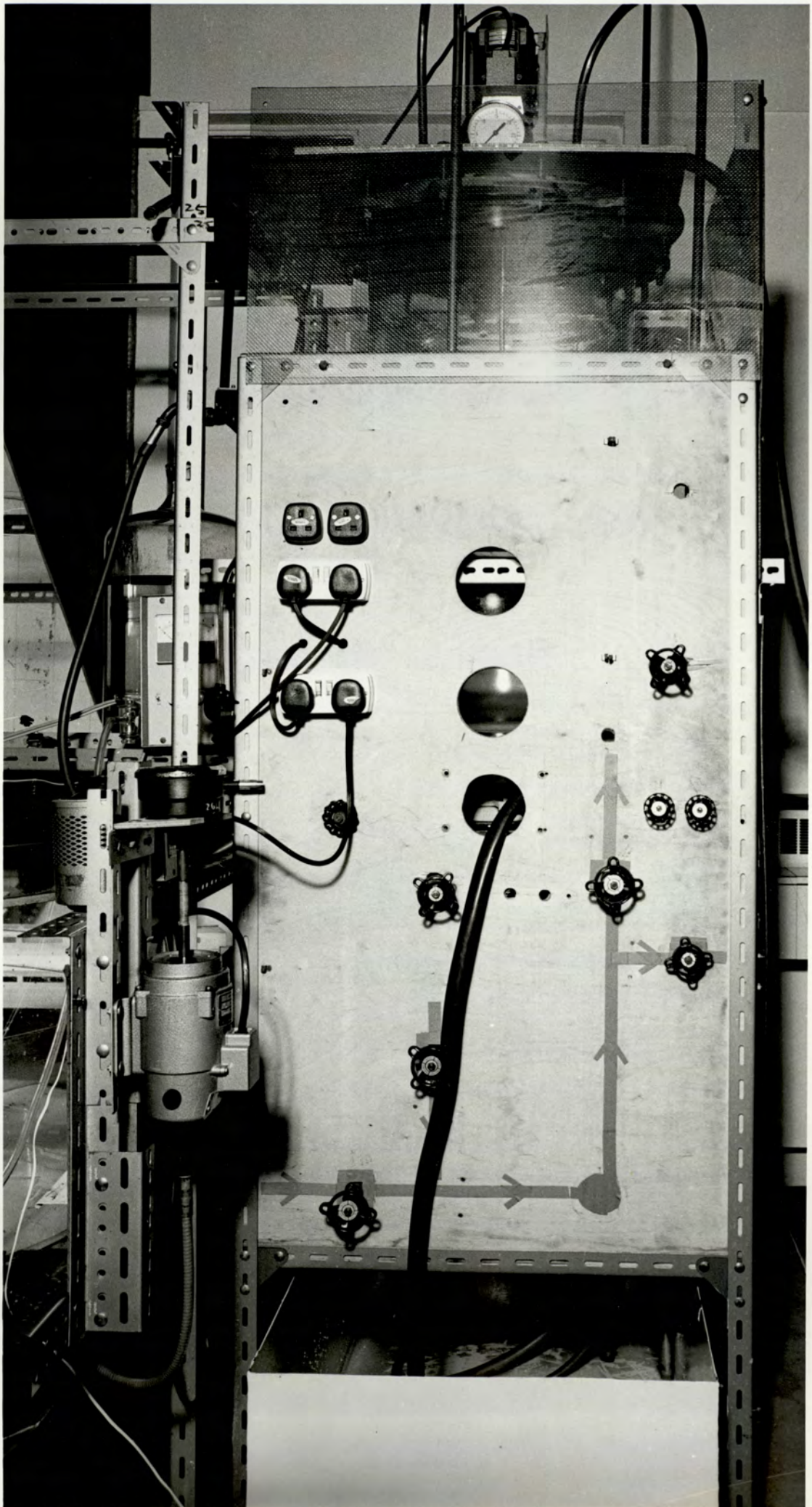

FIGURE_12_FRONT_VIEW OF THE DEGASSER

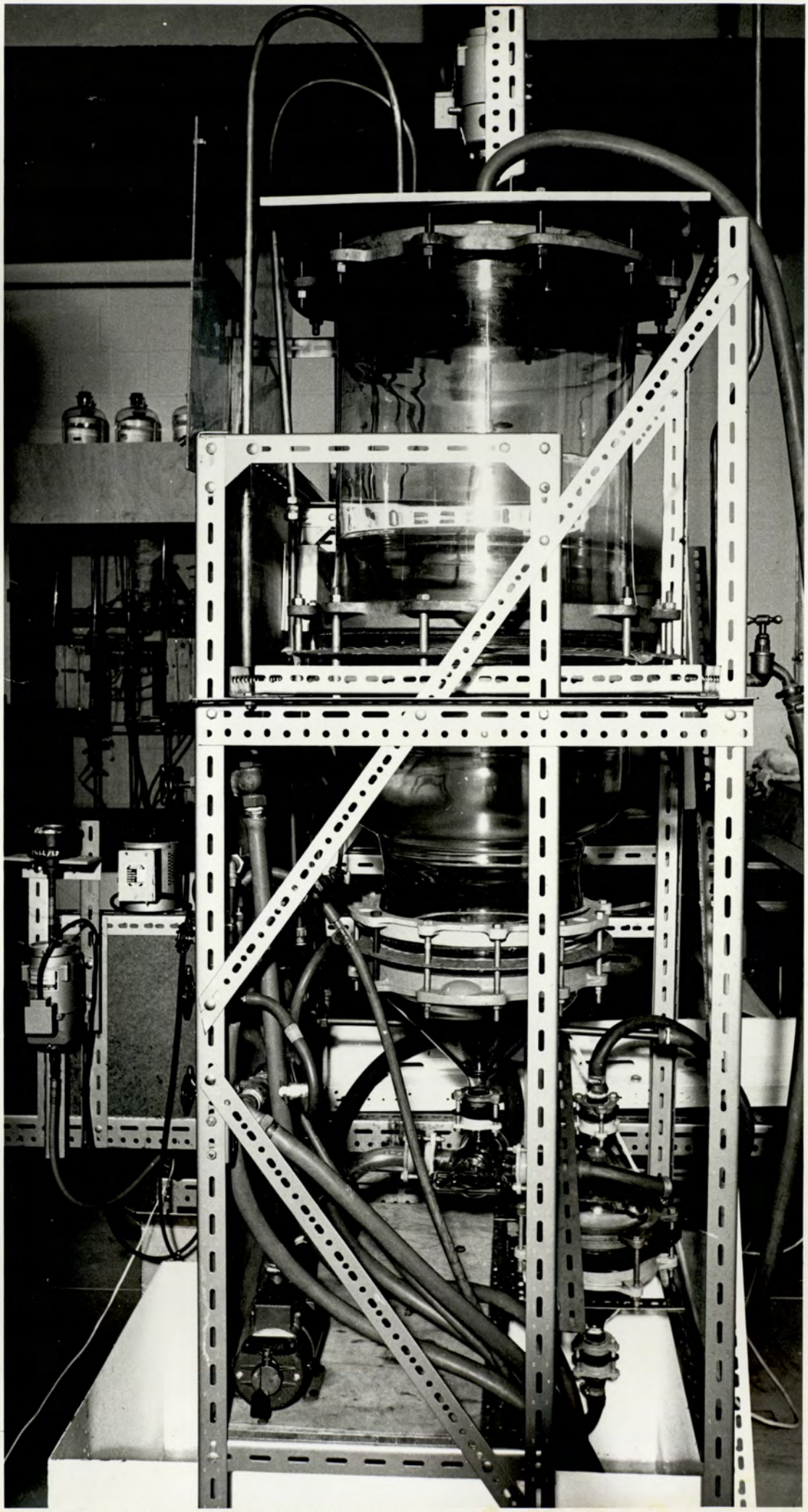

FIGURE_13 _ SIDE_VIEW OF THE DEGASSER

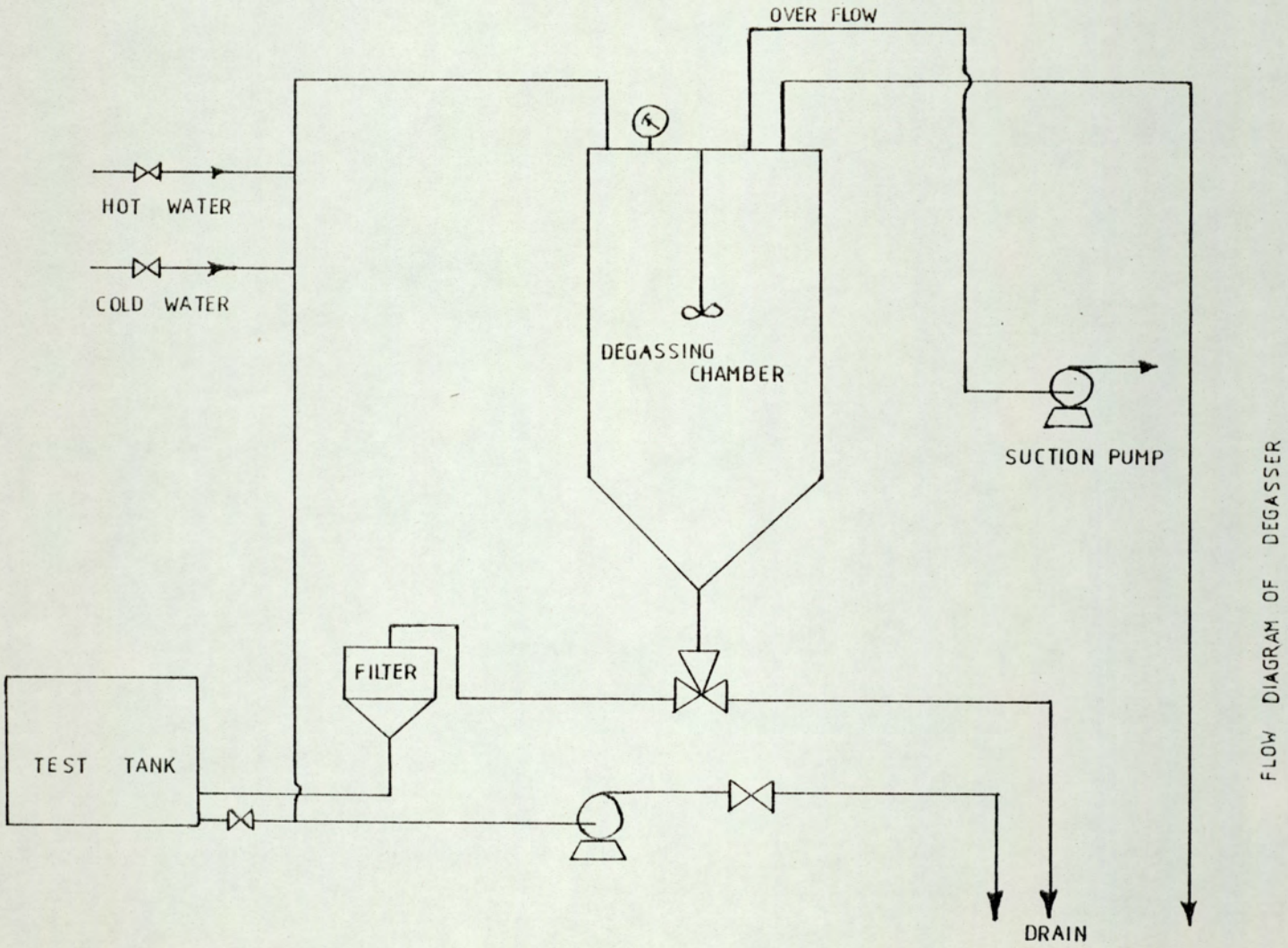

FIGURE_14_ FLOW DIAGRAM OF THE DEGASSER

through a 0.95cm stainless steel shaft with a mechanical shaft seal. The motor was mounted on the top of the aluminium plate and was surrounded with a 7.6cm diameter acrylic tube glued to the plate. This tube was filled with water to cool and lubricate the seal. The water filter was conical in shape and constructed from a 175mm diameter sintered glass plate of porosity No. 1, sealed with rubber gaskets. The other end of the filter was connected to the model tank by a 1cm rubber hose. The filter plate was cleaned with chromic acid after every 1000 liters of water had been filtered.

The method of operating the degasser was to supply a mixture of hot and cold water to obtain the required temperature, while all other lines and the drain valve was shut off. Then the overflow line was opened, and when the vessel was full of water the vacuum pump was switched on to evacuate the system to about 690mm. The agitator was set to operate at 1000RPM for 15 minutes, then the motor was switched off while the vacuum was left for a further 5 minutes to allow all the bubbles produced by the agitator to settle out. After the vacuum pump had been switched off all the water was fed to the model tank via the filter.

6.4 HOT-FILM ANEMOMETRY

6.4.1 EQUIPMENT

This type of anemometer is based on the principle of calibrating flow rate against the thermal loss of heated resistance sensors (115). The sensor is located in the flow path being measured and is consequently cooled. The magnitude of the convective heat loss is dependent on a

number of parameters such as the temperature, pressure, and velocity of the fluid whose flowrate is being determined. By eliminating the effect of all other parameters, the instantaneous heat loss of the sensor is a measure of the instantaneous velocity of the fluid.

The constant temperature anemometer used in this investigation was the DISA 55M10. It consisted of a wheastone bridge and a servo amplifier, shown in figure (15). The active arm of the bridge consisted of the probe and one of the two resistances A or B. shown. The passive bridge arm consisted of the other resistance, the comparison resistor and a few compensating networks which were included to eliminate the influence of the various cable parameters. Any change in the flow rate acting on the probe will affect the temperature of the sensor causing it to become cooler or hotter as the case may be. The resultant resistance change brings about a voltage difference in order to restore the temperature and this voltage is proportional to the flow rate.

The probes used for this study were type R150 coated with 2μ gold which were suitable for use in electrolytic solutions. These probes were of the right angle type, and were connected to the anemometer through a 60.0cm long support and circuit which was connected to earth to prevent damage of the probe. Figure (16) illustrates how the probe support was mounted on the framework of the tank. It was fixed firmly to avoid vibration. The probe was able to traverse the liquid inside the tank and to estimate the liquid velocity at any point near the tank base. The

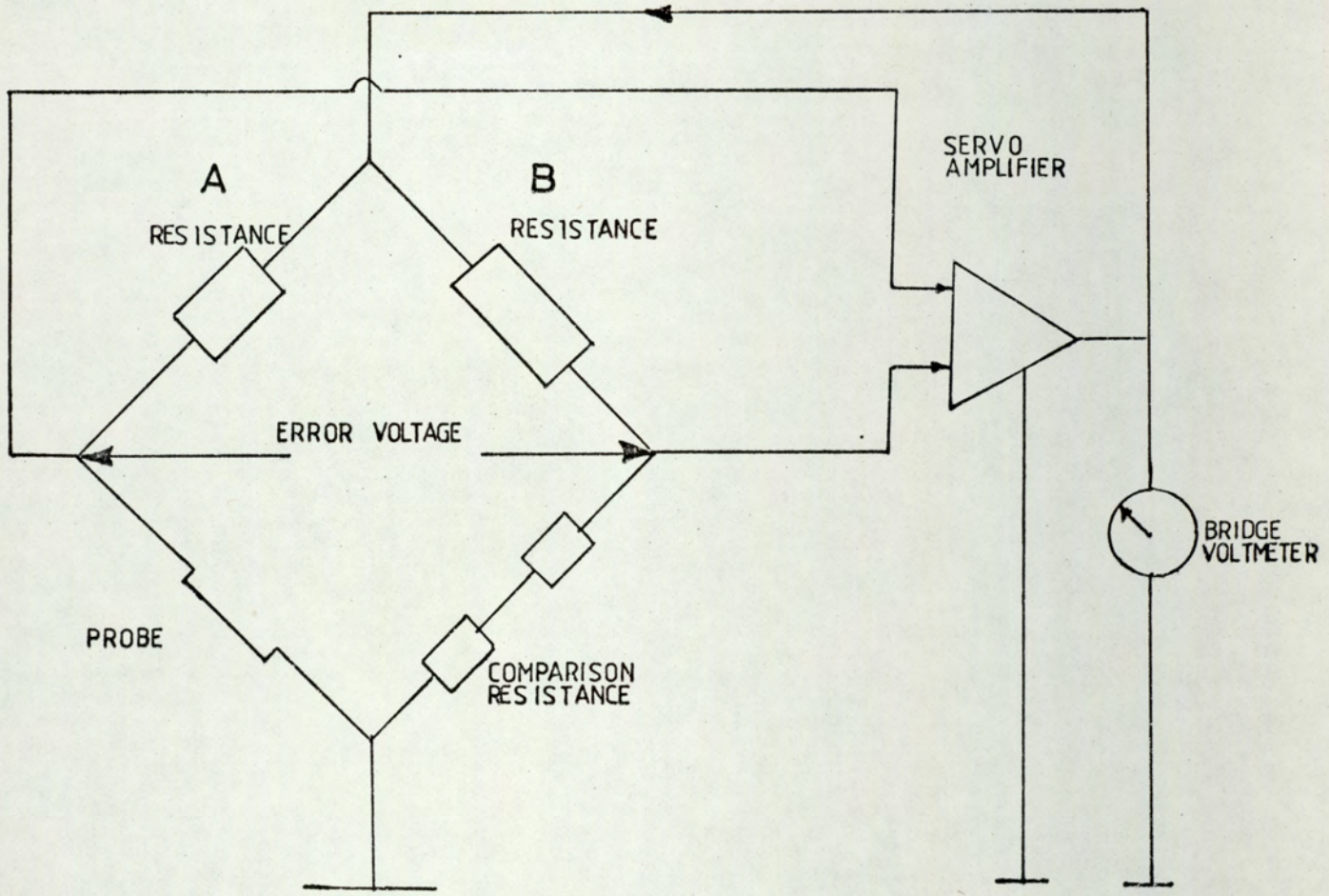

FIGURE -15 - SIMPLIFIED DIAGRAM OF THE CONSTANT TEMPERATURE ANEMOMETER

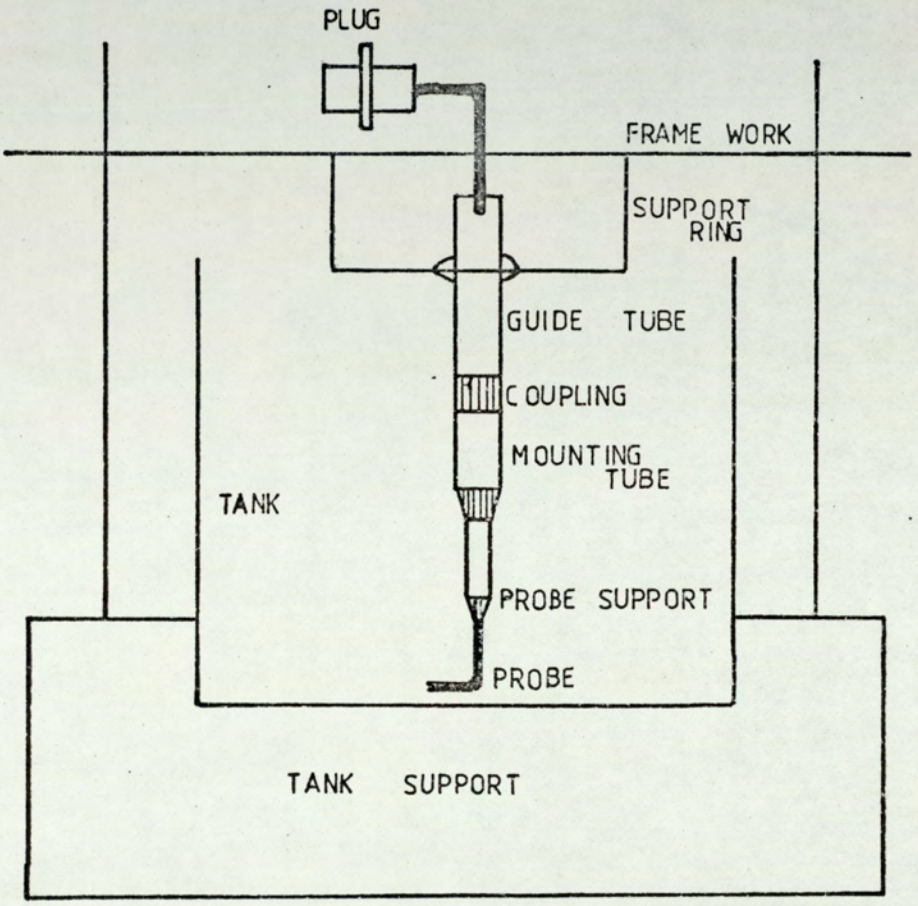

FIGURE-16 - SCHEMATIC REPRESENTATION OF THE HOT FILM PROBE.

height of the probe from the tank base was measured with a micrometer.

6.4.2 CALIBRATION

The anemometer output is the measured voltage. To relate this voltage to the fluid velocity it was necessary to calibrate the anemometer using laminar pipe flow. To maintain a high velocity in the laminar flow, a 1m length of glass pipe 0.65cm diameter was used for the calibration. This pipe shown in figure (17) was connected to a 20 liter aspirator through a needle valve and the water passed through a glass filter before entering the pipe in order to remove any dust particles in the water. A slot was made into the top side of the pipe to permit inserting the probe. The probe was mounted normal to the pipe and fixed by a clamping stand. All the tubing was lagged with glass wool to keep the temperature of the water constant during calibration. Degassed water was used for this purpose.

In order to obtain a mean value of the voltage and to record these values, the anemometer cable was connected to a chart recorder through a set of attenuators and electric filters. Also it was connected to a digital voltometer and electric integrator as shown in figure (18).

The calibration method was as follows:

1. The aspirator was filled with degassed filtered water at $25^{o}C$.
2. The anemometer was switched on and allowed to attain steady state for an hour. Then the bridge arm was balanced.
3. The needle valve was opened to let the water pass through the pipe, and the probe position was adjusted to give maximum

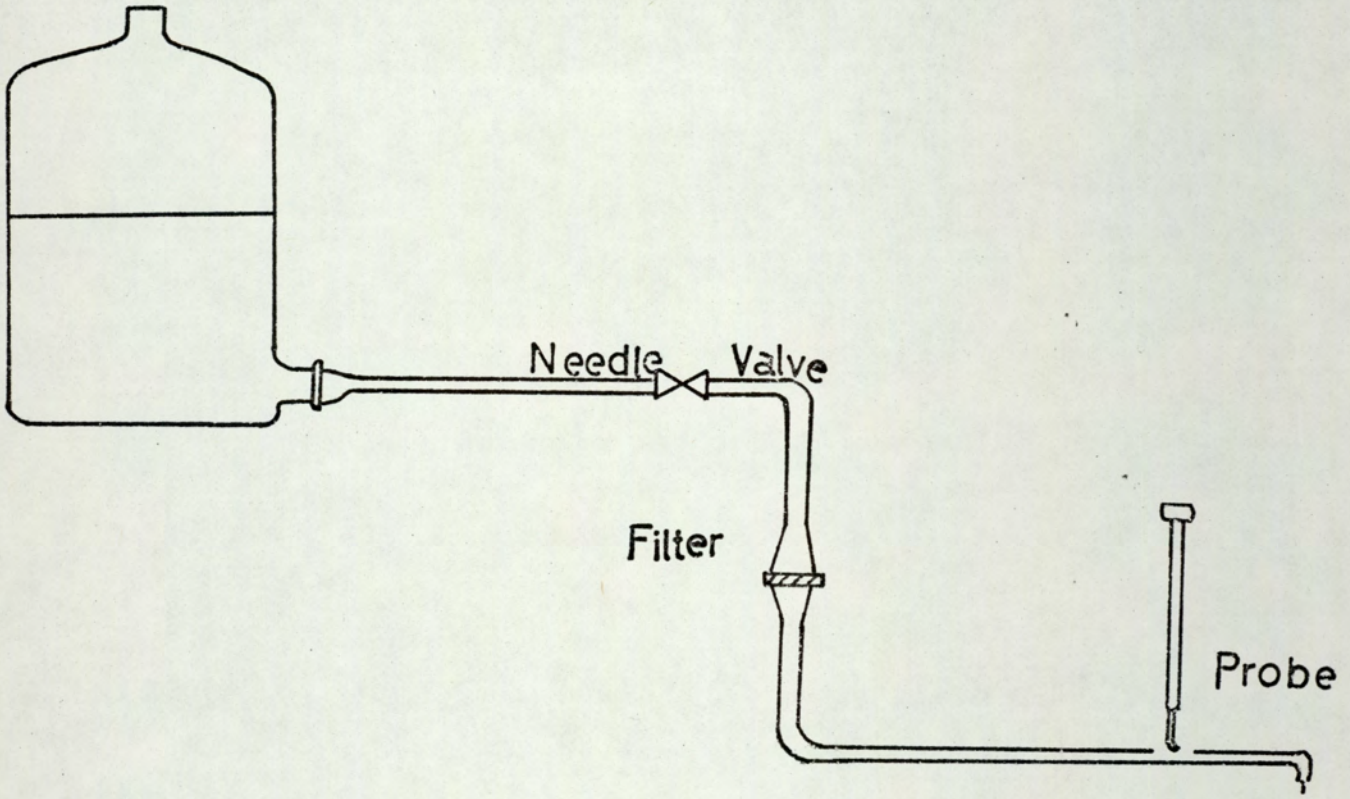

FIGURE -17 - A SIMPLE RIG FOR THE CALIBRATION OF THE HOT FILM ANEMOMETER

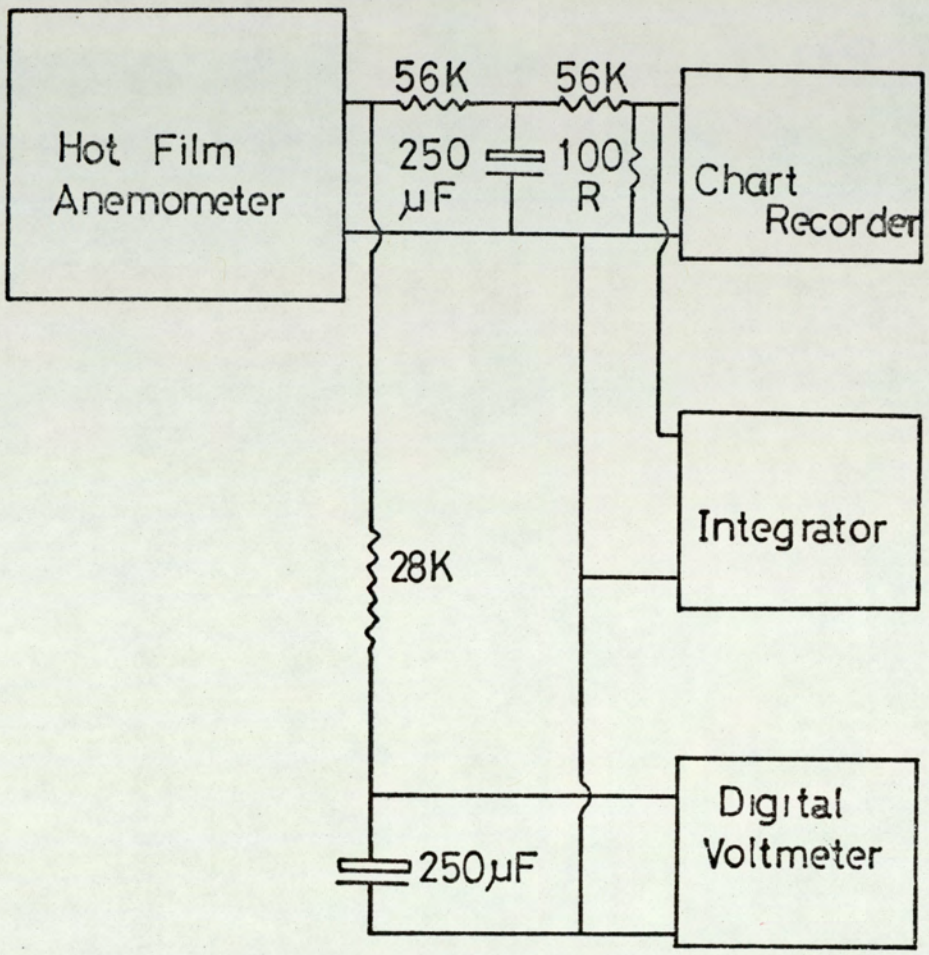

FIGURE_18_HOT FILM ANEMOMETER AND AUXILIARY INSTRUMENTS CONNECTION CIRCUIT

reading on the chart recorder, which indicated that the probe was positioned on the centre-line of the pipe.

4. The flow-rate was increased gradually and measured by weighing the water collected in a measured time interval. The voltage indicated on the digital voltmeter was recorded.

A calibration curve was plotted showing the digital voltmeter reading versus the flow-rate.

A similar procedure was followed in measuring the velocity in the tank. For precise results it was found necessary to average the signal over five minutes by switching the integrator to the "integrate" mode for this length of time.

6.5 PHOTOGRAPHIC TECHNIQUE:

Photographic techniques have a wide application in chemical engineering studies, especially in providing qualitative results. It was decided to use this technique to illustrate the distribution of the laminar sub-layer and its movement around the tank. Both a still camera and a cine camera was used to photograph the distribution of paper pulp solution injected into the liquid in the tank.

Studies of the effects of a cruciform shape baffle were undertaken and the effect of the various parameters on the system were studied.

The method of operation was as follows:

1. A solution of paper pulp was prepared by dissolving coloured papers into a weak solution of sodium hydroxide. The solution was agitated vigrously and heated until all the paper had dissolved in the solution.

2. The model tank was filled with water to the required level, and the impeller started and set to the desired

speed. Other parameters such as the shaft angle, impeller diameter were set to the desired values and were changed as necessary. The impeller speed was varied in the different sets of experiments in order to study their effect.

3. The camera was set and the fluorescent lights around the tank were switched on.

4. The paper pulp solution stored in 20-liter aspirator was injected into the base of the tank contents through a plastic tube. When the pulp commenced to enter the impeller jet, photographs were taken to show its distribution. The cine camera was used as well as the still camera to show the movement of the pulp in the liquid and to locate areas where the pulp tended to accumulate.

5. After repeating the experiment for the different conditions, another set of experiments was performed using a cruciform shape baffle of 10cm x 2cm dimensions. This was placed on the base of the tank in the area where the pulp accumulated most in the first set of experiments. The same procedure was repeated. This set of experiments illustrated the effect of placing a small baffle on the base of the tank.

CHAPTER VII

7 EXPERIMENTAL RESULTS

7.1 INTRODUCTION

The electrochemical technique for the measurements on the boundary layer was first applied to the test channel. The effects of all the parameters on the viscous sub-layer thickness, mass transfer coefficient were studied in detail. These parameters are: Impeller speed, Impeller diameter, Shaft angle, Liquid depth, Viscosity and Density of the solution.

The hot-film anemometer was used to check and compare some of these results. Moreover, photographs were taken to provide a qualitative distribution of the viscous sub-layer. Comparison was made between these results and the full-scale tank results in an attempt to obtain a scale-up procedure.

7.2 TEST CHANNEL - ELECTROCHEMICAL TECHNIQUE

7.2.1 CURRENT-VOLTAGE PLATEAU

In applying the electrochemical technique to the test channel, the electrical current passing through the circuit was measured as a function of the incremental increase of the voltage supplied to the circuit, at different values of Reynolds number. The results obtained are shown in Tables 2,3,4 and are plotted in Figure 19 . A range of N_{Re} between 500 and 3200 was considered by changing the flow rate through the rotameter which had been calibrated previous to the measurements for different viscosities of the solution. Figure 20 is a typical calibration curve for the rotameter used.

It was found from the current-voltage plateau that, as

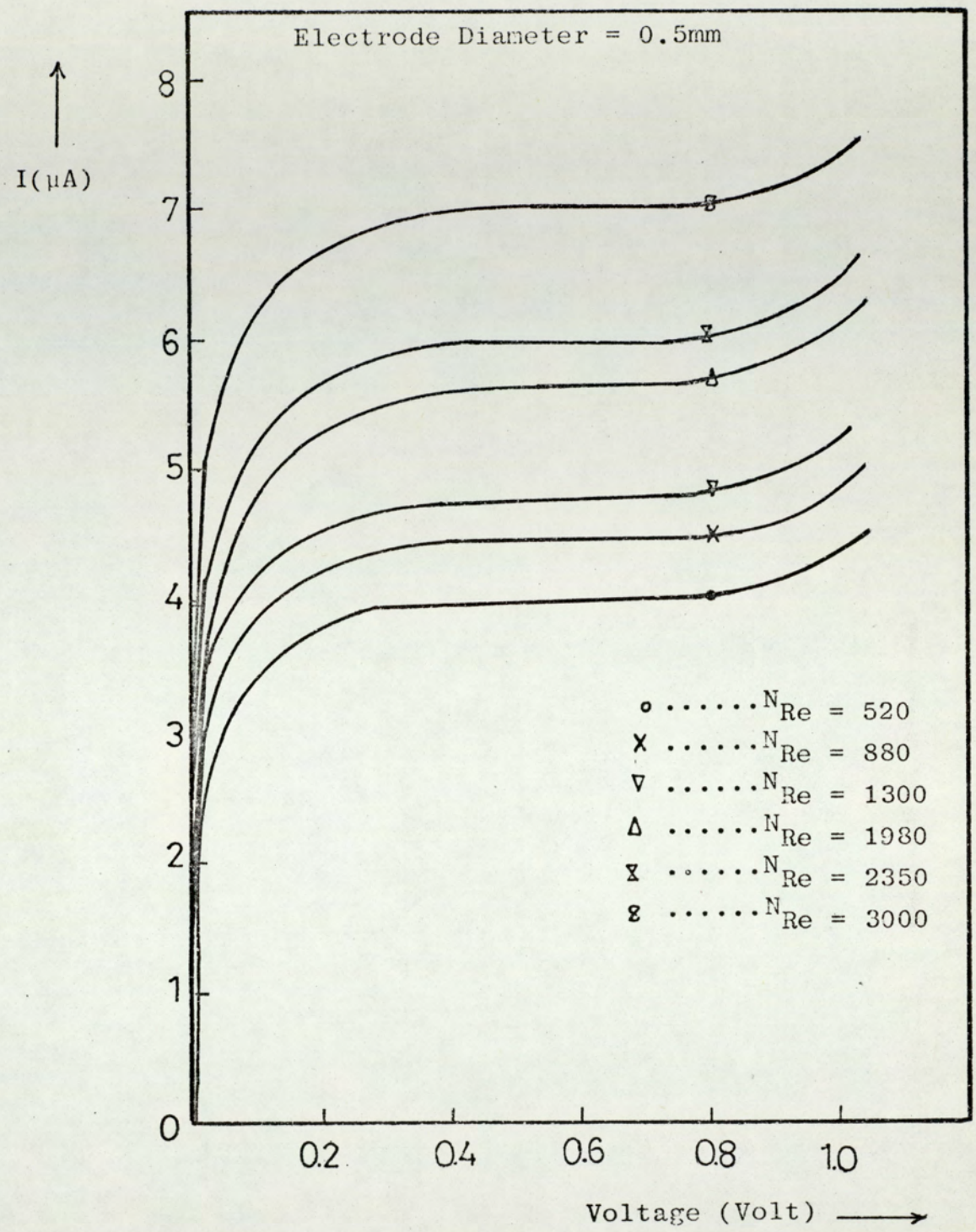

Figure 19 Current-voltage polarization curves for different Reynolds number

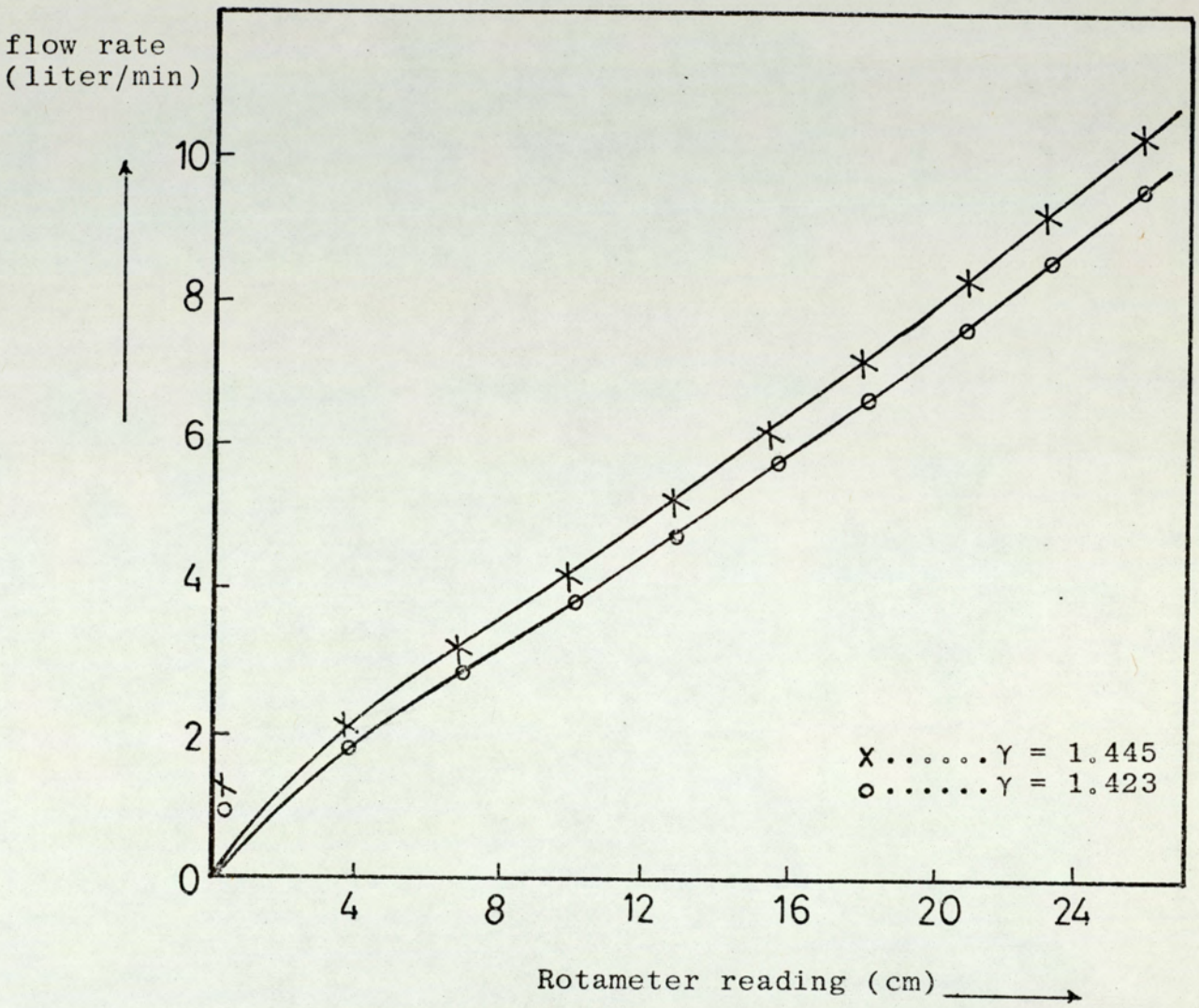

Figure 20 Flow rate as a function of rotameter reading for different Kinematic viscosities of the solution - Calibration Curves -

the voltage first increased, the current increased sharply until the voltage reached a certain value of about 0.3 volt. Then the current became constant and any increase in voltage would not change the value. However, this limiting current increased sharply when the voltage exceeded a value of 0.8 V. It was noticed that it was necessary for a time interval of about three minutes to be taken between each increase of voltage to give time for the current and potential to reach a steady state.

When N_{Re} was increased, by increasing flow rate, the limiting current increased too and tended to shorten the flat portion of the current-voltage curve.

In studying the effect of electrode diameter on the system, the limiting current was plotted as a function of N_{Re} for the three different electrode diameters as in Figure 21 The limiting current was found to increase with increase of the electrode diameter but the ratio of I/A also decreased with increasing the electrode diameter.

7.2.2 MASS TRANSFER COEFFICIENT

The value of the mass transfer coefficient calculated from the measured value of the limiting current (Appendix 4) was plotted against N_{Re} for the different electorde diameters as shown in Figure 22 . There it will be seen that the mass transfer coefficient increased as the Reynolds number increased and the graph shows a change in the slope of the line from a value of 0.184 to 0.484 at N_{Re} = 1400. This indicates the existence of two regimes of flow. Also the mass transfer coefficient increased with the decrease of the electrode diameter. Figure 23 representing the mass transfer coefficient as a function of the velocity gradient at the wall gives a

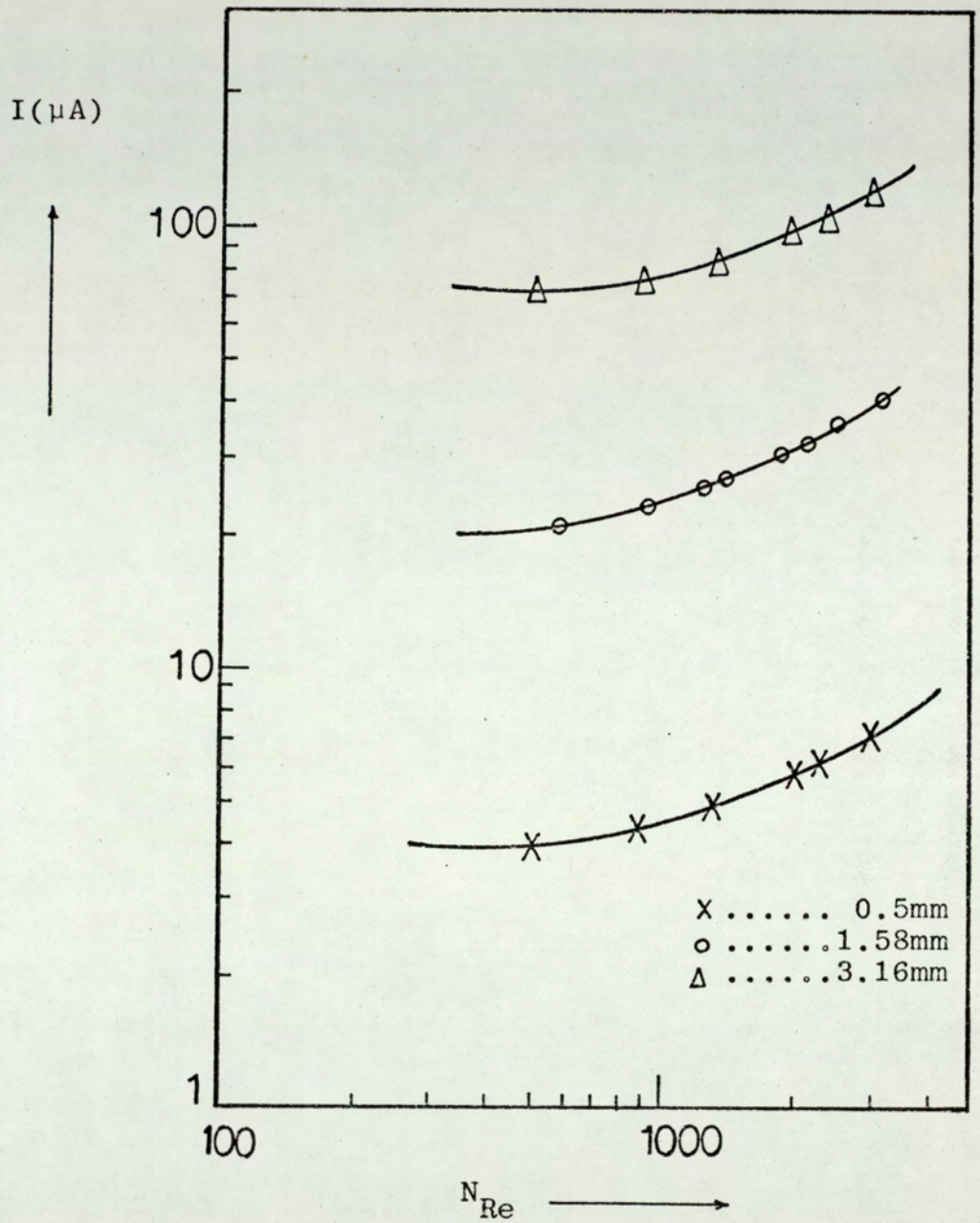

Figure 21 Limiting current as a function of Reynolds number for different electrode diameters.

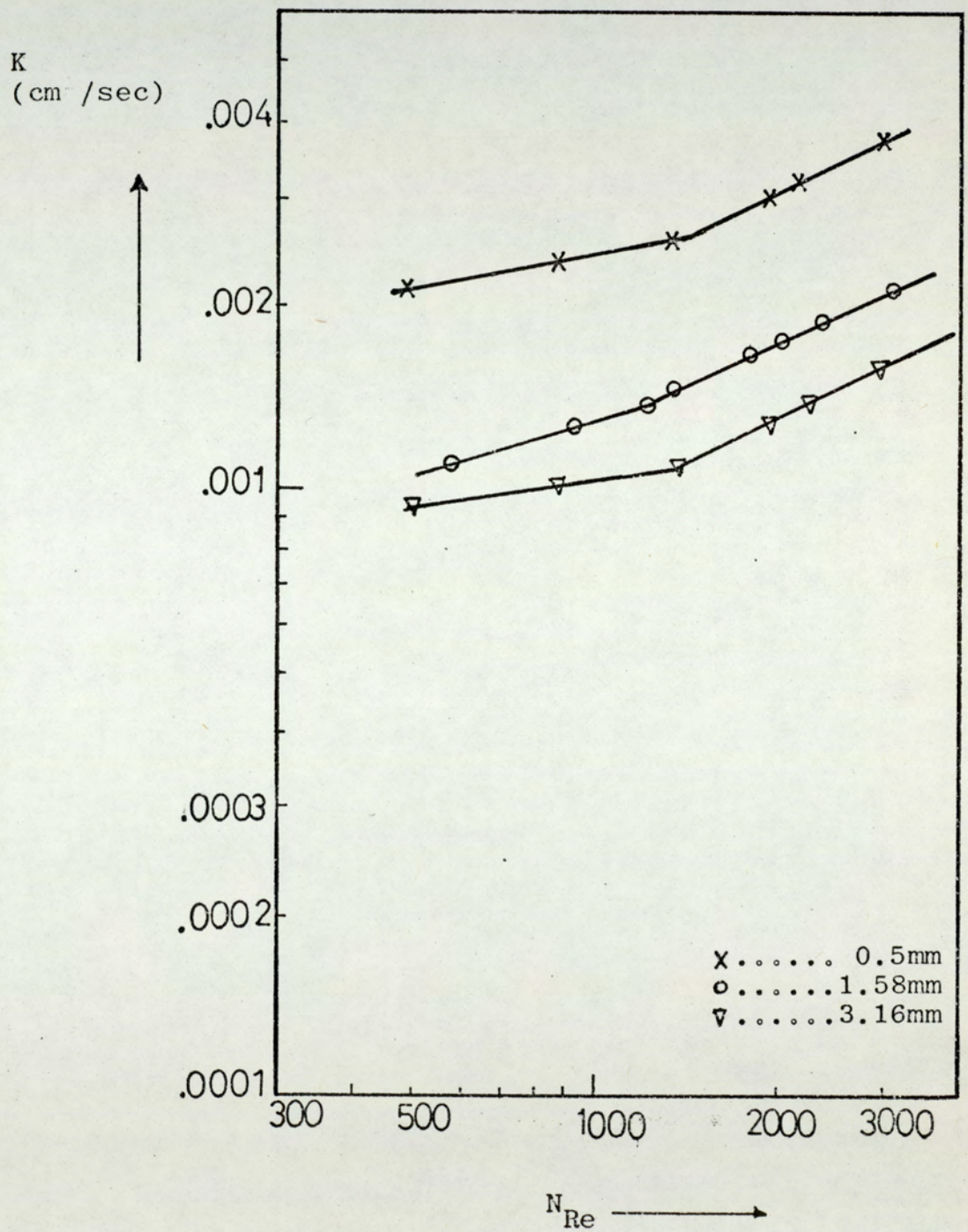

Figure 22 Mass transfer coefficient as a function of Reynolds number for different electrode diameters

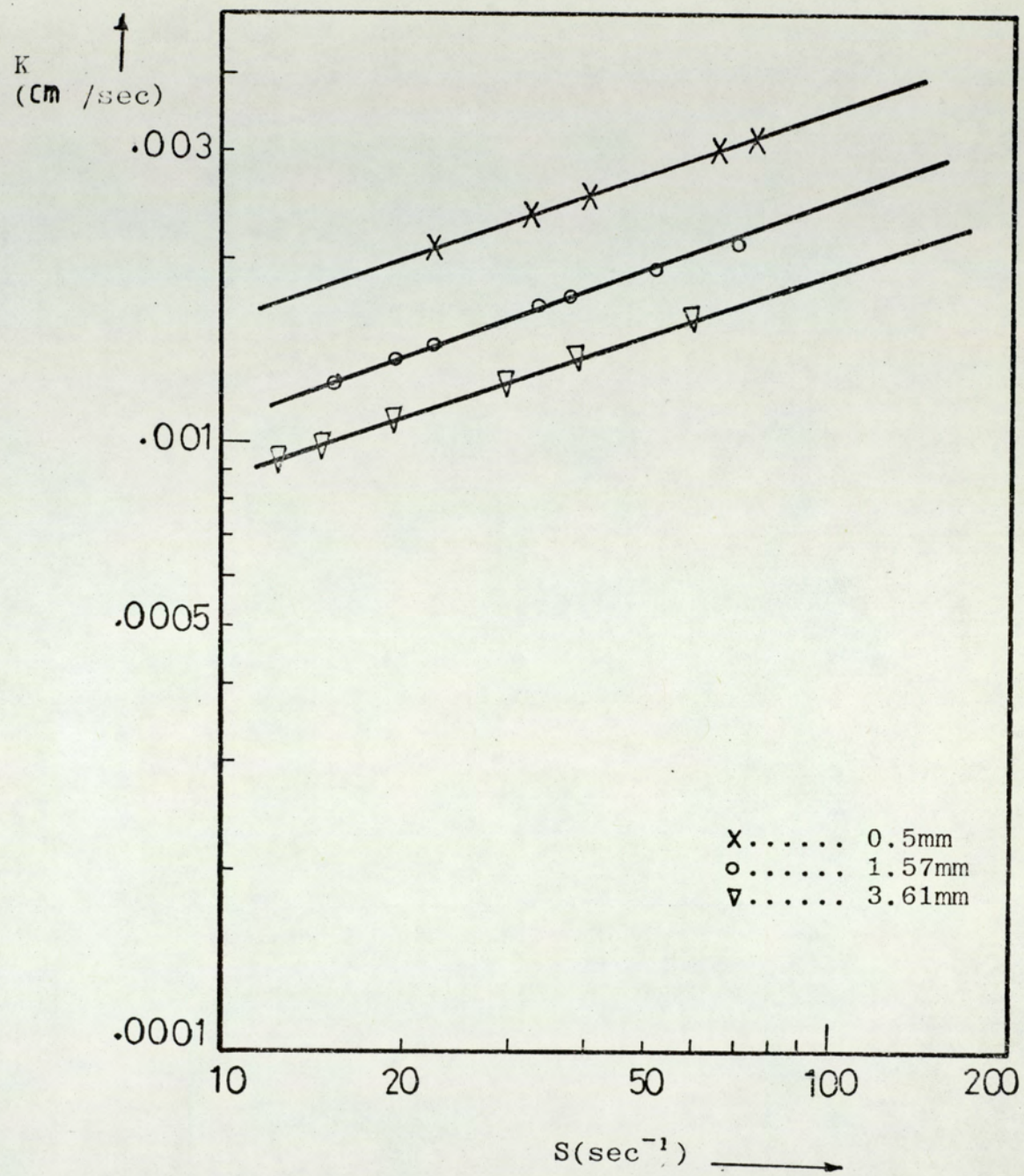

Figure 23 Mass transfer coefficient as a function of velocity gradient for different electrode diameters.

line of 0.333 slope and shows an increase in the mass transfer coefficient with the increase of the wall shear stress.

7.2.3 THICKNESS OF THE VISCOUS SUB-LAYER

The thickness of the viscous sub-layer, calculated from the limiting current is presented in Tables 9, 10 and 11 was plotted against Reynolds number for different electrode diameters as shown in Figure 24. It shows that there is a decrease in thickness with the increase of N_{Re}; also the graph is a straight line of slope -0.323. The decrease in the electrode diameter reduces the value of the thickness estimated and this becomes more pronounced at a low value of N_{Re}. Figure 25 shows that the thickness of the concentration boundary layer is much smaller than that of the viscous sub-layer and the ratio is not more than $\frac{1}{20}$.

7.3 MODEL TANK - ELECTROCHEMICAL TECHNIQUE

In applying the electrochemical technique to the model tank, the limiting current was measured for each of the 22 electrodes built in the base of the tank. Most of the results presented were based on the mean value of the 22 electrodes, except when estimating the distribution of the viscous sub-layer thickness around the tank. In this analysis the value of each electode was determined separately according to its position in the tank.

Using the mathematical model derived by Hanratty (54), the mass transfer coefficient, velocity gradient at the wall, thickness of the concentration boundary layer, friction velocity and the thickness of the viscous sub-layer were

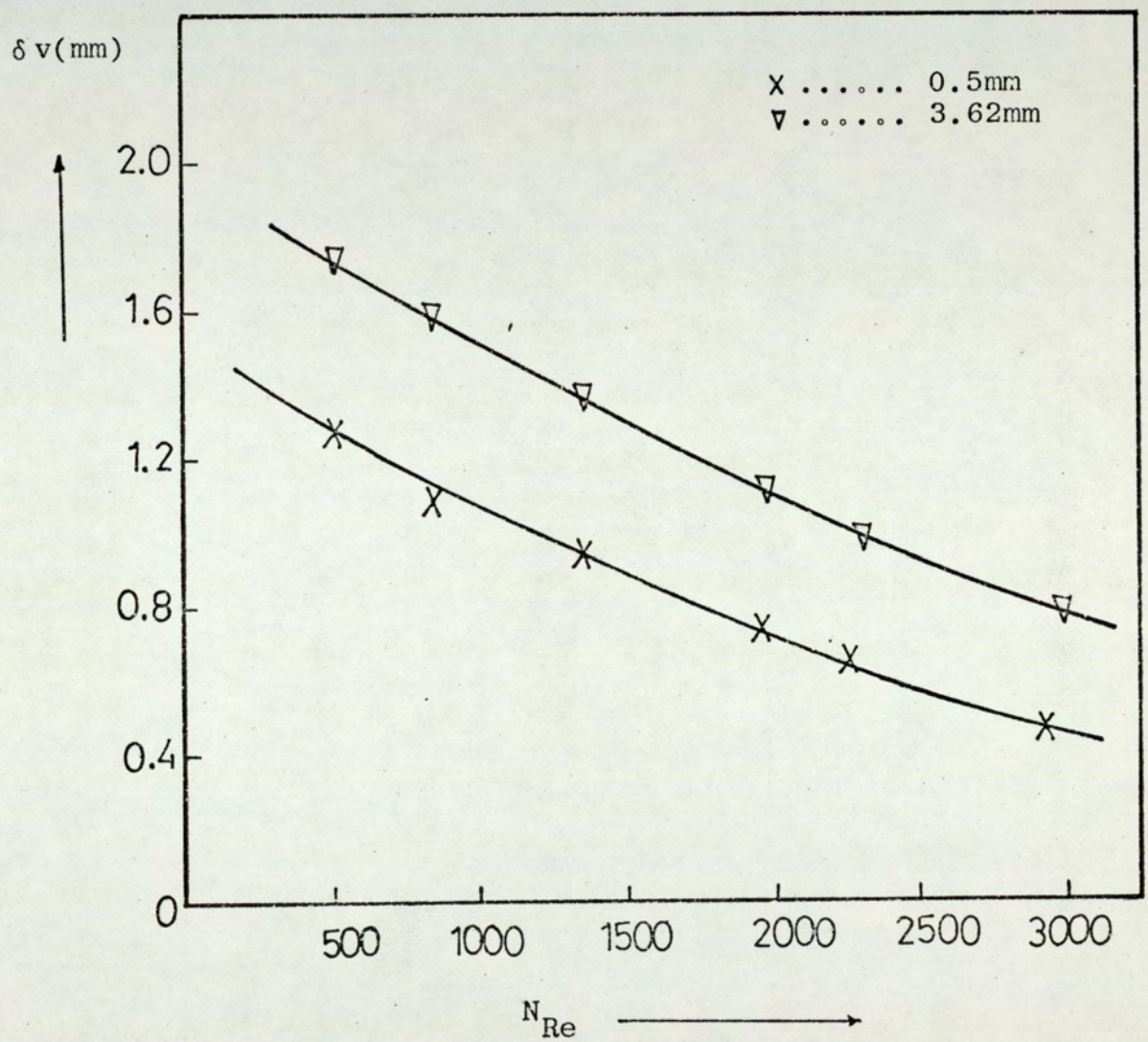

Figure 24 Thickness of the viscous sub-layer as a function of Reynolds number for different electrode diameters.

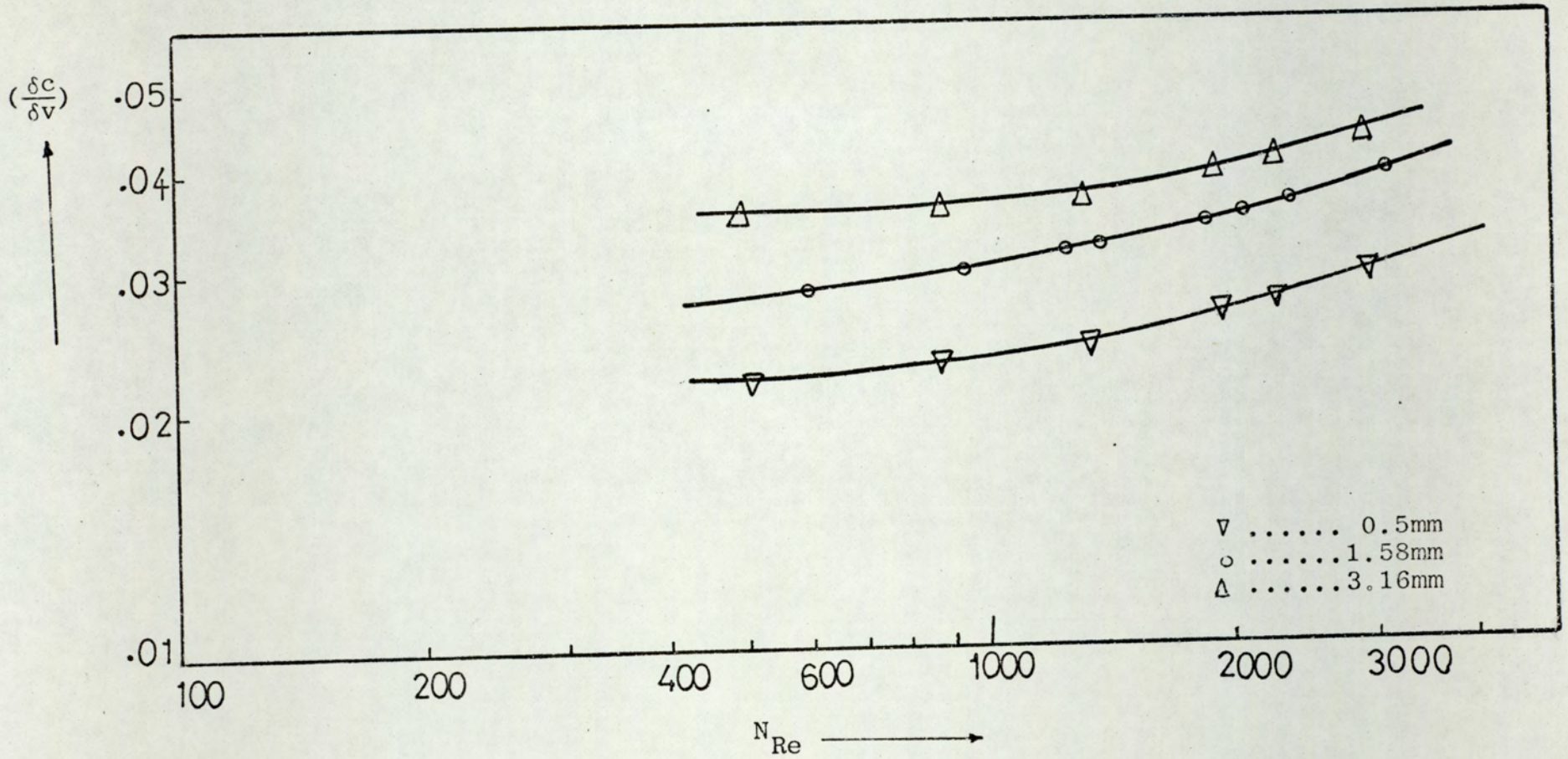

Figure 25 Ratio of the thickness of the concentration boundary layer to the viscous sub-layer as a function of Reynolds number for different electrode diameters.

calculated using the value of the measured limiting current. Details on the model and a sample of calculation is given in Appendix (A4).

7.3.1 LIMITING CURRENT AND CURRENT-VOLTAGE PLATEAU

Figure 19 is a typical current voltage plateau which shows the change of the current with increase of voltage applied. The flat portion of each curve represents the value of the limiting current. As the value of the impeller Reynolds number increased, the value of the limiting current also increased.

The measured limiting current was measured at different values of Impeller speed, Impeller diameter, Liquid depth, Shaft angles, Densities and Viscosities of the solution. These results are tabulated in Tables 12 to 22.

The value of the measured limiting current was increased with increase of impeller speed, impeller diameter, and the Density of the solution as seen in Figure 26 , 27 , 28.

These figures show the effect of the above parameters, on the limiting current while Figure 29 is a plot of the limiting current against the viscosity of the solution and indicates a sharp decrease in the value of the current with the increase of the viscosity. The effect of the shaft angle and the liquid depth on the limiting current shows some different behaviour. The limiting current decreases as the shaft angle is increased in both left and right direction. Figure 30 indicates a maximum value of the limiting current at an angle of 5 degrees to the left. The increase in liquid depth resulted in a fluctuation in the value of the limiting current as shown in Figure 31 .

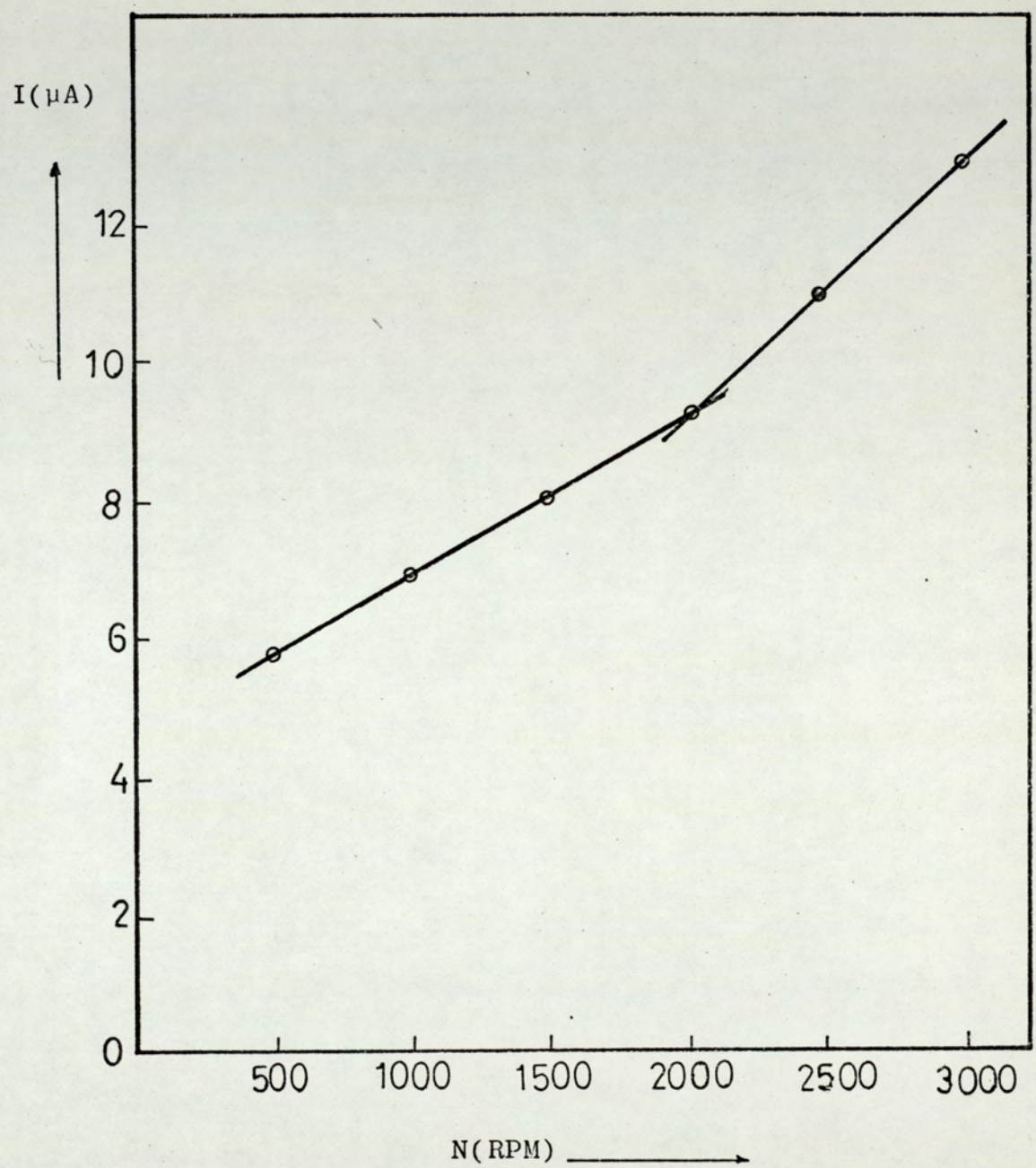

Figure 26 Limiting current as a function of impeller speed

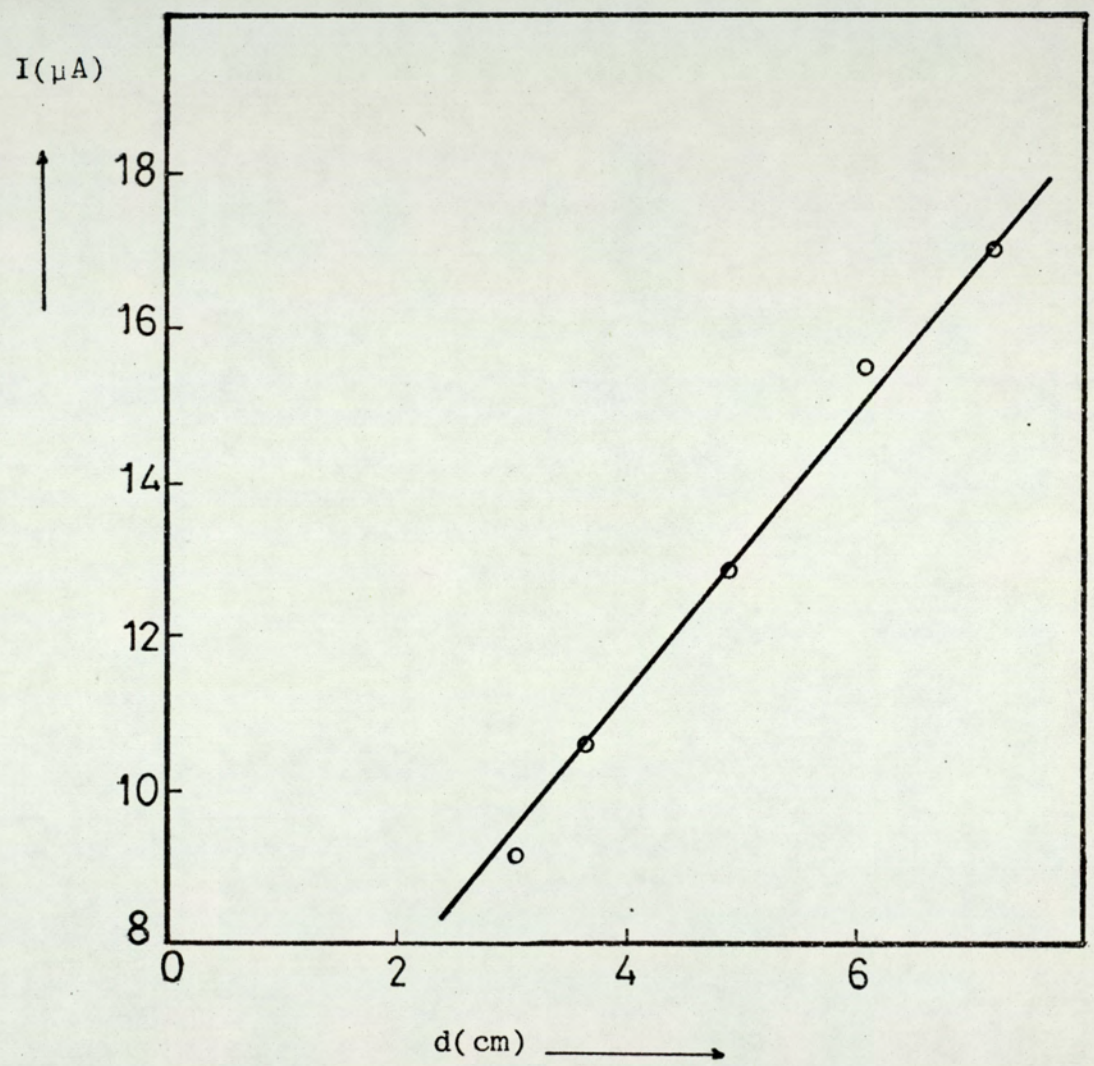

Figure 27 Limiting current as a function of impeller diameter

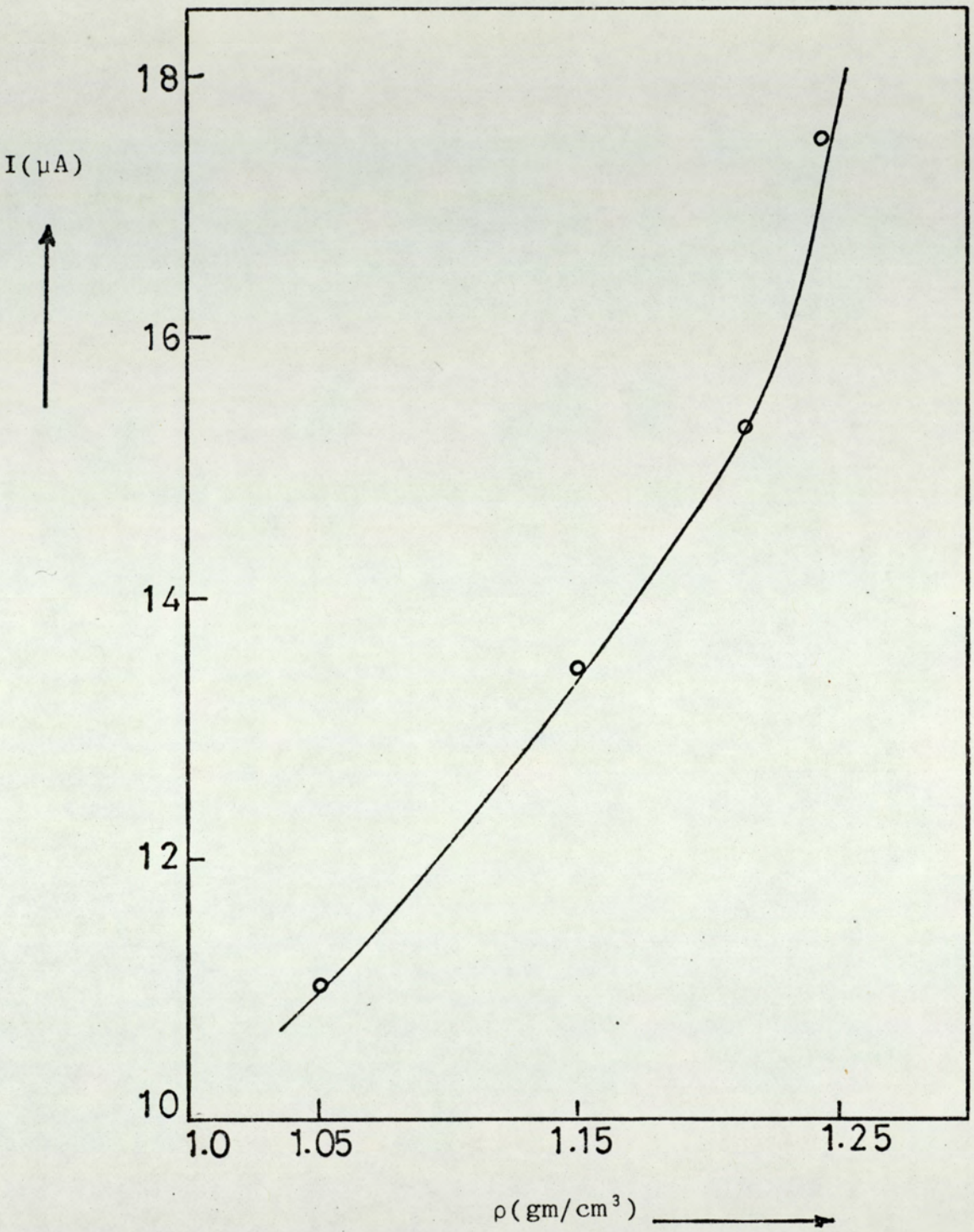

Figure 28 Limiting Current as a Function of Density

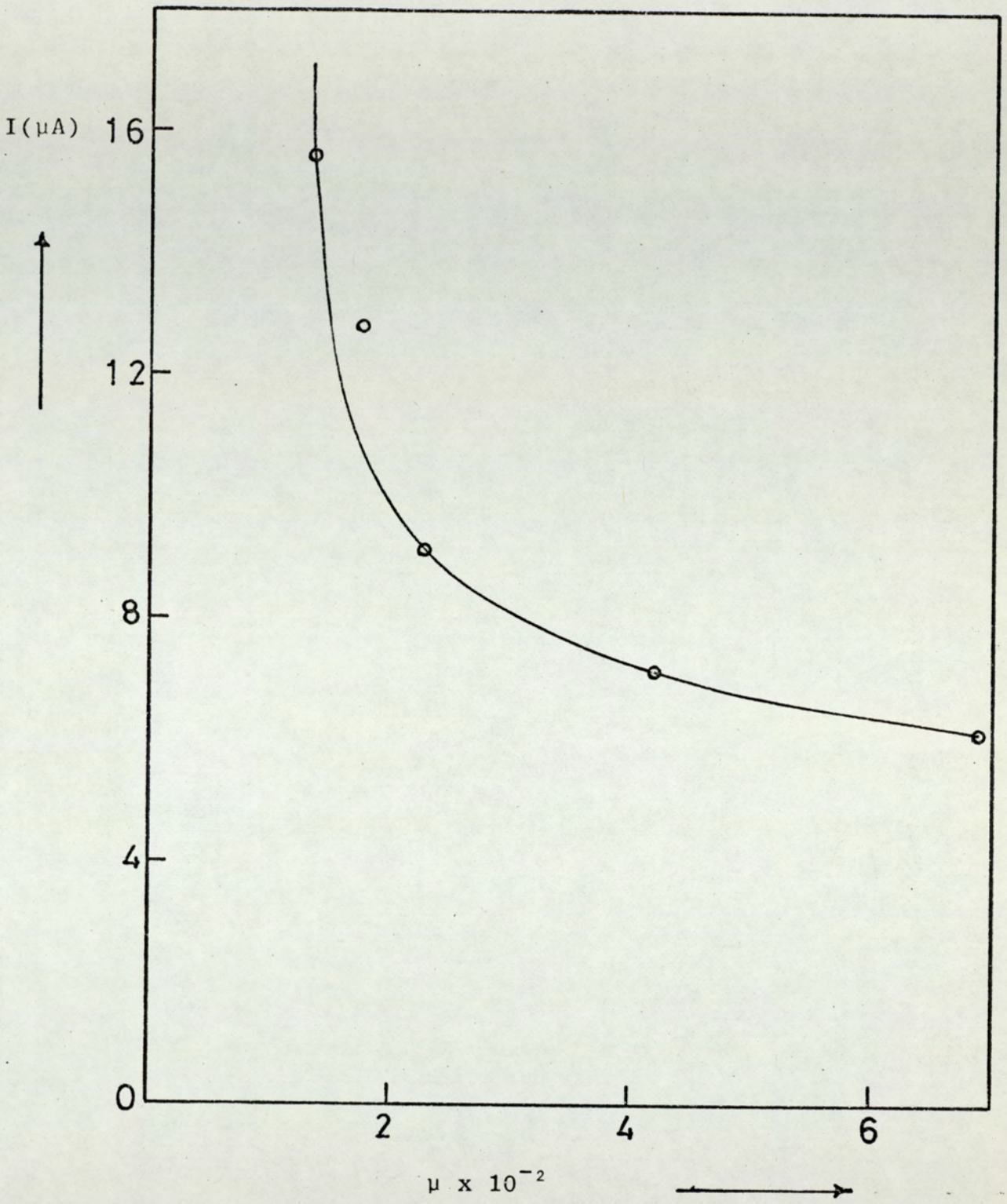

Figure 29 Limiting Current as a Function of Viscosity

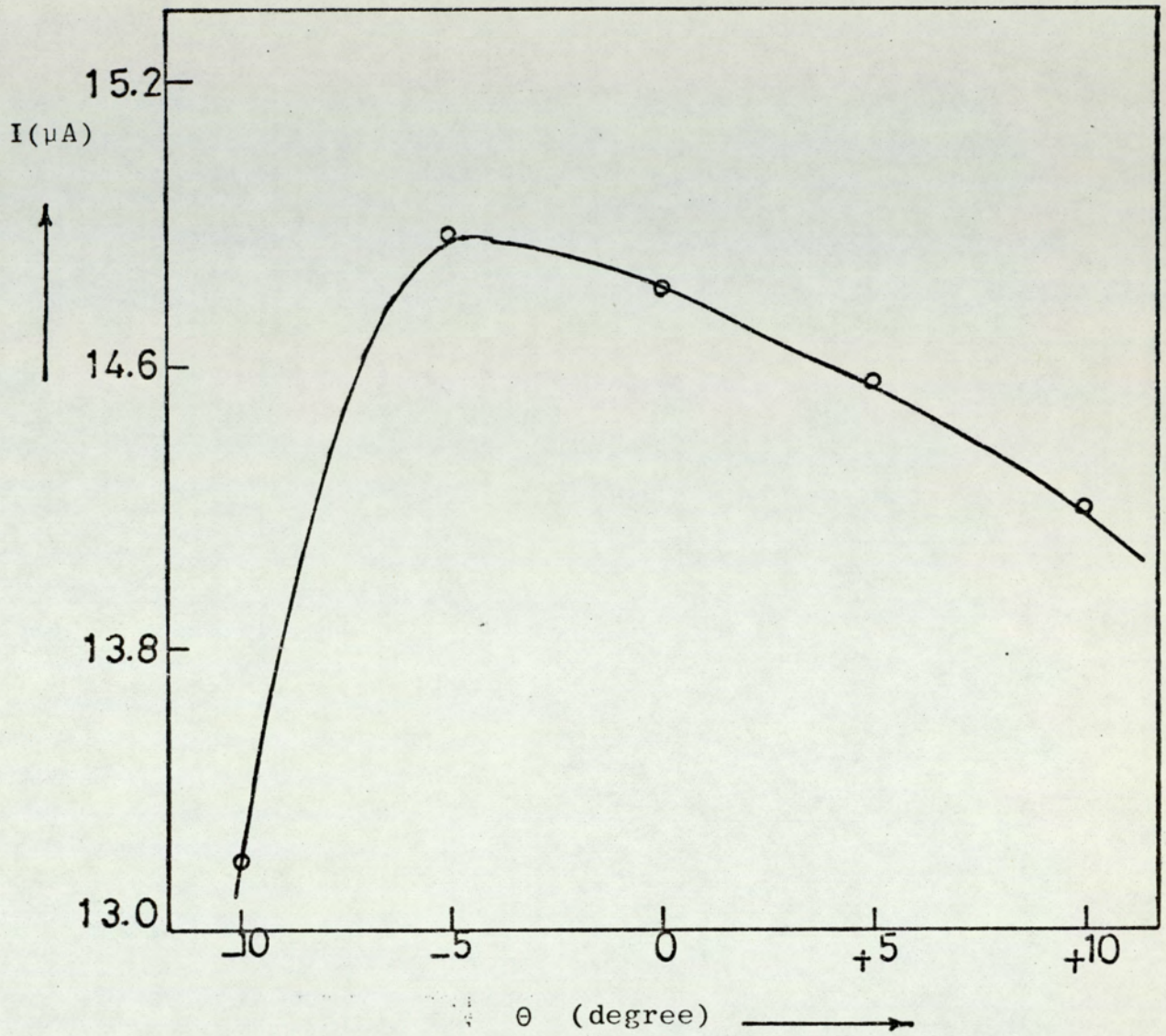

Figure 30 Limiting Current as a Function of Shaft Angle

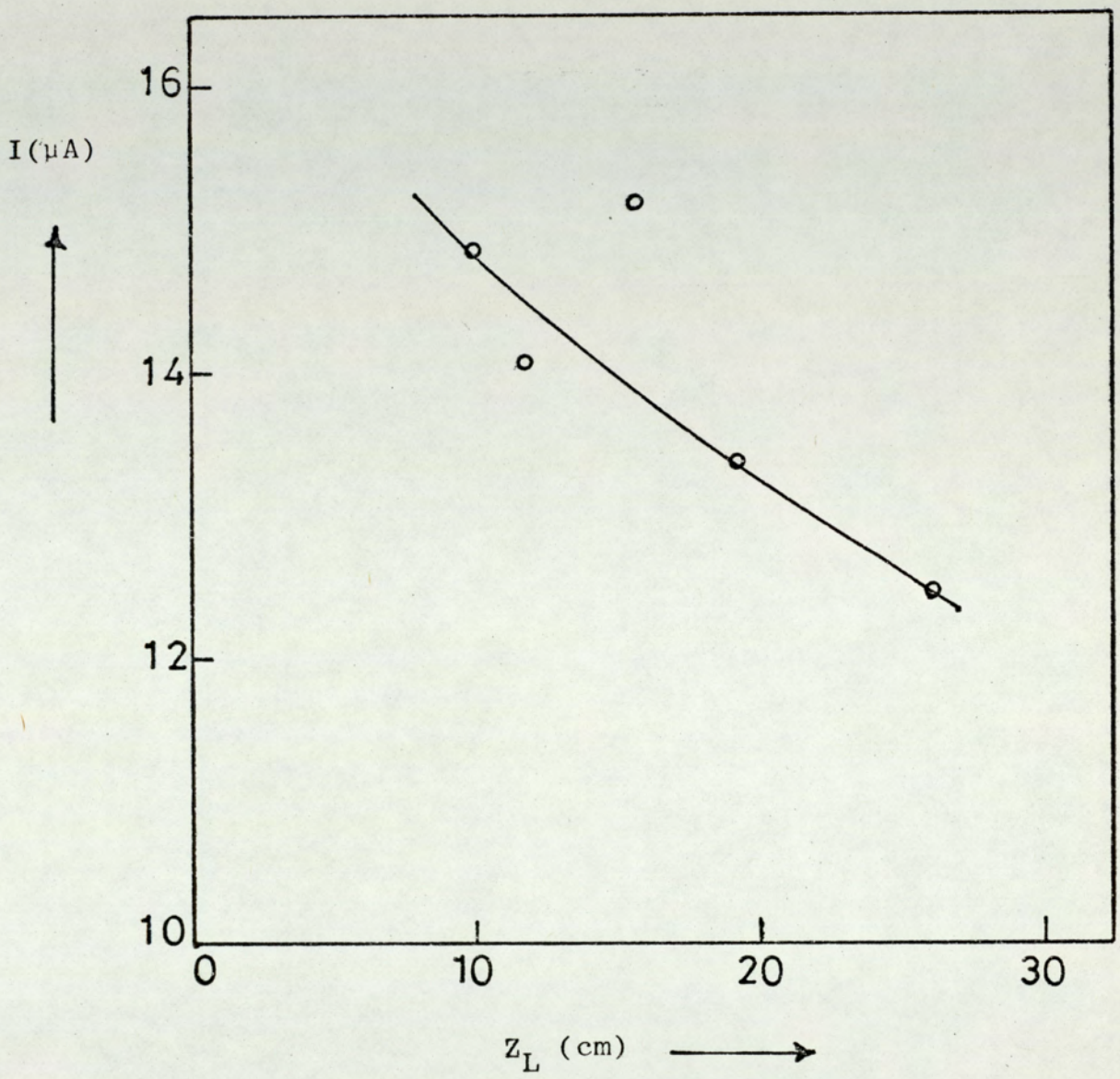

Figure 31 Limiting Current as a Function of Liquid Depth

7.3.2 MASS TRANSFER COEFFICIENT

The mass transfer coefficent was calculated from the measured limiting current using the following equation:

$$K = \frac{I}{C_b nAF} \qquad (7.1)$$

The values of the mass transfer coefficient for the 22 electrodes were calculated at different impeller speeds, impeller diameters, shaft angles, liquid depth, viscosities and densities and the results are listed in tables 23 to 32. Since the reaction was diffusion-controlled, the mass transfer coefficient is directly proportional to the limiting current and the plot of the mass transfer coefficient against the various paraemeters of the system show a similar trend as the limiting current. However, when the mass transfer coefficient was plotted against the impeller speed as seen in Figure 32, the graph was a straight line with a change in slope from 0.6 to 0.9 at a speed of 1750RPM indicating the presence of two different flow regims. The above measurements were carried out using a propeller, 3.6cm diameter, at angle of 5 degrees to the left, and therefore the value of the impeller Reynolds number at which the slope of the line change was equal to 2.75×10^4. This change in slope of the line was not obtained when the mass transfer coefficent was plotted against the impeller diameter as will be seen in Figure 33. The reason was that these measurements were made at an impeller speed of 3000RPM using a range of impeller diameter from 3.0cm to 7.2cm. This gives a minimum value of the impeller Reynolds number of about 3.2×10^4.

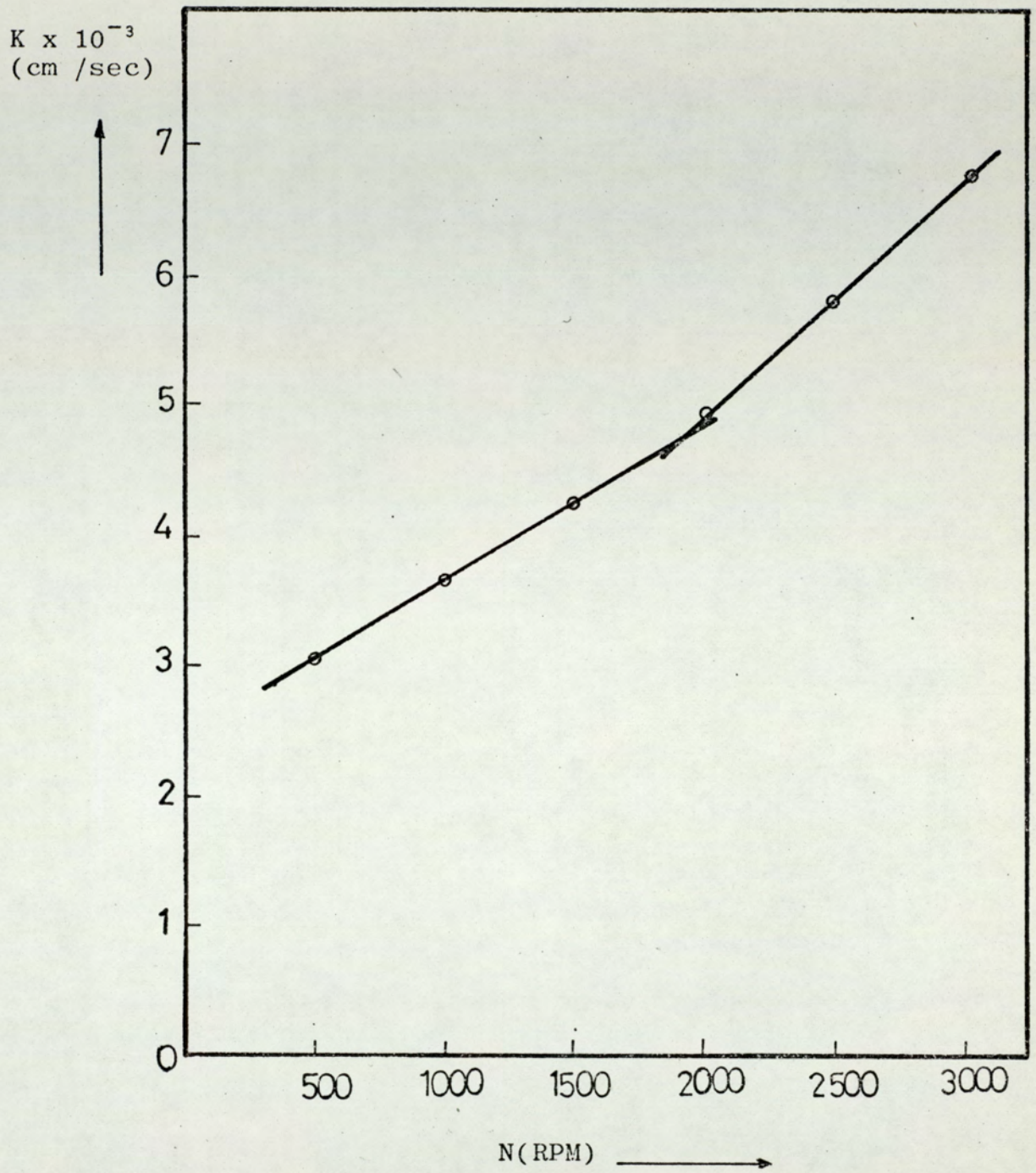

Figure 32 Mass transfer coefficient as a function of impeller speed

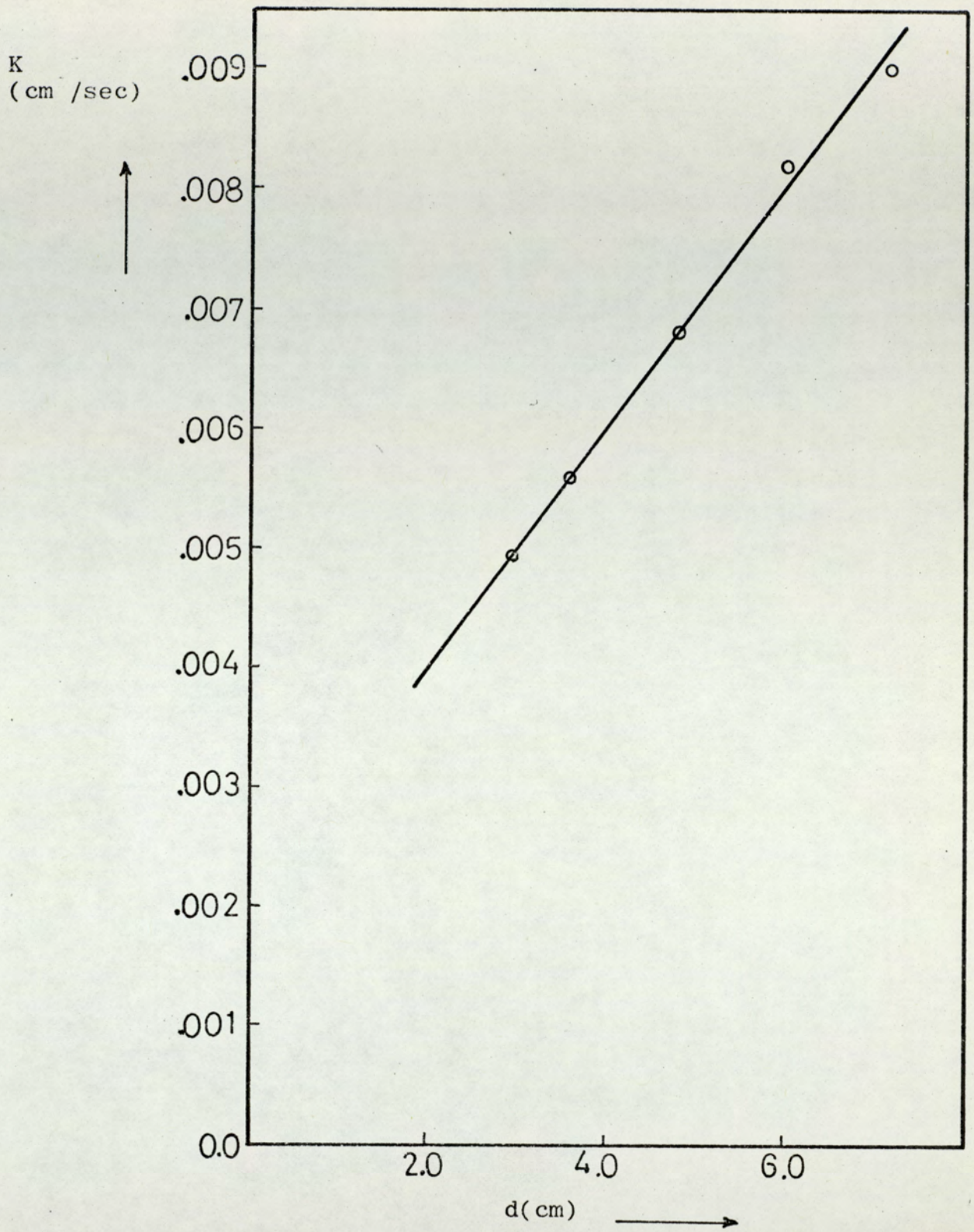

Figure 33 Mass transfer coefficient as a fucntion of impeller diameter

Although, the liquid depth and the shaft angle both affect the mass transfer coefficient, they do not have a direct effect on Reynolds number. In other words, at any value of Reynolds number, as the liquid depth, or shaft angle change, a consequent change in the mass transfer coefficient would occur and it appears that there is a relation between both the shaft angle and the liquid depth. However, at a shaft angle of 5 degree to the left, there is a maximum value for the mass transfer coefficient as in Figure 34.

In studying the effect of the change in the physical properties of the solution on the mass transfer coefficient (viscosity and density), each of the density or the viscosity must be kept constant while the other is changed.

To achieve this a study was carried out : with a solution in which each of the properties was kept approximately constant (1-4% change). The viscosity was changed in the range of 0.0137 to 0.0692 gm/cm sec while the density was changed from 1.077 to 1.245 gm/cm^3. Details of the study is presented in Appendix (A2). Figures 35 and 36 show the effect of the viscosity change and the density change on the mass transfer coefficient respectively. While the increase in the viscosity brings about a decrease in the mass transfer coefficient, the increase in the density of the solution increases its value.

7.3.3 FRICTION VELOCITY

The friction velocity was calculated as in Appendix (A4) using the following equation:

$$U^* = \sqrt{S\gamma} \qquad (7.2)$$

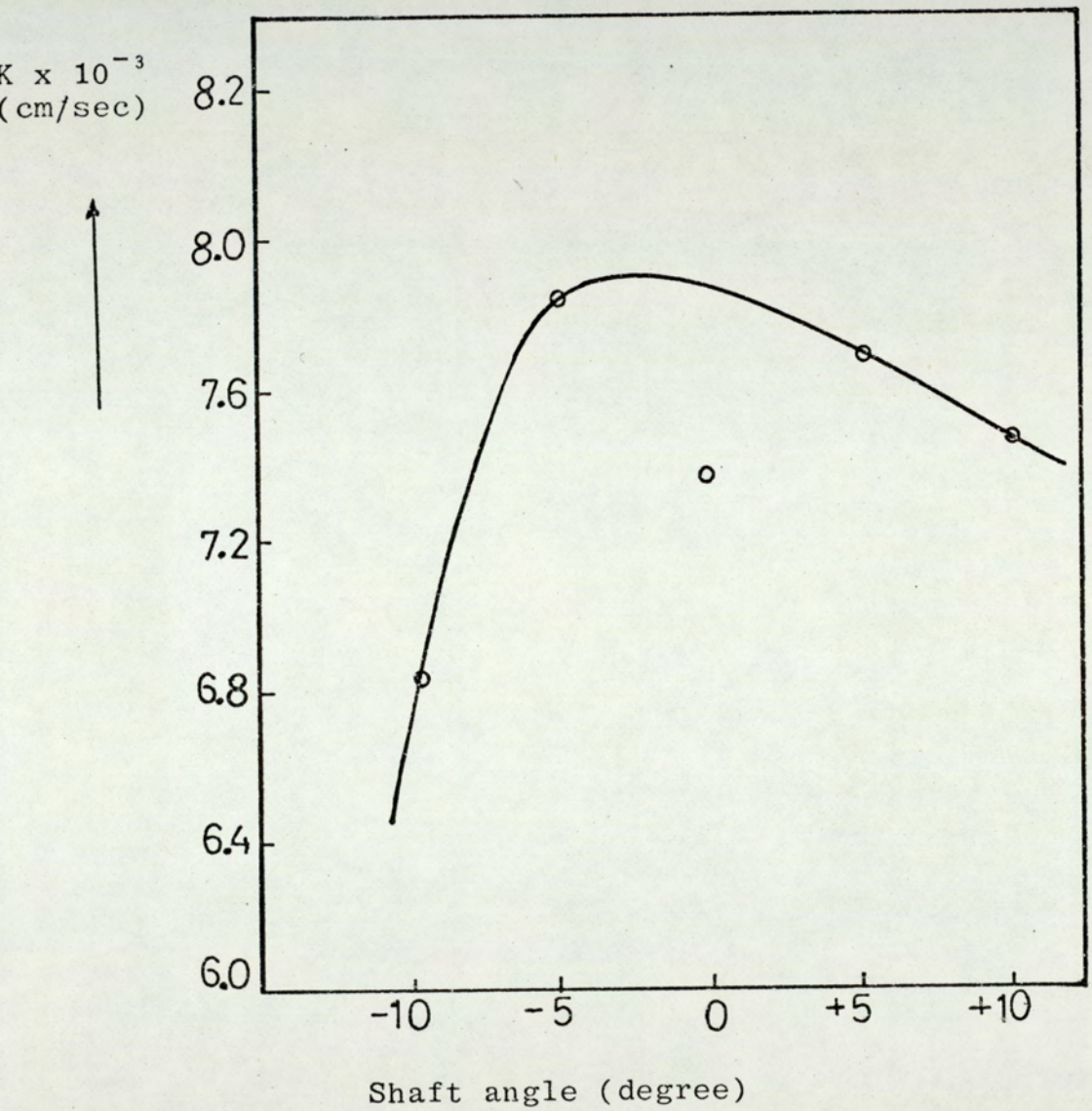

Figure 34 Mass transfer coefficient as a function of impeller shaft angle

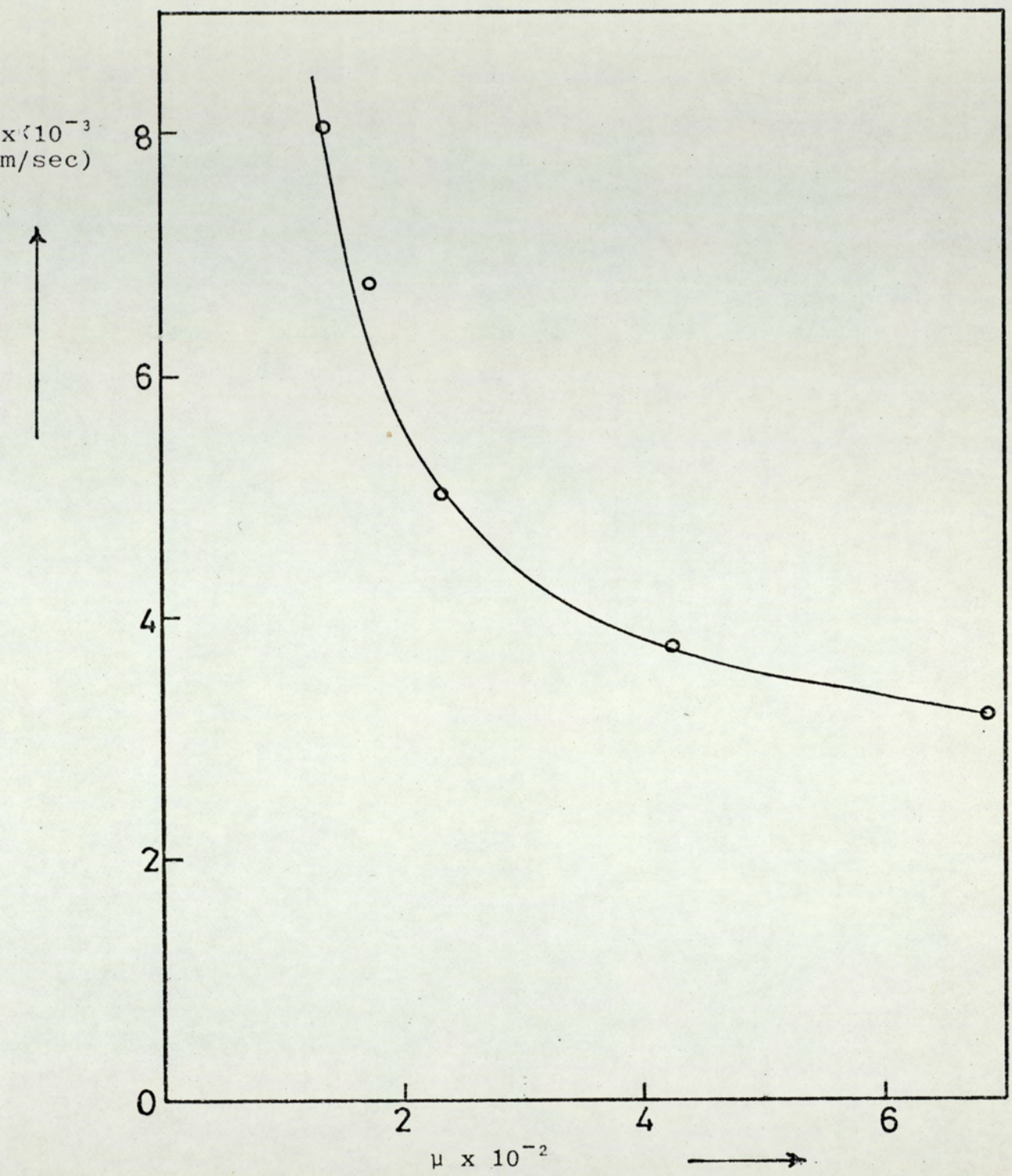

Figure 35 Mass Transfer Coefficient as a Function of Viscosity

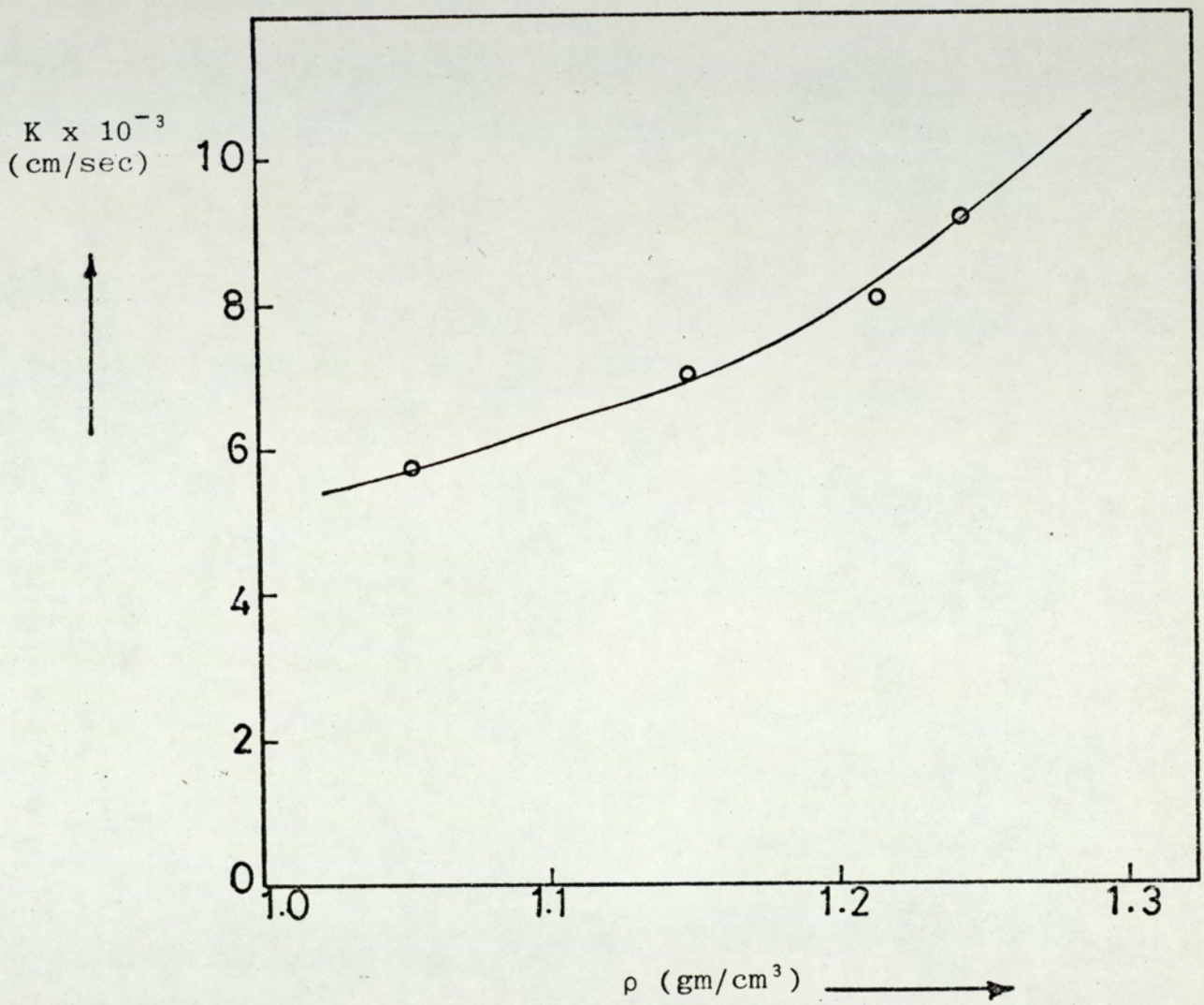

Figure 36 Mass Transfer Coefficient as a Function of Density

All values of the friction velocity and the thickness of the concentration boundary layer are tabulated in Tables 33 to 42 and 43 to 52 respectively.

The friction velocity is plotted against the impeller speed in Figure 37 and against the impeller diameter in Figure 38. Figure 37 shows that as the impeller speed increases, the friction velocity starts to increase and when the speed reaches 1500RPM, increase of the friction velocity become rapid. Figure 38 shows a straight line of slope = 1.15 and indicate a linear increase of friction velocity with increase of impeller diameter.

7.3.4 THICKNESS OF THE VISCOUS SUB-LAYER

The value of the thickness of the viscous sub-lyer was calculated as shown in Appendix (A4) using the following equation:

$$\delta_v = \frac{5\gamma}{U^*} \qquad (7.3)$$

The values, calculated for each electrode in the tank and at different values of the system parameters are listed in Tables 53 to 62.

Since the thickness of the viscous sub-layer was the main object of this study, more attention was paid to the effect of the system parameters on its value, and on the distribution of this layer around the base of the tank.

In studying the effect of the impeller speed on the thickness of the viscous sub-layer, the mean value of the thickness was plotted against impeller speed as shown in Figure 41 . There it will be seen that as the speed increases, the thickness of the viscous sub-layer decreases. However, the curve shows a rapid decrease of the thickness until a

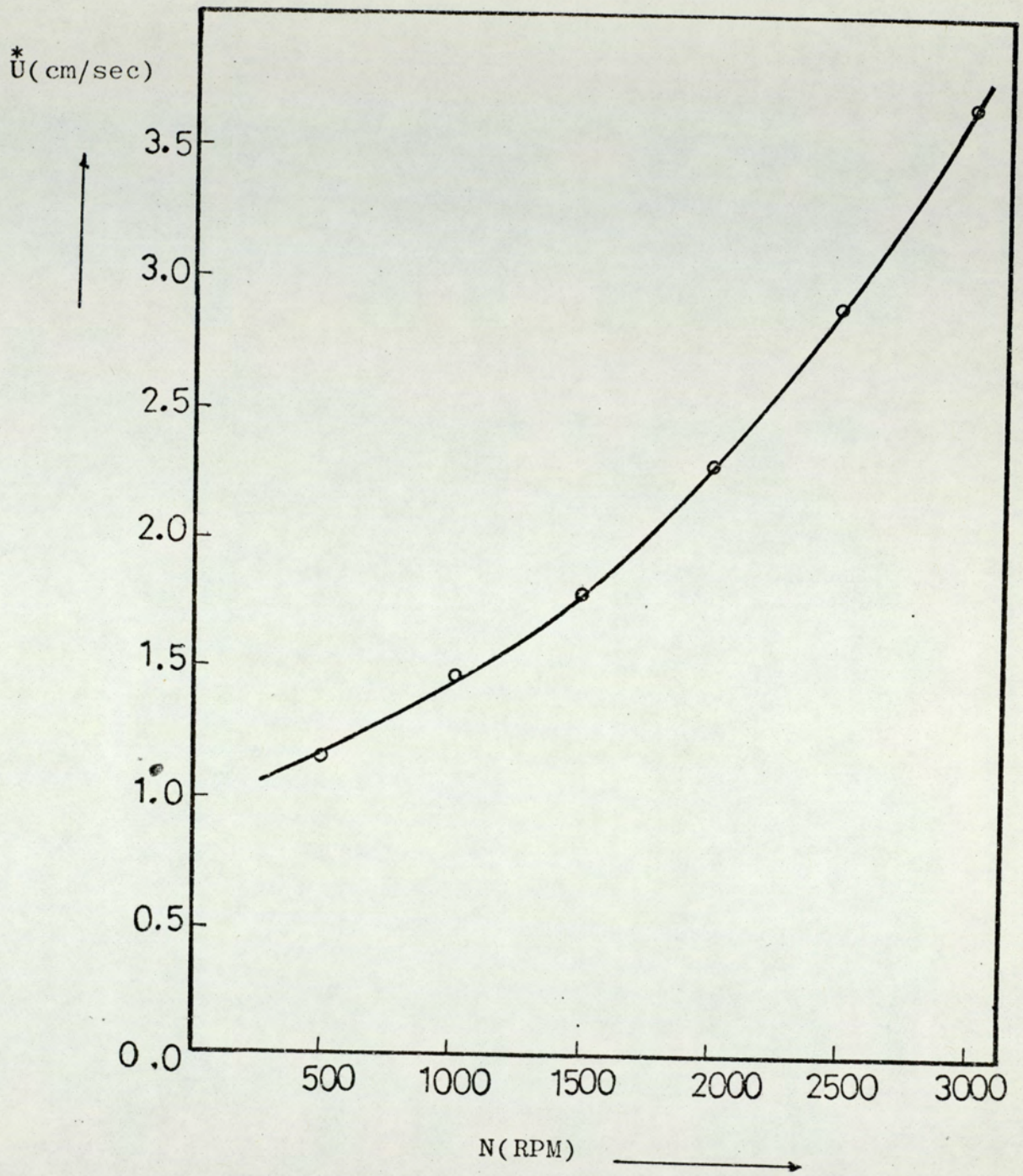

Figure 37 Friction velocity as a function of impeller speed

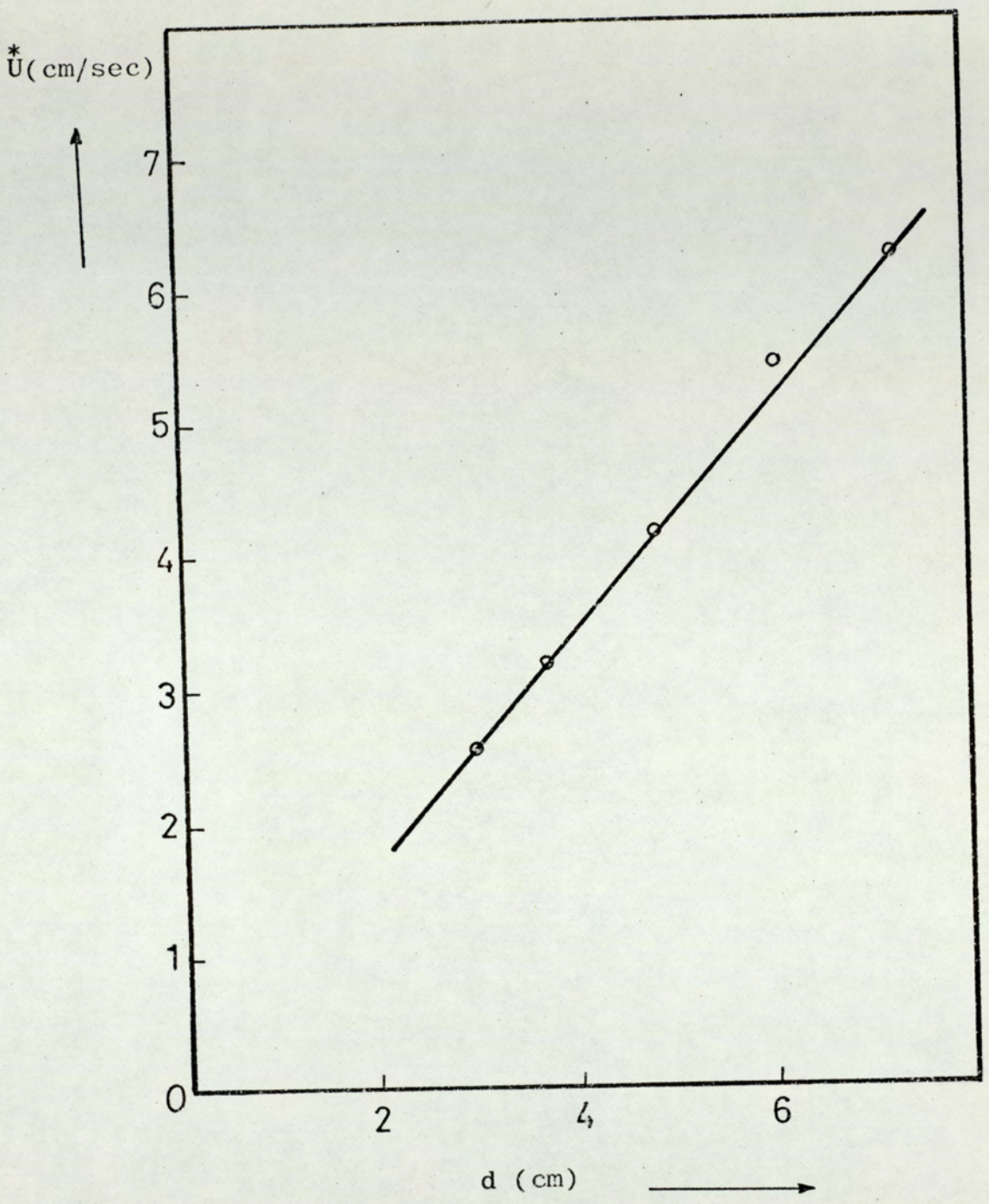

Figure 38 Friction velocity as a function of impeller diameter.

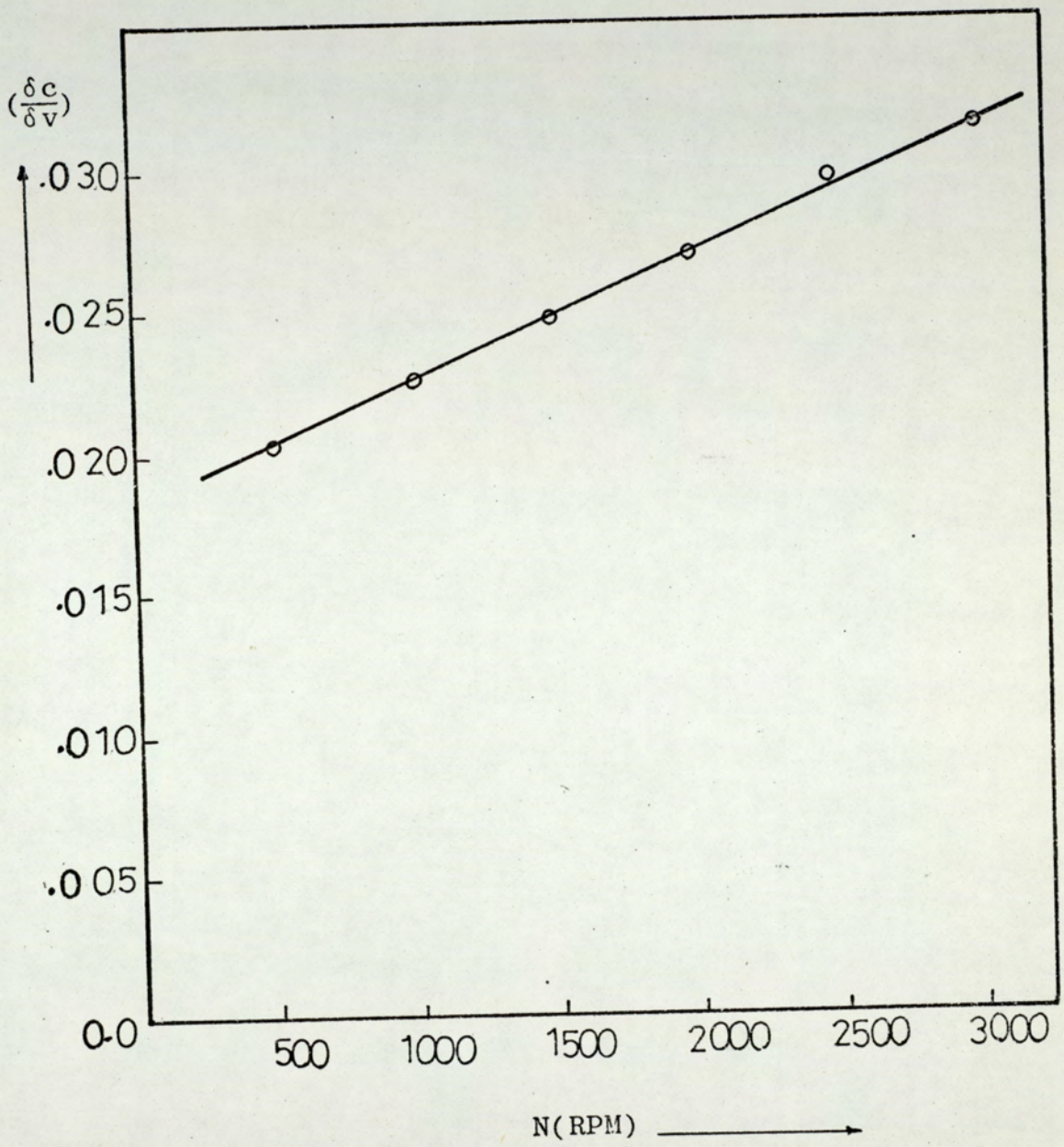

Figure 39 Ratio of the thickness of the concentration boundary layer to the viscous sub-layer as a function of impeller speed

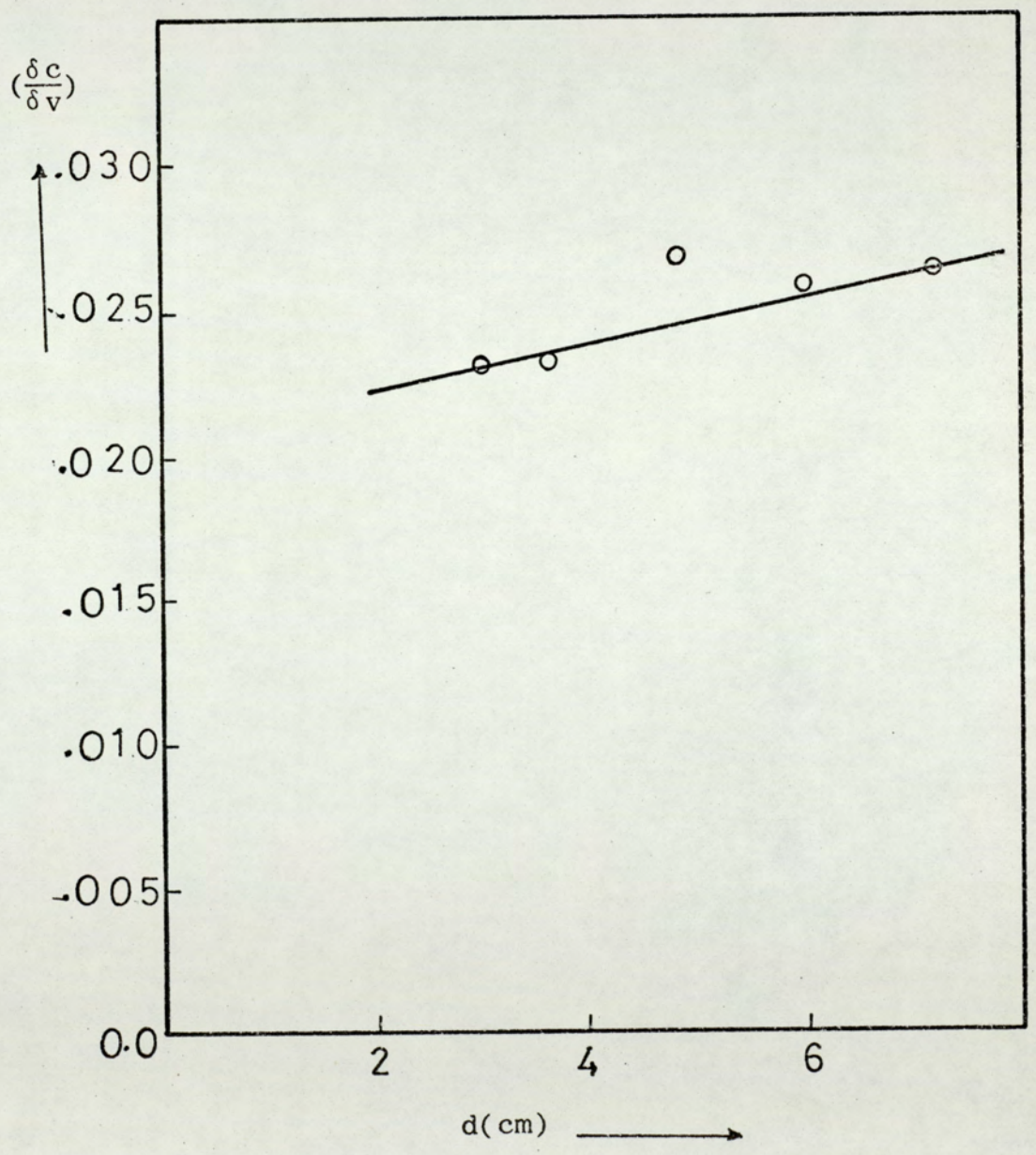

Figure 40 Ratio of the thickness of the concentration boundary layer to the viscous sub-layer as a function of impeller diameter

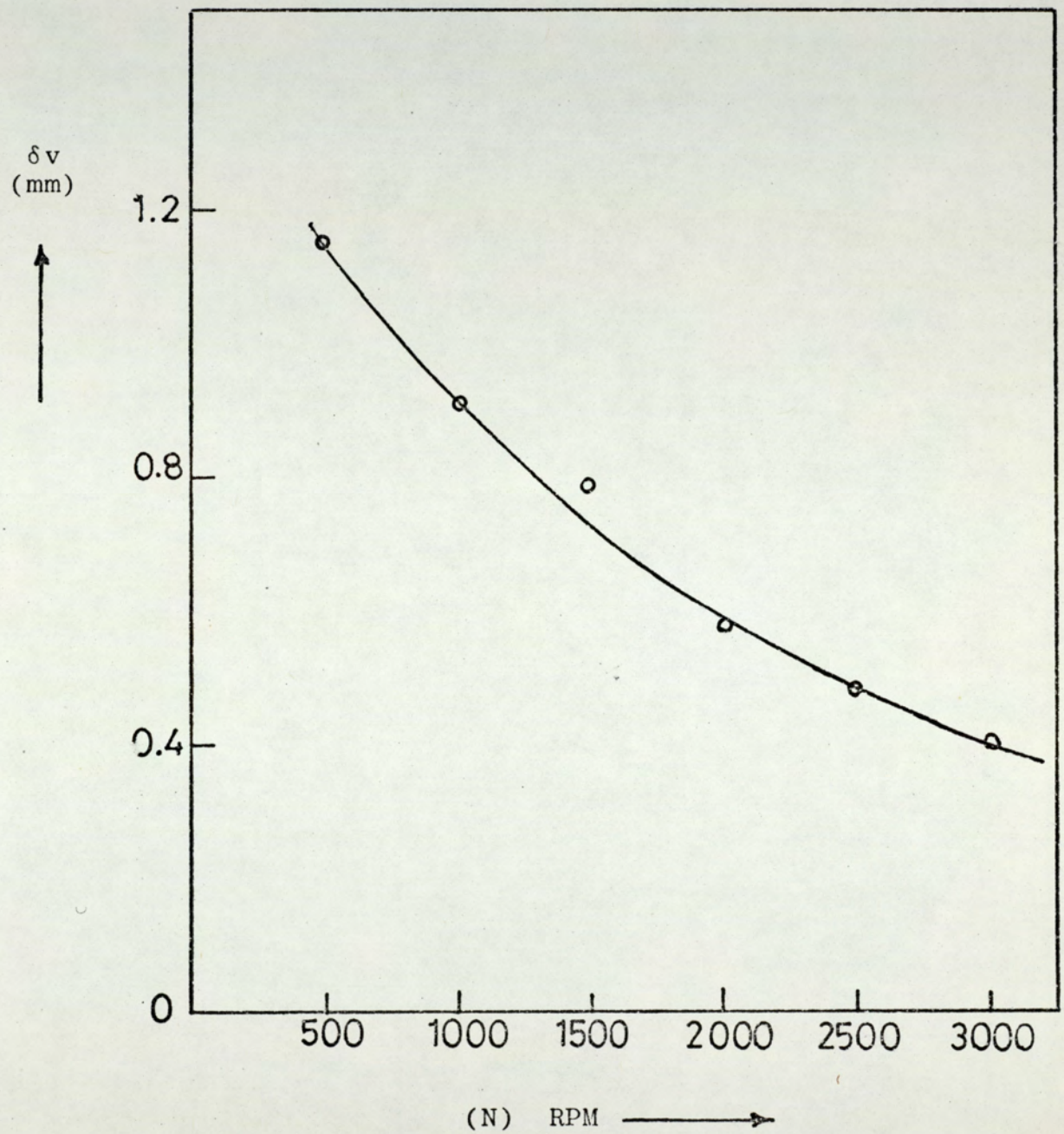

Figure 41 Thickness of the Viscous Sub-layer as a Function of Impeller Speed (Electro-chemical Technique)

speed of about 1500RPM had been achieved where the decrease in the thickness became slower and the curve flattened out. Figure 42 shows the distribution of the viscous sub-layer. thickness around the tank at different values of impeller speeds. Each point shows the actual position of the electrode in the tank and the value of the thickness at that point. The measurements were made using a propeller of 3.6cm diameter arranged at an angle of 5 degrees to the left. The graph shows the increase of the thickness with the decrease of the impeller speed. Moreover it shows how the viscous sub-layer built up according to the flow pattern; which obviously depends on the position of the impeller shaft and its angle.

The thickness of the viscous sub-layer was plotted against the impeller diameter as shown in Figure43 . There it is seen that as the diameter changed from 3.0 to 7.2cm, at a speed of 3000RPM and an angle of 5 degrees to the left, the thickness of the viscous sub-layer decreased rapidly as the diameter was increased from 3.0cm to 6.0cm. However, above this value, the curve became very flat and nearly straight, indicating a very slight decrease in thickness above an impeller diameter of 6.0cm. Figure 44 represents the distribution of the viscous sub-layer around the tank at different values of impeller diameters. The points around the tank represents the actual positions of the electrodes built in the tank. The plot shows the areas where a layer bult-up and where it vanishes. In addition it shows how the thickness decreaseswith the increase of the diameter.

Since the shaft angle hasa majoreffect on the flow pattern, and therefore on the distribution of viscous sub-layer and its thickness around the tank, the mean thickness was plotted against different values of shaft angle between

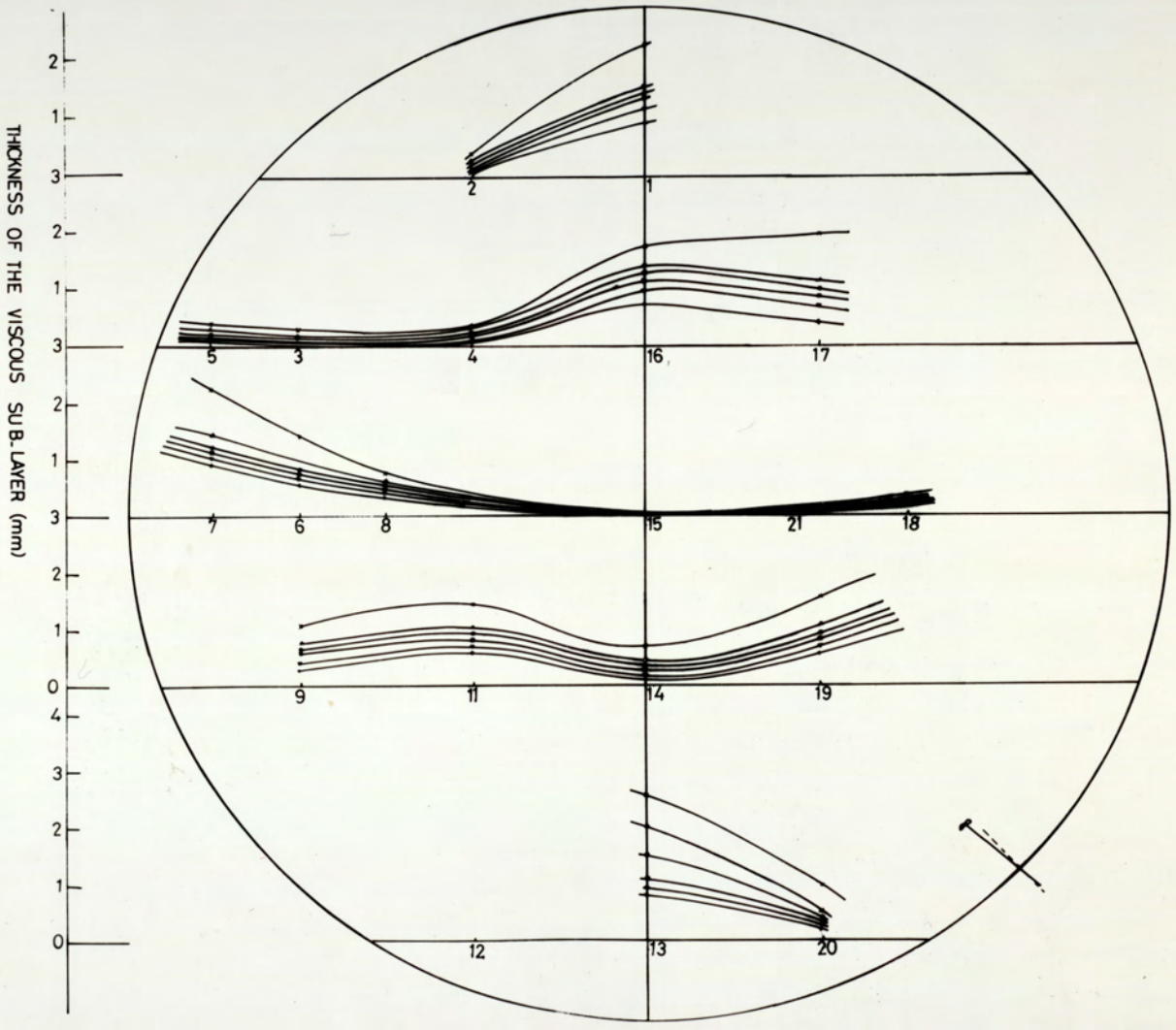

FIGURE_42 - DISTRIBUTION OF THE VISCOUS SUB-LAYER ON THE BASE OF THE TANK FOR DIFFERENT IMPELLER SPEEDS.

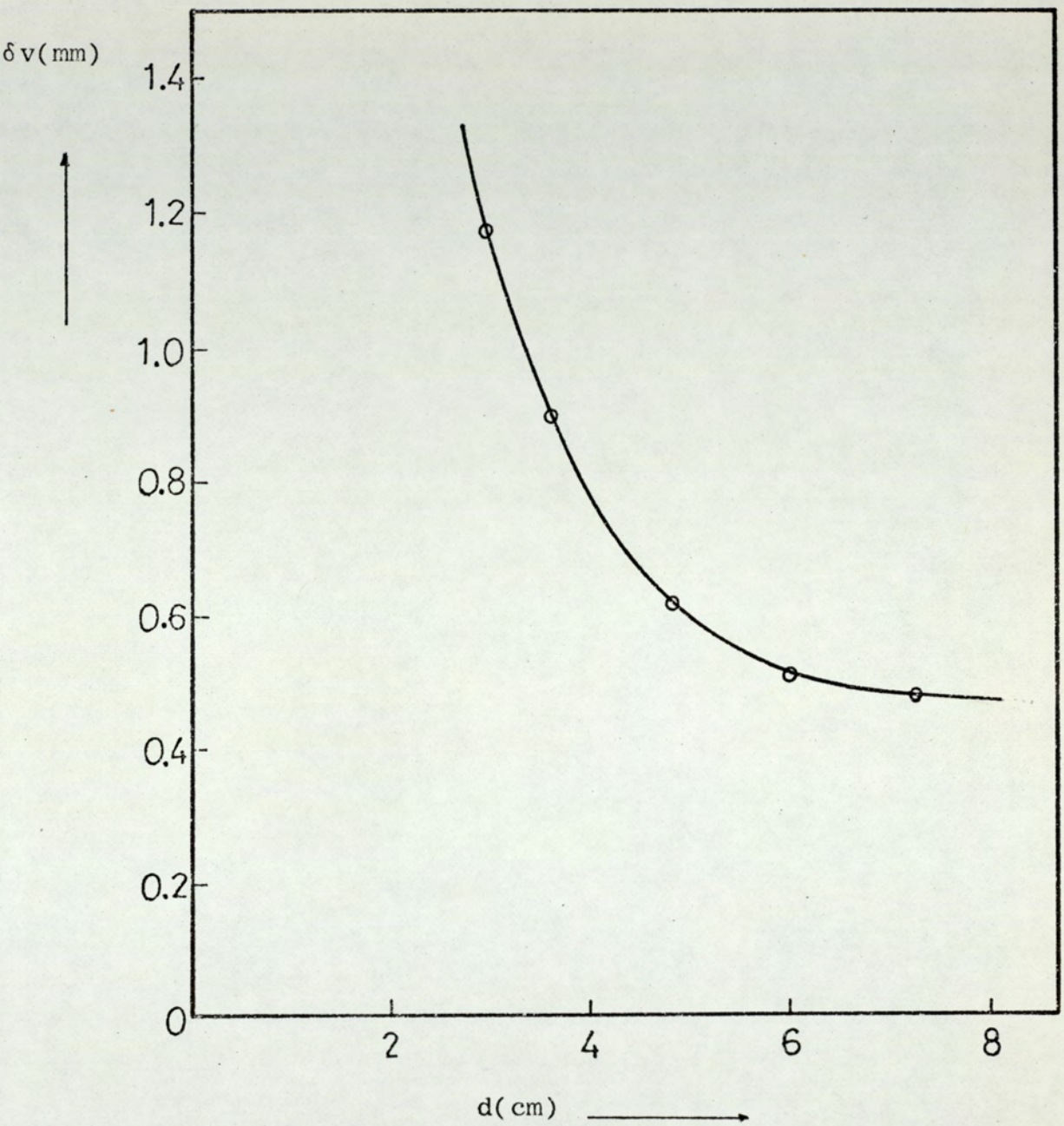

Figure 43 Thickness of the viscous sub-layer as a function of impeller diameter - Electro-chemical technique -

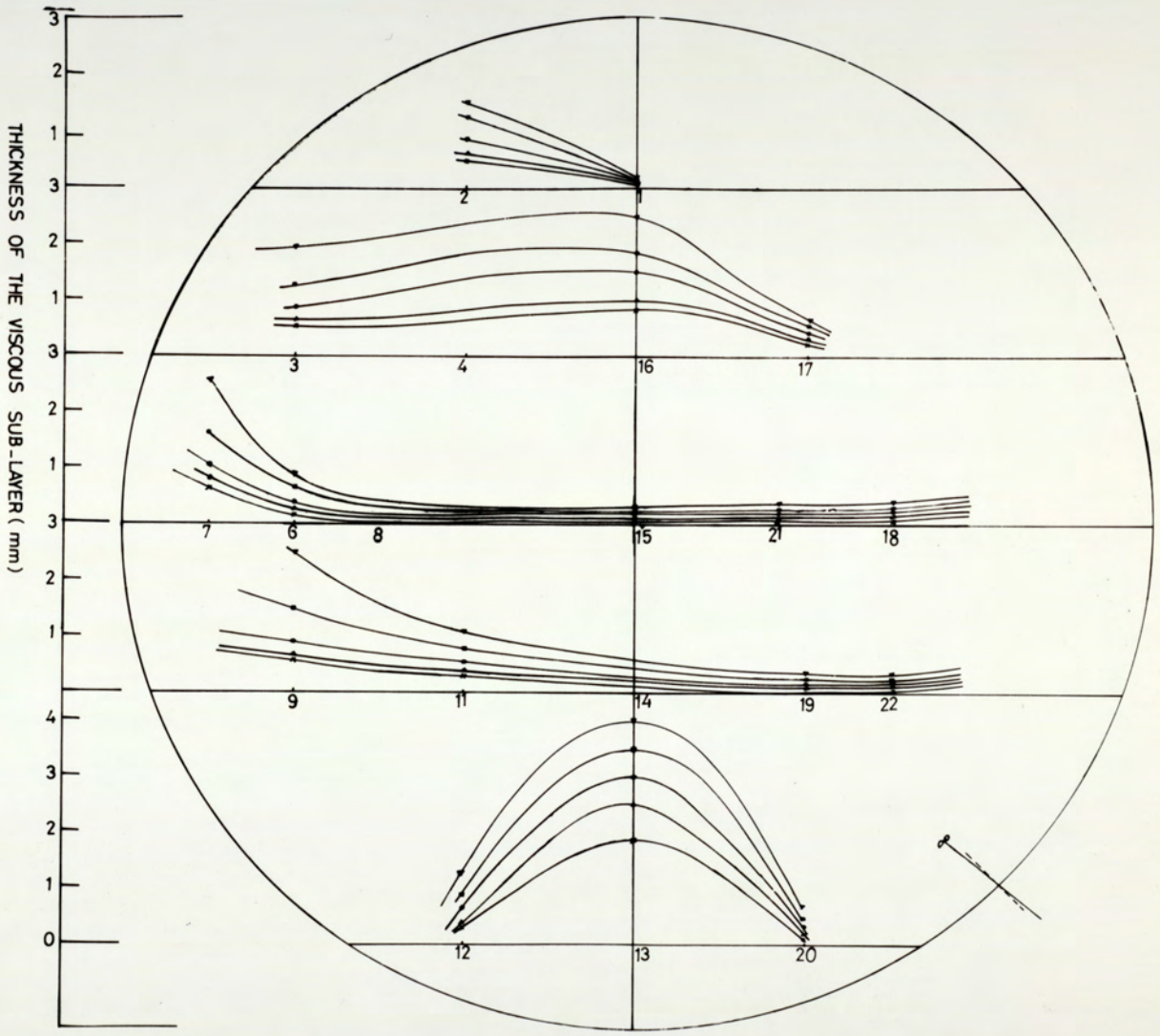

FIGURE-44 - DISTRIBUTION OF THE VISCOUS SUB-LAYER ON THE BASE OF THE TANK FOR DIFFERENT IMPELLER DIAMETERS.

10 degrees to the left to 10 degrees to the right. The impeller diameter was 3.6cm rotating at a speed of 3000RPM. Figure 45 indicates an optimum angle of 5 degrees to the left where the thickness of the viscous sub-layer is minimum. The curve obtained showed an increase in the thickness when the shaft was fixed to the right more than when it was fixed to the left. To display the distribution of the viscous sub-layer at different shaft angles was difficult on one graph as the value of the thickness of the layer changed from one position to another according to the flow pattern rather than the angle itself. Hence the different curves overlapped and therefore, the distribution of the viscous sub-layer around the tank was plotted at each angle in Figures 46, 44, 47, 48, 49. These figures show the distribution of the layer at an angle of -10^{o}, -5, 0, +5, and +10 respectively.

The liquid depth is also a parameter of the system that was studied. The liquid depth was changed between 10-25cm using a 3.6cm diameter impeller fixed at 5 degrees to the left and running at a speed of 3000RPM. Figure 50 represents a plot of the mean value of the viscous sub-layer thickness against the liquid depth and shows a slight increase in the thickness as the liquid depth increased. Figures 51, 52, 53, 54, and 55 represent the distribution of the viscous sub-layer around the tank at a liquid depth of 10cm, 13, 16, 20 and 25cm respectively.

The effect of the viscosity and the density of the solution on the viscous sub-layer was studied separately. In Figure 56, the thickness of the viscous sub-layer was plotted against viscosity which was from 0.0137 to

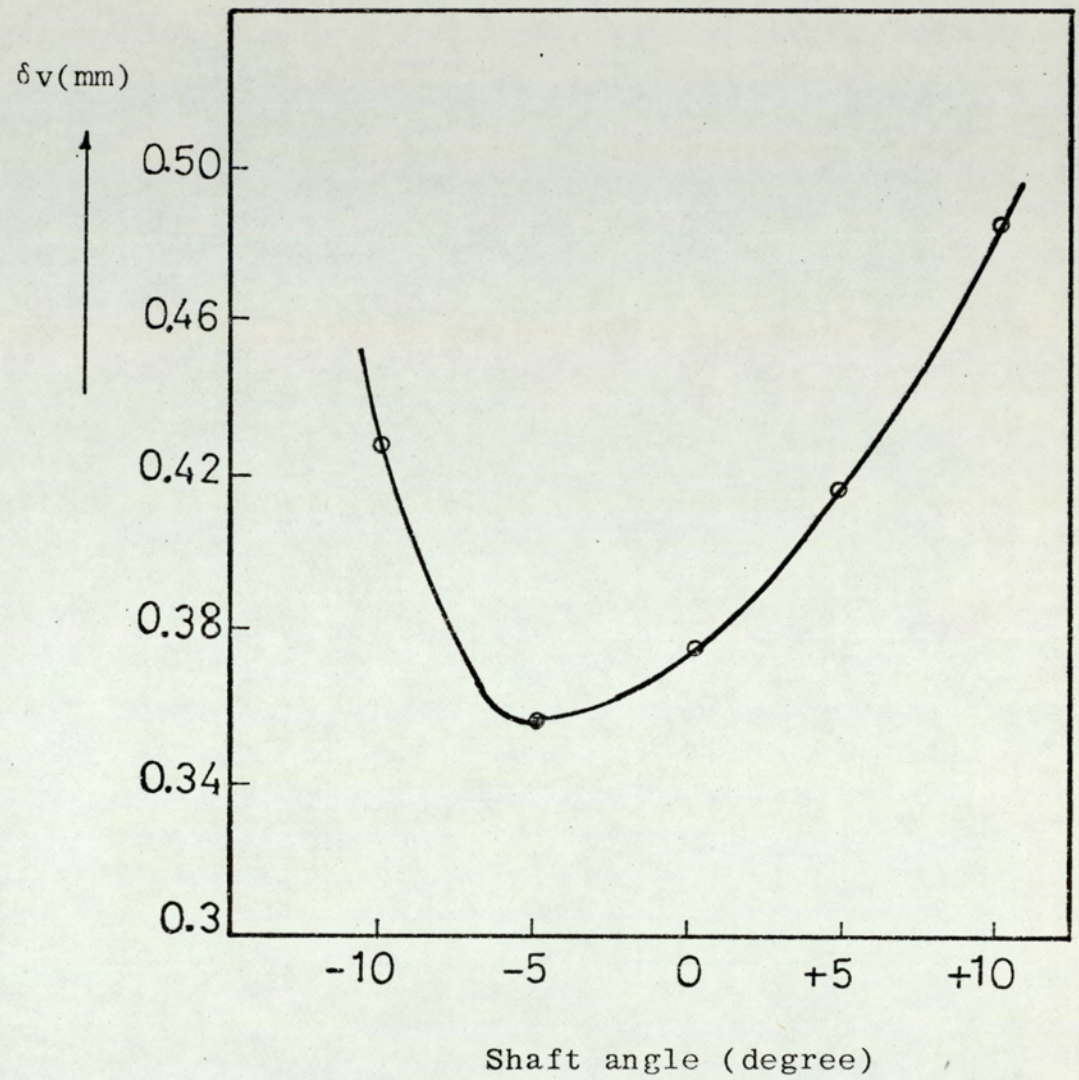

Figure 45 Thickness of the viscous sub-layer as a function of shaft angle - Electro-chemical technique -

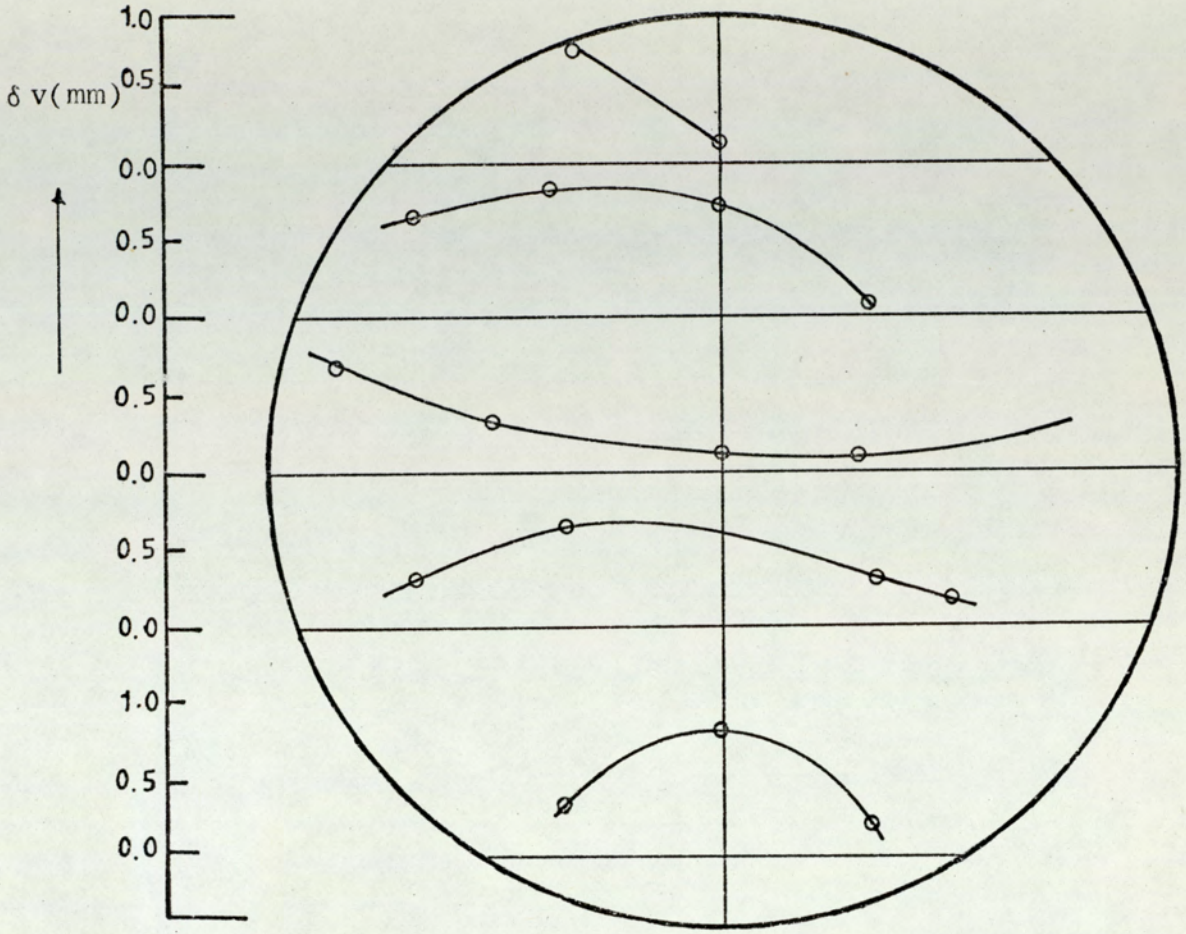

Shaft angle = 10 degrees to the left

Figure 46 Distribution of the viscous sub-layer around the base of the tank

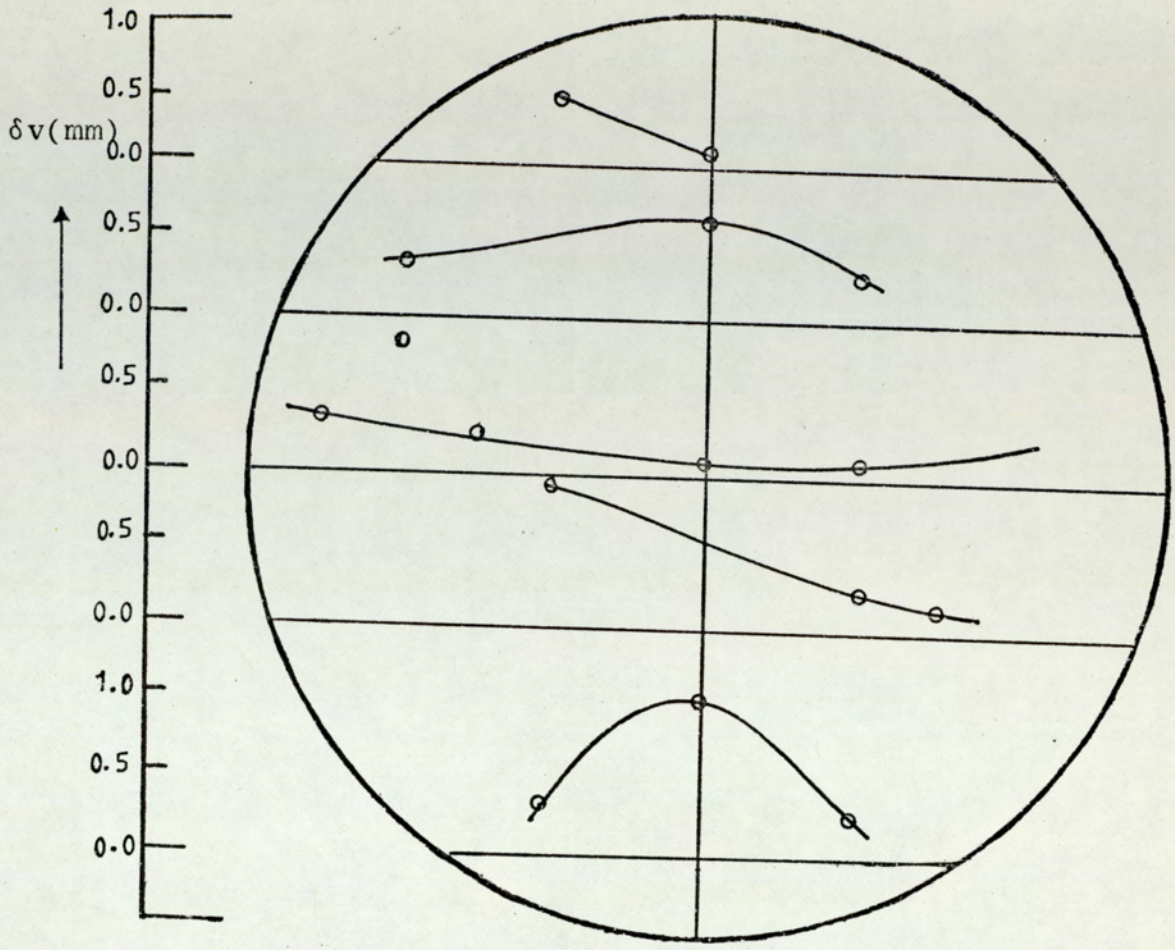

Shaft angle = zero degrees

Figure 47 Distribution of the viscous sub-layer around the base of the tank

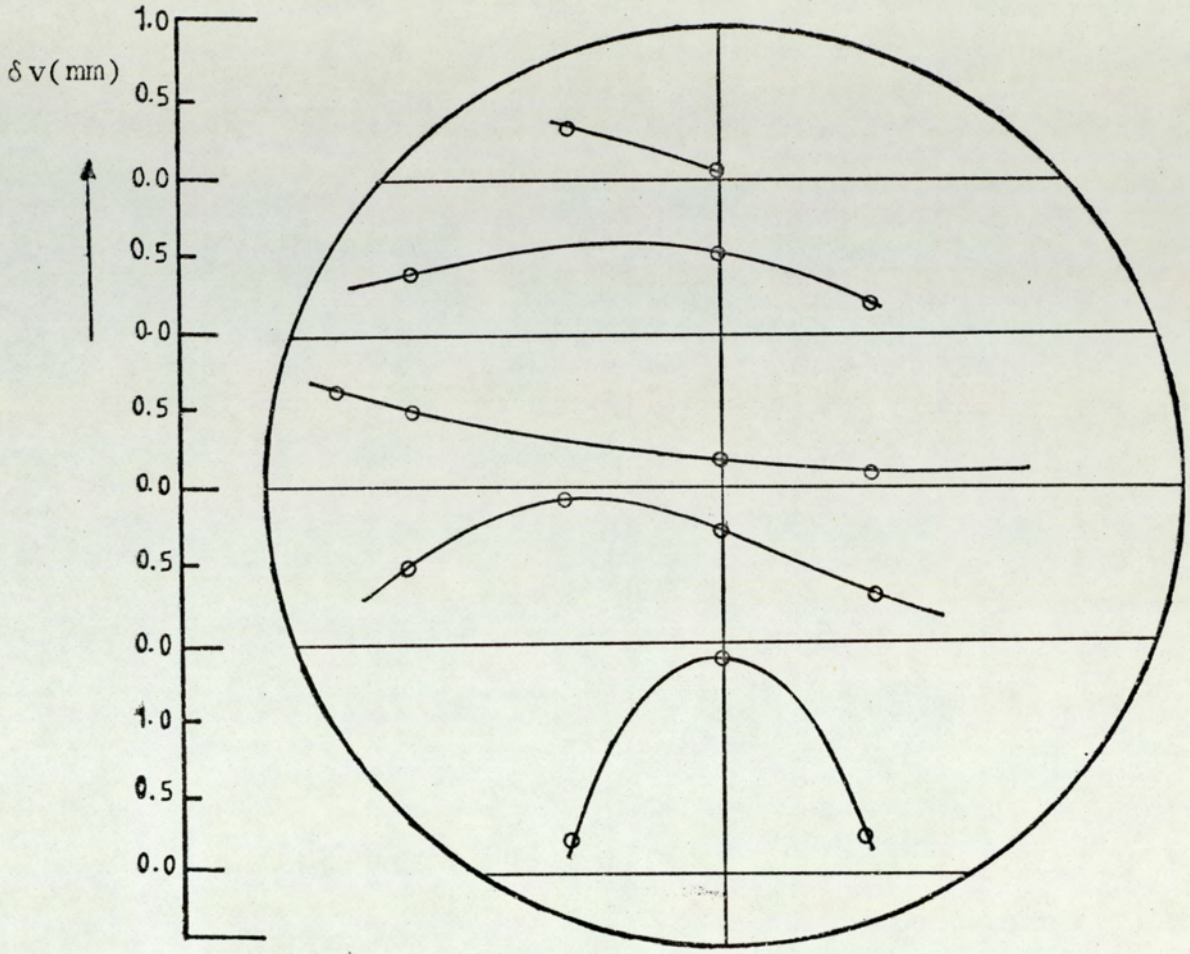

Shaft angle = 5 degrees to the right

Figure 48 Distribution of the viscous sub-layer around the base of the tank

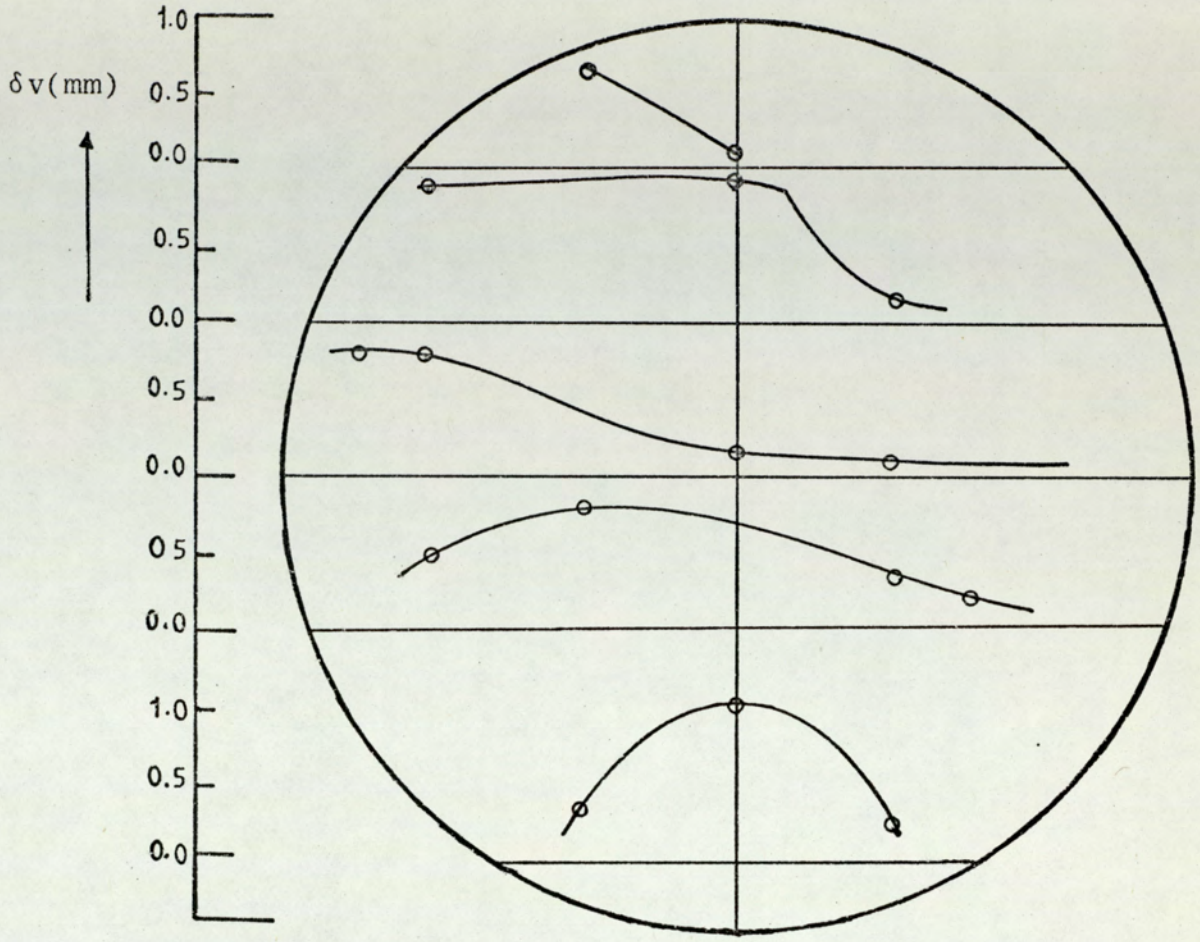

Shaft angle = 10 degrees to the right

Figure 49 Distribution of the viscous sub-layer around the base of the tank

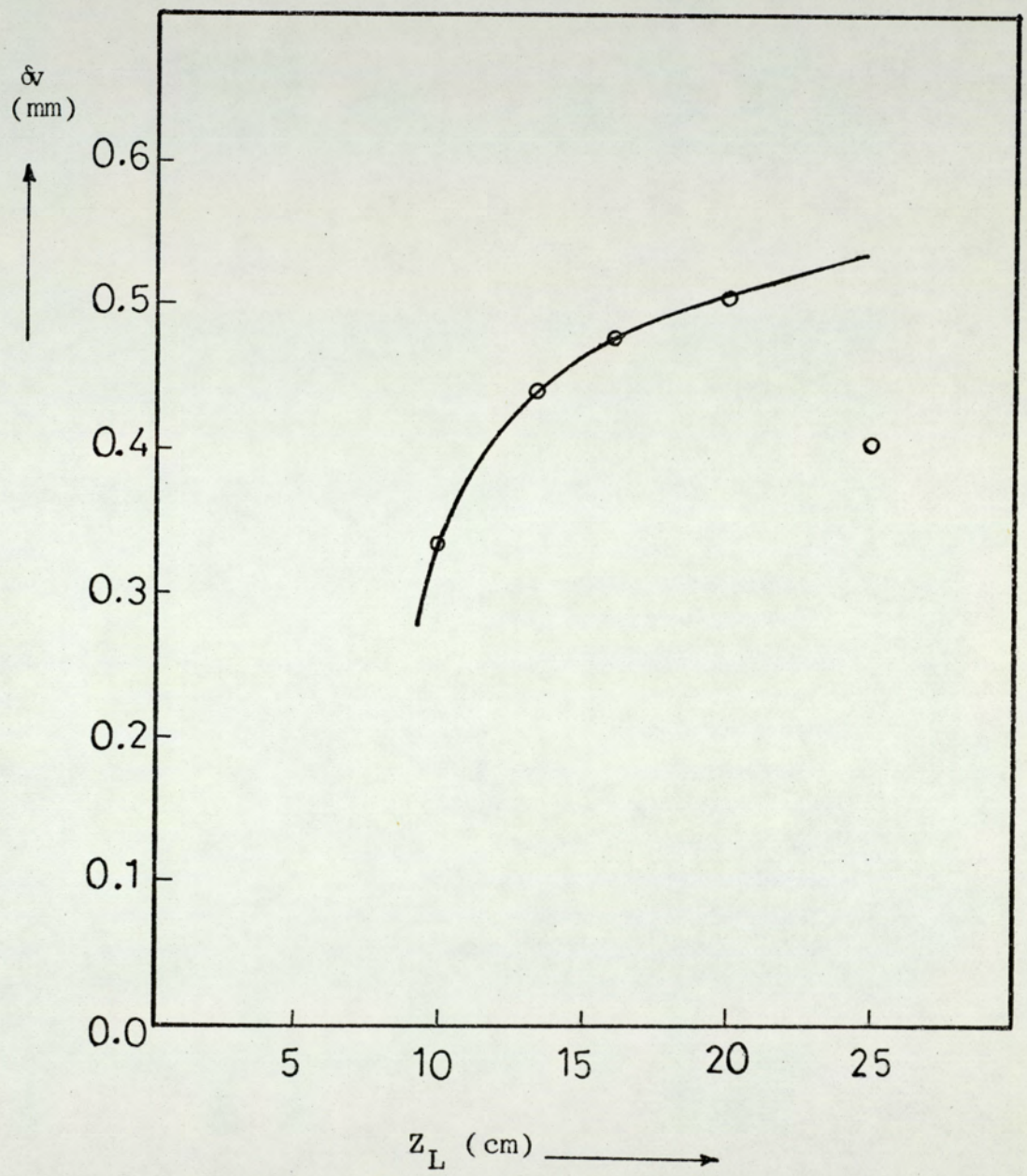

Figure 50 Thickness of the viscous sub-layer as a function of liquid depth - Electro-chemical technique -

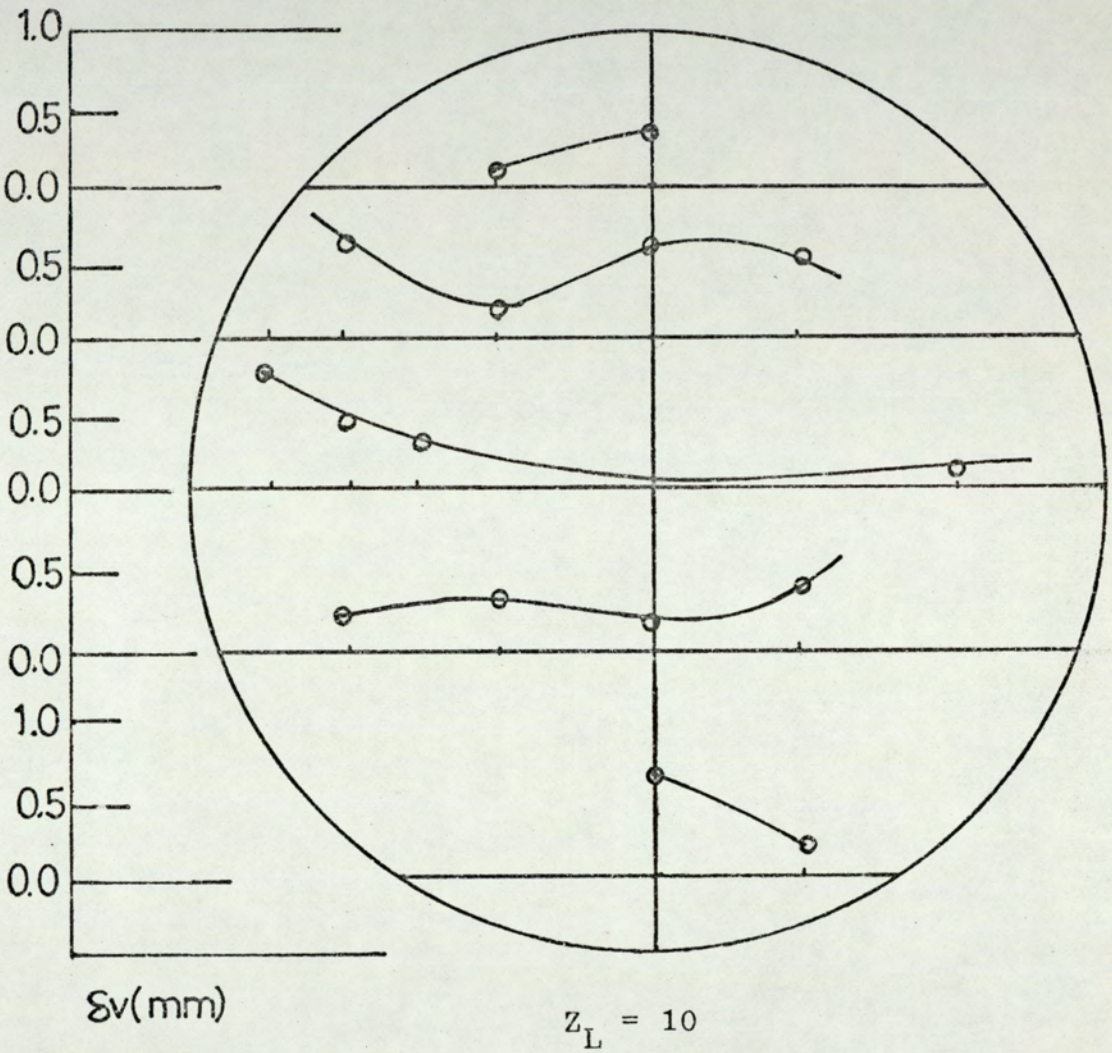

Figure 51 Distribution of the Viscous Sub-layer around the Base of the Tank

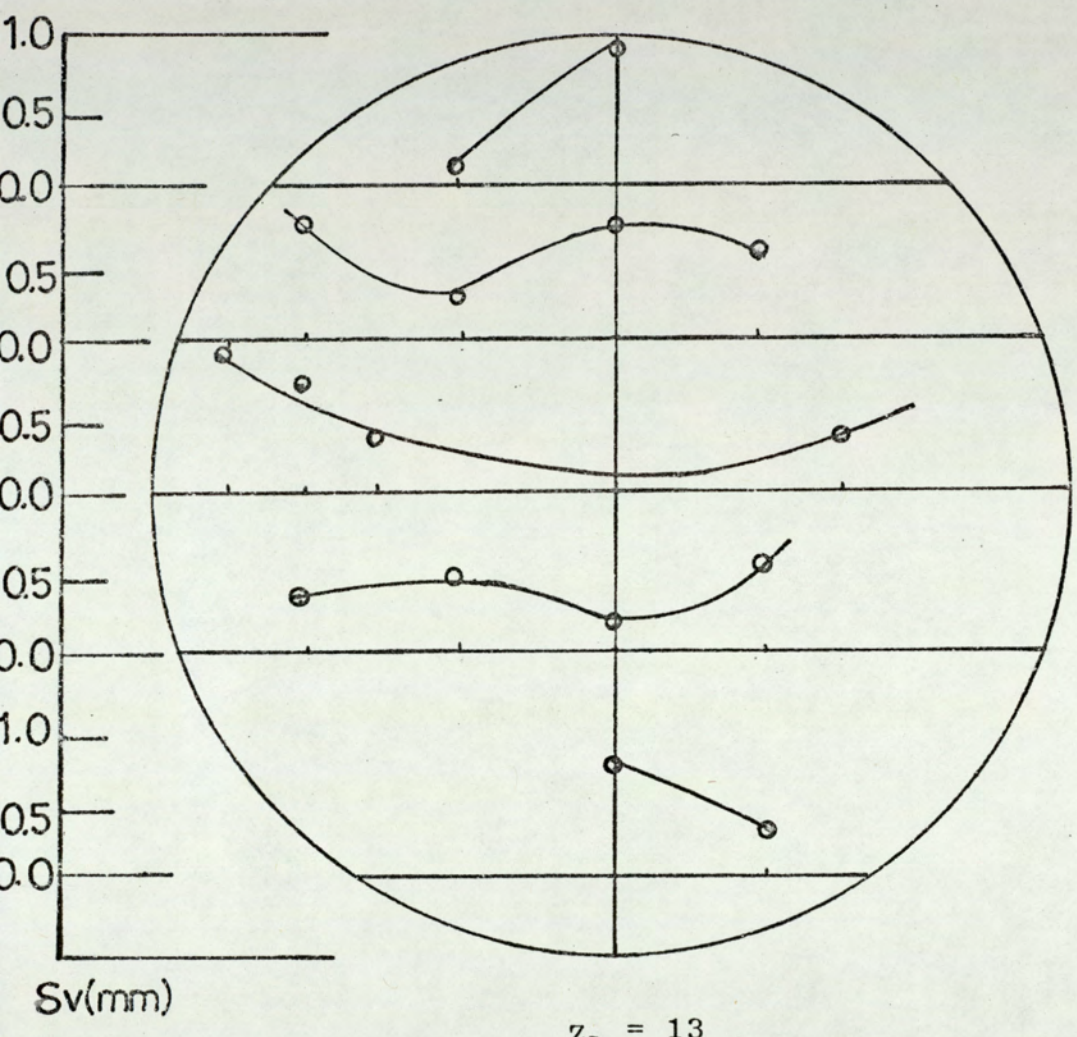

$Z_L = 13$.

Figure 52 Distribution of the Viscous Sub-layer around the Base of the Tank

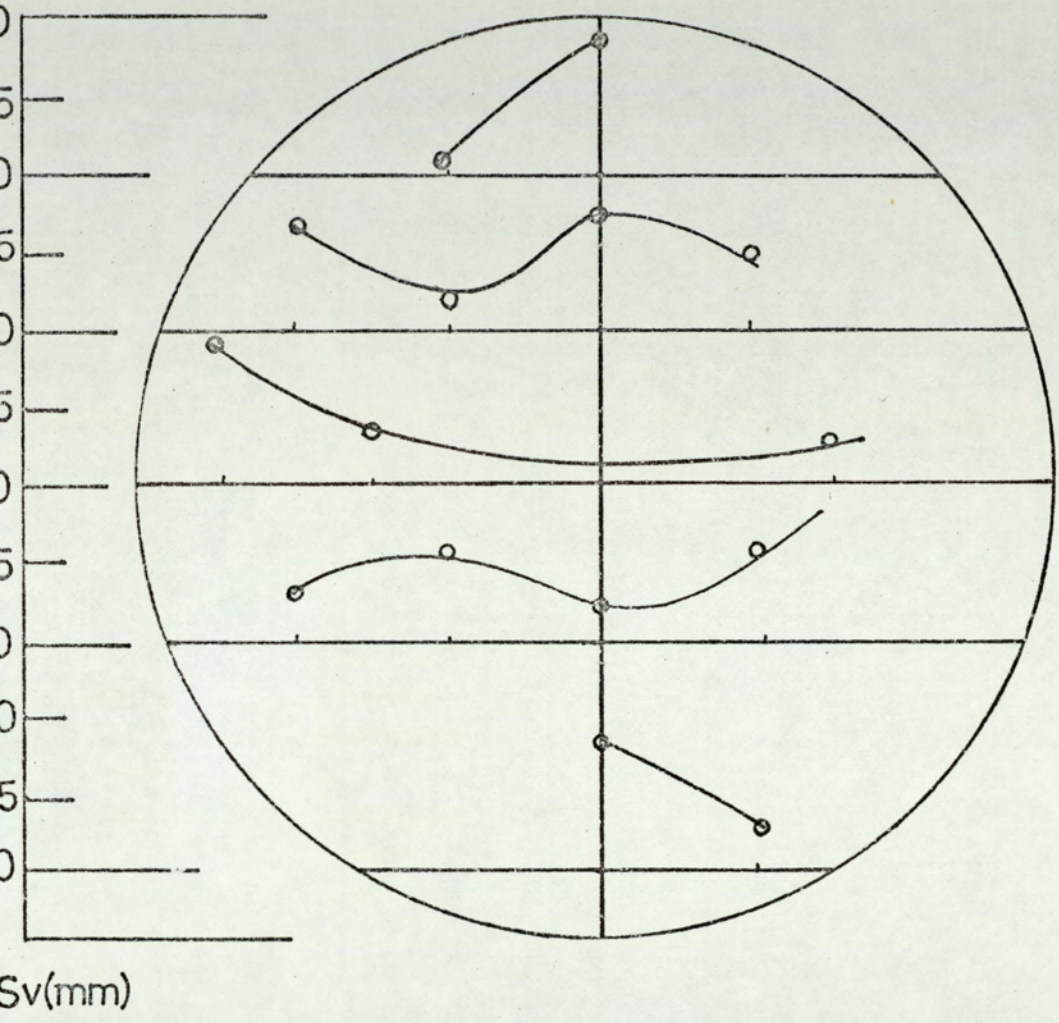

$Z_L = 16$

Figure 53 Distribution of the Viscous Sub-layer around the Base of the Tank

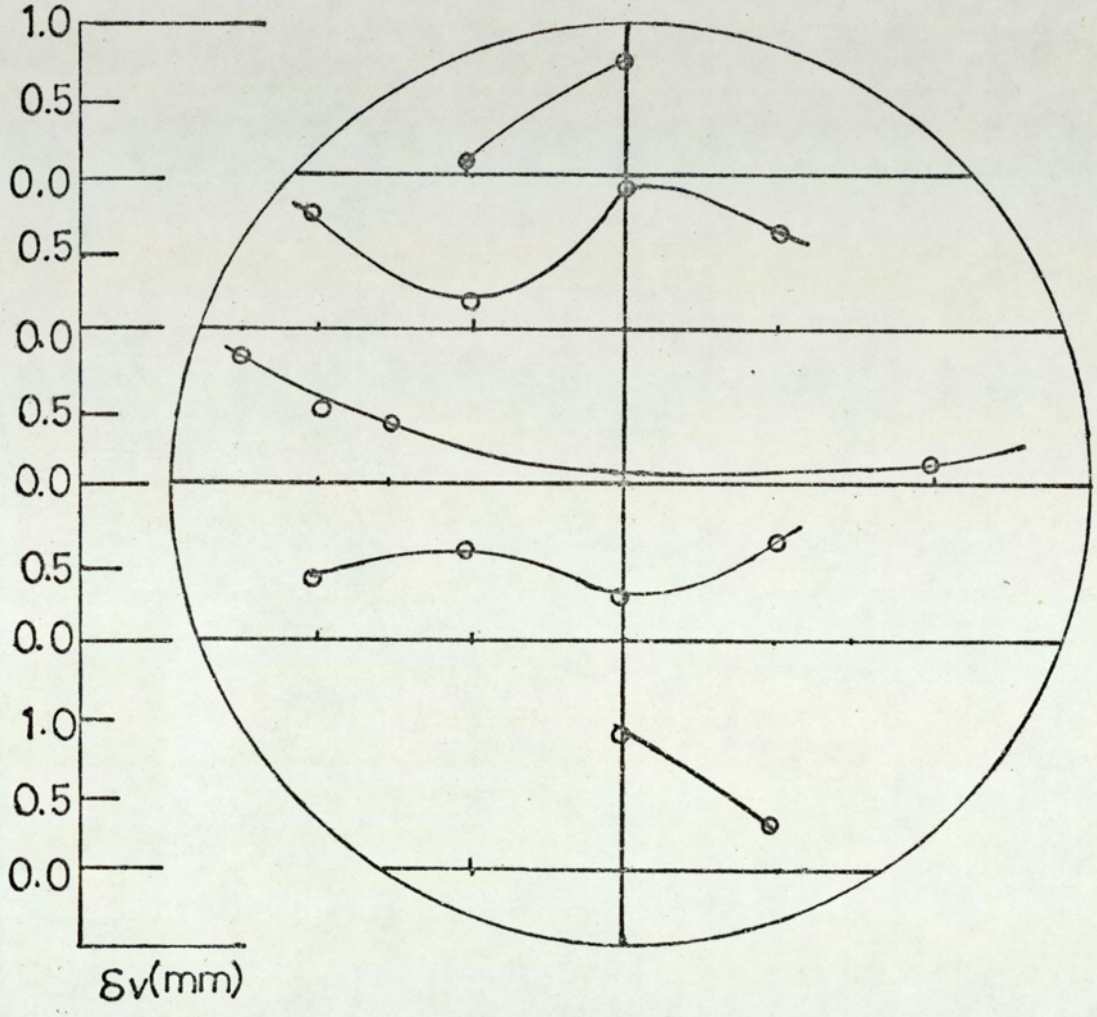

$Z_L = 20$

Figure 54 Distribution of the Viscous Sub-layer around the Base of the Tank

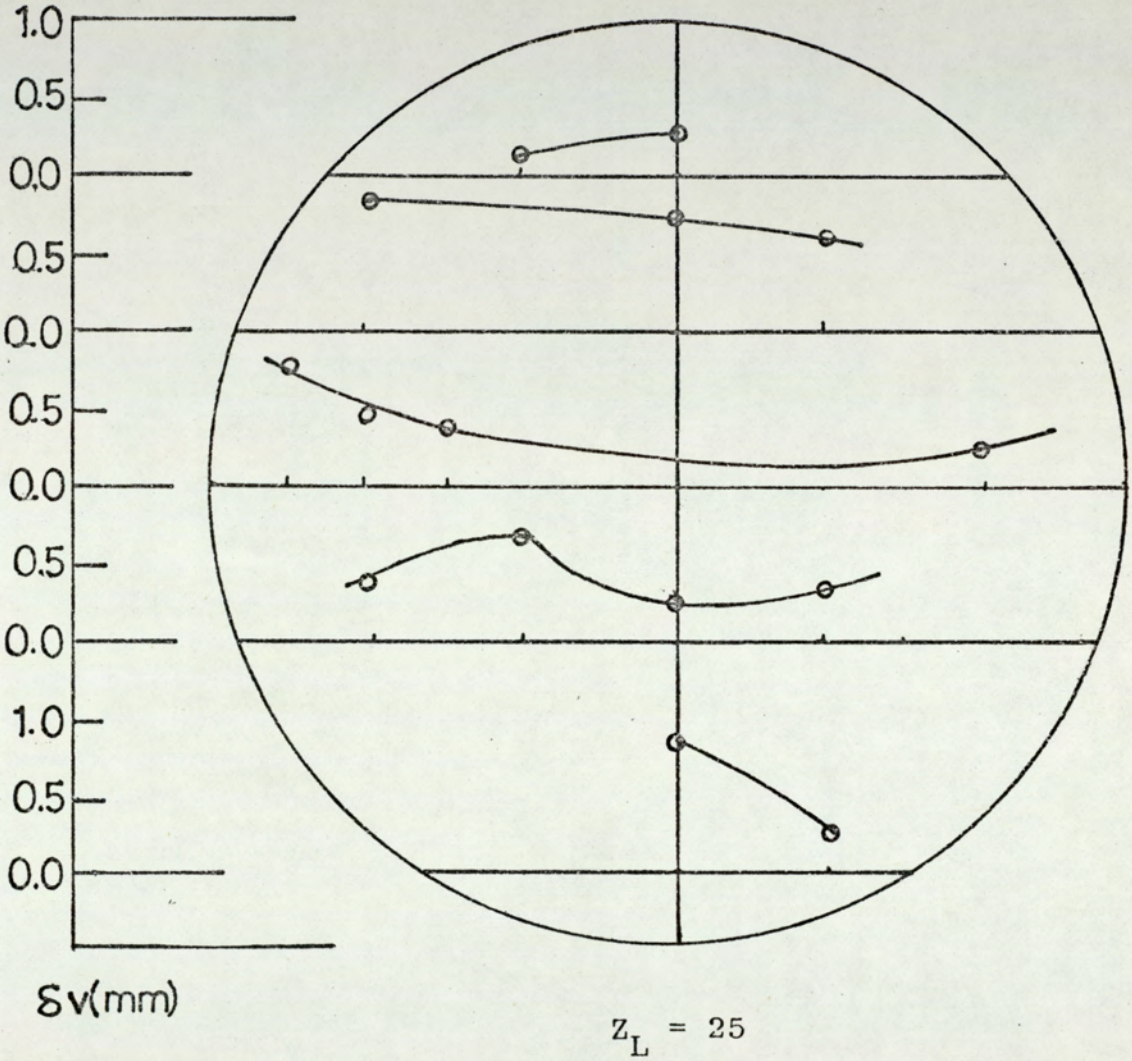

Figure 55 Distribution of the Viscous Sub-layer around the Base of the Tank

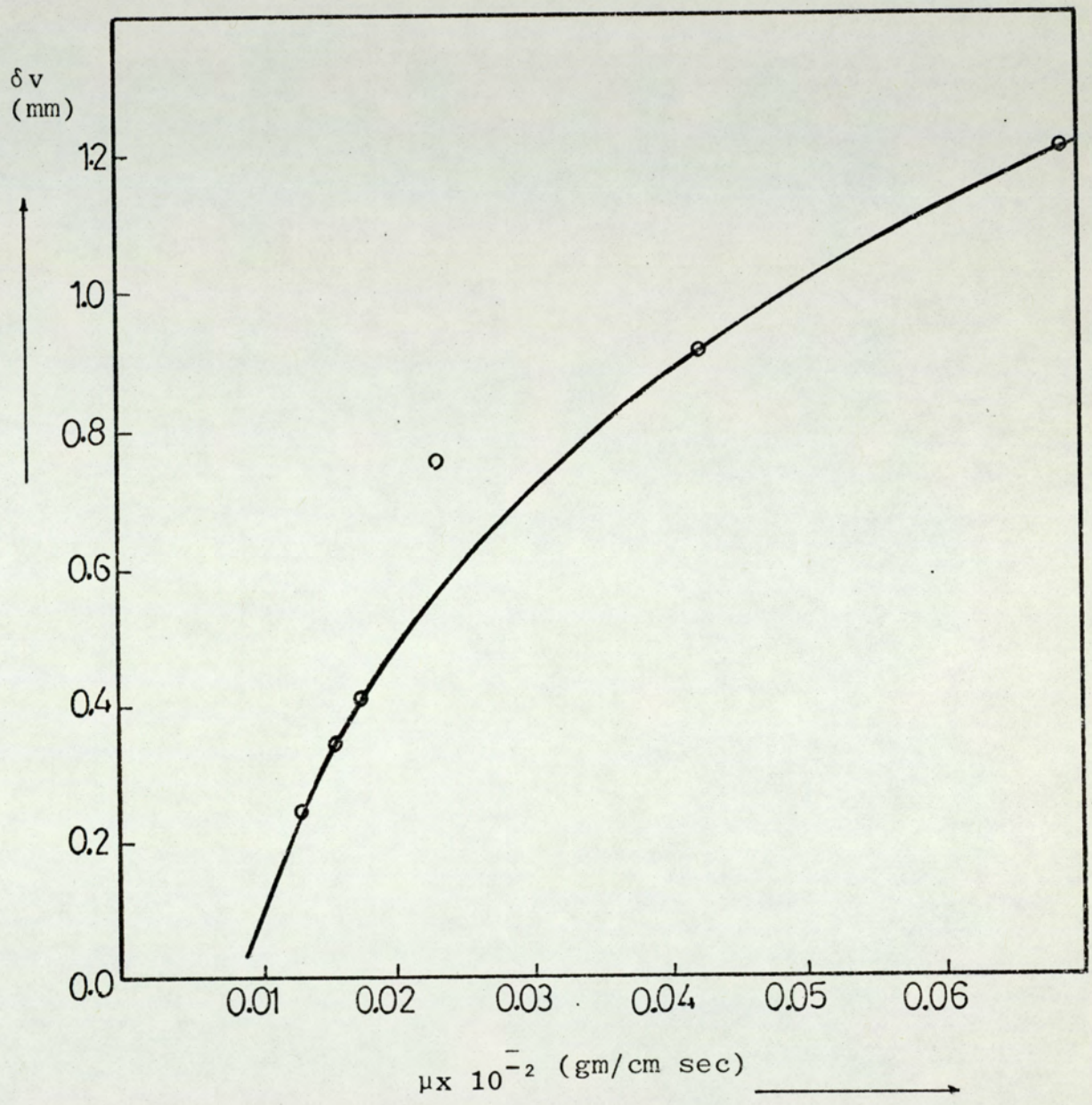

Figure 56 Thickness of the viscous sub-layer as a function of viscosity of the solution - Electro-chemical techniques -

0.069 gm/cm sec using an impeller 3.6cm in diameter fixed at an angle of 5 degrees to the left and rotating at 3000RPM. As the viscosity increased, the thickness of the viscous sub-layer increased rapidly. The increase of the density of the solution decreases the thickness of the viscous sub-layer as shown in Figure 57 , the thickness was plotted against density between 1.077 to 1.245 gm/cm^3 using a 3.6cm diameter impeller running at a speed of 3000RPM and fixed at an angle of 5 degrees to the left.

7.4 MODEL TANK - HOT-FILM ANEMOMETER

7.4.1 CALIBRATION OF THE HOT-FILM PROBE

The hot-film anemometer was calibrated before being used for the measurements. The reading of the voltage was recorded at different flow-rates using the calibration rig as in Tables 63- 66. Then the flow-rate was converted into velocity and with the aid of a regression analysis the best fit for this data was found and the voltage was plotted against the corrected velocity. The results are presented in Figure 58. Each set of experiments were carried-out by first rechecking the calibration (Appendix (A1)).

7.4.2 VISCOUS SUB-LAYER THICKNESS

The values of the thickness of the sub-layer were calcuated as shown in Appendix (A4) using equation (7.3) and the results are tabulated in Tables 67 to 78

All the experiments were carried out using degassed water.

The thickness of the viscous sub-layer plotted against impeller speed which was changed from 500 to 3000RPM as

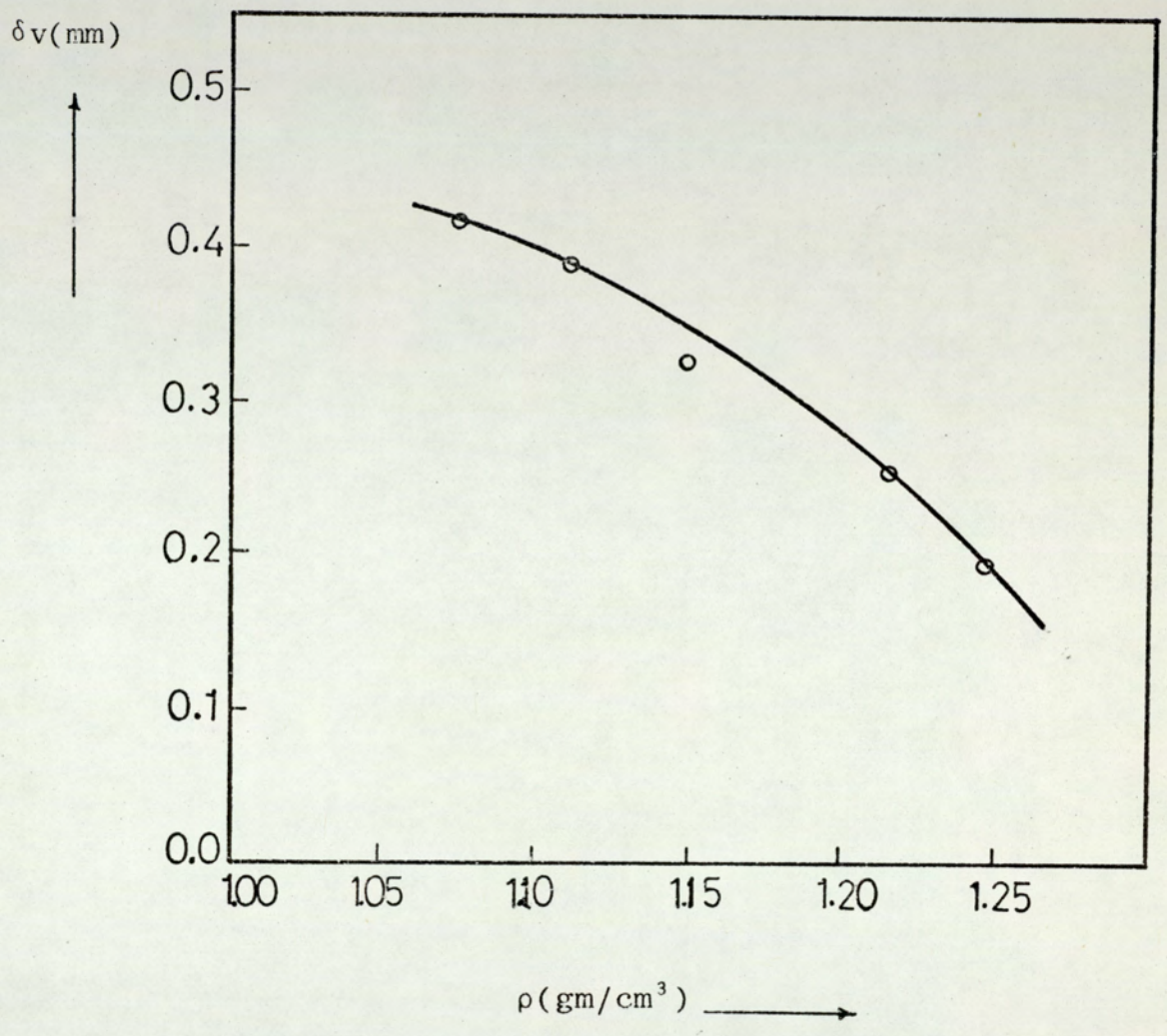

Figure 57 Thickness of the viscous sub-layer as a function of density of solution - Electro-chemical technique -

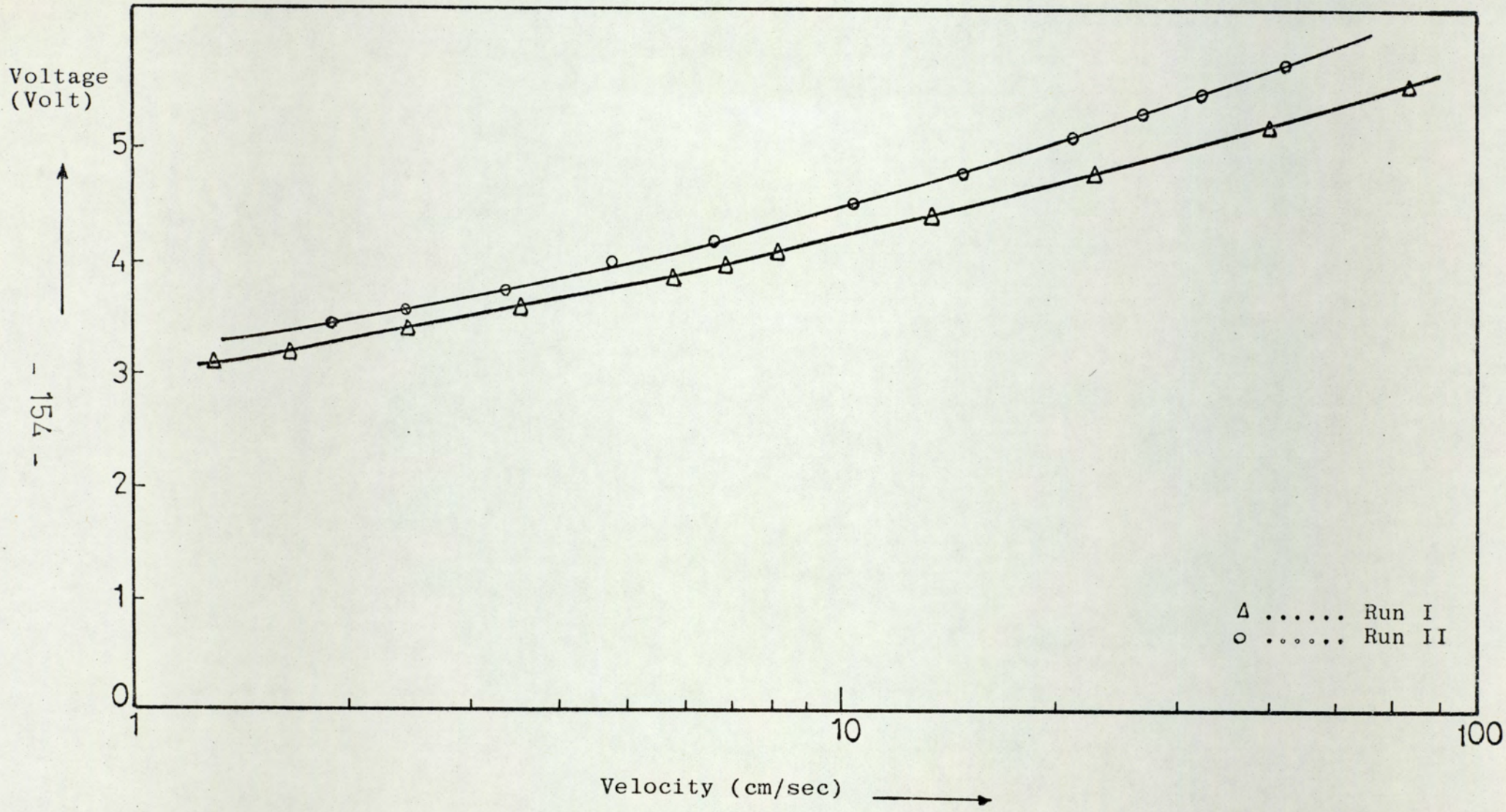

Figure 58 Voltage as a functionof fluid velocity - Calibration curves of the hot-film probe -

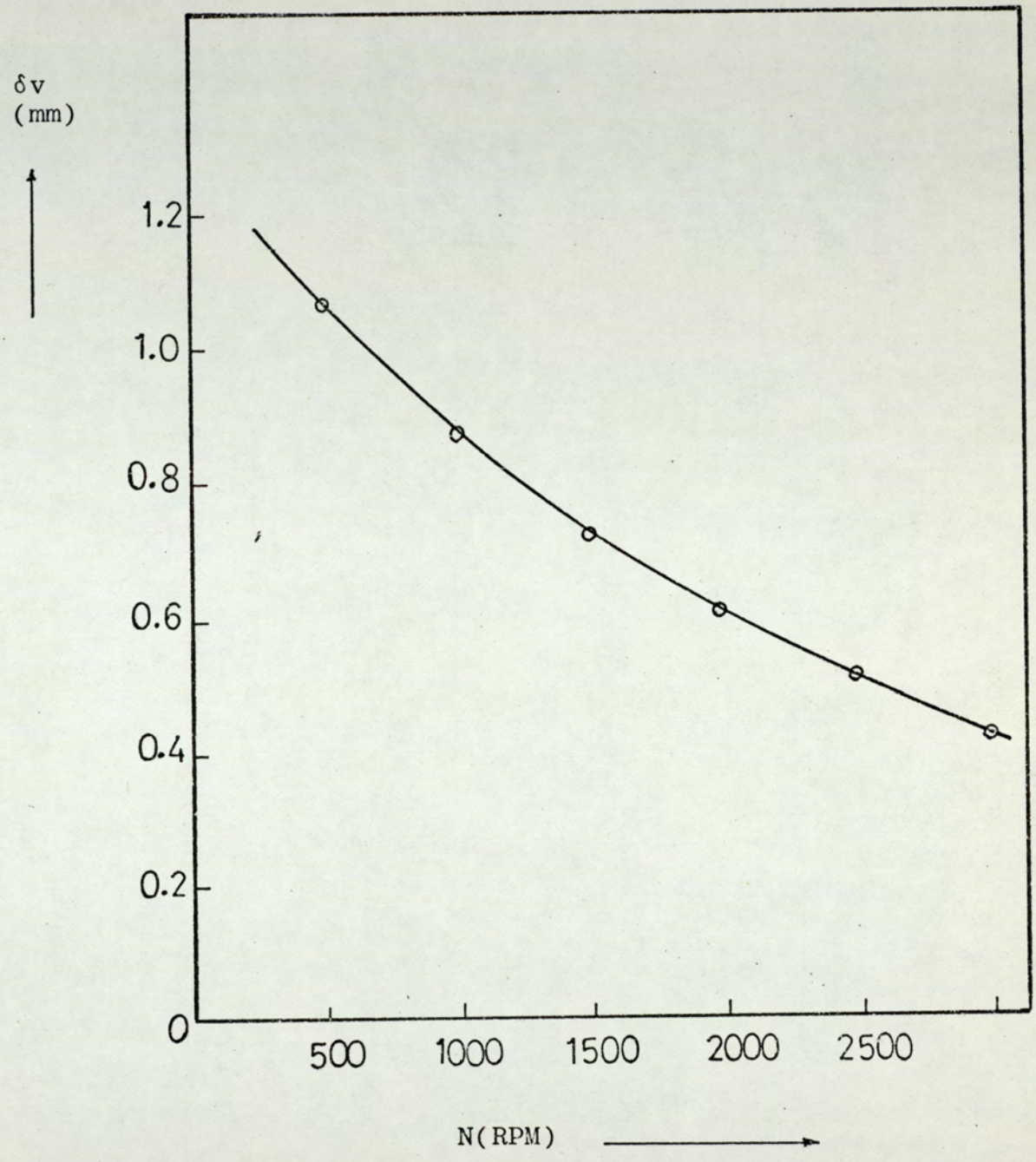

Figure 59 Thickness of the viscous sub-layer as a function of impeller speed - Hot-film anemometer -

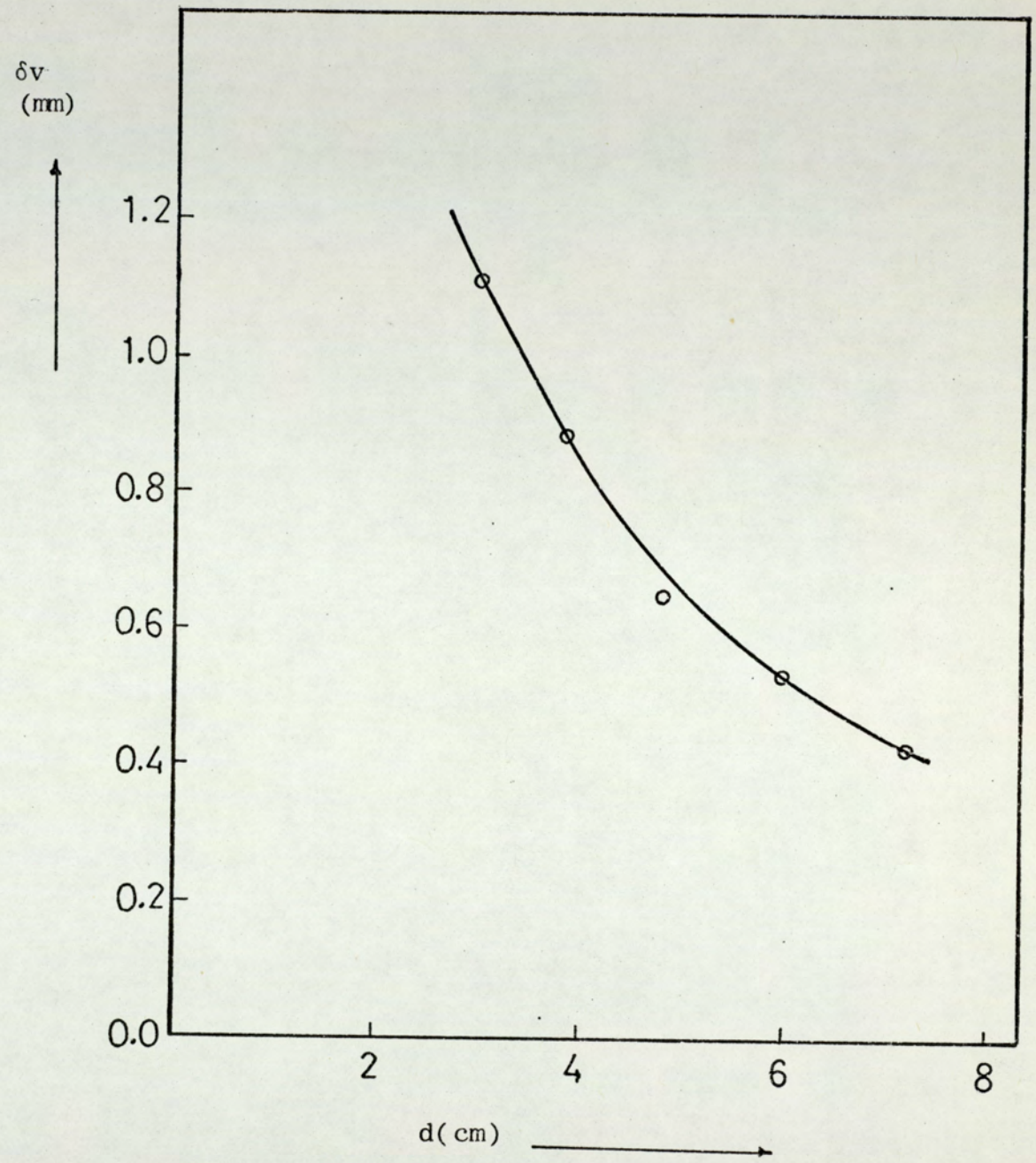

Figure 60 Thickness of the viscous sub-layer as a function of impeller diameter - Hot-film anemometer -

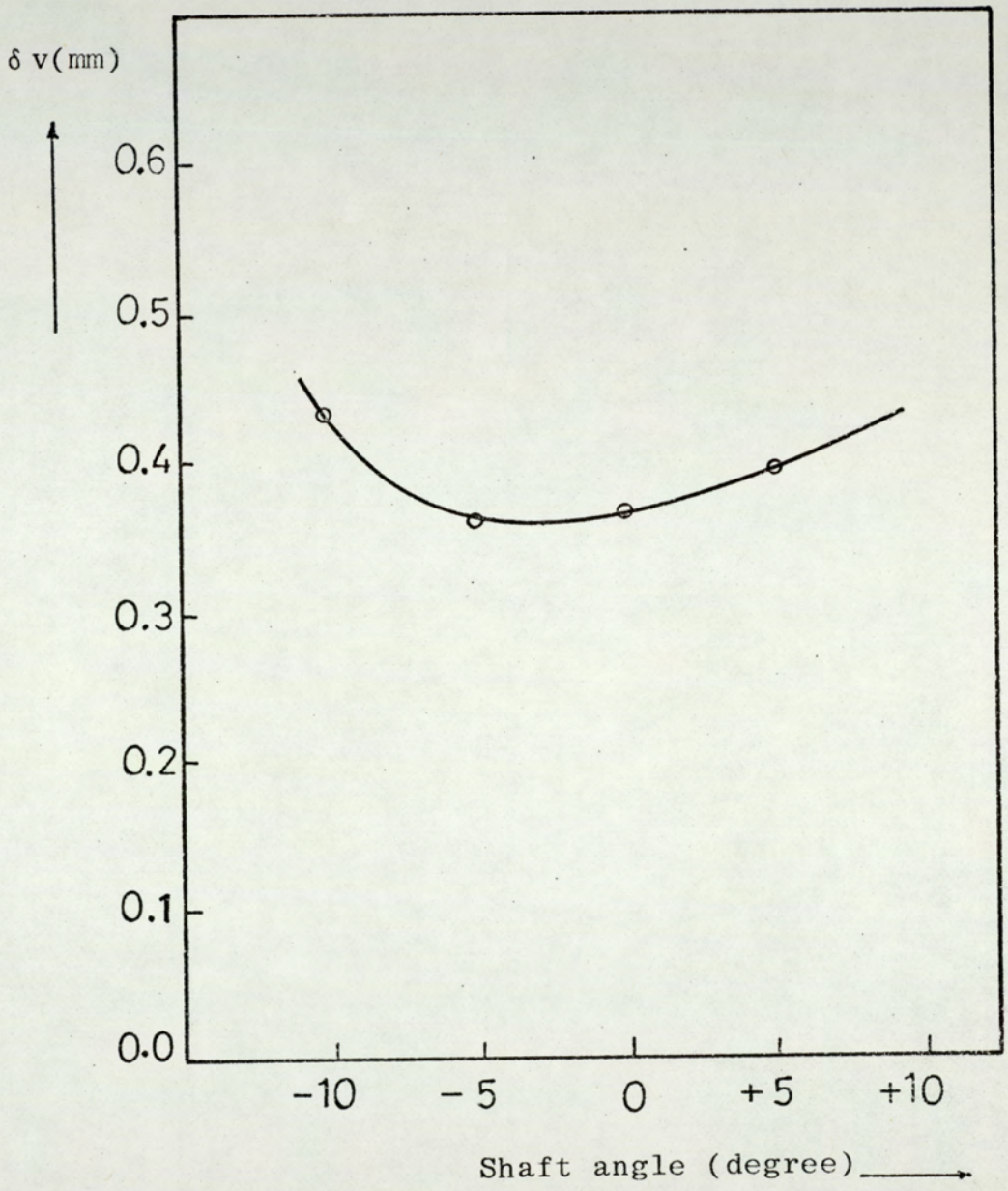

Figure 61 Thickness of the viscous sub-layer as a function of shaft angle - Hot-film anemometer -

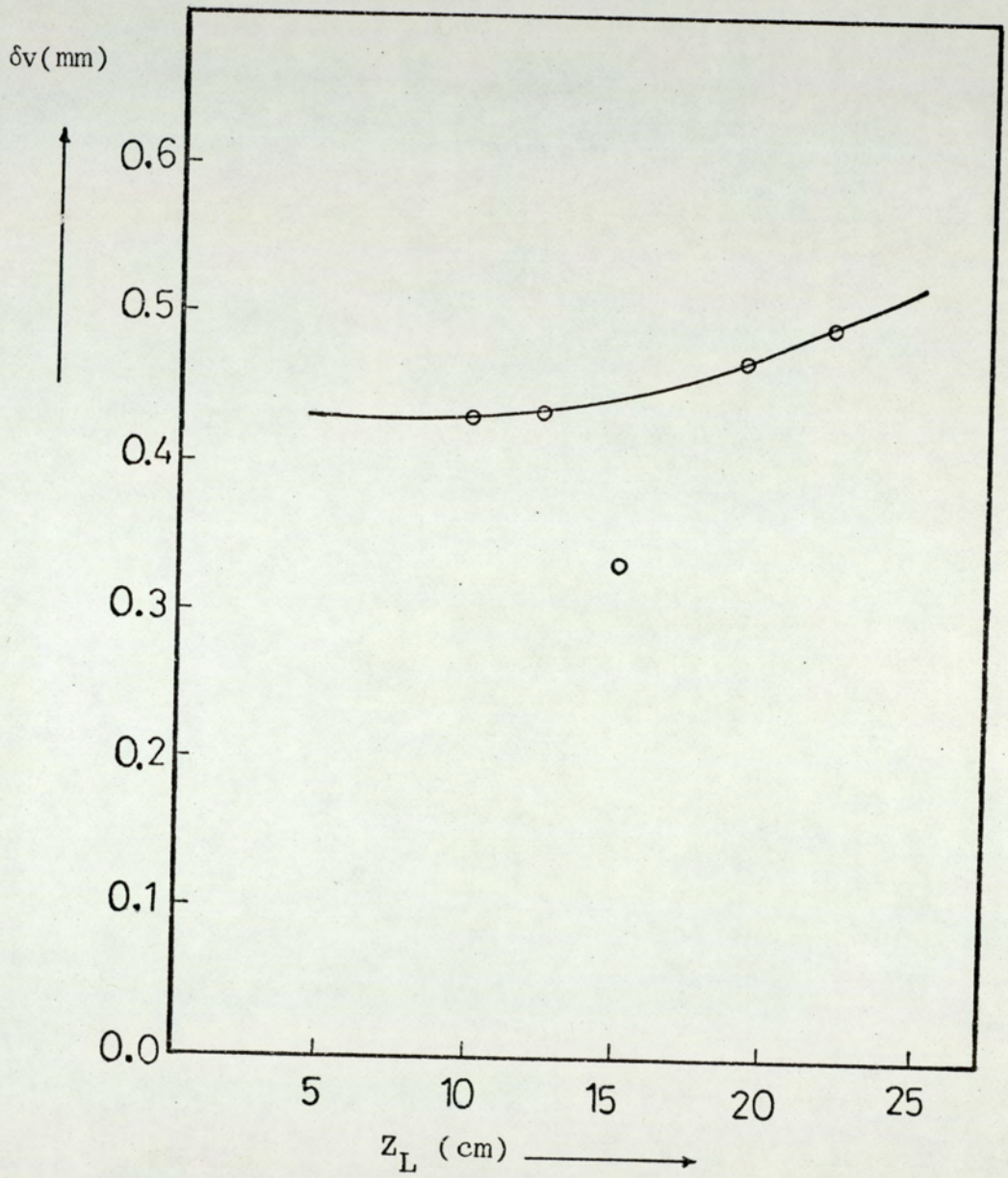

Figure 62 Thickness of the viscous sub-layer as a function of liquid depth - Hot-film anemometer-

as shown in Figure 59. The thickness tends to decrease with the increase of the speed. The decrease is more rapid at lower speeds. Figure 60 represents the thickness of the viscous sub-layer as a function of impeller diameter which was changed from 3.0 to 7.2 at a speed of 3000RPM and an angle of -5^{o}. Again the thickness decreased rapidly with the increase of the diameter. It changed from a value of 1.1mm at an agitater diameter of 3.0cm to 0.415mm at a diameter of 7.2cm.

It was found that the optimum shaft angle that gives a minimum thickness of the viscous sub-layer was again 5 degrees to the left as shown in Figure 61 where the thickness was plotted against the shaft angle between 10 degrees to the left to 5 degrees to the right using impeller running at a speed of 3000RPM. The minimum thickness at an angle of -5^{o} was 0.365mm. The increase of the liquid depth showed a slight increase in the thickness of the viscous sub-layer as shown in Figure 62 where the thickness was plotted against liquid depth changing from 10 to 25cm.

7.5 QUALITATIVE RESULTS ON THE DISTRIBUTION OF THE VISCOUS SUB-LAYER - PHOTOGRAPHIC TECHNIQUE

Experiments were carried-out to study the sedimentation of pulp-paper solution around the tank while the contents were agitated with water. The experiments were carried-out at different impeller speeds, impeller diameters, and shaft angles. The tank was photographed during the process and after sedimentation using both still and cine photography. A cruciform-shaped baffle was used in some of the experiments to find its effect on the thickness of the viscous sub-layer. Figure 63A represents

(A)

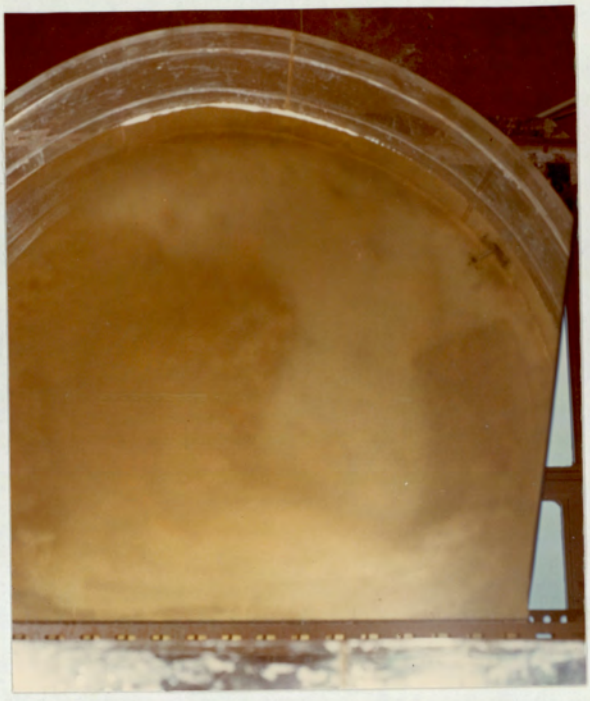

(B)

FIGURE 63 DISTRIBUTION OF PULP ON THE BASE OF THE TANK AT A SHAFT ANGLE OF A) 5° B) 10°

(A)

(B)

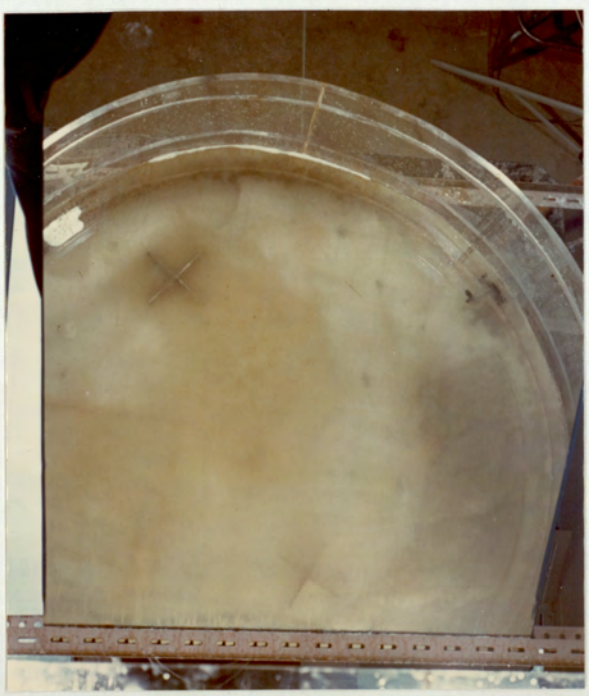

FIGURE_64_DISTRIBUTION OF PULP ON THE BASE OF THE TANK USING A) ONE BAFFLE B) TWO BAFFLES

(A)

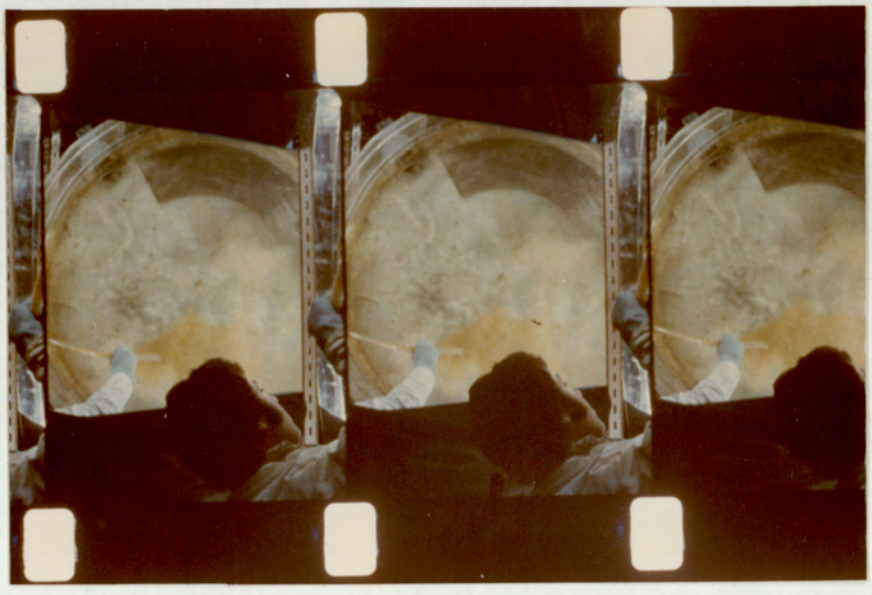

(B)

FIGURE_65_TWO SHOTS FROM A ACINE FILM SHOWING THE EFFECT OF A BAFFLE PLACED ON THE BASE OF THE TANK WITH A SHAFT ANGLE OF A)_5° B)_10°

a complete sedimentation of the pulp after the mixing impeller fixed at 5 degrees to the left and of a speed of 2000RPM. The pulp was collected away from the impeller jet.

Figure 63B represents pulp sedimentation after a process of mixing at a speed of 2000RPM and and angle of 10 degrees to the left. The pulp in this case collected around the centre of the tank rather than to the side. Figuure 64A represents the same process as above except that this time a cruciform shape baffle was used and placed away from the impeller jet. The photograph shows a collection of pulp heavily on the baffle. Using two baffles one opposite to the other in the position in Figure 64B shows that the pulp was collected in an area in between those two baffles.

Figure 65A and 65B represents two shots of a cine film taken when a baffle is placed, while adding the pulp solution and agitating with an angle of 5 and 10 degrees to the left respectively. Both Figures show the movement when the pulp first touched the baffle and lifted up.

7.6 DIMENSIONAL ANALYSIS

The thickness of the viscous sub-layer could be written as a function of the various system parameters as in the following form:

$$\delta_v = f(N, d, Z_L, T\cos\alpha, \rho, \mu, D) \qquad (7.4)$$

Applying the dimensional analysis in Appendix (A3) leads to the equations:

$$\frac{\delta v}{d} = C(N_{Re})^{a} \left(\frac{Z_L}{d}\right)^{b} \left(\frac{T\cos\alpha}{d}\right)^{c} (N_{sc})^{-d} \qquad (7.5)$$

or

$$\frac{\delta v}{d} = C\left(\frac{\rho N d^2}{\mu}\right)^{a} \left(\frac{Z_L}{d}\right)^{b} \left(\frac{T\cos\alpha}{d}\right)^{c} \left(\frac{\rho D}{\mu}\right)^{d} \qquad (7.6)$$

The results obtained in the previous section were subjected to a regression analysis to find the values of c, a, b, c and d using a computer program in Appendix (A3).

It was found that the value of these constants are:

C = 6.425

a = -0.648

b = 0.04

c = 0.0

d = -0.1

Therefore, equation (7.6) can be written as:

$$\frac{\delta v}{d} = 6.425\left(\frac{\rho N d^2}{\mu}\right)^{-0.648} \left(\frac{Z_L}{d}\right)^{0.04} \left(\frac{\rho D}{\mu}\right)^{-0.1} \qquad (7.7)$$

and the correlation agreed with results within accuracy of ±6.3%.

The values of thickness of the sub-layer calculated from the experiments were plotted against those calculated from equation (7.7) and plotted in Figure 66 , where it can be seen that most of the results fall in the region ±6.3%.

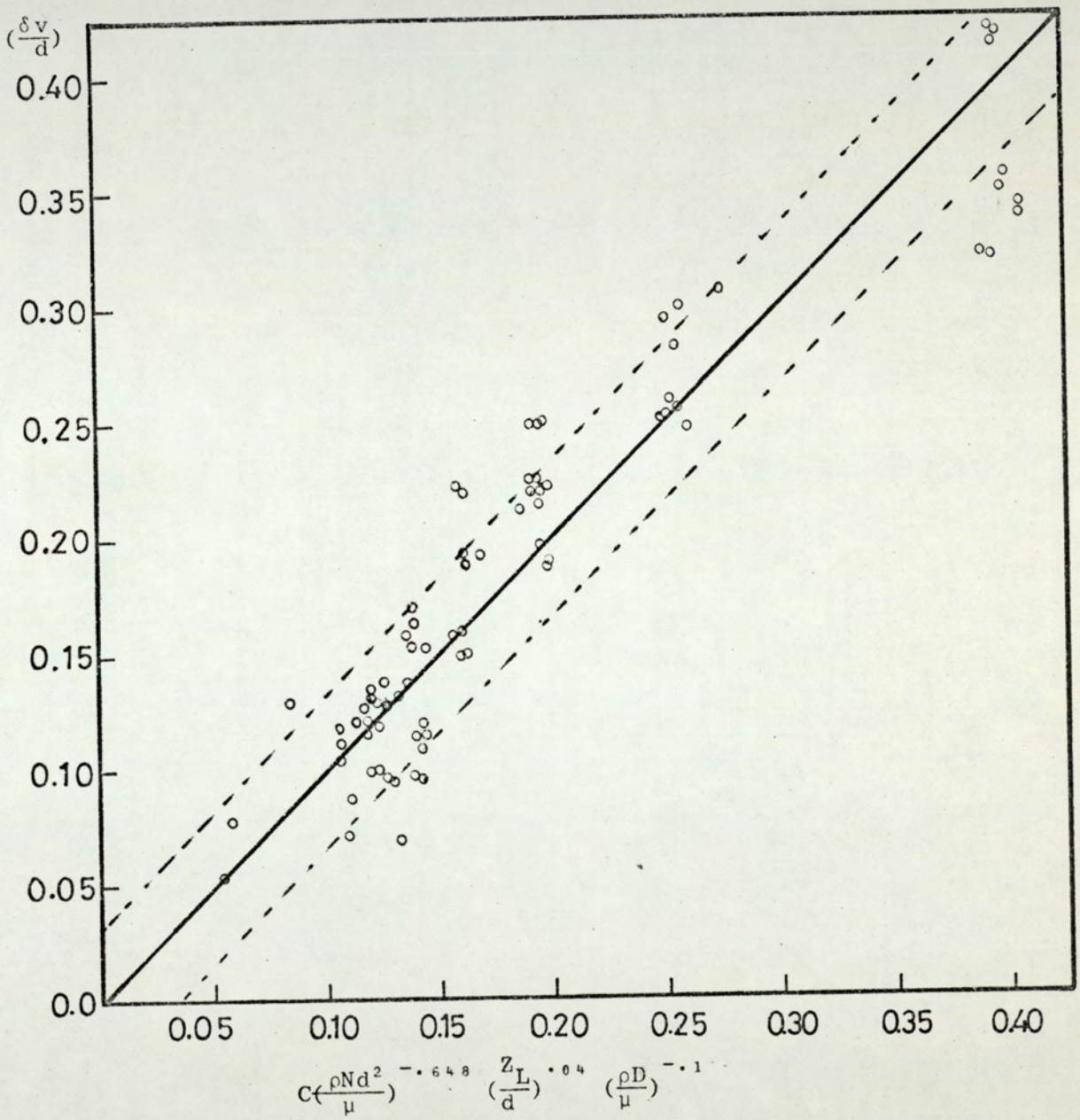

Figure 66 Experimental value of thickness of viscous sub-layer as a function of the theoretical value

7.7 THEORETICAL RESULTS

7.7.1 AXIAL VELOCITY ALONG THE IMPELLER JET

The axial velocity on the boundary of the jet was plotted as a function of distance along the jet at different values of impeller speed and the results are shown in Figure 67 and for different values of impeller diameter in Figure 68. Results are as tabulated in Tables 79 to 90. Both graphs show a rapid decrease in the velocity with increase of distance. That is as the jet travels across the tank, the velocity decreases. Also they show that the increase in both impeller speed and diameter increases the velocity of the jet. From both graphs, it is clear that at large impeller speed or diameter, the velocity decreases more rapidly than at a low value. Figure 69 represents the velocity pro file along the jet.

7.7.2 WALL SHEAR STRESS ALONG THE JET

The shear stress was plotted against the distance from the impeller for different values of impeller speed and presented in Figure 70. Also for different values of impeller diameter as in Figure 71. Again both graphs show a steep decrease in wall shear stress with increase of distance. Also the shear stress decrease with the decrease of the impeller speed and the impeller diameter. Results of shear stress at any point along the jet are in Tables 91 to 96.

7.7.3 THICKNESS OF THE VISCOUS SUB-LAYER

Figure 72, and 73 represent a plot of the thickness of the viscous sub-layer as a function of distance for different impeller speeds and impeller diameters respectively.

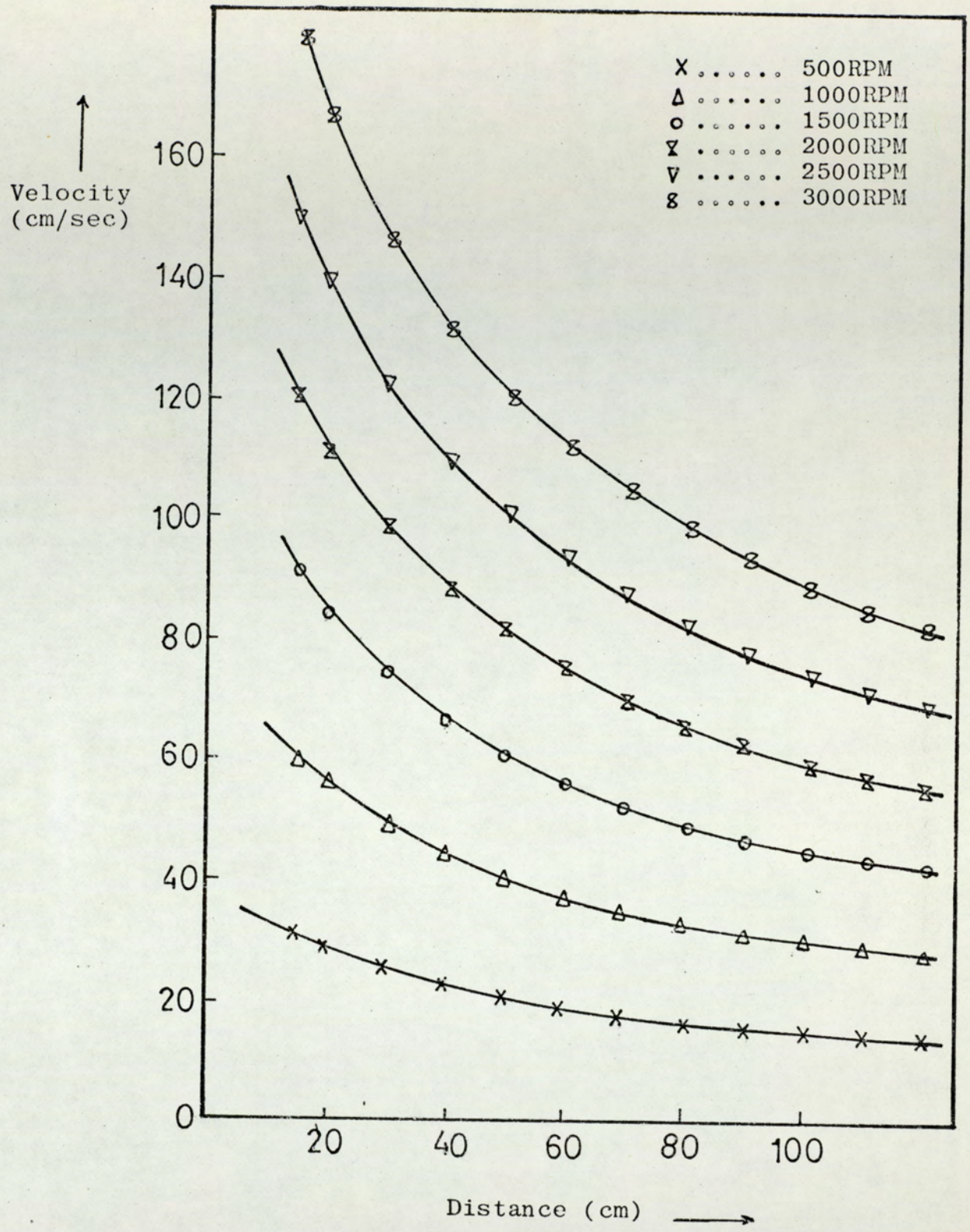

Figure 67 Velocity at the jet boundaries as a function of distance for different impeller speeds

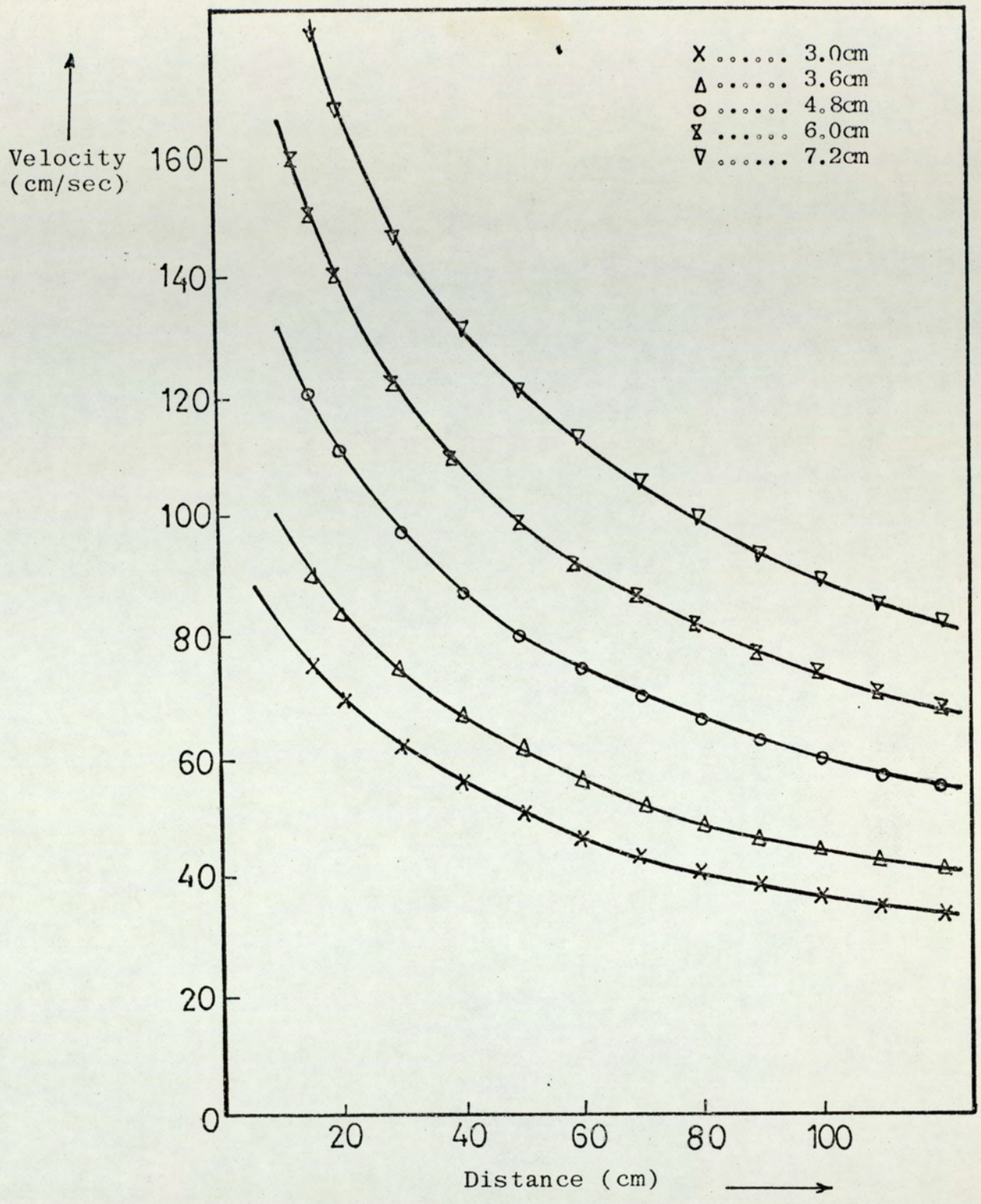

Figure 68 Velocity at the jet boundaries as a function of distance for different impeller diameters.

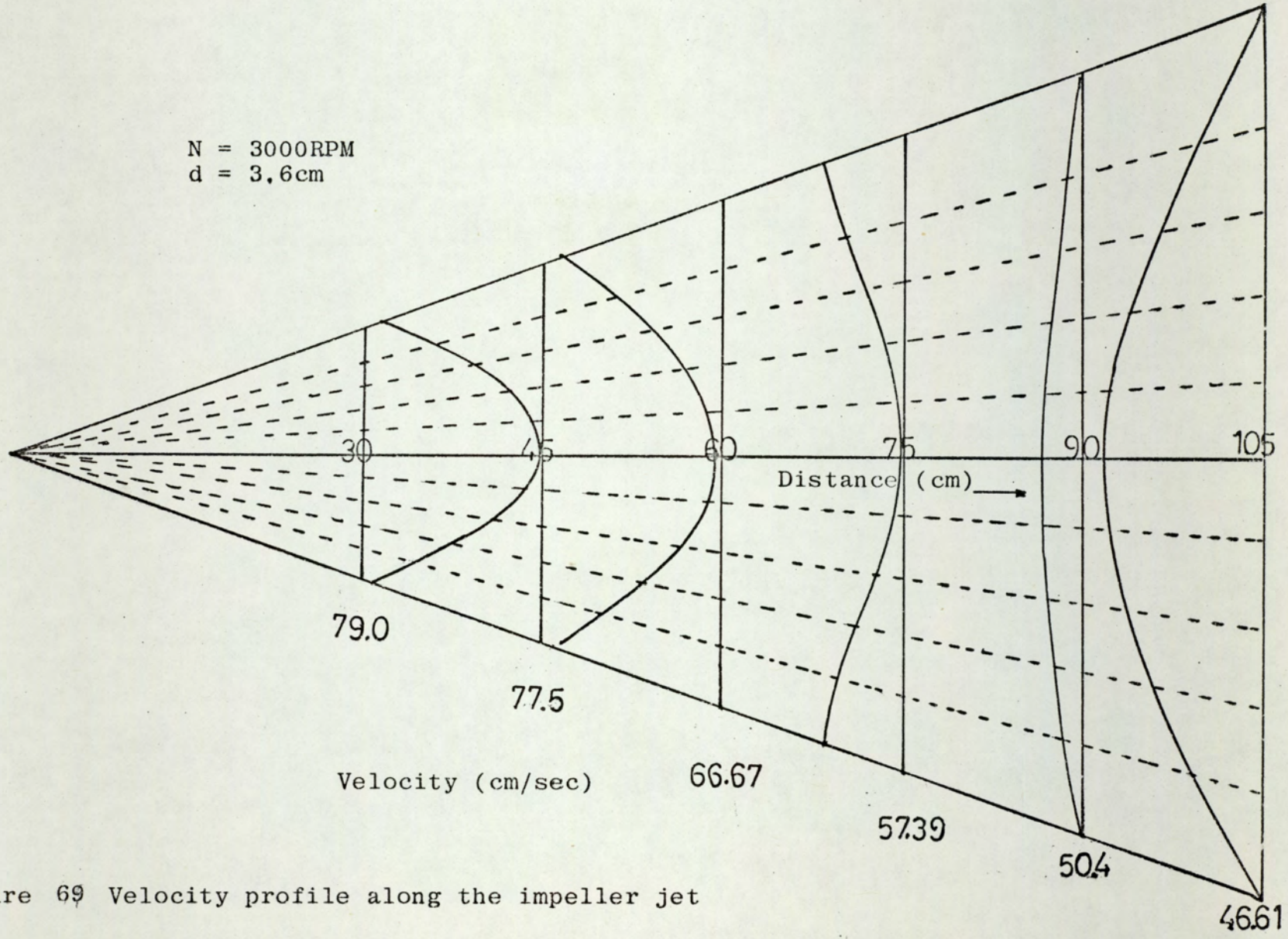

Figure 69 Velocity profile along the impeller jet

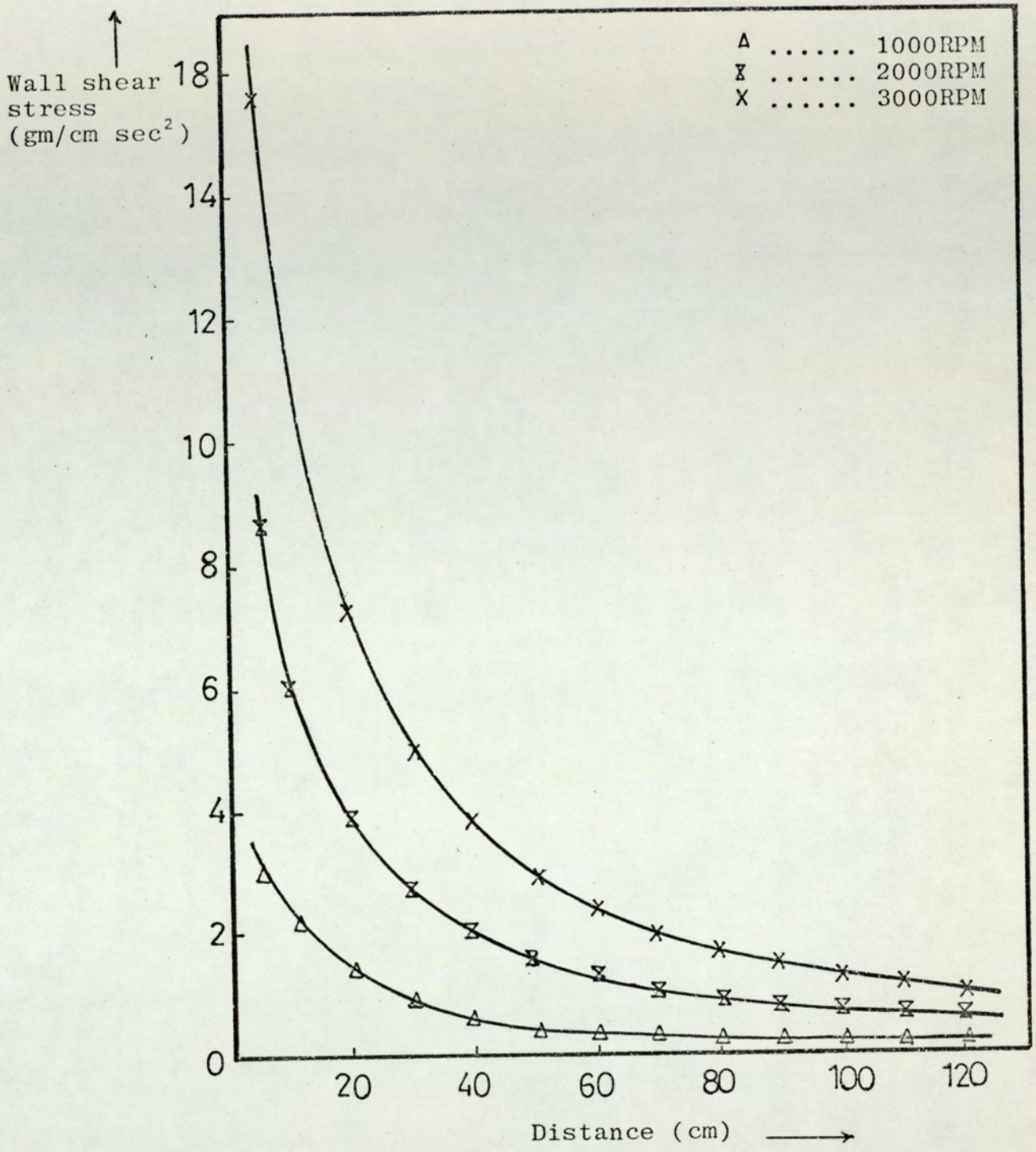

Figure 70 Wall shear stress as a function of distance along the jet at different impeller speeds

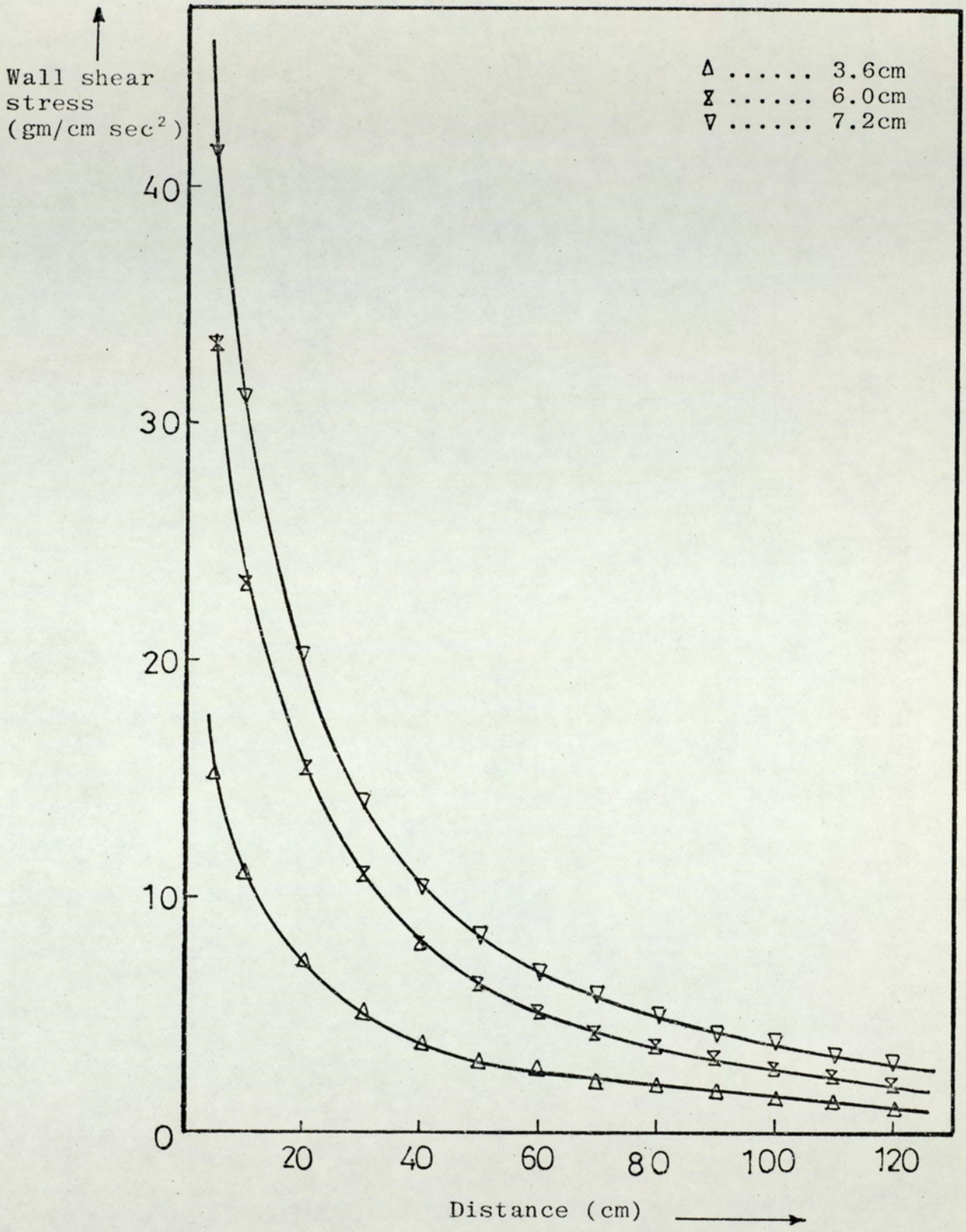

Figure 71 Wall shear stress as a function of distance along the jet at different impeller diameters

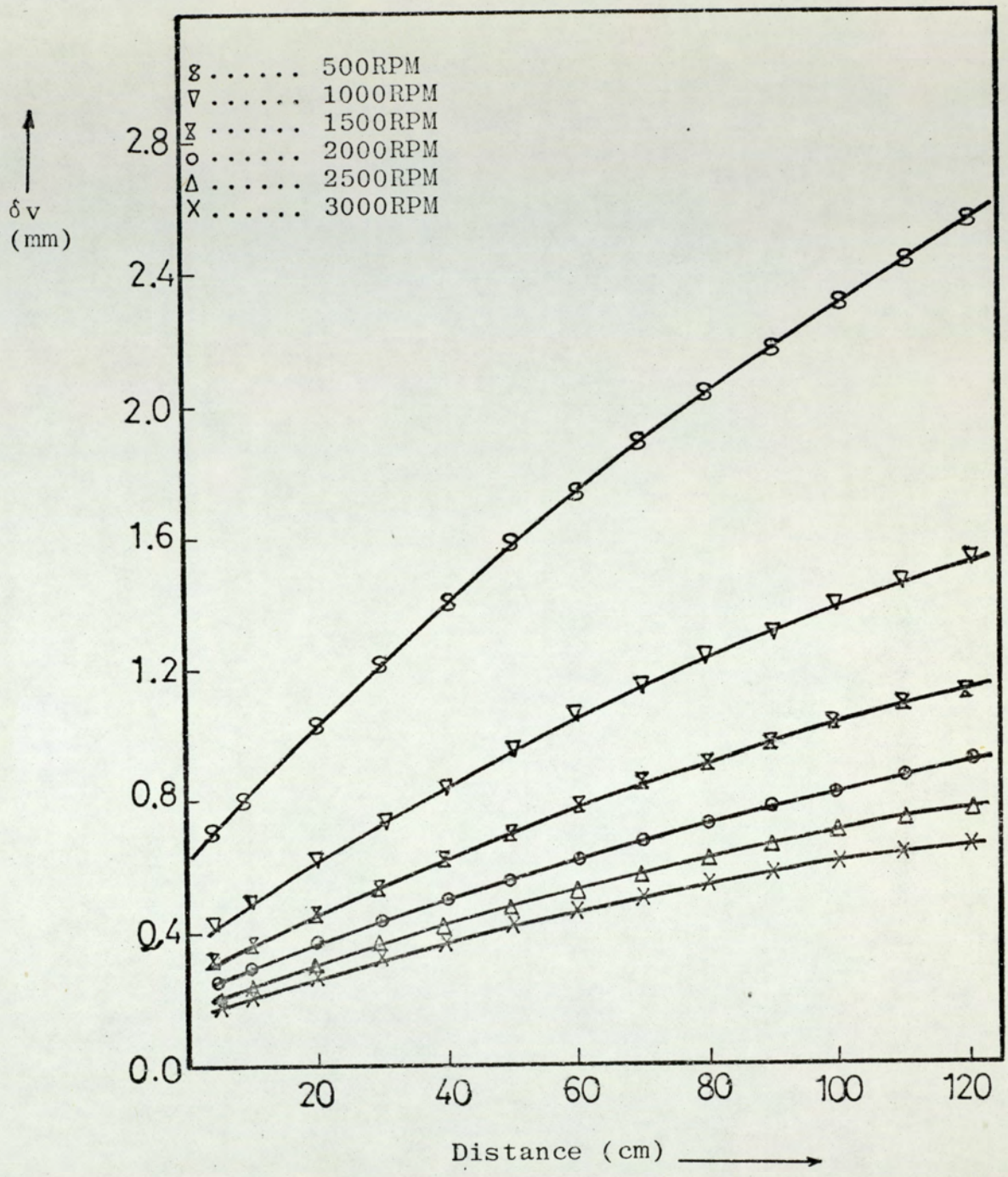

Figure 72 Thickness of the viscous sub-layer as a function of distance along the jet for different impeller speeds

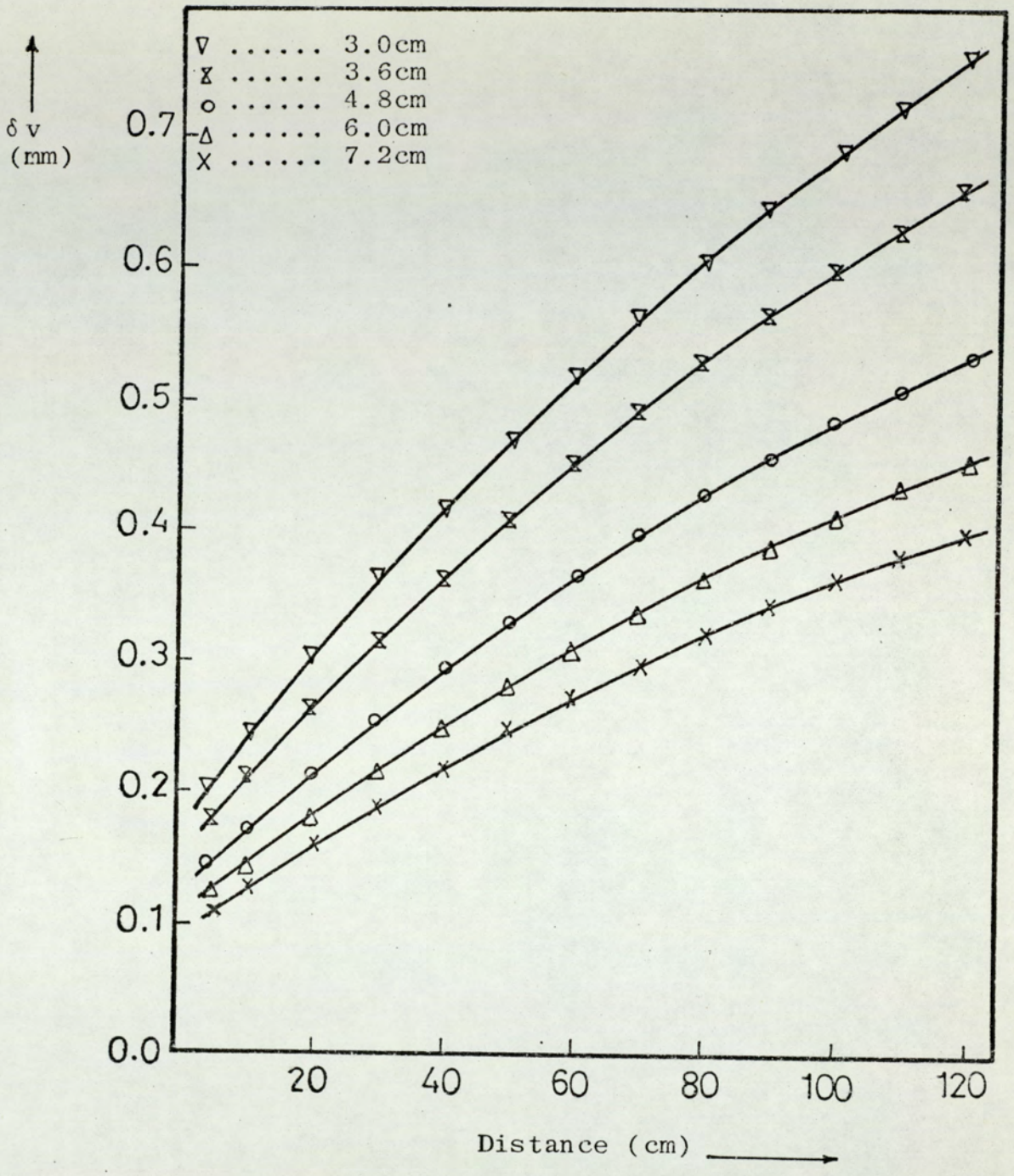

Figure 73 Thickness of the viscous sub-layer as a function of distance along the jet for different imepller diameters

They indicate a fairly rapid increase in thickness with increase of distance; also an increase of the thickness as the impeller speed or the impeller diameter is decreased. The difference between the thickness of high impeller speed or diameter and a low one at a high distance is more than that at a low distance.

7.8 FULL-SCALE TANK RESULTS

Measurements were carried-out on a tank 79.0m in diameter fitted with two side entry propellers, each of 75cm diameter, fixed at 10 degrees to the left and rotating at 350RPM. The height of the tank was 19m and contained crude oil. The layer where the sludge existed was assumed to be the viscous sub-layer and it was assumed that this sludge could not be mixed with the bulk of the oil in the tank. Apart from this layer, the remainder of the sludge was assumed to be uniformly mixed with oil in the tank when the agitators operated, but some will settles into the viscous sub-layer when the mixers are switched off. In addition, there will be a thin layer of hard, packed sludge permenently on the bottom of the tank which will remain there regardless of the extent of agitation and the top of this layer has been assumed to be the bottom of the tank. Therefore, the thickness of the viscous sub-layer was calculated from the following equation;

$$Y_1 = Y_2 + Y_3 + Y_4 \qquad (7.8)$$

The layer Y_2, built up from the sedimentation of sludge

when the mixers were switched off and could be calculated from Stokes law (116) and that the settling velocity at each point in the tank is uniform. Then

$$V_s = \frac{g(\rho_s - \rho)d_\rho^2}{18\mu} \qquad (7.9)$$

and $$Y_2 = V_s t \qquad (7.10)$$

Figure 74A shows the shape and the size of the large particles in the sludge, while Figure 74B shows the fine particles. The fine particles can be neglected and the time of sedimentation considered is that of the large particles only. However, it has been assumed that the particles are spherical with a diameter of 100 μm.

Experiments were carried out to measure the thickness of the sludge after switching off the agitator and leaving the bulk to settle. The thickness of the sludge was measured by inserting a calibrated measuring tape, connected to a heavy metalic ball, through the oil to the surface of the sludge. It was impossible to measure the height of the sludge when the mixers were operating since the impeller jet prevented the metal ball from descending vertically and the depth recorded would have been misleading.

The height of the sludge was measured at different oil depths and Figures 75A and 75B show the distribution of the sludge around the base of the tank after complete settling, while Figures 76A and 76B show the calculated distribution of the viscous sub-layer around the base of the tank at the moment the agitators were stopped.

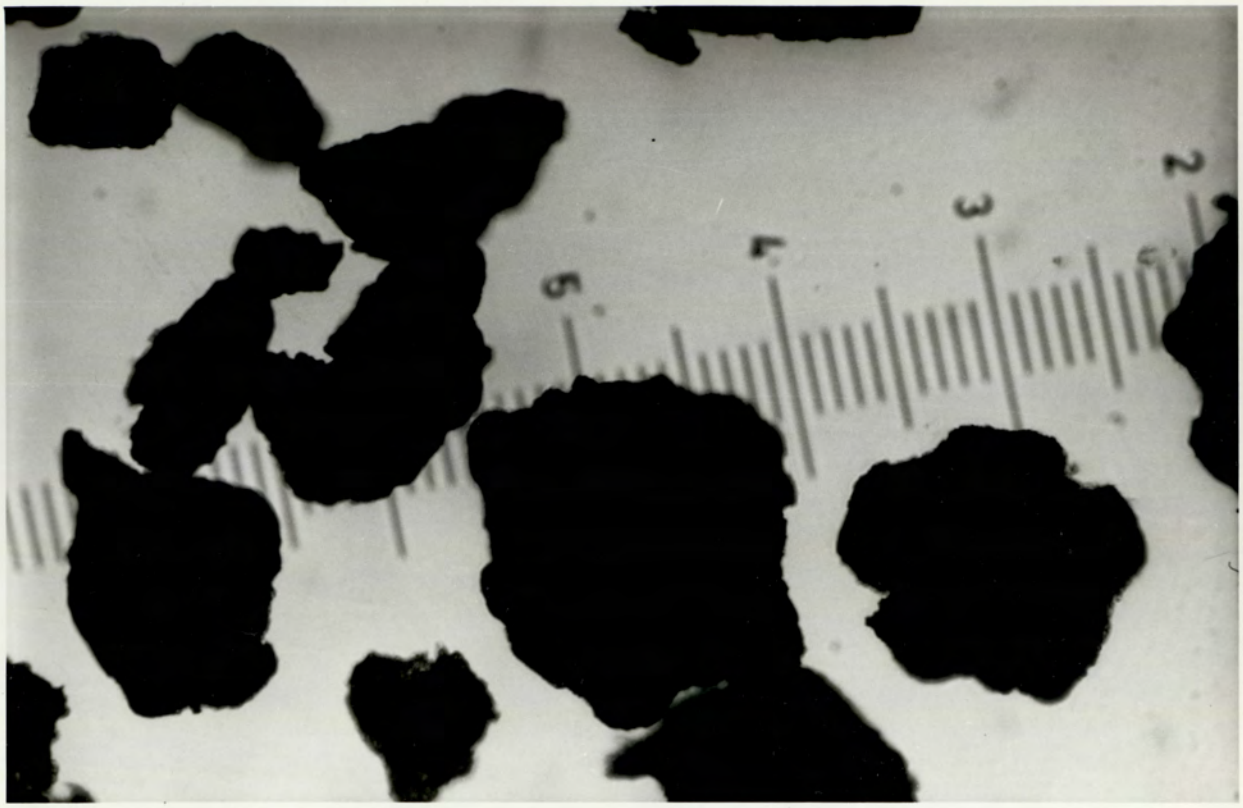

FIGURE_74A_LARGE PARTICLES OF SLUDGE

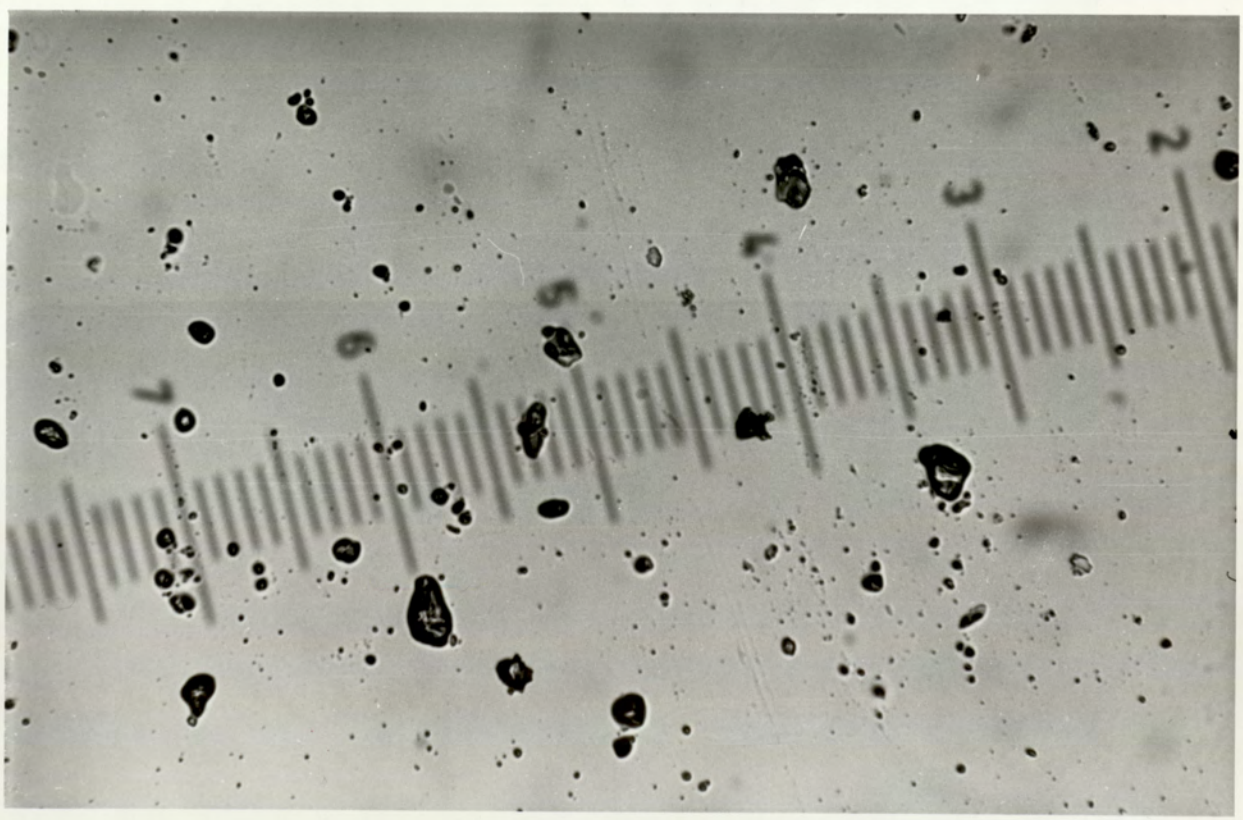

FIGURE_74B_FINE PARTICLES OF SLUDGE

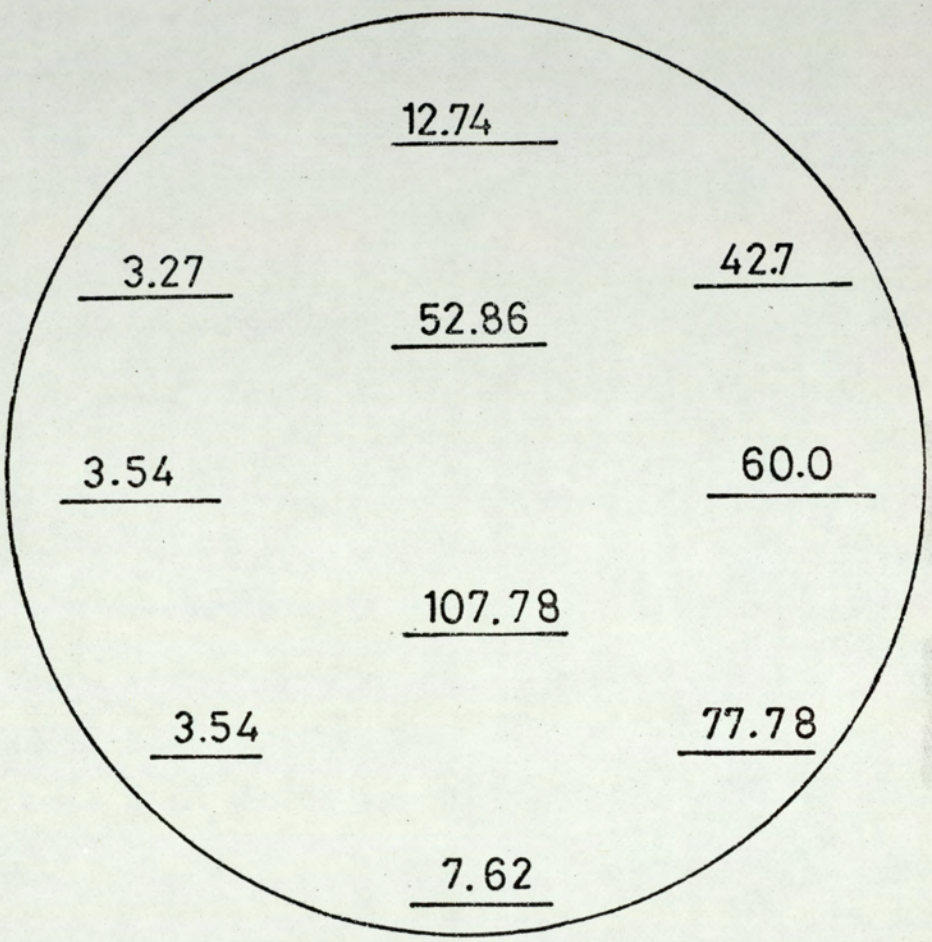

Z_L = 1.65m

Figure 75A Distribution of Sludge on the Base of the 79m Tank

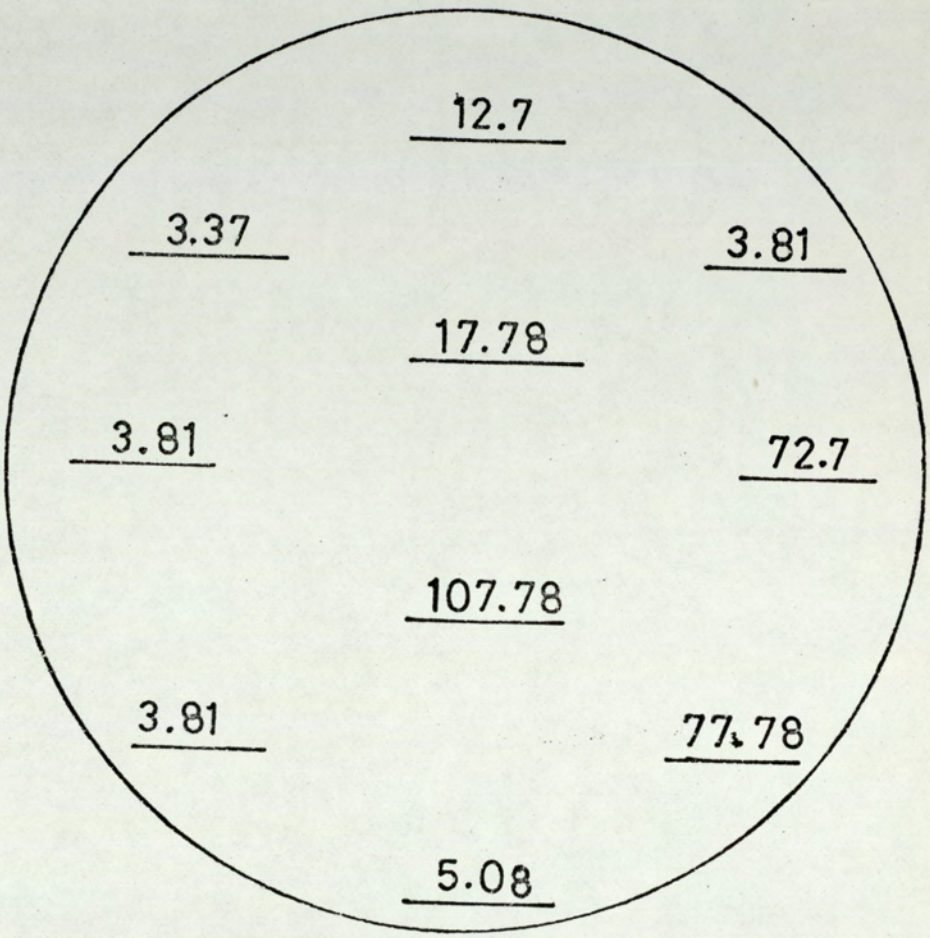

Z_L = 18m

Figure 75B Distribution of Sludge on the Base of the 79m Tank

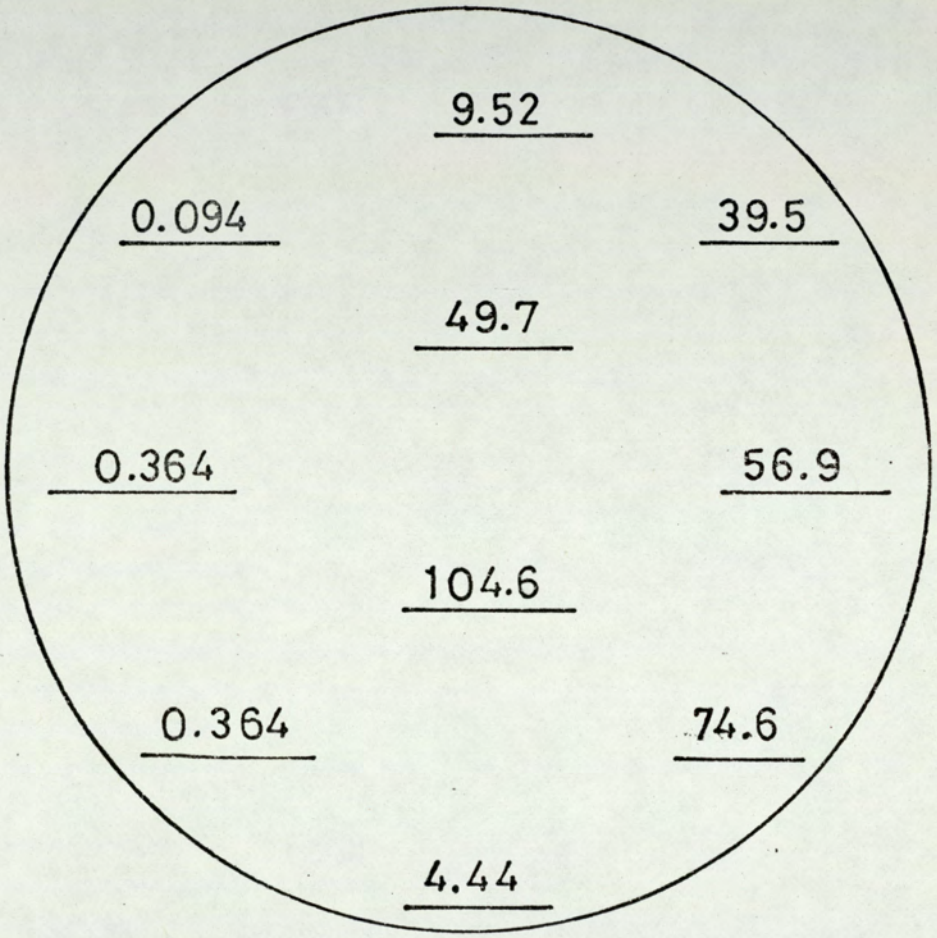

Z_L = 1.65m

Figure 76A Distribution of the Viscous Sub-layer on the Base of the 79m Tank

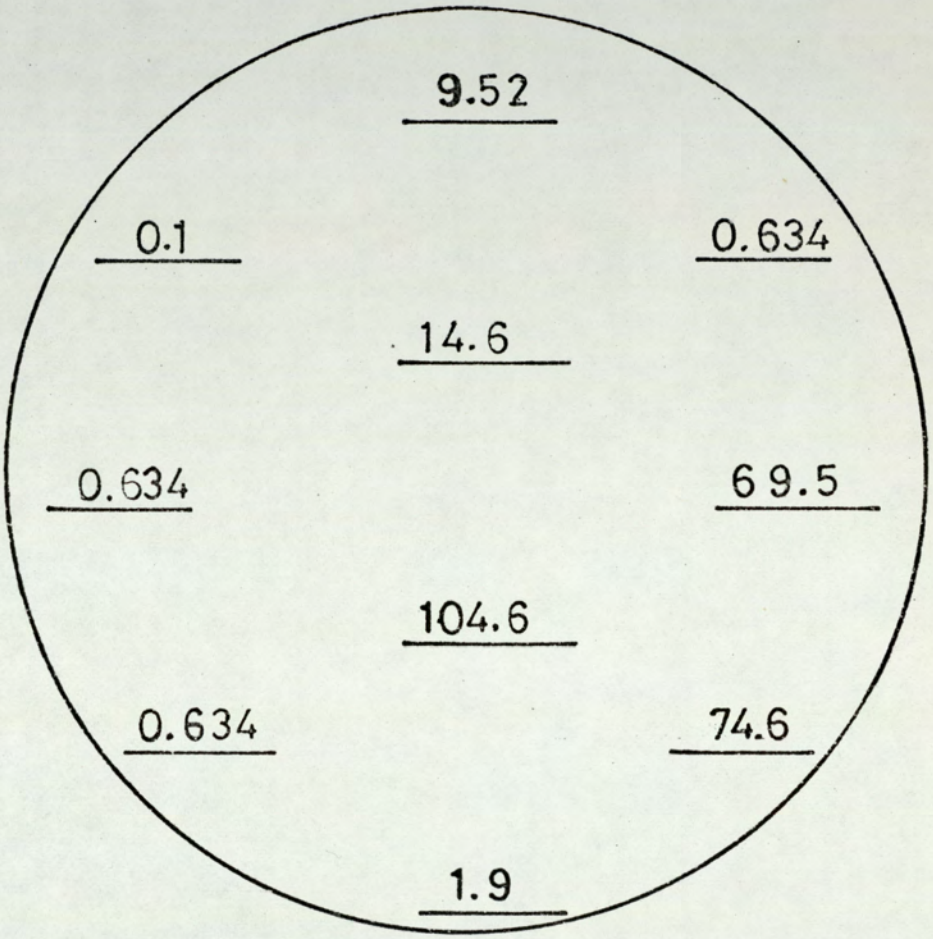

Z_L = 18m

Figure 76B Distribution of the Viscous Sub-layer on the Base of the 79m Tank

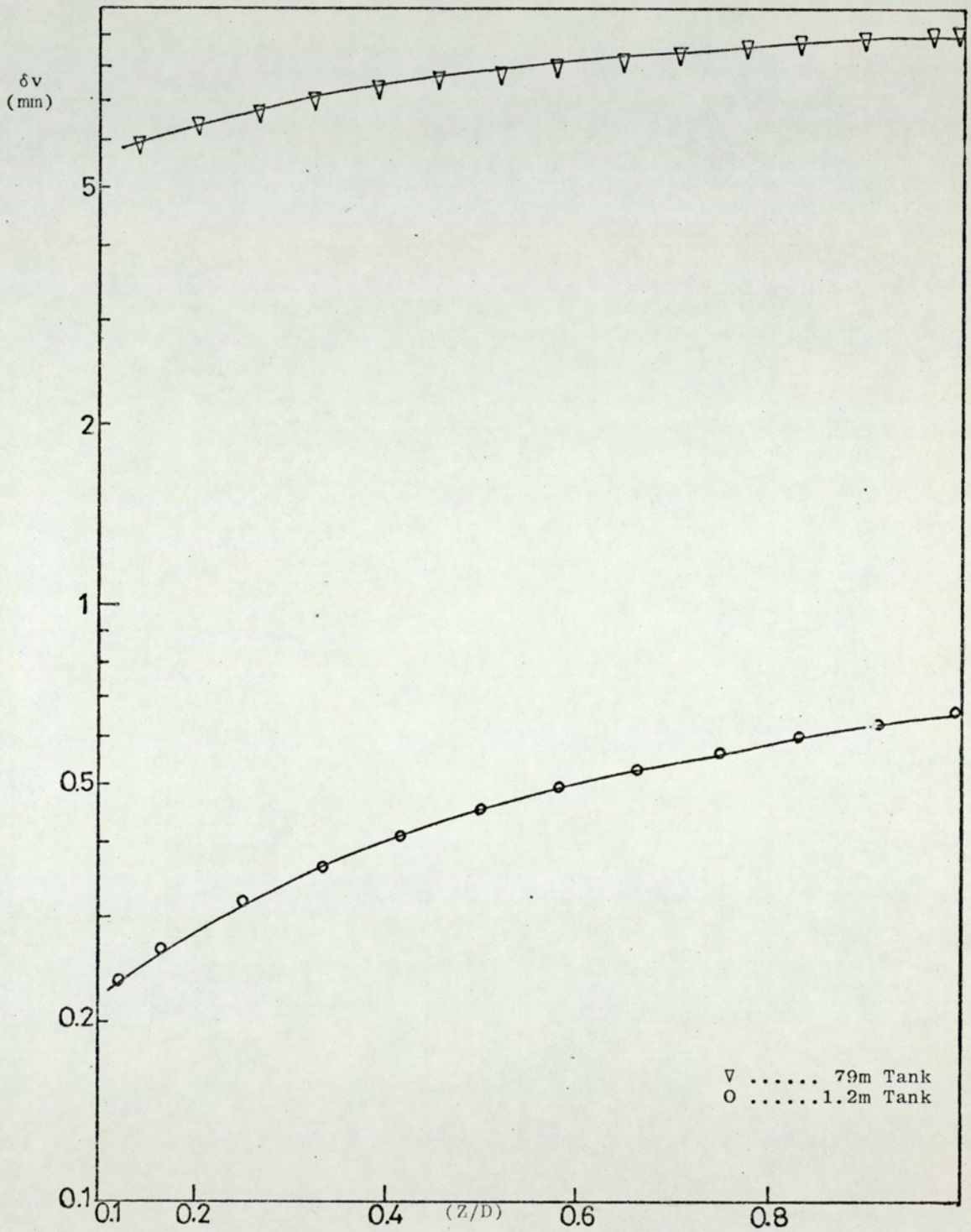

Figure 77 Thickness of the Viscous Sub-layer along the Jet

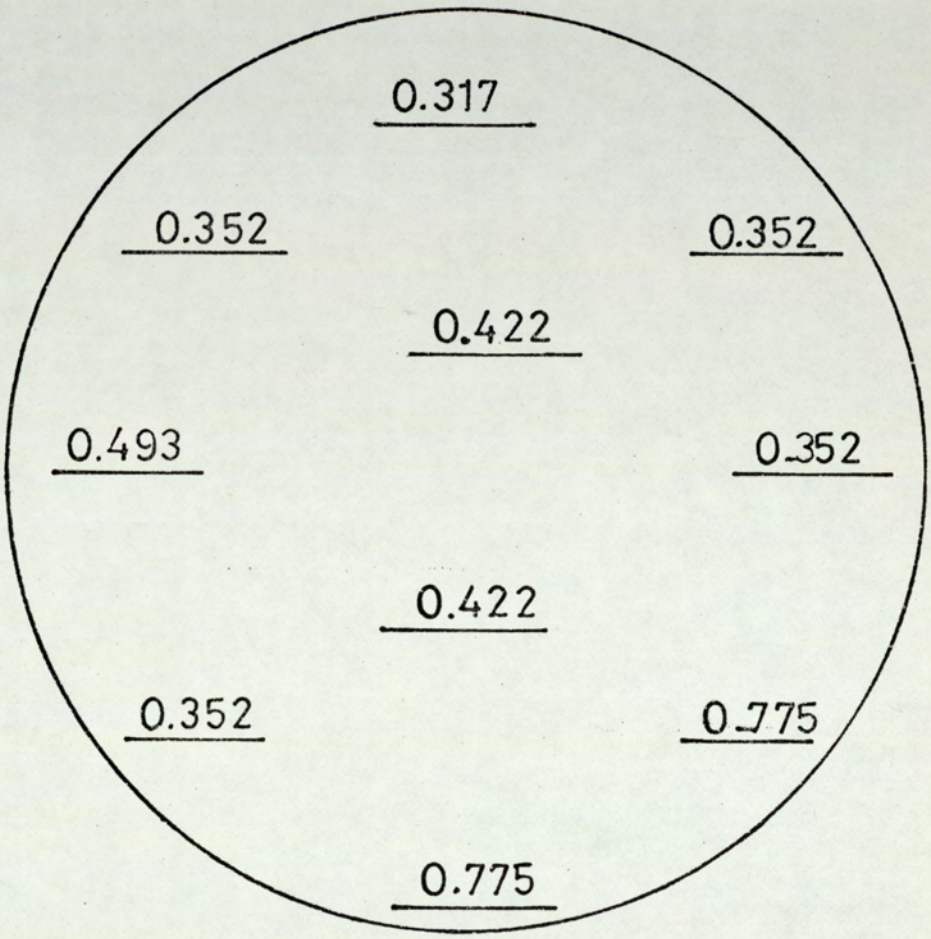

Figure 78 Distribution of the Sludge on the Base of the 60cm Tank

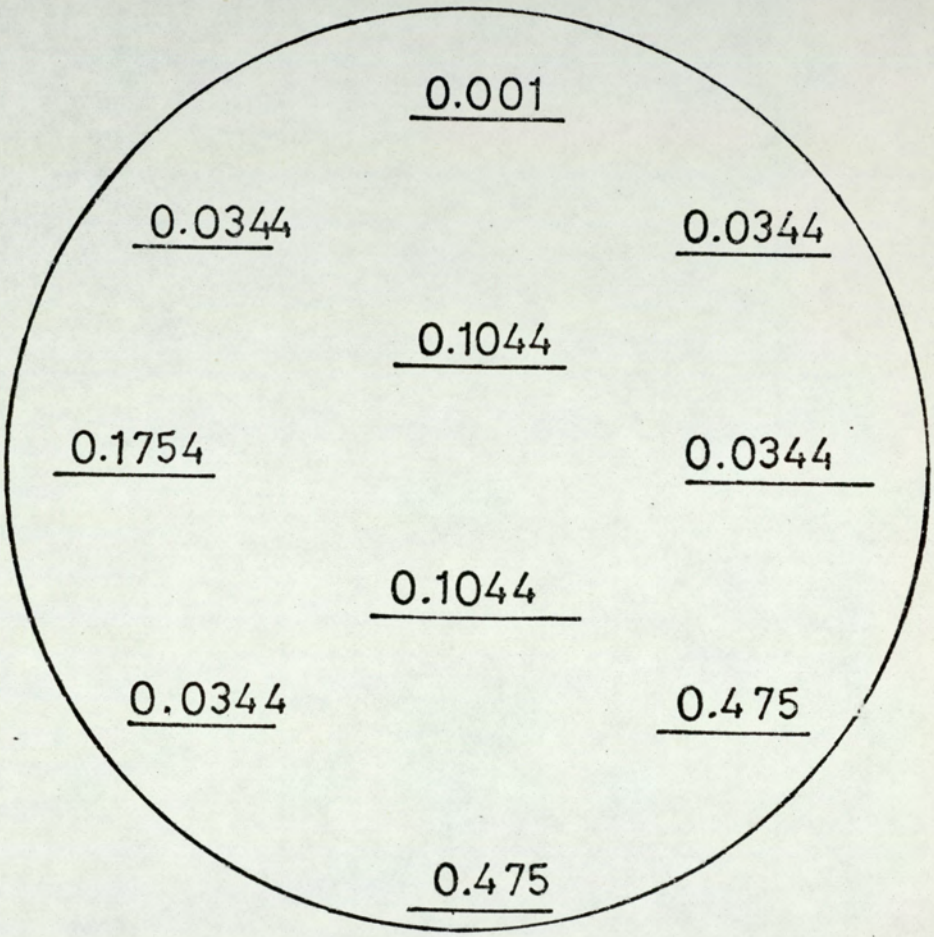

Figure 79 Distribution of the Viscous Sub-layer on the Base of the 60m Tank

The mathematical model has been applied to the full-scale tank and the thickness of the viscous sub-layer along the jet has been estimated, and the results obtained are presented in Tables 101 and 102 and plotted in Figure 77. The thicknesss of the viscous sub-layer is plotted as a function of distance from the impeller and the curve obtained is compared with that obtained from the 1.2m model tank. The average value of the ratio of the thickness of the viscous sub-layer $(\frac{\delta large}{\delta small})$ is 13.0.

A small tank of 60cm diameter was used to compare the distribution of the sludge around the base with that of the full-scale tank. The liquid depth was chosen so that it had the same ratio of $(\frac{T}{Z_L})$ as that of the full-scale tank, but the agitator was placed centrally and vertical. Crude oil was agitated and after switching off the mixer and attaining steady state, the thickness of the sludge distributed around the tank was measured using an ultra sonic probe to detect the height of the sludge. Figure 78 shows the distribution of the sludge after complete sedimentation. The growth of the thickness of the sludge during sedimentation was calculated using equations (7.9) and (7.10) and from this the thickness of the viscous sub-layer was calculated from equation (7.8) and its distribution is shown in Figure (79). The ratio of $(\frac{\delta large}{\delta small})$ is about 11.0.

CHAPTER VIII

8. DISCUSSION

8.1 INTRODUCTION

The results of the experiments using both the electrochemical technique and the hot-film anemometer will be discussed and compared in this Chapter. Also a comparison between the experimental results and those obtained from the theoretical analysis is presented. The significance of all the results and the effect of the parameters on the thickness of the viscous sub-layer is considered, supported by qualitative explanations for the distribution of the viscous sub-layer. Finally some of the experimental results obtained from a full-scale tank are discussed and compared to the 1.2m model tank results.

8.2 VARIFICATION OF THE ELECTROCHEMICAL TECHNIQUE - TEST CHANNEL -:

8.2.1 CURRENT-VOLTAGE PLATEAU

The current-voltage curves presented in Figure 19 describe the change in the electrode current when the applied voltage is increased. It will be noticed that, as the negative potential of the cathode is increased, the current increased exponentially and thereafter approaches a constant value, i.e. the limiting current asymptotically. This increase in the current, when the voltage increased, is caused by the migration of positive ions form the bulk of the solution to accumulate on the surface of the cathode. The current reached the limiting value when the ions transferred to the electrode surface react and the increasing potential

does not result in an increase in the rate of the desired reaction. Therefore, the reaction is diffusion controlled. However, a further increase of the potential over the limiting current region causes a steep increase due to the discharge by a secondary reaction; such as hydrogen evolution on the cathode.

Since at the limiting current the reaction is diffusion controlled, an increase in the rate of diffusion of ions will increase the value of the limiting current under the same condition of electrolysis. This is shown in Figure 21 where curves are plotted at different Reynolds numbers, between 500 and 3200. It is noticed that as the Reynolds number increased the flat portion of the polarization curve is shortened, until at a certain upper limit of the Reynolds number this portion of the curve disappears. This is because, as the Reynolds number increases the reaction will be too slow to remove all ions reaching the electrode surface. However, in these experiments, the Reynolds number was not allowed to exceed this upper limit.

8.2.2 MASS TRANSFER COEFFICIENT

For the same electrode diameter, the rate of mass transfer and the mass transfer coefficient is directly proportional to the limiting current under the same conditions of electrolysis. Therefore, the increase of the Reynolds number which caused an increase in the limiting current will increase the mass transfer coefficient for a certain electrode diameter. Figure 22 shows a change in the slope of the straight line from 0.184 to 0.484 at a Reynolds number of about 1400. This change in the slope indicates the presence of two types of flow; laminar and turbulent. The

mass transfer coefficient increases more slowly in the laminar region, while the increase is rapid for turbulent flow. The point at which the slope changes represents the point of transition from laminar to turbulent.

Although the limiting current decreases with decrease of the electrode diameter, the figure shows that the decrease in the electrode diameter gives a corresponding increase in the mass transfer coefficient from a value 0.93×10^{-3} to 2.1×10^{-3} cm/sec at Reynolds number of 520. Therefore, the ratio of the limiting current to the area of the electrode is an effective factor and increases with decrease of the electrode diameter.

The mass transfer coefficient was plotted versus the velocity gradient at the wall as shown in Figure 23. When the velocity gradient, calculated from the model developed by Hanratty (54), is increased the mass transfer coefficient increases for both laminar and turbulent flow, for any electrode diameter. The straight line has a slope of 0.333. Therefore at any value of wall shear stress:

$$\left(\frac{K_1}{K_2}\right) \alpha \left(\frac{d_{e_2}}{d_{e_1}}\right)^{1/3} \qquad (8.1)$$

8.2.3 THICKNESS OF THE VISCOUS SUB-LAYER

The thickness of the viscous sub-layer decreases with the increase of the Reynolds number as shown in Figure 24 and this decrease is more pronounced at low Reynolds numbers where the flow is laminar. Since the viscous sub-layer very much depends on the viscosity of the fluid, then, as the Reynolds number increase, turbulence will be produced in the flow while the viscosity effect will be negligible and

the friction velocity at the wall increases, thereby decreasing the thickness of the viscous sub-layer. Further increase in the Reynolds number would decrease this thickness only slightly. It is noticed from Figure 25 that the thickness of the concentration boundary layer is much less than the viscous sub-layer and the ratio is not more than $\frac{1}{20}$. This agrees with the assumption that the viscous sub-layer is much larger than the concentration boundary layer and the existance of unsteady flow in this layer.

All the results obtained from the test-channel discussed above, verified the reliability of the electro-chemical technique for the model tank. An electrode diameter of 0.5mm is the best diameter of the three used in the channel experiments. Hanratty (53) showed that for a given flow condition the non-uniformity of the flow increases as the electrode size increases; and the measured mass transfer intensity decreased as the degree of non-uniformity is increased. The measured mass transfer intensity would decrease with increasing electrode size to the point where a very large electrode diameter would average out all the effects of the flow distributions so that the intensity would be zero.

8.3 MODEL TANK - ELECTRO-CHEMICAL TECHNIQUE

8.3.1 LIMITING CURRENT

The current-voltage data, for the 22 electrodes built in the base of the model tank, obtained at different values of the system parameters gave polarization curves of the kind represented in Figure 19. As explained in the previous section, at a certain value of the voltage, the current

became constant and the reaction becomes diffusion controlled. This is called the limiting current and it was found that at certain conditions of the system and the electrolyte, the value of the limiting current changed from one electrode to another, in the tank, depending upon the position of these electrodes. These values could be related to the thickness of the viscous sub-layer.

The increase of the impeller speed or the impeller diameter increases Reynolds number and therefore increases the value of the limiting current due to the increase of the rate of transfer of ions from the bulk of the solution to the cathode surface. The change in the shaft angle revealed a different behaviour. Thus, a maximum value of limting current was obtained at a shaft angle of 5 degrees to the left which confirmed that the flow pattern produced at this angle gives an optimum result for the transfer of ions and therefore of the mass transfe rate. In studying the effect of the physical properties it was found that increasing the viscosity decrease the limiting current. This is due to the decrease of the impeller Reynolds number and the build-up of a viscous flow which retards the transfer of the ions to the electrode surface.

8.3.2 MASS TRANSFER COEFFICIENT

To understand the above results, the mean value of the mass transfer coefficient calculated from the limiting current was plotted against the various parameters as shown in Figures 32, 33, 34, 35, 36. The values of the mass transfer coefficient were averaged over 22 electrodes in the tank in order to study the effect of the various parameters. This,

however, is not valid when studying its distribution over the base of the tank. Then each point was taken seperately. At certain conditions of the system parameters, the mass transfer coefficient differs in value from one point to another depending on position. The points which lie inside the impeller jet (electrodes 20,15,4,3,8) shows a high value of mass transfer coefficient because, inside the jet, there is a high degree of turbulence and a rapid exchange of ions between the bulk of the solution and the electrode surface. At points away from the jet (electrodes 16,19,22, 12,13) a low value of mass transfer coefficient was obtained. Here the degree of turbulence is less and the fluid tends to lose some of its momentum. This distribution also depends on the position of the shaft angle which defines the flow pattern. Therefore, when the angle changes all the electrodes give different values of the mass transfer coefficient according to the new position. Figure 34 showed that an angle of 5 degrees to the left gives a maximum average value of mass transfer coefficent. There are regions of minimum mass transfer and maximum values. When the shaft angle is at a value of 10 degrees at either side, there is a maximum value of mass transfer in the area around the tank walls while the areas in the centre has the least value. This case is exactly opposite when the angle is between zero and 5 degrees to the left.

When the impeller speed is increased, the mass transfer coefficient increased and the change in the slope of the line at a Reynolds number of 2.75×10^4 explain the presence of two regimes of flow; and the transition point occurs at impeller speed of about 1700RPM. Although the

increase in the impeller diameter increases the mass transfer coefficient, there is no sign of change in the type of flow. Since the minimum diameter used gave a value of Reynolds number of about 3.2×10^4 which shows that at any value of impeller diameter used in the experiment, the flow was turbulent always.

8.3.3 THICKNESS OF THE VISCOUS SUB-LAYER

The main object of this study was to estimate the thickness of the viscous sub-layer and to assess the effect of each of the system parameters on the distribution of this layer around the base of the tank, and these results are presented here.

8.3.3.1 EFFECT OF THE SYSTEM PARAMETERS

In studying the effect of the system parameters, the average value of the viscous sub-layer over the 22 electrodes, used was taken to represent the thickness and to study its behaviour. Although averaging the values could be misleading, specially when studying the distribution of this layer around the tank, it is justified in order to find the effect of the parameters since this behaviour, of the average values, does not differ from that of each electrode taken seperately.

Increase of the impeller speed shows a decrease in the thickness of the viscous sub-layer as seen in Figure 41 The curve flattened out at about 1500RPM, indicating a change in the flow from laminar to turbulent. The thickness rapidly decreased in value at lower impeller speeds while at very high impeller speeds, there will be only a small

decrease in thickness. Also operating the agitator at a very high speed increases the power consumption, which means that a very small reduction in the thickness was achieved while increasing the power consumption considerably. This confirms that there is a limit to the increase of the impeller speed above which it would be uneconomical. Increase of the impeller diameter also gives a decrease in the thickness of the viscous sub-layer at a given speed. Because the range of diameters employed was between 3.0cm and 7.2cm and the impeller speed was 3000RPM, equivalent to Reynolds numbe between 3.2×10^4 and 1.5×10^5, the flow is always turbulent. However, there is a sharp decrease in the thickness at a small impeller diameter while there is a very slight decrease in the thickness between 6.0 and 7.2 cm diameter. This means that running an impeller of very high diameter (above 6.0cm) will only cause a dissipation of energy without achieving a noticable decrease in thickness. Therefore, the thickness of the viscous sub-layer is inversely proportional to the impeller Reynolds number.

When changing the physical properties of the solution, increase of the viscosity gives a sharp increase in the thickness due to increase of the viscous forces and a decrease in the degree of turbulence. Increasing the density decreases the thickness of thelayer. This results in an increase in the thickness with increase in the kinematic viscosity of the solution and therefore, the thickness of the viscous sub-layer is directly proportional to the Schmidt number and this effect is more important at high Schmidt number since this thickness becomes much more pronounced than the thickness of the concentration boundary layer.

The shaft angle and the liquid depth were found to affect the thickness of the viscous sub-layer and this seemed to be complex since both affect the flow pattern and therefore the distribution of the sub-layer around the tank. Figure 45 shows an optimum value of shaft angle of 5 degrees to the left at which the thickness of the viscous sub-layer is minimum. As this angle shifts from the optimum, the thickness tends to increase. It suggests that at this angle, the flow pattern produced gives a better circulation of the fluid around the tank and therefore results in reducing the thickness of the sub-layer. The increase of the liquid depth, however, shows a slight increase in the thickness of the viscous sub-layer as shown in Figure 50. It suggests that an increase in the liquid depth decreases the circulation velocity thereby reducing the turbulence which helps to build up the sub-layer on the base of the tank. In Figure 50 some of the points do not lie on the curve. The reason is that these points are taken for solutions having a viscosity that differed slightly during the measurements, which meant a small change in the thickness accordingly. However, if these points were corrected to the actual viscosity, they would fall on the curve.

8.3.3.2 DISTRIBUTION OF THE VISCOUS SUB-LAYER AROUND THE BASE OF THE TANK

In Figure 42 the thickness of the viscous sub-layer is shown to be distributed along the base of the tank and were measured at different impeller speeds. For all results presented the shaft angle was fixed at 5 degrees to the left. It is found from the figures that inside the impeller

jet the thickness of the viscous sub-layer is smaller than elsewhere in the tank and within the jet the thickness near the impeller tip is much less than that away from the impeller. These points are represented by electrode numbers 20, 15,11,8,4,3 while the electrodes located in the circular loops of the flow have higher thickness as in electrodes 12,13,14.5.7 and 16,17,18,19,21. The figure shows that the value of the thickness of the viscous sub-layer at each electrode always decreases with increase of the impeller speed but that the rate of increase is less as the impeller speed become greater.

The distribution of the viscous sub-layer around the tank, measured at different impeller diameters, showed a similar kind of distribution as seen in Figure 44. This is because the shaft angle was fixed at 5 degrees to the left. The decrease in the thickness at high impeller diameters, however, was very small compared to that for a small impeller diameter and an impeller diameter of about 6.0cm could be chosen as the optimum diameter.

The value of the shaft angle and its position has a great effect on the thickness of the viscous sub-layer and on the flow pattern produced. When the impeller shaft is fixed at 5 degrees to the left, the flow will be produced as a jet which travels from the impeller along the tank diameter and when it touches the far-side of the tank wall, it divides into two loops; a small loop to the left of the jet and a large loop to the right; and both loops rejoin each other again at the impeller. The thickness of the viscous sub-layer is minimum near the impeller and grows along the jet as the jet passes along the tank. However, this

thickness is less than in areas in the tank where the two loop exists. The thickness of the viscous sub-layer tend to build-up away from the jet boundaries. When the angle was fixed at 10 degrees, the flow pattern resulted in one loop being produced and this loop circulated around the tank wall. Therefore, the thickness of the sub-layer is thin in the area near the wall while it increases near the centre of the tank.

8.4 MODEL TANK - HOT-FILM ANEMOMETER

8.4.1 CALIBRATION OF THE HOT-FILM PROBE

The hot-film probe used in these experiments was calibrated every time it was utilized since there are many factors that could affect the calibration curve. Also whenever the probe was changed, a new calibration was obtained. The calibration curves are shown in Figure 58, representing a plot of the voltage against the corrected velocity, gives different velocity reading for each set of measurements. The temperature of the fluid and the surrounding affect the calibration, since the readings of the anemometer depends on the heat transfer between the fluid and the probe. Also the presence of dirt particles and air bubbles in the fluid caused some deviation in the curves. Details of the technical aspects of the anemometer are presented in Appendix (A1).

8.4.2 THICKNESS OF THE VISCOUS SUB-LAYER

The thickness of the viscous sub-layer was calculated from the value of the velocity measured very close to the base of the tank. The minimum distance between the edge of

the probe and the tank base was 1mm. All measurements were achieved using degassed water and hot-film probes having 2μm quartz coating to protect them from damage in conducting solutions. However, these probes could not be used in the redox solution since it had a very high conductivity which would result in damage to the probe.

The results of the thickness of the viscous sub-layer calculated from the measurements using water is obviously lower than those obtained by the electro-chemical technique since the viscosity of water is lower than that of the redox solution. However, since results were obtained on the effect of viscosity on the thickness of the sub-layer using the electro-chemical technique, it is possible to extrapolate these results to the viscosity of water in order to compare the two techniques. This, however, is an approximate method since the conditions of the system using one technique could be different from those of the other technique.

The results obtained using the hot-film anemometer for changing impeller speed, impeller diameter, shaft angle, and liquid depth are shown in Figures 59, 60, 61, 62. The curves obtained are similar to those obtained by the electro-chemical technique except for the change of the liquid depth. This gives a slightly different shape of curve. This is because the results obtained for different liquid dpeths, using the electro-chemical technique, were measured at different viscosities. The increase in speed and diameter both indicate a rapid decrease the thickness. Since the hot-film anemometer measured the rate of transfer between the fluid and the probe, the thickness of the viscous

sub-layer measured by this technique will not depend on the diffusivity of the fluid and therefore it is not a function of Schmidt number. The change in the shaft angle showed a minimum thickness of the viscous sub-layer at an angle of 5 degrees to the left which agrees with the results obtained by the electro-chemical technique.

8.5 MATHEMATICAL CORRELATION

The experimental results of the thickness of the viscous sub-layer were subjected to regression analysis and the correlation obtained was:-

$$\left(\frac{\delta v}{d}\right) = 6.425 \left(\frac{\rho N d^2}{\mu}\right)^{-0.648} \left(\frac{Z_L}{d}\right)^{0.04} \left(\frac{\rho D}{\mu}\right)^{-0.1} \qquad (8.2)$$

and is plotted in Figure 66. From the Figure, it will be noticed that most of the points lie around the theoretical line of slope 1.0 and deviate within ±6.3%. The correlation shows that the ratio of the thickness of the viscous sub-layer to the impeller diameter increases with the increase of Schmidt number and with the liquid depth, while it decreases with increase of Reynolds number. It also shows a decrease in the thickness with increase of the impeller diameter. The effect of the shaft angle was neglected in the correlation since the value of the exponent of the group $\left(\frac{T\cos\alpha}{d}\right)$ was 10^{-5}. Although the shaft angle affects the thickness of the viscous sub-layer, this effect is not proportional, as explained in section (8.3) and there is an optimum angle of 5 degrees to the left where the thickness is minimum. This effect however, cannot be expressed in the correlation. This correlation therefore applies at the optimum shaft angle.

8.6 COMPARISON BETWEEN RESULTS OF THE ELECTRO-CHEMICAL TECHNIQUE AND THE HOT-FILM ANEMOMETER

The measurements obtained from the electro-chemical technique were carried out on the redox solution which had a kinematic viscoisty of 1.39×10^{-2} cm ^{2}/sec. Water was used when the hot-film anemometer was employed. Therefore, there must be a difference in the values of the thickness of the viscous sub-layer obtained by each method since the kinematic viscosity is different in each case. To compare these results, the results obtained from the electro-chemical technique was extrapolated to values at kinematic viscosity of 0.01 cm^2/sec which is the same as the water used for the hot-film anemometer. To obtain the same conditions as those used for each technique, the mathematical correlation obtained from regression analysis was used to obtain the values of the thickness of the viscous sub-layer at $\gamma = 0.01 cm^2$/sec. Comparison between these results and those obtained from the hot-film anemometer for different impeller speeds, impeller diameter, shaft angles and liquid depths are in Tables 97 to 100 and are plotted in Figures 80, 81, 82, 83.

It was noticed that there was an average deviation between the results of about 14.5% depending on the conditions of the system. However, since the correlation obtained had a deviation of ±6.3%, the actual average deviation between both results will be of the order of 11.0%. The results obtained by the hot-film anemometer is therefore 11.0% greater than those obtained by the electro-chemical technique. The reason is that the hot-film anemometer does not detect the effect of diffusion on the thickness of the

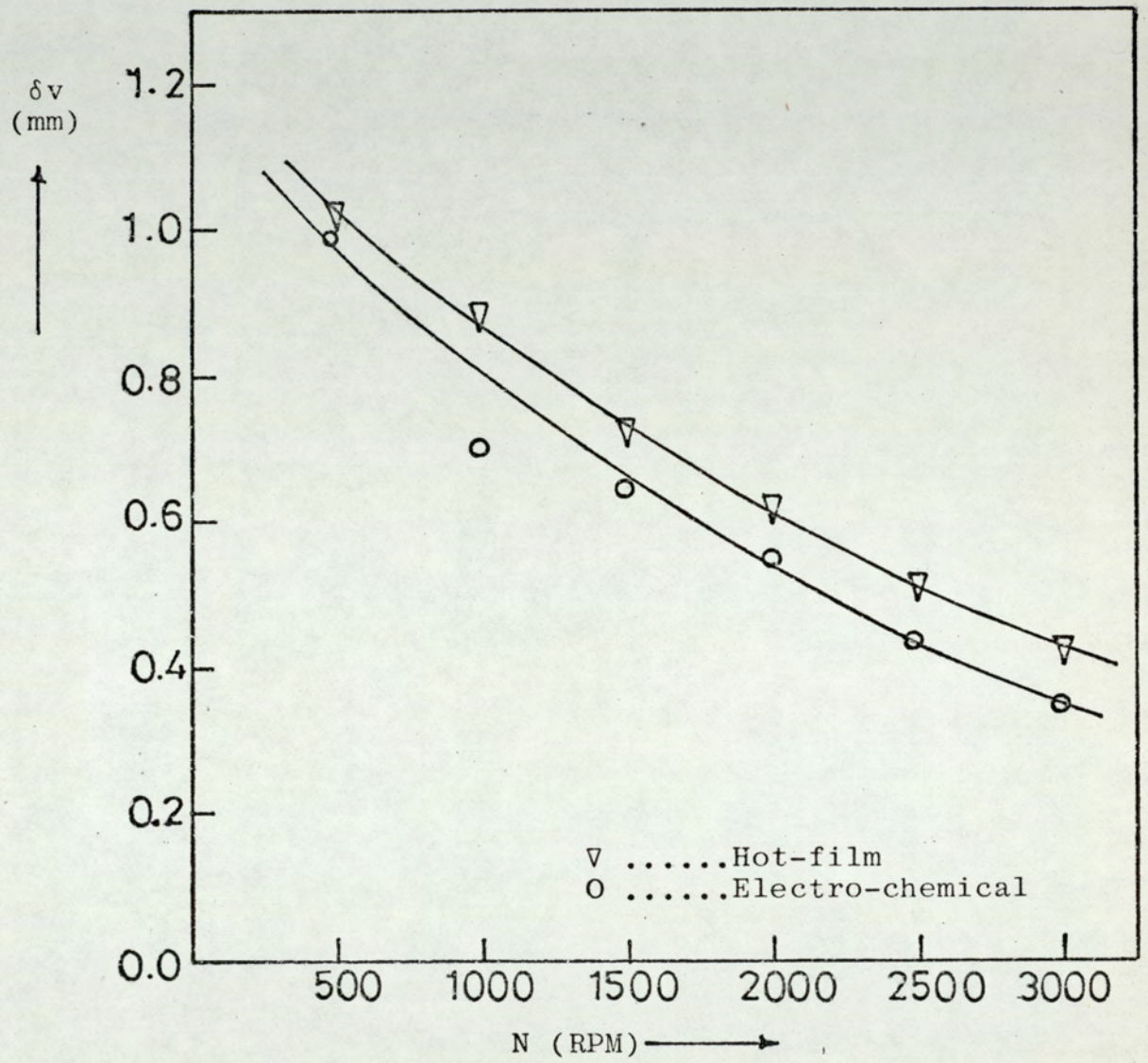

Figure 80 Thickness of the Viscous Sub-layer as a Function of Impeller Speed

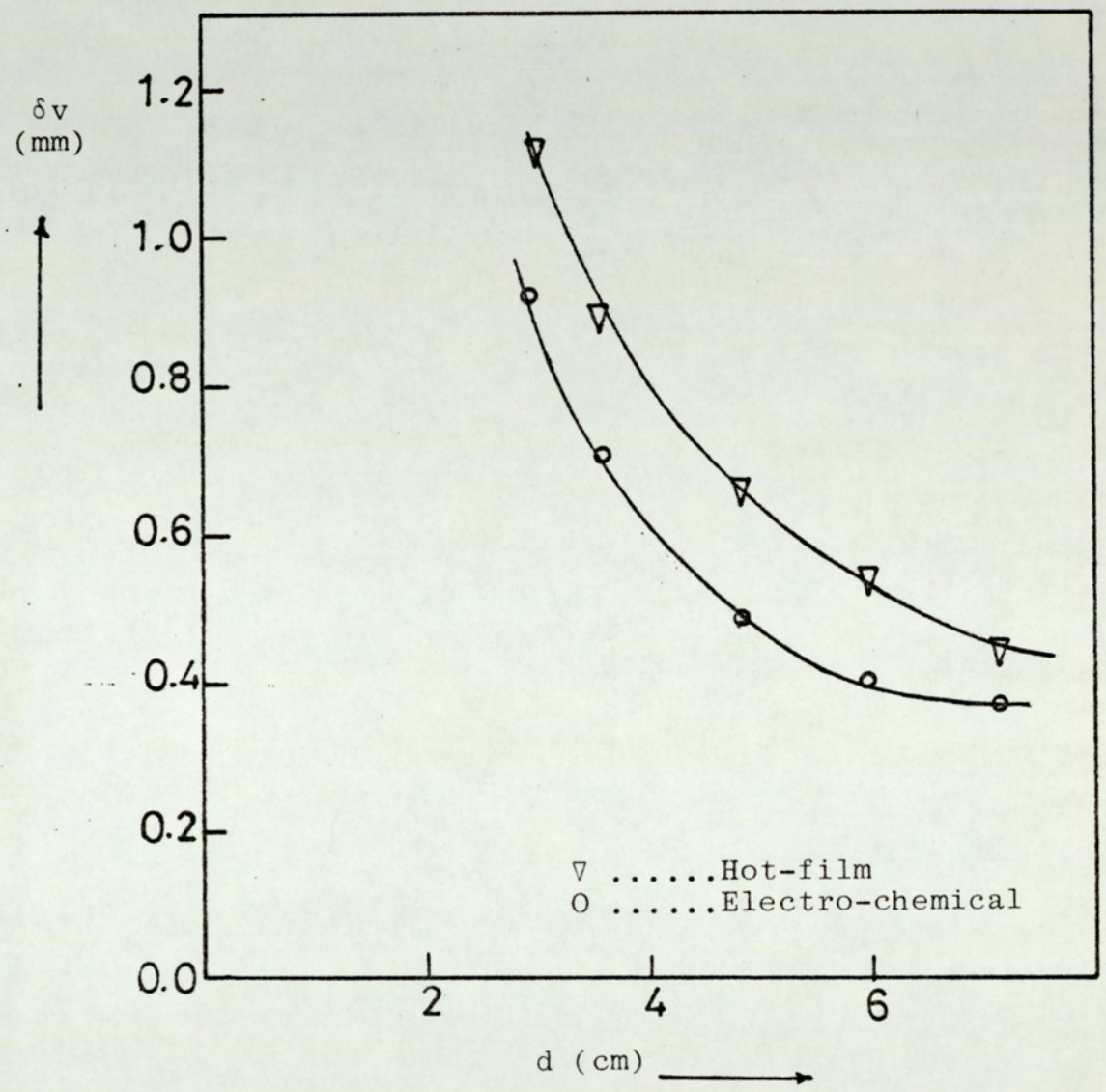

Figure 81 Thickness of the Viscous Sub-layer as Function of Impeller Diameter

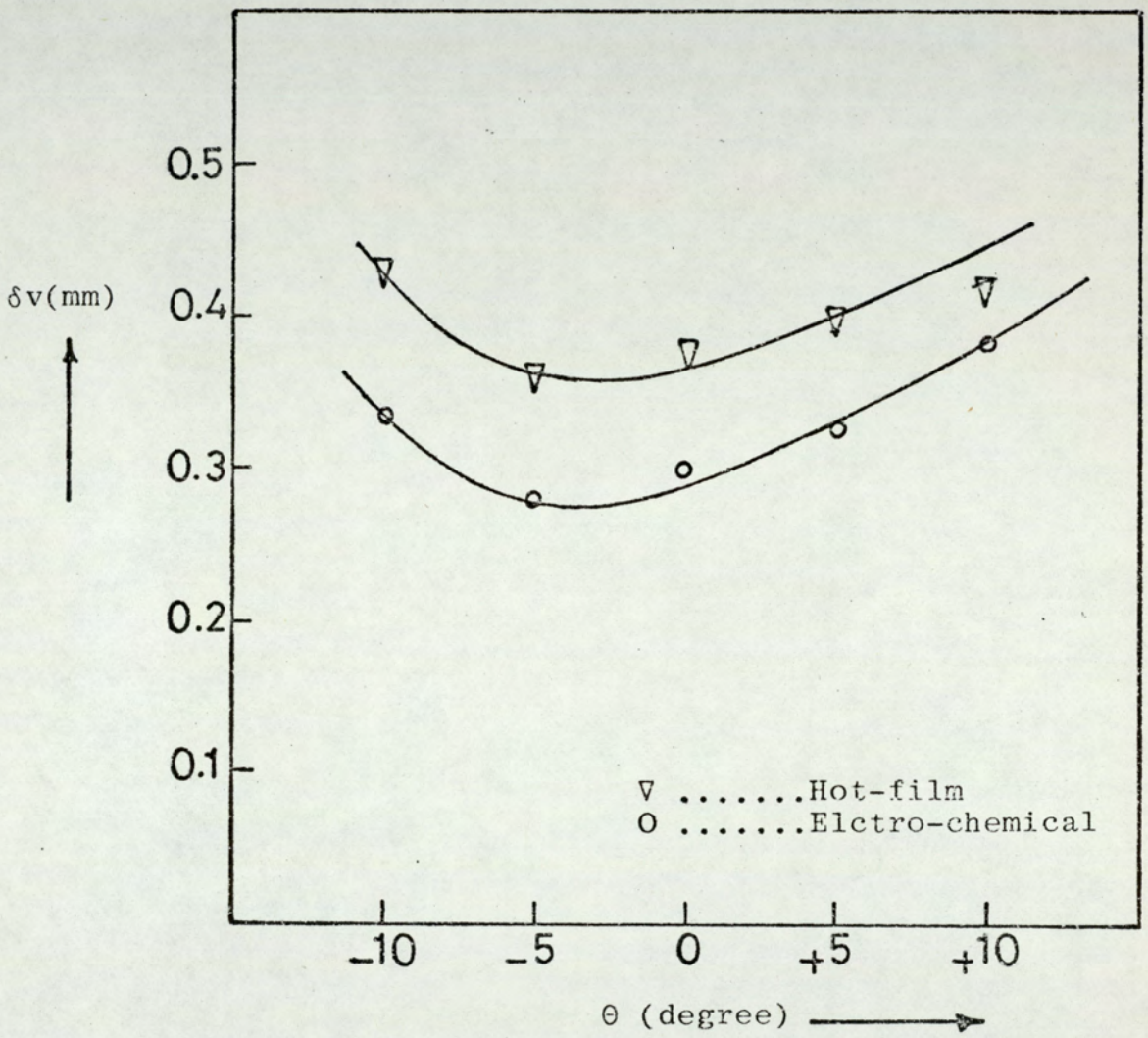

Figure 82 Thickness of the Viscous sub-layer as a Function of Shaft Angle

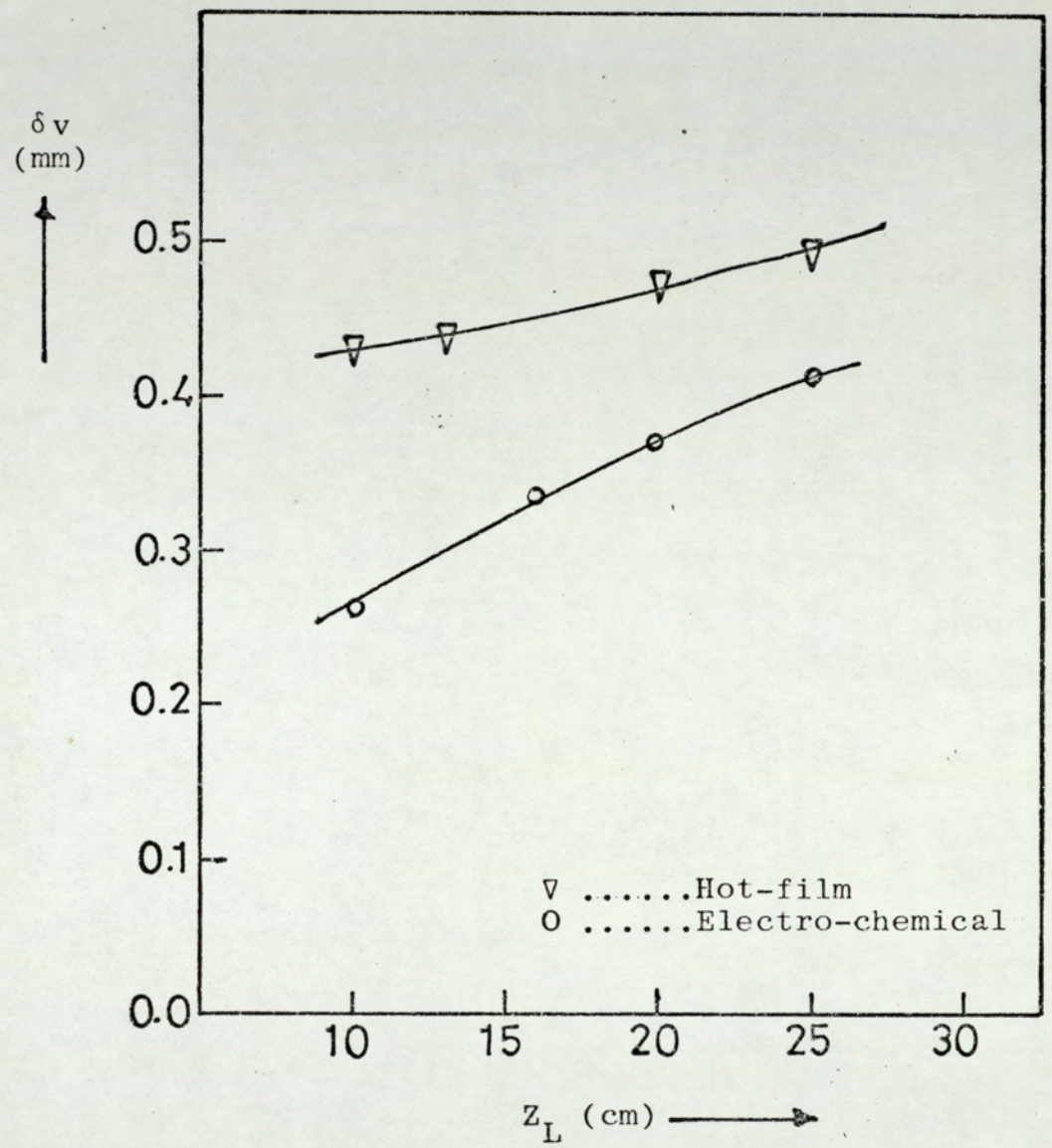

Figure 83 Thickness of the Viscous Sub-layer as a Function of Liquid Depth

viscous sub-layer because it only measures the heat transfer between the fluid and the probe while the electro-chemical technique has the advantage of detecting the diffusion and it depends on a reaction which is diffusion controlled. This will be noticed in the mathematical correlation obtained which shows that the thickness is proportional to $(\frac{\mu}{\rho D})^{0.1}$ so that as the diffusivity coefficient increases, the thickness of the viscous sub-layer decreases. Another limitation of the hot-film anemometer is the disturbances in the viscous sub-layer caused by the introduction of the hot-film probe during measurements. Apart from these limitations, the results obtained by both techniques are in agreement and the curves obtained by both techniques are of the same shape.

8.7 QUALITATIVE RESULTS ON THE DISTRIBUTION OF THE VISCOUS SUB-LAYER

The photographs taken to the sedimentation of paper-pulp solution around the base of the tank enabled the study of the distribution of the viscous sub-layer to be made and shows the flow pattern of the fluid at different shaft angles. Also the use of a small baffle on the base of the tank proved to be effective.

8.7.1 EFFECT OF SHAFT ANGLE AND FLOW PATTERN

Figure 63B is a photograph of the model tank containing paper-pulp which has settled after being mixed with water using a 3.6cm diameter impeller rotating at 2000RPM's and fixed at 10 degrees to the left. It is noticable that the pulp has settled around the centre of the tank while the areas near the tank wall have a very thin layer of pulp. The

distribution of the sediment is mainly affected by the flow pattern produced by the impeller. Since the shaft angle was placed at 10 degrees to the left, the flow pattern produced is a big loop circulating around the tank close to the tank wall. Therefore, the area in the centre has less turbulence which tends to make the sediment shift towards the centre. When the mixer is switched off, the circulation velocity decreases and turbulence dies out quicker in the centre than near the wall leaving the pulp to collect near the centre. Therefore, the thickness of the viscous sub-layer at the area where the pulp is collected is thicker than elsewhere which confirms the results on the effect of the shaft angle on the distribution of the viscous sub-layer.

When the shaft angle was changed from 10.0 degrees to 5.0 degrees, the flow pattern changed too and as a result the distribution of the sediment was different. Figure 63A shows that sedimentation occurs in areas away from the impeller jet and near the tank wall. The flow pattern produced in this will be a jet that travels across the tank and when it reaches the tank wall, divides into two circulating loops. Therefore the sediment collects in the area where the loops existed. Again this is in agreement with the results obtained from the electro-chemical technique.

8.7.2 EFFECT OF THE CRUCIFORM SHAPE BAFFLE

The small cruciform shaped baffle used in the experiments was placed in the area where the pulp sediment collected. Figure 65A and 65B presents two shots of a cine film photographing the process of mixing the pulp solution and the

effect of the existance of the small baffle. The shaft angle was 5 and 10 degrees to the left respectively. It was noticed that when the pulp passed over the baffle, it was lifted into the bulk of the solution. This shows that the baffle helps to mix the pulp with the bulk of the solution. Also, it was noticed that when the mixing process was stopped, the pulp tends to collect in the area where the baffle was placed which infers that beside the mixing effect of the baffle during agitation, it also collects the sediment. This suggests that applying a baffle as a means for location of the zone for removing the sediment. The sedimentation of the pulp on the baffle is shown in Figure 64A

When two baffles were placed on the base of the tank, as shown in Figure 64B, it was found that they both helped to mix the pulp with the solution, but when the agitation was stopped, the pulp collected in the area between the two baffles. This suggests that each of the baffles tends to move the sediment towards the other, resulting in sedimentation of the pulp in between the baffles.

8.8 THEORETICAL ANALYSIS

The mathematical model, representing the flow of fluid from the impeller along the tank consists of a set of first order differential equations which were solved by Runge-Kutta method using a computer program in Appendix (A5) The results of the velocity distribution along the jet are plotted in Figure 67 and 68 shows that the axial velocity of the fluid on the edge of the impeller jet decreases with distance from the impeller. It can also be seen that there is an increase in the jet velocity with increase of the

impeller speed or the impeller diameter. From Figure 69, representing the velocity profile across the jet, it is seen that the velocity is maximum at the jet axis and decreases across the jet to become a minimum at the jet boundries. The profile becomes flatter as the jet distance along the tank increases because the velocity gradient decreases, and turbulence dies out. As a result the amount of entrainment will be reduced. At a distance of 75cm from the impeller tip, the velocity profile becomes a straight line and the velocity is the same across the jet. Thereafter the velocity profile changes in shape and the maximum velocity is found at the jet boundary instead of the jet axis. This happens because the boundary of the jet at this point touches the base of the tank with the result that there will be disturbances in the flow near the base of the tank causing a change in the usual velocity profile.

As the jet travels along the tank, the wall shear stress decreases rapidly for about 30cm from the impeller tip, beyond this it decreases very slow and the curve approaches a straight line, as shown in Figure 70 and 71. , However, an increase in the impeller speed or the impeller diameter results in a corresponding increase in the shear stress. The reason for the rapid decrease of the shear stress with distance, is the decrease in velocity of the jet. As the jet travels along the tank, energy will be dissipated and the effect of the viscosity will be significant. Therefore the thickness of the viscous sub-layer increases accordingly, as shown in Figures 72 and 73 . It is noticed that the increase of the impeller diameter or speed both decrease

the thickness, and this agrees with the experimental results obtained.

Figure 72 shows an increase in thickness from .28mm at a distance of 20cm to 0.66mm at a distance of 120cm when a 3.6cm diameter impeller is rotating at a speed of 3000RPM. This gives an average thickness of 0.433mm along the impeller jet. The experimental results using the electro-chemical technique gives a value of 0.427mm thickness when using the same conditions in the systems which confirms that the agreement is good. Moreover, when selective points in the tank were taken for comparison of the theoretical and experimental results good agreement was obtained. For instance, electrode number 20, 14 6 and 3 gave thickness of 0.22, 0.34, 0.55 and 0.7mm respectively corresponding to distances of approximately 20, 40, 80 and 110 cm from the impeller. The theoretical values of the thickness at these distances are: 0.25, 0.36, 0.54 and 0.64mm. However, the theoretical results does not show the effect of both the liquid depth or the shaft angle since it only covers the area of the jet and remains nearly the same until it touches the tank wall where the flow pattern starts to change.

8.9 79M TANK AND SCALE UP

The thickness of sludge built up during sedimentation was calculated using Stokes law. It was assumed that the particles were spherical and the size of the particles was measured from photographs through the microscope. The average particle was 100 μm in diameter. It was then assumed that settling velocity was constant throughout

the tank.

Figures 76A and 76B show the distribution of the viscous sub-layer and the distribution of sludge at steady state.

From these figures it will be seen that the areas where the impeller jet projected the viscous sub-layer is very thin compared to those away from the jet. This would be expected and agrees with the results of the model tank obtained using the electro-chemical technique. This confirms the effect of the flow pattern on the distribution of this layer. When Figure 76A and 76B are compared, there in an increase in the thickness of the viscous sub-layer at higher oil depths suggesting that the increase in liquid depth increases the thickness of the viscous sub-layer. This, again, agrees with the results of the model tank.

The ratio of the average thickness of the viscous sub-layer in the area of the impeller jet for the 79m tank and the 1.2m tank is about 15.0. This ratio agrees with that obtained from the mathematical model. Also when comparing the average thickness of the viscous sub-layer of the 79m tank to that of the 60cm tank, where both have the same (T/Z_L), the ratio of their thickness is 12.0, and since the ratio of liquid depth in both tanks $(\frac{Z_L \text{ large}}{Z_L \text{ small}})$ is equal to 12.0, the following approximate scale up rule could be useful:

$$(\frac{\delta_{\text{large}}}{\delta_{\text{small}}}) = (\frac{Z_{L \text{ large}}}{Z_{L \text{ small}}}) \quad \text{for constant} \quad (T/Z_L) \qquad (8.3)$$

CHAPTER IX

9 CONCLUSIONS

1. The increase of the impeller speed and the impeller diameter both minimize the thickness of the viscous sub-layer and there is a certain limit above which it is not economical.

2. Although there is an optimum shaft angle of 5 degrees to the left where the thickness of the viscous sub-layer is minumum, the relation with liquid depth gives a complex relationship and both affect the flow pattern.

3. The thickness of the viscous sub-layer measured by the electro-chemical technique is a function of the diffusion coefficient of the solution employed, while the hot-film anemometer does not detect this effect. It is therefore suggested that provided the Schmidt number can be evaluated, the electro-chemical technique affords a suitable method for estimating the thickness of the viscous sub-layer which can be inserted into the dimensional correlation to evaluate scale-up.

4. The small cruciform shaped baffle could be used as a method of minimizing the thickness of the viscous sub-layer since it tends to lift the sediment to the bulk of the solution before settling down on the base of the tank.

5. The velocity along the impeller jet can be estimated by a mathematical model from which the thickness of the viscous sub-layer can be calculated. The amount of fluid entrained into the jet could be calcuated on the assumption that the momentum at any point along the jet is constant.

6. The thickness of the viscous sub-layer increases in areas away from the jet and these depend on the flow pattern in the tank.

7. The electro-chemical technique is suitable to study mixing in tanks and to study the thickness of the viscous sub-layer, and the results obtained are in agreement with those obtained by the hot-film anemometer.

CHAPTER X

10 RECOMMENDATIONS FOR FUTURE WORK

1. Studies of the power consumptions during mixing at the optimum parameters that gives minimum thickness of the viscous sub-layer.

2. Studies on the effect of different types of mixers, number of mixers and the height of the mixer from the bottom of the tank, on the thickness of the viscous sub-layer.

3. Quantitative studies on the effect of the cruciform shaped baffles on the thickness of the viscous sub-layer.

APPENDIX 1

Technical Aspects of the Anemometer

APPENDIX 1

TECHNICAL ASPECTS OF THE ANEMOMETER

A1.1 DISTURBING EFFECTS

A1.1.1 AIR BUBBLES

In measuring the velocity of liquids using the hot-film anemometer, the presence of dissolved gasses in the liquid may cause an irregular drift to the calibration curve. This is due to the formation of bubbles on the heated sensor. As long as the hot sensor is at a higher temperature than the liquid, bubbles will continue to form unless the sensor is cleaned while the anemometer is in the stand-by condition. However, the hot sensor will then attain the temperature of the environment. An alternative way is to keep the water stationary for a certain time so that air bubbles and dirt particles will have time to escape.

Rasmussen (110) found that local super saturation of the water resulting from heating the sensor does not result in bubble formation unless microscopic air bubbles already exist in the liquid and the size of these bubbles exceed a certain threshold value which is determined by surface tension and sensor over heating.

By removing some of the air an under saturated solution will be obtained which will prevent bubble formation for a certain excess temeprature. This could be accomplished by boiling the water or by degassing using a vacuum, since the saturation concentration is proportional to the partial pressure (110). However, the dissolved gas concentration decays exponentially with time and is rather slow if the fluid is stationary. Therefore, the degassing process

should be accelerated by high-frequency vibration (110) or by vigorously shaking the solution.

Bubbles grow only if their initial radius is greater than a certain threshold value and bubbles smaller than this value will shrink and dissolve. Observations under a microscope (110) have shown that if a bubble of sufficient size hits the hot sensor, it will grow until it is large enoughto be sheared off by the stream.

A1.1.2 FLUID TEMPERATURE

Since the heat transfer from the sensor is proportional to the temperature difference between fluid and sensor, any change in fluid temperature will cause a change in bridge voltage leading to a misinterpretation of the signal taken from the anemometer. Also the change in the fluid temperature will change the thermal properties of the fluid causing another error in measurements. Although the variation in thermal properties is very small in air, it is of significant importance when dealing with liquids such as water.

The most accurate method of compensation consists of calibrating the anemometer over the temperature range required during measurements and this can be accomplished by measuring temperature with velocity. A second method, which may be used with some accuracy consists in keeping the over-heating constant using a compensating sensor connected to the anemometer. Bearman (112) derived a formula to correct the hot-wire anemometer results for the affect of ambient temperature drift. The correction formula was based on the assumption that the flow properties around the wire are related to the wire surface

temperature. Alternatively, Kanena and Oka (111) derived a formula for the correction of temperature effect for small velocities, the range over which the correction is valid is dependent on probe design. and on the temperature range in which calibration is carried-out.

A1.1.3 SENSOR CONTAMINATION

The deposition of dirt and chemicals on the sensor may cause substantial changes in the flow sensitivity due to the changing conditions of heat transfer, and by reducing the frequency response. This also depends on the type of flow under measurement . For low velocities the heat transfer is only slightly affected by dirt, while at higher velocities, the heat transfer decreases causing a decrease in flow sensitivity. Although the depostion of dirt increases with increasing velocity; because of the possibilities of a greater number of particles contacting the sensor during any time interval, turbulent flow serves to clean the probe. It was also found that the influence of dirt increases with decreasing wire diameter since the thermal insulation provided by a deposit of a given thickness increases with decreasing perimeter of the covered body (113).

A1.2 DETERMINATION OF OVER-HEATING

The over-heating could be determined on the basis of the individual data of the probe to be used. It has been recommended (113) that a high value of over-heating is applied in order to obtain optimum sensitivity, a high signal-to-noise ratio, and a large output signal. The limitations are the imposed maximum permissible sensor temperature and the specific nature of the measurements.

The following formula (113) is used to calculate the sensor resistance existing at the operating temperature by substituting the probe data:

$$R_1 = R_{Tot} + a_{20} R_{20} (T_{es} - T_{eo})$$

A1.3 EARTH CONNECTION

Correct earthing of the anemometry measuring system is of great importance in protecting the probe from damage due to excessive voltage between it and the conducting medium to be measured. This hazard can be eliminated by carefully earthing both the anemometer and the flow medium and connecting by the circuit shown in Figure (A1.1A) All plug-and-socket connections under water must be sealed carefully. Any ingress of water will tend to cause unstable operating conditions, which might result in destruction of the probe. It is also important that the body of the probe be insulated from earth as a direct short-circuit between both ends of the probe cable shielding can introduce unstability in the system.

Occasionally a ripple in the voltage between the earth points may cause a flow of current through the probe cable shielding that will interfere with the measurements. An attempt may then be made to earth the probe body directly. However, this requires that the earth connection of the anemometer and the earth connection of any auxilary instruments in the set up to be broken (115). Figure (A1.1B) shows a diagram of the proper earthing.

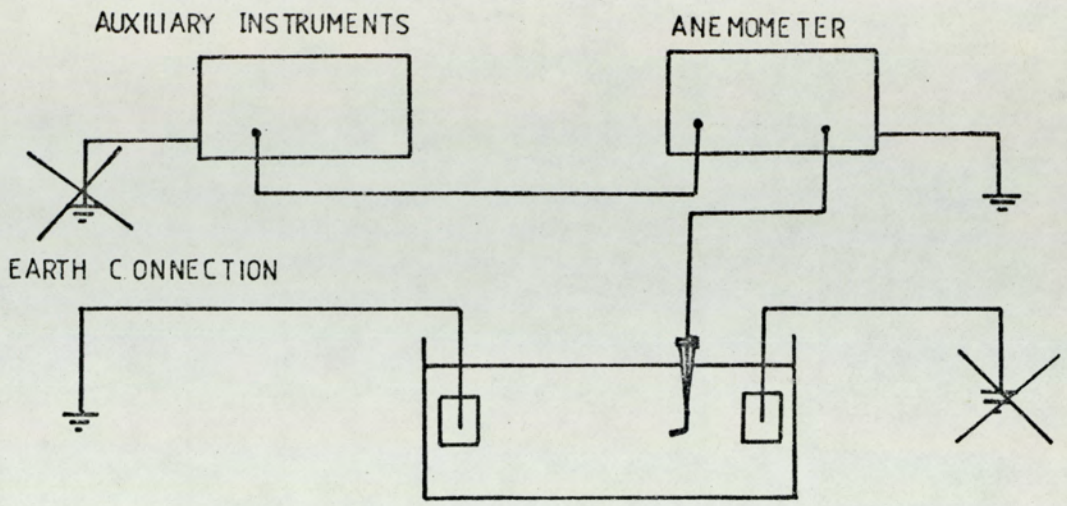

(A)

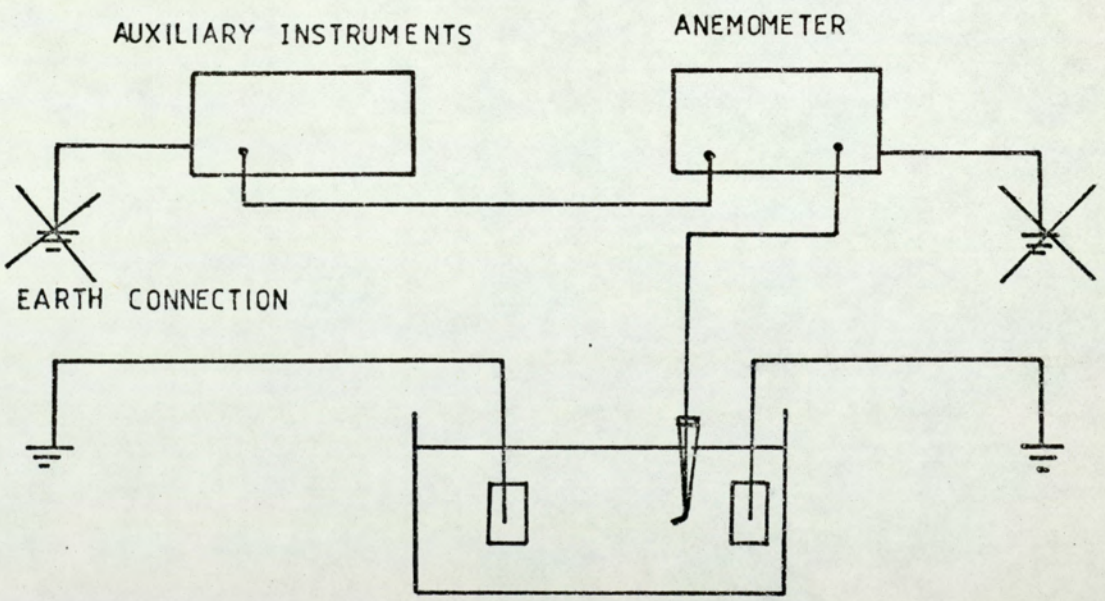

(B)

FIGURE_A1.1_EARTH CONNECTION OF THE ANEMOMETER

APPENDIX 2

A study on changing the viscosity and density of the solution separately

APPENDIX 2

A study on changing the viscosity and density of the solution seperately.

In studying the effect of the system parameters on the viscous sub-layer, the physical properties of the solution used are of great importance. These are the density and viscosity and therefore the effect of each of these properties must be studied seperately. To achieve that, a specific system must be prepared where-by the viscosity of the solution could be changed without changing the density and visa-versa. Many experiments were performed using different chemicals in an attempt to change one of the properties while keeping the other constant.

The first attempt was to add different percentages of sodium chloride (NaCl) to the redox system used in the electro-chemical technique. Results of this experiment are presented in Table A1.1.

Figure A2.1 represents a plot of the viscosity of the solution as a function of the percentage of sodium chloride added to the redox system. The curve obtained indicates an increase in the viscosity with increase of sodium chloride added. The viscosity increased from 1.48×10^{-2} gm/cm sec at pure redox solution to a value of 2.6×10^{-2} gm/cm sec when 22% NaCl was added. Further increase of NaCl above 22% make the solution saturated. The corresponding change of the density is shown in Figure A2.2 where the density was plotted against percentage NaCl added. A straight line

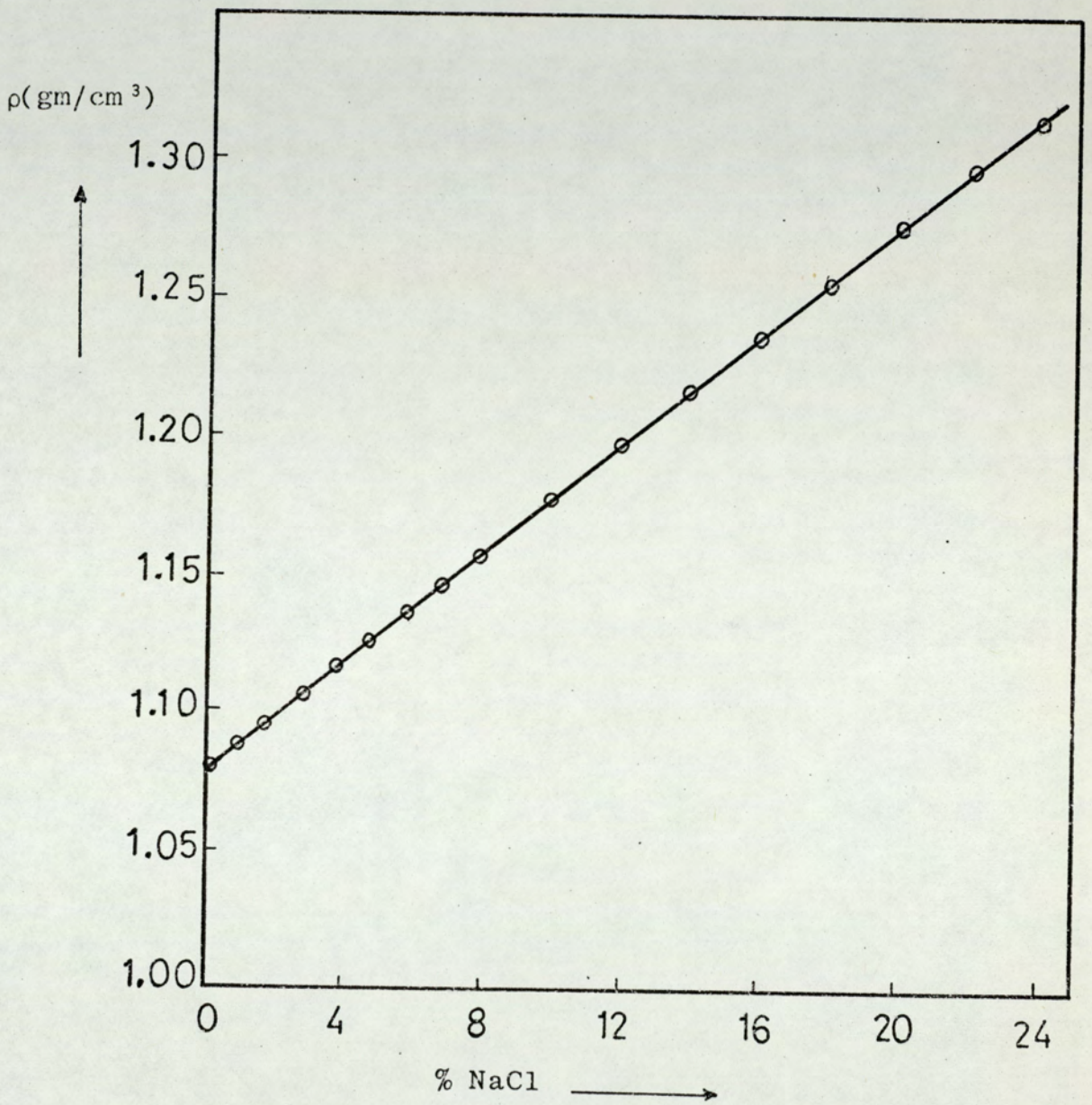

Figure A2.2 Density of the solution as a function of percentage NaCl added.

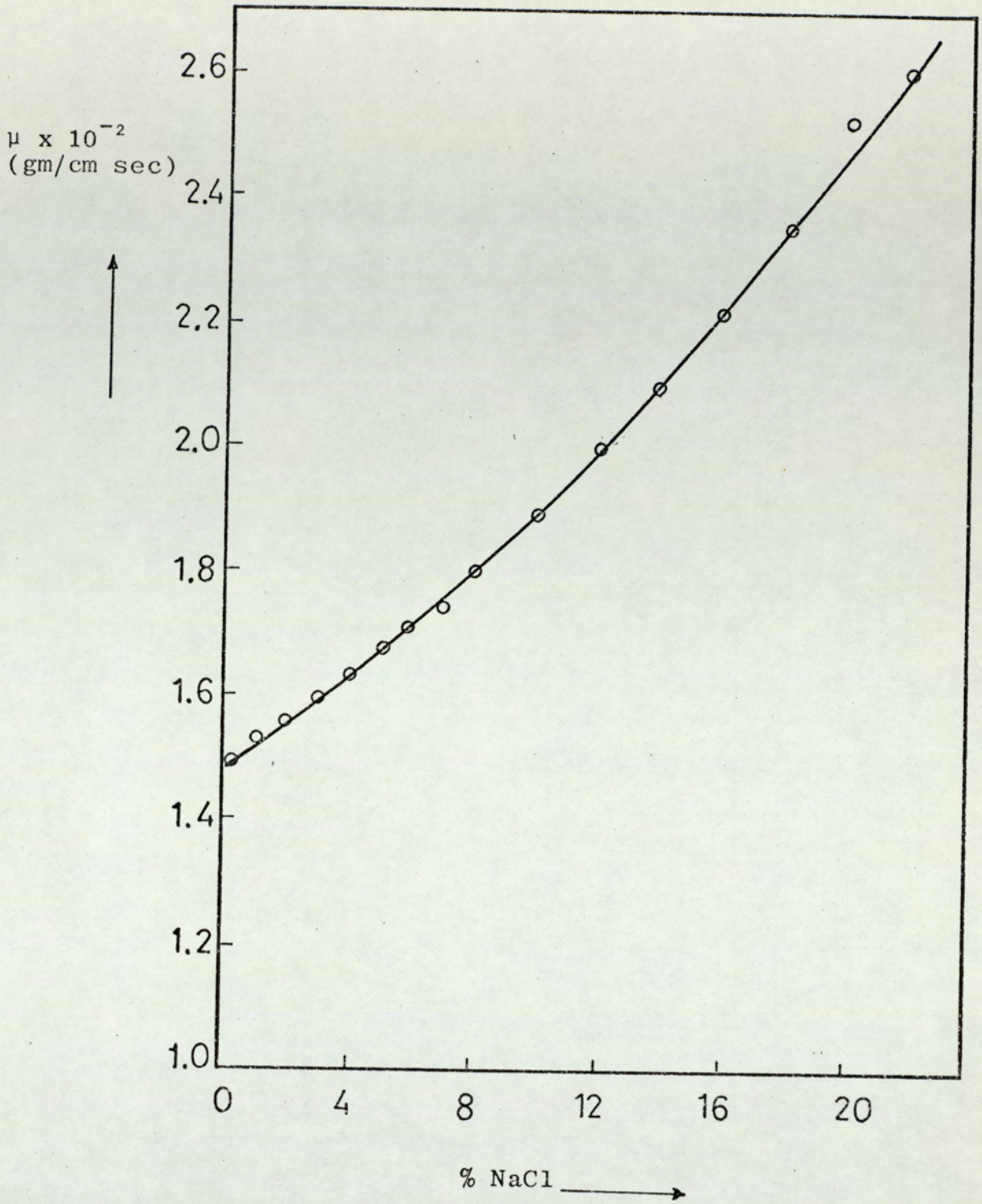

Figure A2.1 Viscosity of the solution as a function of percentage NaCl added.

of slope 0.8 was obtained indicating an increase of density with increase of percentage NaCl added. The density was changed from 1.08 gm/cm^3 for pure redox solution to 1.295 gm/cm^3 at sodium chloride percentage of 22.

Since the sodium chloride increased both the density and viscosity, ethanol was added to the redox-Nacl solution to reduce its density. The results are given in Tables A2.2 to A2.4. Figure A2.3 presents a plot of the viscosity of the mixture against the percentage of ethanol added to a solution of different NaCl concentrations. The graph shows an increase in viscosity with increase of amount of ethanol added for the different concentrations of NaCl present in the solution. The viscosity changes from 1.48 x 10^{-2}gm/cm sec at 0% ethanol to 2.96 x 10^{-2}gm/cm sec at 35% ethanol for NaCl-free solution, while it changes from 2.72 x 10^{-2}gm/cm sec at 5% ethanol to a value of 2.98 x 10^{-2}gm/cm sec at 10% ethanol for a 20% NaCl solution. There was a corresponding decrease in density with the increase of percentage ethanol added to solutions of different concentrations of sodium chloride as in Figure A2.4. Therefore, it was possible to select certain combinations of ethanol and sodium chloride in the solution when it is possible to change one property while keeping the other constant. The combination was tried on the test channel, before applying it to the model tank, using the electro-chemical technique, and it was found that the ethanol present in the solution caused a precipitation and change in colour. Hence Gum Arabic was used to increase the viscosity with only a small change in density. The results are given in Table A2.5. Figure A2.5 represents a plot of the viscosity of the solution against the percentage of Gum Arabic added. The curve gives a fair

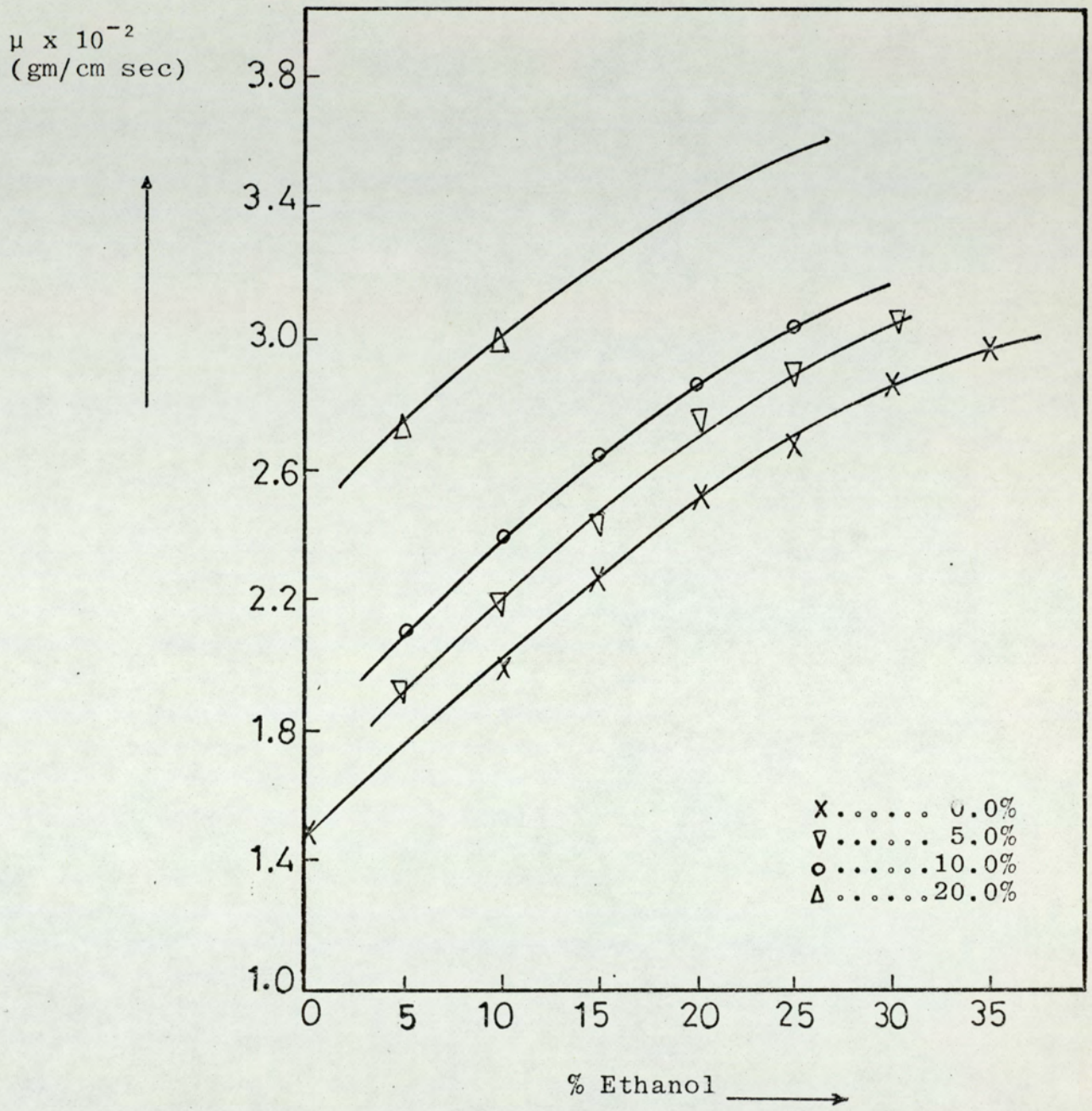

Figure A2.3 Viscosity of the solution as a function of percentage ethanol added for different percentage of NaCl present in the solution.

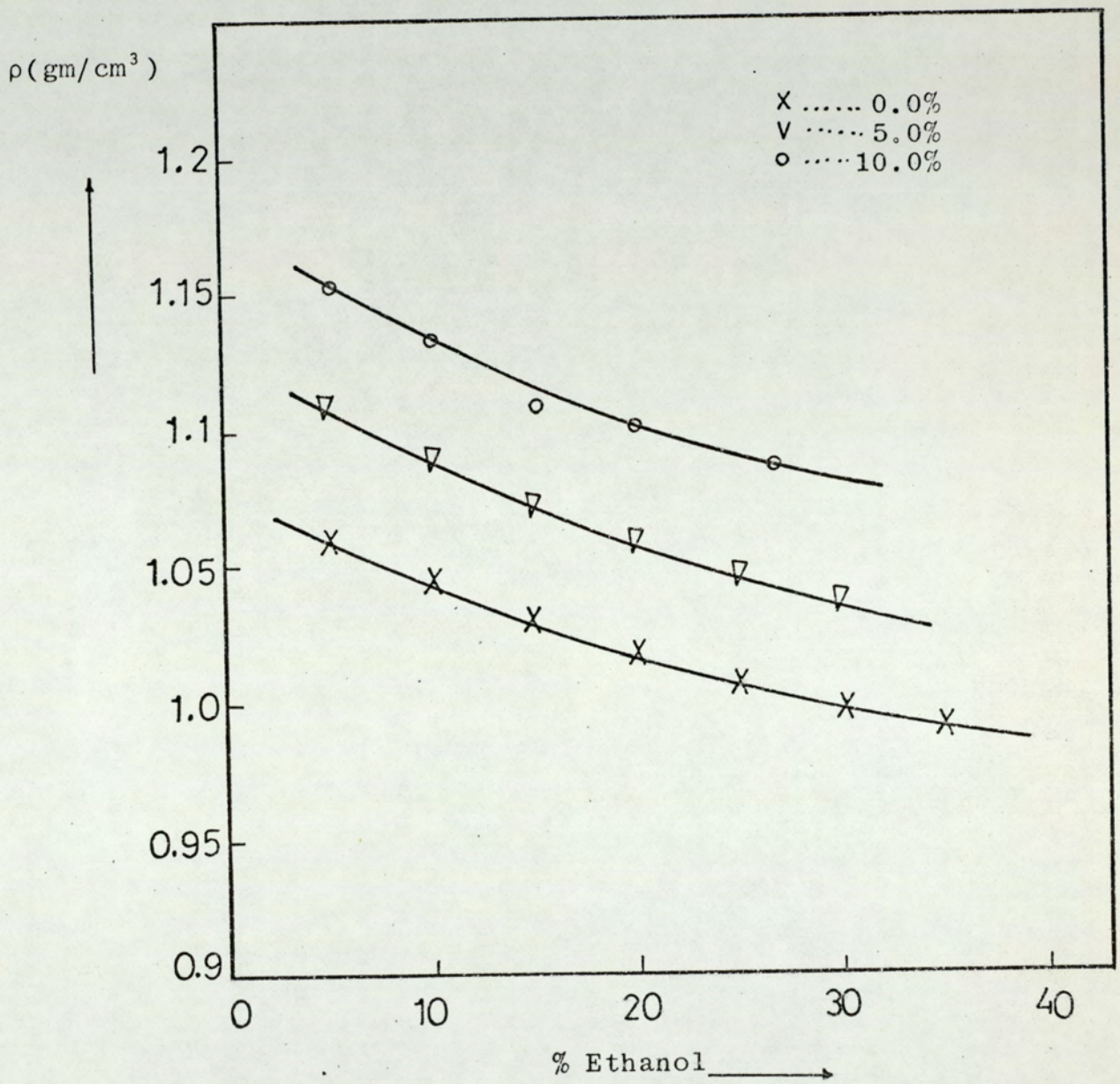

Figure A2.4 Density of the solution as a function of percentage ethanol added for different percentages of NaCl present in the solution

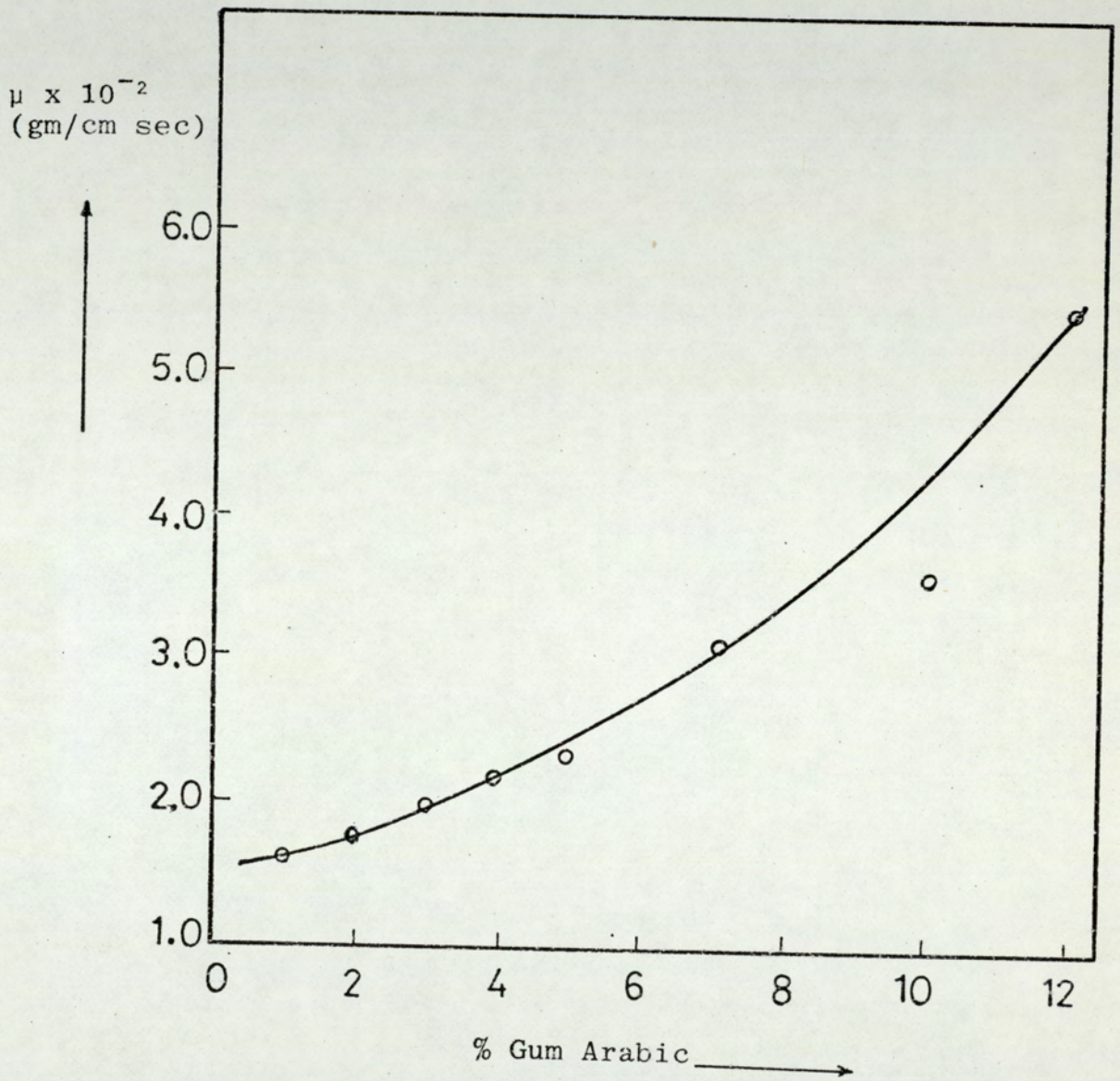

Figure A2.5 Viscosity of the solution as a function of percentage Gum Arabic added.

increase in viscosity from 1.6 x 10^{-2} gm/cm sec at 0.5% gum to 5.45 x 10^{-2} gm/cm sec at 12% gum. Apart from an increase in density of about 7% it was found that using the Gum Arabic for experiments in the model tank is uneconomical due to the large quantity of solution required in the model tank. Therefore this chemical was changed with a cheaper one which gave a large change in the viscosity. The chemical chosen was polyetheylene oxide. Adding 1% of polyethylene oxide gave a viscous solution of 15.0 x 10^{-2} gm/cm sec as shown in Figure A2.6 where the viscosity of the solution was plotted aginst the percentage of polyetheylene oxide added. Using this chemical, a very slight change in density occurs. Therefore it was chosen to change the viscosity with only a very slight change in density.

Following this it was necessary to change the density keeping the viscosity constant. This was accomplished by adding sodium chloride and sodium hydroxide of different concentrations to the solution. Since the redox has already a certain concentration of sodium hydroxide, increasing the concentration will not effect the system since it was used as an indifferent material. Figure A2.7 represents a plot of the viscosity of the solution against the percentage of sodium chloride added for different concentrations of sodium hydroxide in the solution. The curves show an increase of the viscosity with the increase of percentage of sodium hydroxide and sodium chloride respectively. The corresponding densities were plotted in Figure A2.8 where the density is plotted against the percentage of sodium chloride added for different concentrations of sodium hydroxide. The graph is a series of straight lines of 0.7 slopes and indicates a linear increase of the

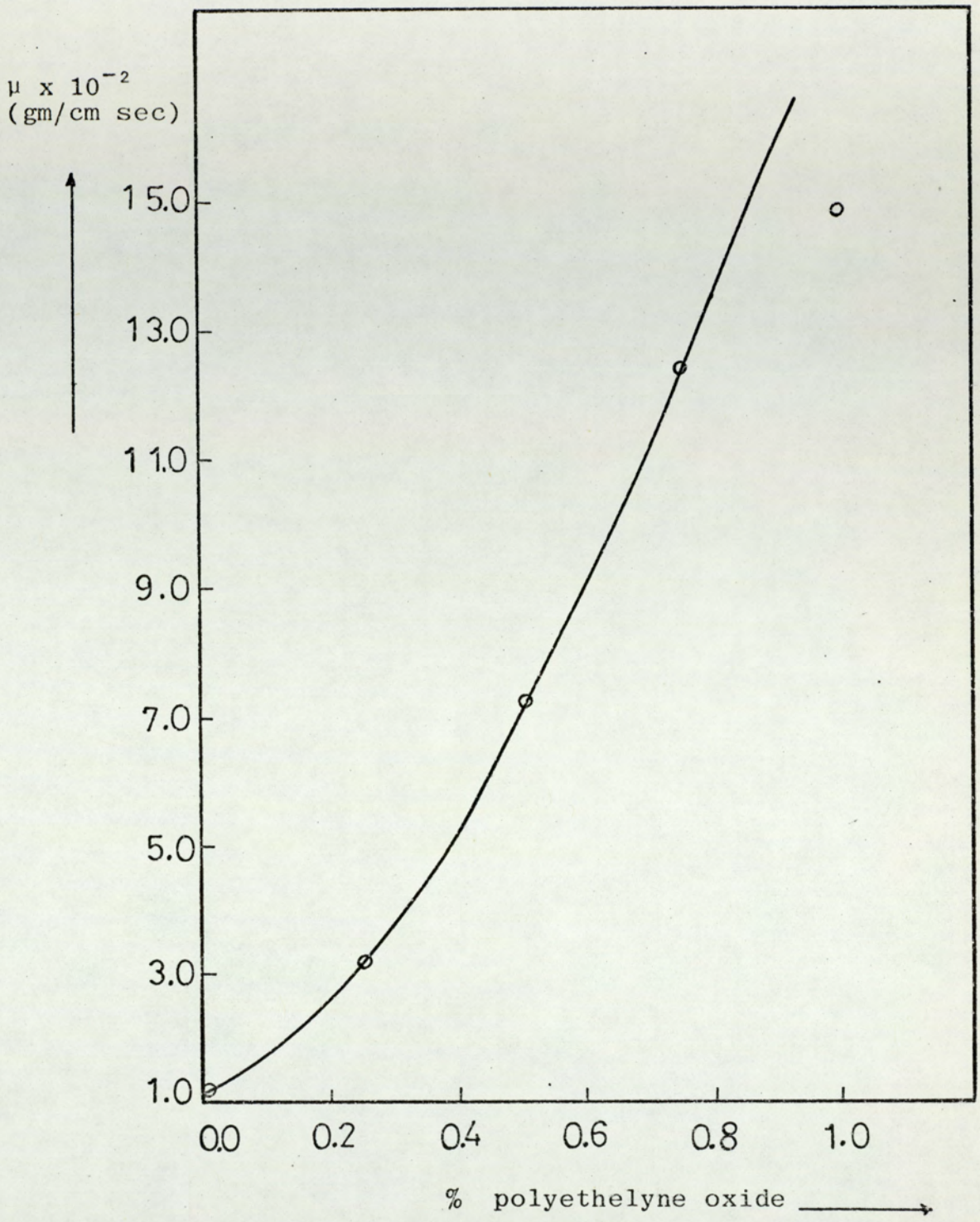

Figure A2.6 Viscosity of the solution as a function of percentage polyetheylene oxide.

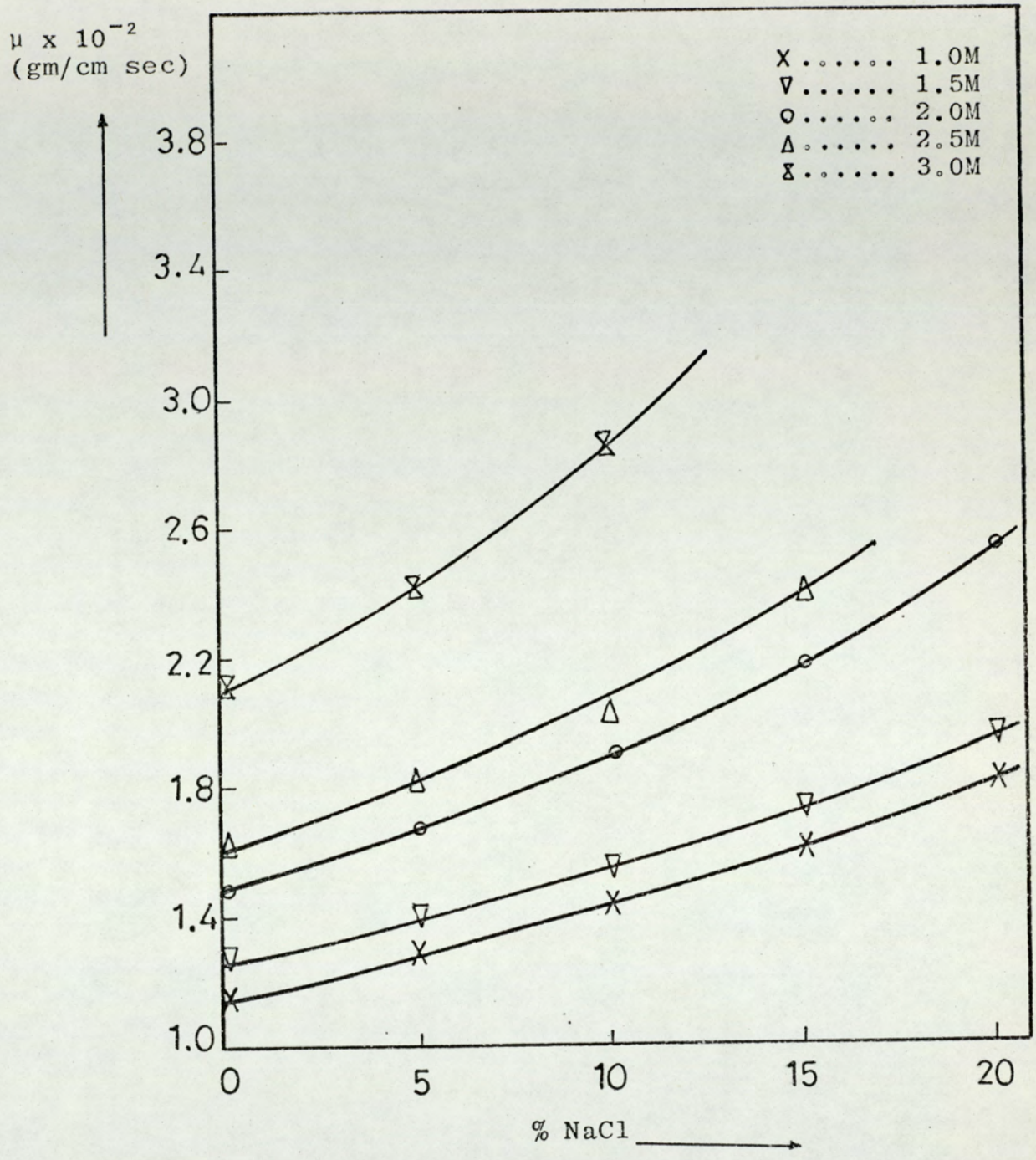

Figure A2.7 Viscosity of the solution as a function of percentage NaCl for different concentrations of NaOH

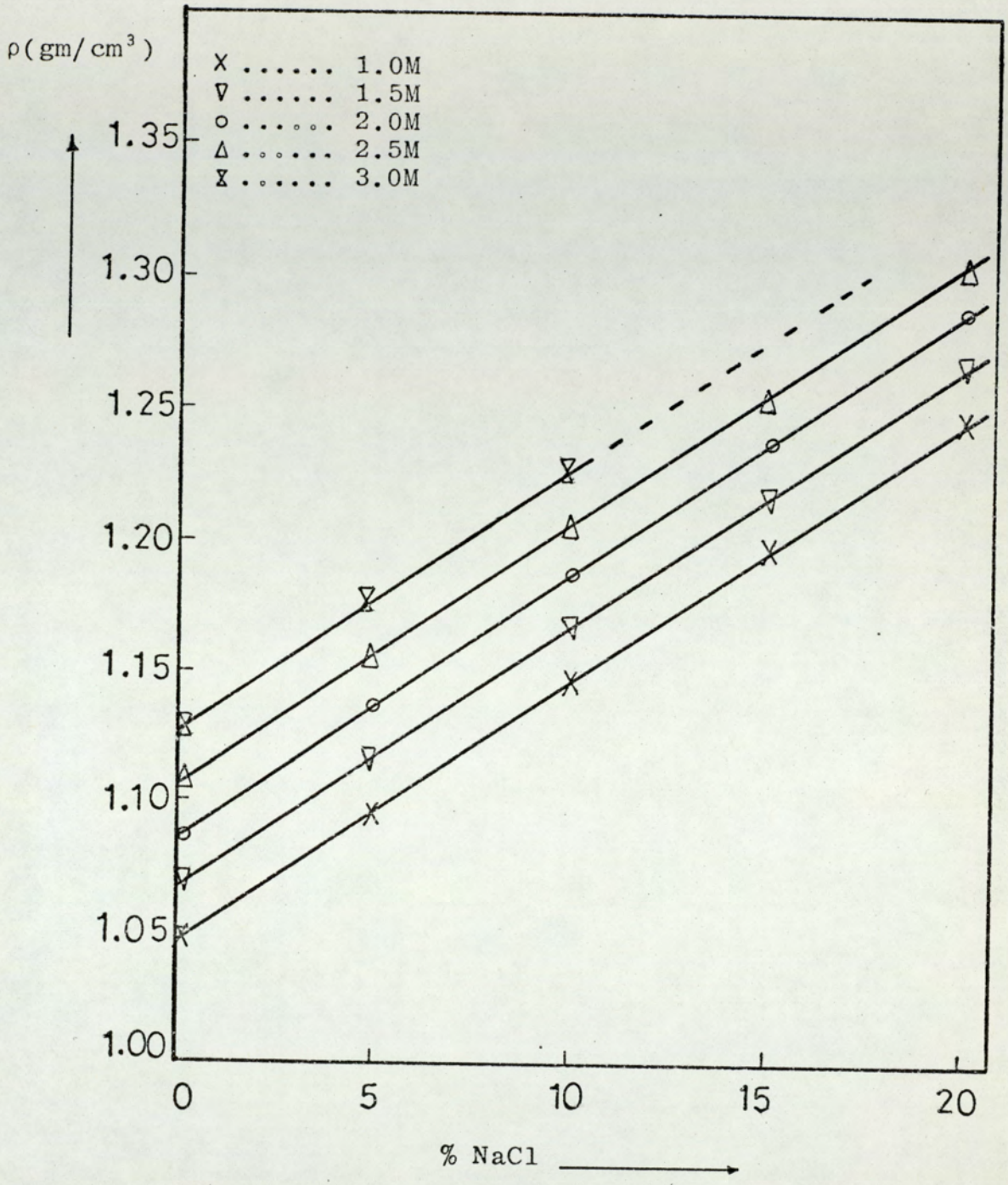

Figure A2.8 Density of the solution as a function of percentage NaCl added for different concentrations of NaOH

density with the increase of concentration of both sodium hydroxide and sodium chloride. Therefore, it was possible to choose certain concentration combinations of sodium hydroxide and sodium chloride which give different densities while maintaining almost the same viscosity. Table A2.8 shows the combination.

APPENDIX 3

Derivation of the dimensionless correlation and the evaluation of its coefficents using mulitple regression analysis.

APPENDIX 3

Derivation of the dimensionless correlation and the evaluation of its coefficients using mulitple regression analysis.

A3.1 DIMENSIONAL ANALYSIS

The effect of the various parameters of the system on the thickness of the viscous sub-layer has been studied seperately and each of the parameters showed a certain behaviour. To express the effect of all these parameters together in one correlation, it is necssary to derive a dimensionless correlation in which all the parameters are arranged in dimensionless groups. Dimensional analysis was used to correlate the thickness of the viscous sub-layer as a function of the impeller speed, impeller diameter, liquid depth, tank diameter, physical properties of the fluid.

Therefore:

$$\delta = \emptyset\ (N, d, Z, T\cos\alpha, \rho, \mu, D) \qquad (A3.1)$$

or

$$\delta = C(N)^a\ (d)^b\ (Z)^c\ (T\cos\alpha)^d\ (\rho)^e\ (\mu)^f\ (D)^g \qquad (A3.2)$$

The dimension of each term may be expressed in terms of mass, length, and time units, and by equating the exponents of mass, length, and time respectively, the following is

obtained:

$$(L) = (\frac{1}{T})^a (L)^b (L)^c (L)^d (\frac{M}{L^3})^e (\frac{M}{LT})^f (\frac{L^2}{T})^g \qquad (A3.3)$$

Therefore:

$$M : o = e + f$$

$$L : 1 = b + c + d - 3e + f + 2g$$

$$T : o = -a - f - g$$

Therefore:

$$e = a + g \qquad (A3.4)$$

$$f = -a - g \qquad (A3.5)$$

$$b = 1 - C - d + 2a \qquad (A3.6)$$

Substituting equations (A3.4, A3.5, A3.6 into equation A3.3 gives:

$$\delta = C(N)^a \ (d)^{1-C-d+2a} \ (Z)^c (T\mathrm{Cos}\alpha)^d (\rho)^{a+g} (\mu)^{-a-g} (D)^g \qquad (A3.7)$$

Rearranging the terms equation (A3.7) gives:

$$(\frac{\delta}{d}) = C(\frac{N\rho D^2}{\mu})^a \ (\frac{Z}{d})^c \ (\frac{T\mathrm{Cos}\alpha}{d})^d \ (\frac{\rho D}{\mu})^g \qquad (A3.8)$$

Since $\frac{N\rho D^2}{\mu} = N_{Re}$

and $\frac{\mu}{D\rho} = N_{sc}$

Therefore, equation (A3.8) can be written as follows:

$$\left(\frac{\delta v}{d}\right) = C(N_{Re})^{a} \left(\frac{Z}{d}\right)^{c} \left(\frac{T\cos\alpha}{d}\right)^{d} (N_{sc})^{h} \qquad (A3.9)$$

where $h = -g$

Equation (A3.9) is a dimensionless correlation which shows the thickness of the viscous sub-layer as a function of Reynolds number, Schimdt number, tank diameter, and liquid depth.

A3.2 COMPUTER PROGRAM:

The values of the coefficients a, c, d, h and the constant (c) in equation (A3.9) were evaluated by a computer program written in Fortran Language, which was processed on the ICL 1900 statistical analysis package number SDS3/ss available at the University of Aston in Birmingham. The above package makes use of multiple regression analysis to evaluate the values of the coefficients, and gives some statistical details. The program was written as follows:

```
UASTATSXDS3
MULTRGLP
ØBSERVATIØNVMATRIXVVVVVVVVVMATRX1
CØLVNAMESVVVVVVVVVVVVVVVVVVMATRX1
THICKNSPEEDNDIAMIMDIAMTALIQDEPDENSITVISCØSDIFFUSSUBDIE
MATRIXVVVVVVVVVVVVVVVVVVVVVMATRX1
VVF1ORO1V.0451V314.2V3.600V119.5V22.00V1.086V0.05V
```

```
ENDVØFVDATA
TRANSFØRMATIØNSVVVMATRX1VVCHANGEVVVVVVMATRX2
VVTHICKN=THICKN
VVSPEEDN=SPEEDN
VVDIAMIM=DIAMIM
VVLIQDEP=LIQDEP
VVDENSIT=DENSIT
VVVISCØS=VISCØS
VVDIFFUS=DIFFUS
VVSUBDIE=SUBDIE
VVTHICKNØ=ALØG10(THICKN/DIAMIM)
VVGUSSNØ=ALØG10((SPEEDN*DENSIT*DIAMIM**2)/(VISCØS))
VVDIAMNØ=ALØG10(DIAMTA/DIAMIM)
VVDEPTNØ=ALØG10(LIQDEP/DIEMIM)
VVPATRNØ=ALØG10(DENSIT*DIFFUS*SUBDIE/VISCØS)
CRØSSVPRØDUCTVVVVVVVVVVVVVVMATRX2
CØVARIANCEVVVVVVVVVVVVVVVVMATRX2
CØRRELATIØNVVVVVVVVVVVVVVVVMATRX2
PRINTVMEANSVVVVVVVVVVVVVVVVMATRX1VVLPVVVS
PRINTVMEANSVVVVVVVVVVVVVVVVMATRX2VVLPVVVS
PRINTVCØRRELATIØNVVVVVVVVVMATRX2VVLP
REGRESSIØNVANALYSISVVVVVVVMATRX2VVVVVVVVCØVA
DEPENDANTVVARIABLEVVVVVVVTHICKNØ
INDEPENDENTVVARIABLESVATVSIGVLEVELVV99.00
VVGUSSNØDIAMNØDEPTNØPATRNØ
PRINTVREGRESSIØNVLP
GETVØFF
****
```

APPENDIX 4

Calculation of the thickness of the viscous sub-layer

APPENDIX 4

Calculation of the thickness of the viscous sub-layer

A4.1 HANRATTY'S MODEL

In the electo-chemical technique, the limiting current measured by applying a certain potential, is a direct measure of the mass transfer coefficnet since the reaction is diffusion-controlled. Therefore:

$$K = \frac{I}{C_b nAF} \qquad (A4.1)$$

Hanratty (54) developed a model where by he related the mass transfer coefficient to the velocity gradient at the wall, assuming that the flow is uniform over the electrode surface and the concentration boundary-layer thickness is less than the viscous sub-layer thickness. Also assuming that the fluid properties are constant and from the mass balance of ferricyanide he obtained the following equation:

$$\frac{\delta c}{\delta t} + v\frac{\delta c}{\delta y} + U_\ell \frac{\delta c}{\delta \ell} = D\left(\frac{\delta_2 c}{\delta y^2} + \frac{\delta_2 c}{\delta \ell^2} + \frac{\delta_2 c}{\delta m^2}\right) \qquad (A4.2)$$

By simplification and solving the above equation, he obtained this final solution:

$$K = \frac{3}{2\cdot\Gamma(4/3)\,(9)^{1/3}} \left(\frac{D^2 S}{0.82\,de}\right)^{1/3} \qquad (A4.3)$$

The average concentration boundary layer thickness was approximated by the nearest diffusion-layer concept (114) as:

$$\delta_c = \frac{D}{K} \qquad (A4.4)$$

Then he defined the viscous sub-layer thickness as the point where the average velocity data deviate from a linear variation with distance from the wall. This occurs at $y^+ = 5$, and the viscous sub-layer thickness was given as:

$$\delta_v = \frac{5\gamma}{U^*} \qquad (A4.5)$$

where

$$U^* = \sqrt{S\gamma} \qquad (A4.6)$$

A4.2 SAMPLE OF CALCULATIONS

The method of calculations can be summarized using the measured values of the limiting current to calculate the mass transfer coefficient, velocity gradient at the wall, thickness of the concentration boundary layer, friction velocity and the viscous sub-layer thickness respectively.

Data required for the calculation are:

Limiting Current (I):	10μA
Ferricyanide Concentration(C_b):	0.01gm mole/liter
No. of electrons (n):	1 gr ion/gr mole

Faraday's number (F): 96501 Columbs/gr ion

Kinematic Viscosity (γ): 1.37×10^{-2} cm^2/sec

Diffusion Coefficient (D): 5.62×10^{-6} cm^2/sec

Electrode Diameter (d_e): 0.05cm

Therefore:

$$K = \frac{10 \times 10^{-6}}{0.01 \times 10^{-3} \times (\frac{0.05}{2})^2 \times \pi \times 1 \times 96501}$$

$$= 5.277 \times 10^{-3} \text{ cm/sec}$$

$$S = 1.546K^3 de/D^2$$

$$= 1.546 \times (5.277 \times 10^{-3})^3 \times 0.05/(5.62 \times 10^{-6})^2$$

$$= 359.64 \text{ sec}^{-1}$$

$$\delta_c = \frac{D}{K}$$

$$= \frac{5.62 \times 10^{-6}}{5.277 \times 10^{-3}}$$

$$= 1.065 \times 10^{-2} \text{ mm}$$

$$U^* = \sqrt{S\gamma}$$

$$= \sqrt{359.64 \times 1.37 \times 10^{-2}}$$

$$= 2.22$$

$$\delta_v = \frac{5\gamma}{U^*}$$

$$= \frac{5 \times 1.37 \times 10^{-2}}{2.22}$$

$$= 0.30856 \text{ mm}$$

APPENDIX 5

A computer program to solve first order differential equations using Runge-Kutta.

```
      MASTER GHASSAN
      DIMENSION Y(3),DERY(3),AUX(8,3),A(4),B(4)
     1,C(4),PRMT(5),XV(3000),YV1(3000),YV2(3000)
C THE AIM OF THIS PROGRAM IS TO SOLVE
C ASET OF FIRST-ORDER DIFFERENTIAL EQATIONS
C USING RUNG-KUTTA METHOD AND PLOTTING THE
C RESULTS OBY THE PLOTTER USING THE
C UAGHOUST SUBROUTINES.
      COMMON RCON
      COMMON VCON
      COMMON SPED
      COMMON DIME
      COMMON VISC
      EXTERNAL FCT
      EXTERNAL OUTP
      GO TO 217
C UAGHOUST SUBROUTINES USED TO PLOT
C THE RESULTS OBTAINED FROM SOLVING THE EQUATIONS.
      CALL GHREGION (-0.2,1.5,-0.2,2.0)
      CALL GHLIMITS (5.0,30.0,5.0,25.)
      CALL GHAXESSI (0.1,0.1)
      CALL GHCRSIZE(0.9)
      CALL GHCRSET(1)
      CALL GHPLOTCL (.5,1.6,21HVELOCITY DISTRIBUTION,21)
      CALL GHPLOTCL (.5,1.6,20HIN LAMINAR SUB-LAYER,20)
      CALL GHPLOTCL (0.3,-0.2,16HTANK DIAMETER(M),16)
      ANGLE=3.14159/2.0
      CALL GHROTATE (-0.1,0.2,ANGLE)
      CALL GHPLOTCL (-0.1,0.2,16HVELOCITY (M/MIN),16)
      CALL GHUNROT
  217 NOMB=1
      ITER=0
      WRITE(2,591)
  591 FORMAT(//,3H    ,'RESULTS OF THE SOLUTION OF THE
     1DIFFERENTIAL EQUATIONS USING RUNG-KUTTA METHOD')
      WRITE(2,883)
  883 FORMAT('-----------------------------------')
C VALUES OF THE INITIAL CONDITIONS
      SPED=50.0
      VISC=0.00008268/60.0
      DIME=0.036
      DON=.4
  799 VCON=1.16183*DON
      IF(DON-.5)898,898,535
  898 RCON=0.19365
      WRITE(2,511)DON
  511 FORMAT(//,3H    ,'RESULTS FOR DON=',F6.4)
      WRITE(2,512)
  512 FORMAT('-------------------')
      PRMT(1)=0.15
      PRMT(2)=1.2
      PRMT(3)=0.001
      PRMT(4)=0.05
      PRMT(5)=0.0
      WRITE(2,375)
```

```
375 FORMAT(/,2H  ,'DISTANCE',5X,'Y(1)',5X,
   1'DERY(1)',5X,'Y(2)',5X,'DER(2)',5X,'VR')
     WRITE(2,207)
207 FORMAT('-----------------------------------',/)
     Y(1)=VCON*SPED*DIME/1.16183
     Y(2)=5.33
     VZ=VCON*DIME*SPED/1.16183
     RCONY=RCON*SPED*DIME
     VCONY=VCOV*SPED*DIME
     DERY(1)=-0.5
     DERY(2)=-0.5
     Z1=0.15
     TZ=VCON*DIME*SPED/1.16183
     NDIM=2
C CALLING FOR THE SUBROUTINE TO SOLVE
C THE EQUATIONS
     CALL RKGS(PRMT,Y,DERY,NDIM,IHLF,AUX,XV,YV1,YV2
    1,NOMB,ITER)
965  DON=DON+0.1
     GO TO 799
535  GO TO 333
     CALL GHCRSIZE(0.1)
     CALL GHCRSET(3)
     CALL GHCURPTO (XV,YV1,1,NOMB,11)
     CALL GHPOINT (XV(1),YV(2))
     CALL GHCURPTO (XV,YV2,1,NOMB,21)
     CALL GHGREND
333  CONTINUE
     END
     SUBROUTINE RKGS(PRMT,Y,DERY,NDIM,IHLF
    1,AUX,XV,YV1,YV2,NOMB,ITER)
C SUBROUTINE RKGS USE THE METHOD OF RUNG-KUTTA T
C TO SOLVE FIRST-ORDER DIFFERENTIAL EQUATIONS AND
C OPTIMISING THE STEP LENGTH.
     DIMENSION Y(3),DERY(3),AUX(8,3),A(4),B(4)
    1,C(4),PRMT(5),XV(3000),YV1(3000),YV2(3000)
     NOMB=1
     NDIM=2
     DO 1 I=1,NDIM
   1 AUX(8,I)=.06666667*DERY(I)
     X=PRMT(1)
     XEND=PRMT(2)
     H=PRMT(3)
     PRMT(5)=0.
     CALL FCT(X,Y,DERY,VR)
     IF(H*(XEND-X))38,37,2
   2 A(1)=.5
     A(2)=.2928932
     A(3)=1.707107
     A(4)=.1666667
     B(1)=2.
     B(2)=1.
     B(3)=1.
     B(4)=2.
     C(1)=.5
     C(2)=.2928932
     C(3)=1.707107
```

```
112         C(6)=.5
113         DO 3 I=1,NDIM
114         AUX(1,I)=Y(I)
115         AUX(2,I)=DERY(I)
116         AUX(3,I)=0.
117       3 AUX(6,I)=0.
118         IREC=0
119         H=H+H
120         IHLF=-1
121         ISTEP=0
122         IEND=0
123       4 IF((X+H-XEND)*H)7,6,5
124       5 H=XEND-X
125       6 IEND=1
126     7   CALL OUTP(X,Y,DERY,IREC,NDIM,PRMT,
127        1XV,YV1,YV2,NOMB,ITER,VR)
128         IF(PRMT(5))40,8,40
129       8 ITEST=0
130       9 ISTEP=ISTEP+1
131         J=1
132      10 AJ=A(J)
133         BJ=B(J)
134         CJ=C(J)
135         DO 11 I=1,NDIM
136         R1=H*DERY(I)
137         R2=AJ*(R1-BJ*AUX(6,I))
138         Y(I)=Y(I)+R2
139         R2=R2+R2+R2
140      11 AUX(6,I)=AUX(6,I)+R2-CJ*R1
141         IF(J-4)12,15,15
142      12 J=J+1
143         IF(J-3)13,14,13
144      13 X=X+.5*H
145      14 CALL FCT(X,Y,DERY,VR)
146         GO TO 10
147      15 IF(ITEST)16,16,20
148      16 DO 17 I=1,NDIM
149      17 AUX(4,I)=Y(I)
150         ITEST=1
151         ISTEP=ISTEP+ISTEP-2
152      18 IHLF=IHLF+1
153         X=X-H
154         H=.5*H
155         DO 19 I=1,NDIM
156         Y(I)=AUX(1,I)
157         DERY(I)=AUX(2,I)
158      19 AUX(6,I)=AUX(3,I)
159         GO TO 9
160      20 IMOD=ISTEP/2
161         IF(ISTEP-IMOD-IMOD)21,23,21
162      21 CALL FCT(X,Y,DERY,VR)
163         DO 22 I=1,NDIM
164         AUX(5,I)=Y(I)
165      22 AUX(7,I)=DERY(I)
166         GO TO 9
167      23 DELT=0.
168         DO 24 I=1,NDIM
```

```
169      26 DELT=DELT*AUX(8,I)*ABS(AUX(4,I)-Y(I))
170         IF(DELT-PRMT(6))28,28,25
171      25 IF(IHLF-20)26,36,36
172      26 DO 27 I=1,NDIM
173      27 AUX(4,I)=AUX(5,I)
174         ISTEP=ISTEP+ISTEP-4
175         X=X-H
176         IEND=0
177         GO TO 18
178      28 CALL FCT(X,Y,DERY,VR)
179         DO 29 I=1,NDIM
180         AUX(1,I)=Y(I)
181         AUX(2,I)=DERY(I)
182         AUX(5,I)=AUX(6,I)
183         Y(I)=AUX(5,I)
184      29 DERY(I)=AUX(7,I)
185         CALL OUTP(X-H,Y,DERY,IHLF,NDIM,PRMT,
186        1XV,YV1,YV2,NUMB,ITER,VR)
187         IF(PRMT(5))40,30,40
188      30 DO 31 I=1,NDIM
189         Y(I)=AUX(1,I)
190      31 DERY(I)=AUX(2,I)
191         IREC=IHLF
192         IF(IEND)32,32,39
193      32 IHLF=IHLF+1
194         ISTEP=ISTEP/2
195         H=H+H
196         IF(IHLF)4,33,33
197      33 IMOD=ISTEP/2
198         IF(ISTEP-IMOD-IMOD)4,34,4
199      34 IF(DELT-.02*PRMT(6))35,35,4
200      35 IHLF=IHLF+1
201         ISTEP=ISTEP/2
202         H=H+H
203         GO TO 4
204      36 IHLF=11
205         CALL FCT(X,Y,DERY,VR)
206         GO TO 39
207      37 IHLF=12
208         GO TO 39
209      38 IHLF=13
210      39 CALL OUTP(X,Y,DERY,IHLF,NDIM,PRMT,
211        1XV,YV1,YV2,NUMB,ITER,VR)
212      40 RETURN
213         END
214         SUBROUTINE FCT(X,Y,DERY,VR)
215   C THIS SUBROUTINE CONTIAN THE THREE DIFFERENTIAL
216   C EQUATIONS AND THE PARAMETRS USED.
217         DIMENSION DERY(3),Y(3)
218         COMMON RCON
219         COMMON VCON
220         COMMON SPED
221         COMMON DIME
222         VISC=0,00008268/60,0
223         WIDT=0,0005
224         Z1=0,15
225         VZ=VCON*DIME*SPED/1,16183
```

```
      DERVZ=-3.7
      TZ=VCON*DIME*SPED/1.1616
      RCONY=RCON*SPED*DIME
      VCONY=VCON*SPED*DIME
      FACTR=(VCON*SPED*DIME)/(EXP(X))
      FACTS=RCON*SPED*DIME/(EXP(X))
      ASLA=1./(.066*(Y(1)**2)+.088*Y(1)*FACTR-
     1.004*(FACTR**2))
      ASLB=FACTR*(.004*(Y(1)**2)+.024*FACTR*FACTR*
     1.072*FACTR*Y(1))
      ASLC=((VISC*(Y(1)-FACTR)/((TZ**2)*(DIME**2)
     1*Y(1)))-4./(3.*VZ))
      ASLE=(.22*(Y(1)**2)+.16*FACTR*Y(1)+
     1.12*(FACTR**2))
      ASLF=ASLA*(ASLB+(ASLC*(ASLE**2)))
      DERY(1)=ASLF
      ASLG=1.0/(.22*Y(1)+
     1.8*FACTR)
      ASLH=(.08*FACTS*Y(1))-(.096*Y(2)*FACTR)
     1+(.18*FACTR*FACTS)
      ASLI1=.0176*(Y(1)**2)*FACTS
      ASLI2=.0308*Y(1)*FACTR*FACTS
      ASLI3=.0216*FACTS*(FACTR**2)
      ASLI4=.1256*Y(2)*(Y(1)**2)
      ASLI5=.1334*Y(2)*Y(1)*FACTR
      ASLI6=.049*Y(2)*(FACTR**2)
      ASLJ=ASLF*(ASLI1+ASLI2+ASLI3-
     1ASLI4-ASLI5-ASLI6)/ASLE
      ASLK=(.1898*Y(1)*Y(2))+(.01*Y(1)*FACTS)
     1+(.1652*Y(2)*FACTR)-(.08*FACTR*FACTS)
      ASLL=(.16*Y(1)*FACTR)+(.24*(FACTR**2))
      ASLM=ASLK*ASLL/ASLE
      ASLN=8.*VISC*(.33*Y(2)-2.833*FACTS)/
     1(TZ*(DIME**2))
      ASLO=(1.366*Y(2)+.3*FACTS)
      ASLP=(ASLG*ASLH)+ASLJ+(ASLK*ASLL/ASLE)
     1+((ASLN-ASLO)*ASLE)/TZ
      DERY(2)=ASLP
      ASLQ=(.5*Y(1)+.2*FACTR)
      ASLR=(.44*Y(1)+.16*FACTR)
      ASLS=(.16*Y(1)*FACTR+.24*(FACTR**2))
      ASLT=(TZ*(DIME**2))/8.0
      ASLU=((TZ**2)*(DIME**2))/(8.*ASLE)
      VR=(ASLU**.5)*((ASLT/ASLU)+((((
     1ASLQ*ASLR)/ASLE)-.3)*ASLF)-(((
     1ASLQ*ASLS)/ASLE)-(.2*FACTR)))
      RETURN
      END
      SUBROUTINE OUTP(X,Y,DERY,IHLF,NDIM,PRMT,
     1XV,YV1,YV2,NOMB,ITER,VR)
C THIS SUBROUTINE CONTAIN THE WRITTING
C STATEMENTS OF THE RESULTS AND THE EQUATIONS
C TO CALCULATE THE VELOCITY OF THE JET
C AT DIFFERENT POSITIONS ACROSS THE JET.
      DIMENSION Y(3),DERY(3),PRMT(5),YV1(3000),
     1YV2(3000),XV(3000)
      COMMON RCON
```

```
      COMMON VCON
      COMMON SPED
      COMMON DIME
      COMMON VISC
      ITER=ITER+1
      IF(X-0.15)92,92,84
   84 IF(X-1.2)86,92,86
   86 IF(ITER-50)91,92,92
   92 WRITE(2,99)X,Y(1),DERY(1),Y(2),DERY(2)
   99 FORMAT(1H ,F6.4,2(2X,F9.4,2H  ,3X,E8.2))
      DIY=0.0
  463 PROF=(2.*(DIY**2)-(DIY**3))
      PROG=(1.-(2.*(DIY**2))*(DIY**3))
      FACTR=(VCON*SPED*DIME)/EXP(X)
      FACTS=(RCON*SPED*DIME)/EXP(X)
      VZRD=Y(1)*PROF*FACTR*PROG
      VFRD=Y(2)*PROF*FACTS*PROG
      VRRD=VR*PROF
      WRITE(2,800)DIY,VZRD,VFRD,VRRD
  800 FORMAT(1H ,4(5X,F9.4))
      DIY=DIY+0.2
      IF(DIY-1.0)463,463,645
  645 GO TO 721
   95 YV1(NOMB)=Y(1)
      YV2(NOMB)=Y(2)
      XV(NOMB)=X
      NOMB=NOMB+1
  721 ITER=0
   91 RETURN
      END
      FINISH
****
```

TABLE 2 AVERAGE CURRENT AS A FUNCTION OF VOLTAGE FOR DIFFERENT ROTAMETER READINGS

Electrode Diameter: 0.5mm
Density of Solution: 1.077gm/cm^3
Viscosity of Solution: 1.557gm/cm sec

Voltage Volts \ Rotameter Reading cm	2.5	5.5	11	17	22	26
0.1	3.6	4.0	4.3	5.0	5.25	6.25
0.2	4.0	4.45	4.7	5.55	5.8	6.8
0.3	4.0	4.5	4.8	5.7	6.0	7.0
0.4	4.0	4.5	4.8	5.7	6.0	7.0
0.5	4.0	4.5	4.8	5.7	6.0	7.0
0.6	4.0	4.5	4.8	5.7	6.0	7.0
0.7	4.0	4.5	4.8	5.7	6.0	7.0
0.8	4.0	4.5	4.8	5.7	6.0	7.0
0.9	4.3	4.75	5.0	5.95	6.3	7.3
1.0	4.7	5.1	5.4	6.3	6.6	7.6

TABLE 3 AVERAGE CURRENT AS A FUNCTION OF VOLTAGE FOR DIFFERENT ROTAMETER READINGS

Electrode Diameter: 1.587mm
Density of Solution: 1.077gm/cm^3
Viscosity of Solution: 1.533gm/cm sec

Voltage (v) \ Rotameter Reading (cm)	3.5	6.5	9.5	12.5	17	21	24	26
0.1	15	17	21.5	22.5	25	28.5	29	32
0.2	20	21	25	26	29.5	31	34	37
0.3	21	23	26	27	31	32	35.5	39
0.4	21	23	26	27	31	32.5	36	40
0.5	21	23	26	27	31	32.5	36	40
0.6	21	23	26	27	31	32.5	36	40
0.7	21	23	26	27	31	32.5	36	40
0.8	21	23	26	27	31	32.5	36	40
0.9	22	24	27	28.5	32.5	33.5	37	42
1.0	25	28	30	32.5	35	36	40	46

TABLE 4 AVERAGE CURRENT AS A FUNCTION OF VOLTAGE FOR DIFFERENT ROTAMETER READINGS

Electrode Diameter: 3.175mm
Density Solution: 1.077 gm/cm^3
Viscosity of Solution: 1.557gm/cm sec

Voltage (v) \ Rotameter reading (cm)	2.5	5.5	11	17	22	26
0.1	63	70	75	85	94	105
0.2	71	74	81	93	102	115
0.3	71	75	82	95	104	119.5
0.4	71	75	82	95	104	120
0.5	71	75	82	95	104	120
0.6	71	75	82	95	104	120
0.7	71	75	82	95	104	120
0.8	71	75	82	95	104	120
0.9	74	79	85	98	107	123
1.0	80	86	92	104	114	128

TABLE 5 ROTAMETER CALIBRATION RESULTS

FLOW RATE AS A FUNCTION OF ROTAMETER SCALE FOR DIFFERENT VISCOSITIES

Rotameter Scale (cm) \ Viscosity (gm/cm sec)	1.533	1.557
0.3	0.951	1.028
3.9	1.914	2.056
7.0	2.871	3.085
10.1	3.828	4.113
13.0	4.785	5.141
15.7	5.742	6.170
18.2	6.699	7.201
20.9	7.656	8.226
23.2	8.613	9.255
25.7	9.570	10.283

TABLE 6 LIMITING CURRENT AS A FUNCTION OF REYNOLDS NUMBER

Electrode Diameter: 0.5mm
Density of Solution: 1.077gm/cm^3
Viscosity of Solution: 1.557gm/cm sec

Rotameter Reading (cm)	Flow Rate (liter/min)	N_{Re}	Limiting Current (μA)
2.5	1.5	512	4.0
5.5	2.6	881	4.5
11	4.5	1339	4.8
17	6.65	1978	5.7
22	8.7	2292	6.0
26	11.3	2978	7.0

TABLE 7 LIMITING CURRENT AS A FUNCTION OF REYNOLDS NUMBER

Electrode Diameter: 1.587mm
Density of Solution: 1.077gm/cm^3
Viscosity of Solution: 1.533gm/cm sec

Rotameter Reading (cm)	Flow Rate (Liter/min)	N_{Re}	Limiting Current (μA)
3.5	1.7	590	21
6.5	2.71	940	23
9.5	3.62	1256	26
12.5	4.58	1384	27
17	6.2	1873	31
21	7.82	2092	32.5
24	8.93	2390	36
27	11.7	3131	40

TABLE 8 LIMITING CURRENT AS A FUNCTION OF REYNOLDS NUMBER

Electrode Diameter: 3.175mm
Density of Solution: 1.077gm/cm^3 sec
Viscosity of Solution: 1.557gm/cm sec

Rotameter Reading (cm)	Flow Rate (Liter/min)	N_{Re}	Limiting Current (μA)
2.5	1.5	512	71
5.5	2.6	881	75
11	4.5	1339	82
17	6.65	1978	95
22	8.7	2292	104
26	11.3	2978	120

TABLE 9 VISCOUS SUB-LAYER THICKNESS AS A FUNCTION OF REYNODLS NUMBER

Electrode Diameter: 0.5mm
Density of Solution: 1.077gm/cm^3
Viscosity of Solution: 1.557gm/cm sec

Reynolds Number	Limiting Current (μA)	Mass Transfer Coef. x 10^3 (cm^2/sec)	Velocity Gradient (sec^{-1})	Thickness of Concentration Boundry Layer x 10^2 (mm)	Friction Velocity (cm/sec)	Thickness of Viscous Sub-layer (mm)
512	4.0	2.105	22.66	2.676	0.572	1.263
881	4.5	2.375	32.78	2.366	0.696	1.039
1339	4.8	2.533	39.780	2.219	0.766	0.943
1978	5.7	3.008	66.614	1.868	0.992	0.729
2292	6.0	3.150	76.490	1.784	1.052	0.687
2978	7.0	3.694	123.378	1.521	1.350	0.536

TABLE 10 VISCOUS SUB-LAYER THICKNESS AS A FUNCTION OF REYNOLDS NUMBER

Electrode Diameter: 1.587mm
Density of Solution: 1.077gm/cm^3
Viscosity of Solution: 1.533gm/cm sec

Reynolds Number	Limiting Current (A)	Mass Transfer Coef. x 10^3 cm^2/sec	Velocity Gradient (sec^{-1})	Thickness of Concentration Boundry Layer x 10^2 (mm)	Friction Velocity cm/sec	Thickness of Viscous Sub-layer (mm)
590	21	1.099	10.325	5.112	0.383	1.856
940	23	1.260	15.542	4.460	0.470	1.513
1256	26	1.340	19.596	4.128	0.528	1.348
1384	27	1.421	22.241	3.957	0.563	1.265
1873	31	1.623	33.215	3.463	0.688	1.035
2092	32.5	1.707	38.172	3.345	0.737	0.966
2390	36	1.884	52.019	2.982	0.861	0.827
3131	40	2.049	71.356	2.684	1.008	0.706

TABLE 11 VISCOUS SUB-LAYER THICKNESS AS A FUNCTION OF REYNOLDS NUMBER

Electrode Diameter: 3.175mm
Density of Solution: 1.077gm/cm^3
Viscosity of Solution: 1.557gm/cm sec

Reynolds Number	Limiting Current (μA)	Mass Transfer Coef. x 10^3	Velocity Gradient (sec^{-1})	Thickness of Concentration Boundry Layer (mm)x 10^2	Friction Velocity (cm/sec)	Viscous Sub-layer Thickness (mm)
512	71	0.929	12.47	6.047	0.4246	1.7025
881	75	0.9816	14.7	5.576	0.461	1.568
1339	82	1.0732	19.21	4.935	0.527	1.372
1978	95	1.2434	29.87	4.293	0.657	1.10
2292	104	1.361	39.192	3.903	0.753	0.960
2978	102	1.5706	60.205	3.328	0.933	0.775

TABLE 12 LIMITING CURRENT AS A FUNCTION OF IMPELLER SPEED FOR THE DIFFERENT ELECTRODES

Impeller Diameter: 3.6cm
Liquid Depth: 10cm
Shaft Angle: -5^{o}
Density of Solution: 1.092 gm/cm^{3}
Viscosity of Solution: 1.55×10^{-2} gm/cm sec

Electrode No. \ Impeller Speed	500	1000	1500	2000	2500	3000
1	5.5	6.2	6.8	8.5	9.5	11.0
2	7.0	10.5	13.0	16.0	21.0	25.0
3	2.3	2.9	3.8	4.5	5.7	6.5
4	7.0	8.5	9.5	11.0	13.0	15.0
5	20.0	22.0	24.0	26.0	28.0	32.0
6	3.4	4.3	5.2	6.5	7.3	8.0
7	2.5	3.0	3.5	4.0	5.0	5.5
8	4.0	5.7	6.8	7.5	9.0	10.0
9	6.0	7.0	8.5	9.5	11.0	14.0
10	9.0	10.0	11.0	13.0	15.0	17.0
11	3.8	5.0	6.0	7.2	8.0	9.5
13	2.4	3.0	3.5	4.1	5.0	6.5
14	6.5	8.0	9.5	11.5	14.0	17.5
16	2.7	3.2	4.0	5.0	5.7	6.5
17	3.0	3.8	4.6	5.3	6.2	7.0
18	9.0	10.5	12.0	14.0	17.0	21.0
19	5.0	5.8	6.5	7.2	8.0	8.5
20	5.7	6.5	7.2	8.0	9.0	12.0

Table 13 - Limiting Current as a Function of Impeller Speed for the Different Electrodes

Liquid depth: 13cm
Impeller diameter: 3.6cm
Shaft angle: -5° (to the left)
Density of solution: 1.092 gm/Cm^3
Viscosity of solution: 1.42 gm/CmSec

Impeller speed RPM \ Electrode no	1	2	3	4	5	6	7	8	9	10	11	12	13	14	15	16	17	18	19	20
500	2.7	9.0	2.2	11.0	16.0	3.0	2.2	4.8	5.2	4.5	3.5	28.0	2.3	5.0	29.0	2.5	2.7	5.5	3.0	3.2
1000	3.0	12.0	2.8	13.0	19.0	4.0	3.0	6.0	7.0	6.0	5.0	32.0	2.7	8.0	35.0	3.5	3.7	7.0	4.0	6.0
1500	3.5	15.0	3.2	14.0	20.0	4.5	3.2	7.0	7.5	8.0	6.0	38.0	3.5	10.0	40.0	4.2	4.5	7.5	4.6	7.5
2000	3.7	19.0	3.5	15.0	25.0	5.0	3.5	8.0	9.0	9.0	7.0	57.0	4.0	12.0	55.0	4.5	5.0	8.0	5.0	9.0
2500	4.2	21.0	4.2	17.0	27.0	5.2	3.7	8.5	9.7	9.8	7.5	31.0	4.5	14.0	82.0	4.7	5.5	8.5	5.7	9.5
3000	4.7	23.5	5.5	11.5	29.0	5.5	4.0	9.0	10.0	10.0	7.8	63.0	5.5	16.0	120.0	5.5	6.5	9.0	6.5	10.0

TABLE 14 LIMITING CURRENT AS A FUNCTION OF IMPELLER SPEED FOR THE DIFFERENT ELECTRODES

Impeller Diameter: 3.6cm
Liquid Depth: 16cm
Shaft Angle: -5^{o}
Density of Solution: $1.092 gm/cm^{3}$
Viscosity of Solution: $1.55 \times 10^{-2} gm/cm\ sec$

Electrode No. \ Impeller Speed (RPM)	500	1000	1500	2000	2500	3000
1	2.7	3.5	3.6	3.7	4.2	5.0
2	9.0	12.0	14.0	16.0	25.0	27.0
3	2.7	3.2	3.5	4.5	5.0	6.0
4	13.0	15.1	15.2	16.0	17.5	16.0
5	9.0	10.1	11.0	11.5	16.0	17.0
6	3.7	4.5	4.8	5.7	6.5	7.0
7	2.7	3.7	4.0	3.2	4.5	5.0
8	5.5	6.5	7.0	7.5	8.5	10.0
9	4.5	5.5	6.0	7.2	9.5	10.0
10	7.5	9.0	9.5	10.0	11.0	14.0
11	3.7	4.5	5.0	5.5	6.5	7.0
13	2.90	3.0	3.7	4.5	5.0	5.5
14	6.0	8.5	9.0	10.0	15.0	17.0
16	3.2	3.7	3.8	4.2	4.7	5.5
17	3.0	4.2	4.5	5.0	6.0	7.5
18	9.0	9.5	9.0	9.5	10.0	12.0
19	3.5	4.5	5.0	5.5	6.0	7.0
20	5.0	7.5	8.6	9.0	11.0	13.0

TABLE 15 LIMITING CURRENT AS A FUNCTION OF IMPELLER SPEED FOR THE DIFFERENT ELECTRODES

Impeller Diameter: 3.6cm
Liquid Depth: 20cm
Shaft Angle: -5^{o}
Density of Solution: 1.092 gm/cm^{3}
Viscosity of Solution: 1.55×10^{-2} gm/cm sec

Electrode No. \ Impeller Speed	500	1000	1500	2000	2500	3000
1	2.2	2.6	3.1	3.7	4.5	5.5
2	6.0	7.0	8.5	16.0	20.0	25.0
3	2.3	3.0	3.5	4.1	4.5	5.8
4	9.0	10.0	11.0	13.0	14.0	15.0
5	9.0	10.0	11.5	13.0	14.0	15.5
6	2.7	4.2	5.2	6.7	7.0	8.0
7	2.1	3.1	3.8	4.6	5.0	5.5
8	4.0	5.0	6.0	6.5	7.0	8.7
9	4.5	5.3	5.7	6.0	6.5	9.0
10	11.0	12.0	13.0	14.0	16.0	18.0
11	3.5	4.0	4.7	5.0	5.7	7.0
13	2.2	2.5	3.0	3.5	4.0	5.0
14	6.0	7.0	8.0	9.0	10.0	12.0
16	2.5	3.0	3.7	4.0	4.2	4.5
17	2.5	3.0	4.0	5.0	5.5	6.5
18	7.5	8.0	9.5	10.5	11.5	15.0
19	3.7	4.0	4.5	4.7	5.0	6.0
20	4.7	5.2	6.2	8.5	9.0	11.0

TABLE 16 LIMITING CURRENT AS A FUNCTION OF IMPELLER SPEED FOR THE DIFFERENT ELECTRODES

Impeller Diameter: 3.6cm
Liquid Depth: 25cm
Shaft Angle: -5^{o}
Density of Solution: 1.092 gm/cm^{3}
Viscosity of Solution: 1.55×10^{-2} gm/cm sec

Electrode No. \ Impeller Speed (RPM)	500	1000	1500	2000	2500	3000
1	9.0	10.5	12.0	15.0	12.0	17.0
2	7.7	8.5	11.0	13.0	19.0	21.0
3	2.5	2.8	3.5	4.0	4.7	5.2
4	10.0	12.0	14.0	17.0	20.0	23.0
5	9.5	11.0	12.5	14.0	15.0	16.5
6	3.7	4.5	5.0	6.5	7.0	8.0
7	2.3	2.8	3.5	4.0	4.7	5.5
8	4.5	5.2	6.2	7.0	7.5	8.7
9	5.0	5.5	6.7	7.2	8.2	9.0
10	12.0	14.0	16.0	18.0	19.0	21.0
11	3.3	4.0	4.5	5.1	5.7	6.2
13	2.8	3.2	3.8	4.2	4.7	5.2
14	5.5	7.5	8.5	9.0	10.5	12.5
16	3.0	3.6	4.0	4.8	5.2	5.7
17	3.2	3.8	4.3	5.2	5.7	6.5
18	8.0	8.5	9.5	10.5	11.0	12.5
19	4.4	5.2	5.8	7.0	8.5	9.5
20	6.2	7.0	8.0	9.2	10.0	11.5

Table 17 - Limiting Current as a Function of Impeller Diameter for the Different Electrodes

Impeller speed: 3000RPM
Impeller shaft angle: -5°
Liquid depth: 11cm
Density of solution: 1.077 gm/cm^3
Viscosity of solution: 1.378×10^{-2} gm/cm sec

Impeller Diameter (cm) \ Electrode no	1	2	3	6	7	8	9	10	11	12	13	15	16	17	18	19	20	21	22
7.2	40.0	7.5	6.5	15.0	6.0	6.5	6.5	20.5	10.0	10.0	3.0	31.0	5.0	12.0	45.0	4.5	17.0	52.0	27.0
6.0	38.0	6.5	6.0	13.0	5.5	6.0	6.0	18.5	8.5	9.0	2.5	30.0	4.5	10.5	42.0	4.0	15.0	48.0	23.0
4.8	34.0	5.0	5.0	11.0	4.5	5.0	5.0	13.5	7.0	6.5	2.0	24.0	3.5	8.5	38.0	3.5	13.0	40.0	16.0
3.6	32.0	4.0	4.0	8.0	3.5	4.0	3.5	12.0	5.5	5.0	1.5	16.0	3.0	7.0	34.0	3.0	10.0	36.0	12.0
3.0	27.0	3.5	3.0	6.0	2.5	3.0	2.5	9.5	4.5	4.0	1.0	12.0	2.5	6.0	30.0	2.5	8.5	32.0	9.0

Table 18 - Limiting Current as a Function of the Impeller Shaft Angle for the Different Electrodes

Impeller speed: 3000RPM
Impeller diameter: 3.6cm
Liquid depth: 11cm
Density of solution: 1.077 gm/cm^3
Viscosity of solution: 1.378×10^{-2} gm/cm sec

shaft angle (degree) \ Electrode no	1	2	3	6	7	8	9	10	11	12	13	15	16	17	19	20	21	22
-10^o	34.0	5.0	6.0	5.0	6.0	11.0	10.0	21.0	8.0	12.0	5.0	24.0	5.5	10.0	13.0	18.0	30.0	16.0
-5^o	40.0	9.5	10.0	6.0	7.5	10.5	9.0	23.0	8.0	9.5	5.0	26.0	5.0	17.0	12.0	15.0	36.0	20.0
0^o	37.0	7.0	9.0	4.0	4.5	11.0	8.0	19.5	5.0	9.0	3.5	29.0	7.0	11.0	12.5	12.0	35.0	20.0
$+5^o$	42.0	9.5	8.5	7.5	6.0	9.0	7.5	20.0	4.5	13.0	3.0	23.0	6.5	13.0	10.0	13.0	42.0	24.0

Table 19 - Limiting Current as a Function of Liquid Depth for the Different Electrodes

Impeller speed: 3000RPM
Impeller diameter: 3.6cm
Shaft angle: -5^{o}
Density of solution: 1.092 gm/cm^{3}
Viscosity of soluiton: 1.42×10^{-2} gm/cmSec

Liquid depth (cm) \ Electrode no	1	2	3	5	6	7	8	9	10	11	13	14	16	17	18	19	20	21
10	19.0	15.0	15.0	2.2	6.5	7.0	7.5	7.0	14.0	10.0	3.7	1.0	4.5	7.5	30.0	9.0	7.0	26.0
13	21.0	16.0	20.0	28.0	7.0	6.5	8.0	7.0	17.0	11.5	4.2	1.2	6.0	9.5	38.0	12.0	9.0	32.0
16	23.0	11.0	28.0	25.0	8.0	7.0	8.0	7.5	19.5	13.0	4.7	1.3	5.0	10.5	40.0	14.0	10.0	38.0
19	19.0	10.0	21.0	30.0	7.0	6.0	8.0	6.5	18.5	12.0	4.0	1.2	4.0	10.0	35.0	13.0	8.0	35.0
22	25.0	6.0	7.5	29.0	8.0	7.0	10.0	7.5	21.0	10.0	4.5	1.6	4.5	5.0	50.0	15.0	14.0	40.0

Table 20 - Limiting Current as a Function of Liquid Depth for the Different Electrodes

Impeller speed: 3000RPM
Impeller Diameter: 3.6cm
Shaft angle: -5^{o}
Density of solution: 1.092 gm/cm^{3}
Viscosity of solution: 1.42×10^{-2} gm/cm sec

Liquid depth (cm) \ Electrode no	1	2	3	4	5	6	7	8	9	10	11	13	14	16	17	18	19	20
10	11.0	25.0	6.5	15.0	32.0	8.0	5.5	10.0	14.0	17.0	9.5	6.0	17.5	6.5	7.0	21.0	8.5	12.0
13	4.7	23.5	5.5	11.5	29.0	5.5	4.0	9.0	10.0	10.0	7.8	5.5	16.0	5.5	6.5	9.0	6.5	10.0
16	5.0	27.0	6.0	16.0	17.0	7.0	5.0	10.0	10.0	14.0	7.0	5.5	17.0	5.5	7.5	12.0	7.0	13.0
20	5.5	25.0	5.8	15.0	15.5	8.0	5.5	8.7	9.0	18.0	7.0	5.0	12.0	4.5	6.5	15.0	6.0	11.0
25	17.0	21.0	5.2	23.0	16.5	8.0	5.5	8.7	9.0	21.0	6.2	5.2	12.5	5.7	6.5	12.5	9.5	11.5

TABLE 21 LIMITING CURRENT AS A FUNCTION OF THE DENSITY OF THE SOLUTION FOR THE DIFFERENT ELECTRODES

Impeller Speed: 3000RPM
Impeller Diameter: 3.6cm
Liquid Depth: 15cm
Shaft Angle: -5^{o}

Electrode No.	Density (gm/cm^3)	1.051	1.150	1.215	1.245
	Viscosity (gm/cm sec)	0.0172	0.0178	0.0178	0.0181
1		6.5	8.0	10.0	12.0
2		6.5	8.5	11.0	15.0
3		5.0	6.0	8.0	11.0
4		20.0	22.0	23.0	26.0
6		15.0	17.0	19.0	20.0
7		16.0	18.0	20.0	22.0
8		17.0	19.0	22.0	24.0
9		12.0	15.0	16.0	17.0
10		12.0	15.0	17.0	20.0
11		11.0	15.0	17.0	21.0
13		11.0	15.0	17.0	21.0
14		12.0	16.0	17.0	18.0
16		5.0	5.5	6.0	6.5
17		6.5	8.0	8.5	11.0
18		12.0	16.0	17.0	18.0
19		11.0	15.0	17.0	21.0
20		15.0	17.0	19.0	20.0
21		9.0	11.0	14.0	16.0
22		7.0	9.0	12.0	14.0

TABLE 22 LIMITING CURRENT AS A FUNCTION OF THE VISCOSITY OF THE SOLUTION FOR THE DIFFERENT ELECTRODES

Impeller Speed: 3000RPM
Impeller Diameter: 3.6cm
Liquid Depth: 15cm
Shaft Angle: -5^{o}

Electrode No.	Density (gm/cm^3)	1.049	1.051	1.052	1.055	1.058
	Viscosity (gm/cm sec)	0.01354	0.01723	0.02314	0.0422	0.0692
1		15.0	12.0	9.0	8.0	6.0
2		13.5	11.0	8.0	6.0	5.0
3		12.5	9.0	5.0	5.0	4.0
4		15.0	12.0	9.0	8.0	7.0
5		22.0	18.0	14.0	10.0	9.0
6		6.0	9.5	8.0	6.0	5.0
7		18.0	15.0	12.0	8.0	7.0
8		6.5	5.5	5.0	4.0	4.0
9		22.0	18.0	13.0	9.5	7.0
10		16.5	13.5	9.0	6.5	6.0
11		6.0	5.0	4.0	3.0	2.5
13		14.0	11.5	9.0	6.0	5.0
14		18.0	15.0	12.0	8.0	7.0
16		14.0	11.0	9.0	7.0	6.0
17		6.5	5.5	4.5	3.5	3.0
18		6.0	5.0	4.0	3.0	3.0
19		22.0	18.0	14.0	10.0	9.0
20		25.0	18.0	13.0	9.0	8.0
21		24.0	18.0	14.0	10.0	9.0
22		30.0	25.0	18.0	12.0	10.0

TABLE 23 MASS TRANSFER COEFFICIENT (K x 10^3) AS A FUNCTION OF IMPELLER SPEED FOR THE DIFFERENT ELECTRODES

Impeller Diameter: 3.6cm
Liquid Depth: 10cm
Shaft Angle: -5^o
Density of Solution: 1.092 gm/cm^3
Viscosity of Solution: 1.55×10^{-2} gm/cm sec

Electrode No. \ Impeller Speed (RPM)	500	1000	1500	2000	2500	3000
1	2.903	3.272	3.588	4.486	5.014	5.805
2	3.694	5.541	6.861	8.444	11.038	13.194
3	1.214	1.531	2.005	2.375	3.008	3.4305
4	3.694	4.486	5.014	5.805	6.861	7.916
5	10.555	11.611	12.66	13.722	14.777	16.888
6	1.794	2.269	2.744	3.430	3.853	4.222
7	1.319	1.583	1.847	2.111	2.639	2.902
8	2.111	3.008	3.588	3.958	4.750	5.277
9	3.166	3.694	4.486	5.014	5.805	7.388
10	4.75	5.277	5.805	6.861	7.916	8.972
11	2.005	2.639	3.166	3.800	4.222	5.014
13	1.266	1.583	1.847	2.164	2.639	3.430
14	3.43	4.222	5.014	6.069	7.389	9.236
16	1.425	1.688	2.111	2.639	3.008	3.430
17	1.583	2.005	2.428	2.797	3.272	3.694
18	4.75	5.541	6.333	7.388	8.972	11.083
19	2.639	3.061	3.430	3.800	4.222	4.486
20	3.008	3.430	3.80	4.222	4.750	6.333

TABLE 24 MASS TRANSFER COEFFICIENT ($K \times 10^3$) AS A FUNCTION OF IMPELLER SPEED FOR THE DIFFERENT ELECTRODES

Impeller Diameter: 3.6cm
Liquid Depth: 13cm
Shaft Angle: -5^{o}
Density of Solution: 1.092 gm/cm^3
Viscosity of Solution: 1.55×10^{-2} gm/cm sec

Electrode No \ Impeller Speed RPM	500	1000	1500	2000	2500	3000
1	1.425	1.583	1.847	1.953	2.216	2.4805
2	4.75	6.333	7.916	10.027	11.083	12.402
3	1.161	1.477	1.688	1.847	2.216	2.903
4	5.805	6.8609	7.388	7.916	8.972	6.096
5	8.444	10.027	10.555	13.195	42.495	15.305
6	1.583	2.111	2.375	2.639	2.744	2.903
7	1.161	1.583	1.6888	1.847	1.953	2.111
8	2.533	3.166	3.694	4.222	4.486	4.7498
9	2.744	3.694	3.958	4.75	5.119	5.278
10	2.375	3.166	4.222	4.75	5.172	5.278
11	1.847	2.639	3.166	3.695	3.958	4.116
13	1.2138	1.425	1.847	2.111	2.375	2.903
14	2.638	4.222	5.277	6.333	7.388	8.444
16	1.3194	1.8472	2.2166	2.375	2.4805	2.903
17	1.425	1.953	2.375	2.639	2.903	3.43
18	2.093	3.694	3.958	4.222	4.486	4.75
19	1.583	2.111	2.428	2.639	3.008	3.4305
20	1.688	3.166	3.958	4.75	5.0137	5.278

TABLE 25 MASS TRANSFER COEFFICIENT ($K \times 10^3$) AS A FUNCTION OF IMPELLER SPEED FOR THE DIFFERENT ELECTRODES

Impeller Diameter: 3.6cm
Liquid Depth: 16cm
Shaft Angle -5^o
Density of Solution: 1.092 gm/cm^3
Viscosity of Solution: 1.55×10^{-2} gm/cm sec

Electrode No. \ Impeller Speed (RPM)	500	1000	1500	2000	2500	3000
1	1.425	1.847	1.8999	1.953	2.2166	2.639
2	4.75	6.333	7.388	8.444	13.194	14.25
3	14.25	1.6888	1.847	2.375	2.639	3.1666
4	6.861	7.916	8.022	8.444	9.236	8.444
5	4.75	5.277	5.805	6.069	8.444	8.972
6	1.953	2.375	2.533	3.008	3.43	3.694
7	1.425	1.953	2.111	1.688	2.375	2.639
8	2.903	3.43	3.694	3.958	4.486	5.277
9	2.375	2.903	3.166	3.7999	5.0137	5.277
10	3.958	4.75	5.014	5.277	5.805	7.388
11	1.953	2.375	2.639	2.902	3.43	3.694
13	1.3194	1.583	1.953	2.375	2.639	2.903
14	3.1666	4.486	4.75	5.277	7.916	8.972
16	1.6888	1.953	2.006	2.2166	2.48	2.903
17	1.5833	2.2166	2.375	2.639	3.166	3.958
18	4.75	5.014	4.75	5.0137	5.277	6.333
19	1.847	2.375	2.639	2.902	3.166	3.694
20	2.639	3.958	4.486	4.75	5.805	6.861

TABLE 26 MASS TRANSFER COEFFICIENT ($K \times 10^3$) AS A FUNCTION OF IMPELLER SPEED FOR THE DIFFERENT ELECTRODES

Impeller Diameter: 3.6cm
Liquid Depth: 20cm
Shaft Angle: -5^o
Density of Solution: 1.092 gm/cm^3
Viscosity of Solution: 1.55×10^{-2} gm/cm sec

Electode No. \ Impeller Speed (RPM)	500	1000	1500	2000	2500	3000
1	1.161	1.372	1.636	1.953	2.375	2.903
2	3.166	3.694	4.486	8.444	10.555	13.194
3	1.214	1.583	1.847	2.164	2.375	3.061
4	4.750	5.277	5.805	6.861	7.388	7.916
5	4.750	5.277	6.069	6.861	7.383	8.180
6	1.425	2.216	2.744	3.536	3.694	4.222
7	1.108	1.636	2.005	2.428	2.639	2.903
8	2.111	2.639	3.166	3.430	3.694	4.592
9	2.375	2.797	3.008	3.166	3.430	4.750
10	5.805	6.333	6.861	7.388	8.444	9.500
11	1.847	2.111	2.480	2.639	3.008	3.694
13	1.161	1.319	1.583	1.847	2.111	2.639
14	3.166	3.694	4.222	4.750	5.277	6.333
16	1.319	1.583	1.953	2.111	2.216	2.375
17	1.319	1.583	2.111	2.639	2.903	3.430
18	3.960	4.222	5.014	5.541	6.069	7.916
19	1.952	2.111	2.375	2.480	2.639	3.1665
20	2.480	2.744	3.272	4.486	4.750	5.805

TABLE 27 MASS TRANSFER COEFFICIENT ($K \times 10^3$) AS A FUNCTION OF IMPELLER SPEED FOR THE DIFFERENT ELECTRODES

Impeller Diameter: 3.6cm
Liquid Depth: 25cm
Shaft Angle: -5^o
Density of Solution: 1.092 gm/cm^3
Viscosity of Solution: 1.55×10^{-2} gm/cm sec

Electrode No. \ Impeller Speed (RPM)	500	1000	1500	2000	2500	3000
1	4.750	5.541	6.333	7.916	6.333	8.972
2	4.064	4.486	5.805	6.861	10.027	11.083
3	1.319	1.477	1.847	2.111	2.480	2.744
4	5.277	6.333	7.388	8.972	10.555	12.138
5	5.014	5.805	6.597	7.388	7.916	8.708
6	1.953	2.375	2.639	3.430	3.694	4.222
7	1.214	1.477	1.847	2.111	2.480	2.903
8	2.375	2.744	3.272	3.694	3.958	4.592
9	2.639	2.903	3.536	3.800	4.327	4.750
10	6.333	7.388	8.444	9.500	10.030	11.083
11	1.742	2.111	2.375	2.692	3.008	3.272
13	1.477	1.688	2.005	2.216	2.480	2.744
14	2.903	3.958	4.486	4.750	5.541	6.597
16	1.583	1.899	2.111	2.533	2.744	3.008
17	1.688	2.005	2.270	2.744	3.008	3.430
18	4.222	4.486	5.014	5.542	5.805	6.597
19	2.322	2.744	3.061	3.694	4.486	5.014
20	3.272	3.694	4.222	4.855	5.277	6.069

TABLE 28 MASS TRANSFER COEFFICIENT ($K \times 10^3$) AS A FUNCTION OF IMPELLER DIAMETER FOR THE DIFFERENT ELECTRODES

Impeller Speed: 3000RPM
Liquid Depth: 11cm
Shaft Angel: -5^0
Density of Solution: $1.077 gm/cm^3$
Viscosity of Solution: $1.484 \times 10^{-2} gm/cm\ sec$

Electrode No. \ Impeller Diameter (cm)	3.0	3.6	4.8	6.0	7.2
1	14.35	16.888	17.944	20.054	21.11
2	1.847	2.111	2.639	3.43	3.958
3	1.583	2.111	2.639	3.161	3.43
6	3.167	4.222	5.805	6.861	7.916
7	1.32	1.847	2.375	2.903	3.1665
8	1.583	2.111	2.639	3.161	3.431
9	1.319	1.847	2.639	3.161	3.431
10	5.104	6.333	7.125	9.764	10.82
11	2.375	2.903	3.695	4.486	5.277
12	2.111	2.639	3.43	4.75	5.277
13	5.278	0.792	1.055	1.319	1.583
15	6.333	8.444	12.666	15.833	16.361
16	1.32	1.583	1.847	2.375	2.639
17	3.167	3.694	4.486	5.542	6.333
18	15.833	17.944	20.05	22.166	23.75
19	1.32	1.583	1.847	2.111	2.375
20	4.486	5.278	6.861	7.916	8.972
21	16.888	18.999	21.11	25.333	27.443
22	4.75	6.333	8.444	12.138	14.25

TABLE 29 MASS TRANSFER COEFFICIENT ($K \times 10^3$) AS A FUNCTION OF SHAFT ANGLE FOR THE DIFFERENT ELECTRODES

Impeller Speed: 3000RPM
Impeller Diameter: 3.6cm
Liquid Depth: 11cm
Density of Solution: 1.077 gm/cm^3
Viscosity of Solution: 1.484×10^{-2} gm/cm sec

Electrode No. \ Shaft Angle (Degree)	-10^o	-5^o	0^o	$+5^o$	$+10^o$
1	17.944	21.11	19.527	22.166	15.833
2	2.639	5.014	4.486	5.014	3.167
3	3.167	5.278	4.750	4.486	2.639
6	2.638	3.167	2.639	3.958	2.639
7	3.167	3.958	4.750	3.167	2.903
8	5.805	5.542	5.278	4.750	3.958
9	5.277	4.750	4.486	3.958	3.958
10	11.083	12.139	10.027	10.555	10.555
11	4.222	4.222	2.639	2.375	2.639
12	6.333	5.014	4.750	6.861	5.278
13	2.639	2.639	2.375	1.583	2.375
15	12.666	13.720	15.305	12.138	15.833
16	2.903	2.639	4.222	3.431	2.639
17	5.278	8.972	5.805	6.861	17.944
19	6.861	6.333	6.597	5.278	5.278
20	9.410	7.916	6.333	6.861	5.805
21	15.833	18.999	18.471	22.166	21.111
22	8.444	10.555	10.555	12.666	10.027

TABLE 30 MASS TRANSFER COEFFICIENT ($K \times 10^3$) AS A FUNCTION OF LIQUID DEPTH FOR THE DIFFERENT ELECTRODES

Impeller Speed: 3000RPM
Impeller Diameter: 3.6cm
Shaft Angle: -5°
Density of Solution: $1.092 gm/cm^3$
Viscosity of Solution: 1.55×10^{-2} gm/cm sec

Electrode No. \ Liquid Depth (cm)	10	13	16	19	22
1	10.03	11.083	12.138	10.03	13.194
2	7.916	8.444	5.805	5.278	3.166
3	7.916	10.555	14.77	11.083	3.958
5	15.305	14.777	13.194	15.83	15.305
6	3.43	3.694	4.222	3.694	4.222
7	3.694	3.4304	3.3694	3.166	3.694
8	3.958	4.222	4.222	4.222	5.277
9	3.694	3.694	3.958	3.43	3.958
10	7.388	8.972	10.291	9.763	11.083
11	5.277	6.07	6.86	6.333	5.277
13	1.953	2.211	2.48	3.111	2.375
14	0.528	0.6333	0.68	0.6333	0.8444
16	2.375	3.167	2.639	2.111	2.375
17	3.958	5.014	5.541	5.277	2.639
18	15.833	20.05	21.11	18.471	26.39
19	4.75	6.333	7.39	6.861	7.916
20	3.694	4.75	5.28	4.222	7.39
21	13.722	16.888	20.05	18.471	21.11

TABLE 31 MASS TRANSFER COEFFICIENT ($K \times 10^3$) AS A FUNCTION OF DENSITY FOR THE DIFFERENT ELECTRODES

Impeller Speed: 3000RPM
Impeller Diameter: 3.6cm
Liquid Depth: 15cm
Shaft Angle: -5^{o}

Electrode No.	Density (gm/cm^3)	1.051	1.150	1.215	1.245
	Viscosity (gm/cm sec)	0.0172	0.0178	0.0176	0.0181
1		3.430	4.222	5.277	6.333
2		3.430	4.486	5.805	7.916
3		2.639	3.166	4.222	5.805
4		10.555	11.610	12.139	13.722
6		7.916	8.972	10.027	10.555
7		8.444	9.500	10.555	11.611
8		8.972	10.027	11.611	12.666
9		6.333	7.916	8.444	8.972
10		6.333	7.916	8.972	10.555
11		5.805	7.916	8.972	11.083
13		5.805	7.196	8.972	11.083
14		6.333	8.444	8.972	9.500
16		2.639	2.903	3.166	3.430
17		3.430	4.222	4.486	5.806
18		6.333	8.444	8.972	9.500
19		5.805	7.916	8.972	11.083
20		7.916	8.972	10.027	10.555
21		4.750	5.805	7.389	8.444
22		3.694	4.750	6.333	7.389

TABLE 32 MASS TRANSFER COEFFICIENT (K x 10^3) AS A FUNCTION OF VISCOSITY FOR THE DIFFERENT ELECTRODES

Impeller Speed: 3000RPM
Impeller Diameter: 3.6cm
Liquid Depth: 15cm
Shaft Angle: -5°

Electrode No.	Density (gm/cm^3)	1.049	1.051	1.052	1.055	1.058
	Viscosity (gm/cm sec)	0.01354	0.11723	0.02314	0.0422	0.0692
1		7.916	6.333	4.750	4.222	3.166
2		7.125	5.805	4.222	3.166	2.639
3		6.597	4.750	2.639	2.639	2.111
4		7.916	6.333	4.750	4.222	3.694
5		11.610	9.500	5.389	5.277	4.750
6		3.166	5.014	4.222	3.166	2.639
7		9.500	7.916	6.333	4.222	3.694
8		3.430	2.903	2.639	2.111	2.111
9		11.611	9.500	6.861	5.014	3.694
10		8.708	7.125	4.751	3.430	3.166
11		3.166	2.639	2.111	1.583	1.319
13		7.389	6.070	4.750	3.166	2.639
14		9.500	7.916	6.330	4.222	3.694
16		7.389	5.805	4.750	3.694	3.166
17		3.430	2.903	2.375	1.847	1.583
18		3.166	2.639	2.111	1.583	1.583
19		11.611	9.500	7.389	5.277	4.750
20		13.194	9.500	6.861	4.750	4.222
21		12.666	9.500	7.389	5.277	4.750
22		15.833	13.194	9.500	6.333	5.277

TABLE 33 FRICTION VELOCITY AS A FUNCTION OF IMPELLER SPEED FOR THE DIFFERENT ELECTRODES

Impeller Diameter: 3.6cm
Liquid Depth: 10cm
Shaft Angle: -5^{o}
Density of Solution: 1.092 gm/cm^3
Viscosity of Solution: 1.55×10^{-2} gm/cm sec

Electrode No. \ Impeller Speed (RPM)	500	1000	1500	2000	2500	3000
1	0.9235	1.105	1.269	1.774	2.096	2.612
2	1.326	2.436	3.356	4.582	6.889	8.950
3	0.2497	0.354	.5303	0.683	.974	1.186
4	1.326	1.774	2.096	2.612	3.355	4.159
5	6.404	7.388	8.417	9.492	10.607	12.96
6	0.4488	0.638	.849	1.186	1.412	1.62
7	0.283	0.372	.461	.573	.8005	.923
8	0.573	0.9743	1.270	1.471	1.933	2.264
9	1.0522	1.326	1.774	2.096	2.612	3.750
10	1.933	2.264	2.611	3.356	4.159	5.018
11	0.5303	0.8005	1.052	1.383	1.62	2.096
13	0.2662	0.372	.4688	.594	.8005	1.186
14	1.1864	1.62	2.096	2.792	3.750	5.241
16	0.3176	.4098	.573	.8004	.974	1.186
17	0.372	.5303	.706	.873	1.105	1.326
18	1.933	2.436	2.976	3.759	5.018	6.889
19	0.8005	1.000	1.186	1.383	1.62	1.774
20	0.9743	1.186	1.383	1.62	1.933	2.976

TABLE 34 FRICTION VELOCITY AS A FUNCTION OF IMPELLER SPEED FOR THE DIFFERENT ELECTRODES

Impeller Diameter: 3.6cm
Liquid Depth: 13cm
Shaft Angle: -5^{o}
Density of Solution: 1.092 gm/cm^3
Viscosity of Solution: 1.55×10^{-2} gm/cm sec

Electrode No. \ Impeller Speed (RPM)	500	1000	1500	2000	2500	3000
1	0.317	0.371	0.468	0.5086	0.615	0.7282
2	1.93	2.971	4.152	5.919	6.877	8.141
3	.2332	0.3384	0.409	0.468	0.615	0.922
4	2.607	3.35	3.743	4.152	5.009	2.787
5	4.574	5.919	6.392	8.933	10.027	11.161
6	0.371	0.571	0.682	0.799	0.847	0.922
7	0.2332	0.371	0.409	0.468	0.508	0.572
8	0.7516	1.05	1.323	1.617	1.771	1.93
9	0.847	1.323	1.468	1.93	2.159	2.26
10	0.682	1.05	1.617	1.93	2.193	2.26
11	0.468	0.799	1.05	1.323	1.468	1.557
13	0.2493	0.317	0.468	0.571	0.682	0.922
14	0.799	1.617	2.26	2.971	3.743	4.574
16	4.282	0.468	0.615	0.682	0.728	0.922
17	0.317	0.5086	0.682	0.799	0.922	1.184
18	0.9218	1.323	1.468	1.617	1.771	1.93
19	0.3714	0.572	0.705	0.799	0.972	1.184
20	0.4091	1.05	1.468	1.93	2.093	2.26

TABLE 35 FRICTION VELOCITY AS A FUNCTION OF IMPELLER SPEED FOR THE DIFFERENT ELECTRODES

Impeller Diameter: 3.6cm
Liquid Depth: 16cm
Shaft Angle: -5^{o}
Density of Solution: 1.092 gm/cm^3
Viscosity of Solution: 1.55×10^{-2} gm/cm sec

Electrode No. \ Impeller Speed (RPM)	500	1000	1500	2000	2500	3000
1	0.3233	0.4773	0.4978	0.5187	0.6274	0.815
2	1.968	3.03	3.818	4.664	9.111	10.226
3	0.2333	0.417	0.477	0.6958	0.815	1.0712
4	3.416	4.234	4.319	4.664	5.336	4.6649
5	1.968	2.305	2.659	2.842	4.664	5.109
6	0.5187	0.696	0.7665	0.992	1.208	1.35
7	0.3233	0.5188	0.583	0.4172	0.6958	0.815
8	0.9402	1.208	1.350	1.497	1.8063	2.305
9	0.696	0.9401	1.071	1.408	2.134	2.305
10	1.497	1.968	2.134	2.305	2.659	3.818
11	0.5187	0.696	0.815	0.9401	1.208	1.35
13	0.2881	0.378	0.5188	0.6958	0.815	0.9402
14	1.0712	1.806	1.968	2.305	4.234	5.109
16	0.4172	0.5187	0.54	0.6274	0.7427	0.9402
17	0.3787	0.6274	0.696	0.815	1.0712	1.497
18	1.968	2.134	1.968	2.134	2.305	3.03
19	0.477	0.6958	0.815	0.9401	1.0715	1.35
20	0.815	1.497	1.806	1.968	2.659	3.4164

TABLE 36 FRICTION VELOSITY AS A FUNCTION OF IMPELLER SPEED FOR THE DIFFERENT ELECTRODES

Impeller Diameter: 3.6cm
Liquid Depth: 20cm
Shaft Angle: -5°
Density of Solution: 1.092 gm/cm^3
Viscosity of Solution: 1.55×10^{-2} gm/cm sec

Electrode No. \ Impeller Speed (RPM)	500	1000	1500	2000	2500	3000
1	.233	.3001	.391	.509	.683	.923
2	1.052	1.326	1.774	4.582	6.4004	8.949
3	.249	.372	.469	.594	.683	1.000
4	1.933	2.264	2.612	3.355	3.750	4.159
5	1.933	2.264	2.792	3.355	3.750	4.369
6	.318	.616	.849	1.241	1.326	1.62
7	.218	.391	.530	.706	.8005	.923
8	.573	.8005	1.052	1.186	1.326	1.837
9	.683	.873	.975	1.052	1.186	1.933
10	2.612	2.976	3.356	3.750	4.582	5.467
11	.469	.573	.729	.8005	.971	1.236
13	.234	.283	.372	.469	.573	.8005
14	1.052	1.326	1.62	1.933	2.264	2.976
16	.283	.372	.509	.573	.616	.683
17	.283	.372	.573	.8005	.923	1.186
18	1.470	1.62	2.096	2.436	2.792	4.159
19	.509	.573	.683	.729	.8005	1.052
20	.729	.849	1.105	1.774	1.933	2.612

TABLE 37 FRICTION VELOCITY AS A FUNCTION OF IMPELLER SPEED FOR THE DIFFERENT ELECTRODES

Impeller Diameter: 3.6cm
Liquid Depth: 25cm
Shaft Angle: -5^{o}
Density of Solution: 1.092 gm/cm^3
Viscosity of Solution: 1.55×10^{-2} gm/cm sec

Electrode No. \ Impeller Speed (RPM)	500	1000	1500	2000	2500	3000
1	1.933	2.436	2.976	4.159	2.976	5.018
2	1.529	1.774	2.612	3.355	5.929	6.889
3	0.283	.335	.468	.573	.729	.849
4	2.264	2.976	3.750	5.018	6.404	7.897
5	2.096	2.612	3.164	3.750	4.159	4.798
6	.509	.683	.8005	1.186	1.326	1.62
7	.249	.335	0.461	.573	.729	.923
8	.683	.849	1.105	1.326	1.470	1.837
9	.8005	.923	1.241	1.383	1.681	1.933
10	2.976	3.750	4.582	5.467	5.929	6.989
11	.429	.973	.683	.825	.974	1.105
13	.335	.409	.530	.616	.729	.849
14	.923	1.470	1.774	1.933	2.436	3.164
16	.372	.489	.573	.753	.849	.974
17	.410	.530	.638	.849	.974	1.186
18	1.62	1.774	2.096	2.436	2.612	3.164
19	.661	.849	1.000	1.326	1.774	2.096
20	1.105	1.326	1.62	1.998	2.264	2.792

TABLE 38 FRICTION VELOCITY (cm/sec) AS A FUNCTION OF IMPELLER DIAMETER FOR THE DIFFERENT ELECTRODES

Impeller Speed: 3000RPM
Liquid Depth: 11cm
Shaft Angle: -5°
Density of Solution: $1.077 gm/cm^3$
Viscosity of Solution: 1.484×10^{-2} gm/cm sec

Electrode No. \ Impeller Diameter (cm)	3.0	3.6	4.8	6.0	7.2
1	9.877	12.74	13.95	16.49	17.81
2	.46	.563	.787	1.166	1.44
3	.366	.563	.787	1.034	1.166
6	1.034	1.02	2.56	3.3	4.09
7	.278	.46	.672	.91	1.034
8	.366	.563	.787	1.034	1.166
9	.278	.46	.787	1.034	1.166
10	2.06	2.92	3.49	5.6	6.53
11	.672	.91	1.3	1.744	2.22
12	.563	.787	1.166	1.9	2.22
13	.07	.129	.198	.278	.366
15	2.92	4.5	8.27	11.56	12.15
16	0.278	0.366	.46	0.672	0.787
17	1.034	1.3	1.744	2.39	2.92
18	11.56	13.95	16.49	19.16	21.25
19	.278	.366	.46	.563	.672
20	1.744	2.226	3.3	4.09	4.93
21	12.74	15.2	17.81	23.41	26.4
22	1.9	2.92	4.5	7.76	9.87

TABLE 39 FRICTION VELOCITY AS A FUNCTION OF SHAFT ANGLE FOR THE DIFFERENT ELECTRODES

Impeller Speed: 3000RPM
Impeller Density: 3.6cm
Liquid Depth: 11cm
Density of Solution: 1.077gm/cm^3
Viscosity of Solution: 1.484×10^{-2} gm/cm sec

Electrode No. \ Shaft Angle (Degree)	-10^o	-5^o	0^o	$+5^o$	$+10^o$
1	13.95	17.81	15.84	19.16	11.56
2	0.787	2.06	1.744	2.06	1.034
3	1.034	2.22	1.9	1.744	.787
6	0.787	1.034	0.787	1.44	.787
7	1.034	1.44	1.9	1.034	0.91
8	2.56	2.39	2.22	1.9	1.44
9	2.22	1.9	1.744	1.44	1.44
10	6.77	7.76	5.83	6.3	6.3
11	1.02	1.02	0.787	0.672	.787
12	2.92	2.06	1.9	3.3	2.22
13	0.787	0.787	.672	0.366	0.672
15	8.27	9.33	10.99	7.76	11.56
16	0.91	0.787	1.02	1.166	.787
17	2.22	4.993	2.56	3.3	13.95
19	3.3	2.92	3.11	2.226	2.22
20	5.3	4.09	2.92	3.3	2.56
21	11.56	15.2	14.57	19.16	17.81
22	4.5	6.3	6.3	8.27	5.83

TABLE 40 FRICTION VELOCITY AS A FUNCTION OF LIQUID DEPTH FOR THE DIFFERENT ELECTRODES

Impeller Speed: 3000RPM
Impeller Diameter: 3.6cm
Shaft Angle: -5^{o}
Density of Solution: $1.092 gm/cm^{3}$
Viscosity of Solution: $1.55 \times 10^{-2} gm/cm\ sec$

Electrode No. \ Liquid Depth (cm)	10	13	16	19	22
1	5.877	6.83	7.828	5.877	8.8704
2	4.123	4.54	2.588	2.244	1.043
3	4.123	6.35	10.514	6.83	1.457
5	11.082	10.51	8.87	11.66	11.082
6	1.176	1.312	1.606	1.314	1.606
7	1.314	1.759	1.314	1.043	1.314
8	1.457	1.605	1.606	1.606	2.244
9	1.314	1.314	1.457	1.176	1.457
10	3.717	4.914	6.11	5.65	6.83
11	2.244	2.767	3.326	2.95	2.244
13	.505	.6108	.723	.5677	.6774
14	.071	.0933	.1052	.0933	.1436
16	.677	1.043	.7934	.5677	.6774
17	1.457	2.078	2.415	2.244	.7934
18	11.66	16.62	17.95	14.695	25.09
19	1.916	2.95	3.717	3.326	4.1226
20	1.314	1.916	2.244	1.606	3.717
21	9.408	12.845	16.622	14.694	17.953

TABLE 41 FRICTION VELOCITY AS A FUNCTION OF DENSTIY FOR THE DIFFERENT ELECTRODES

Impeller Speed: 3000RPM
Impeller Diameter: 3.6cm
Liquid Depth: 15cm
Shaft Angle: -5^{o}

Electrode No.	Density (gm/cm^3)	1.051	1.150	1.215	1.245
	Viscosity (gm/cm sec)	0.0172	0.0178	0.0176	0.0181
1		1.1271	1.688	2.282	3.006
2		1.271	1.850	2.633	4.201
3		.858	1.097	1.633	2.638
4		6.862	7.700	7.962	9.587
6		4.457	5.230	5.978	6.478
7		4.910	5.700	6.456	7.463
8		5.378	6.180	7.448	8.502
9		3.189	4.335	4.620	5.069
10		3.189	4.335	5.060	6.468
11		2.799	4.335	5.060	6.959
13		2.799	4.335	5.060	6.959
14		3.189	4.775	5.060	5.522
16		.858	.962	1.061	1.199
17		1.271	1.688	1.789	2.638
18		3.139	4.775	5.060	5.522
19		2.799	4.335	5.060	6.959
20		4.457	5.230	5.978	6.468
21		2.071	2.722	3.781	4.628
22		1.421	2.015	3.000	3.788

TABLE 42 FRICTION VELOCITY AS A FUNCTION OF VISCOSITY FOR THE DIFFERENT ELECTRODES

Impeller Speed: 3000RPM
Impeller Diameter: 3.6cm
Liquid Depth: 15cm
Shaft Angle: -5^{o}

Electrode No.	Viscosity (gm/cm sec)	0.01354	0.01723	0.02314	0.0422	0.0692
	Density (gm/cm^3)	1.049	1.051	1.052	1.055	1.058
1		3.953	3.189	2.399	2.714	2.254
2		3.375	2.799	2.011	1.763	1.715
3		3.007	0.072	.994	1.341	1.227
4		3.953	3.189	2.399	2.714	2.841
5		7.021	5.860	4.655	3.793	4.141
6		.999	2.250	2.011	1.763	1.715
7		5.196	4.480	3.695	2.714	2.841
8		1.128	.989	.993	.959	1.227
9		7.021	5.860	4.166	3.512	2.841
10		4.560	3.806	2.399	1.988	2.254
11		.9999	.858	.711	.623	.606
13		3.564	2.992	2.399	1.763	1.715
14		5.196	4.457	3.695	2.714	2.841
16		3.564	2.799	2.399	2.222	2.255
17		1.128	.989	.848	.785	.797
18		.999	.858	.711	.623	.797
19		7.021	5.86	4.655	3.793	4.141
20		8.505	5.86	4.166	3.238	3.471
21		7.999	5.86	4.655	3.793	4.141
22		11.180	9.59	6.787	4.986	4.850

TABLE 43 THICKNESS OF THE CONCENTRATION BOUNDARY LAYER ($mm \times 10^2$) AS A FUNCTION OF IMPELLER SPEED FOR THE DIFFERENT ELECTRODES

Impeller Diameter: 3.6cm
Liquid Depth: 10cm
Shaft Angle: -5^0
Density of Solution: 1.092 gm/cm^3
Viscosity of Solution: 1.55×10^{-2} gm/cm sec

Electorde No. \ Impeller Speed (RPM)	500	1000	1500	2000	2500	3000
1	1.936	1.717	1.566	1.253	1.121	0.968
2	1.5212	1.014	0.819	0.665	.507	.426
3	4.630	3.672	2.802	2.366	1.868	1.638
4	1.5212	1.253	1.121	0.968	.819	.710
5	0.5324	0.484	0.444	0.401	.380	.333
6	3.132	2.476	2.048	1.638	1.459	1.331
7	4.259	3.550	3.043	2.662	2.129	1.936
8	2.662	1.868	1.566	1.419	1.183	1.065
9	1.775	1.521	1.253	1.121	0.968	.761
10	1.183	1.065	0.968	0.819	0.710	.626
11	2.802	2.130	1.775	1.479	1.331	1.121
13	4.437	3.550	3.043	2.597	2.130	1.638
14	1.638	1.331	1.121	0.926	0.761	.609
16	3.944	3.328	2.662	2.130	1.868	1.638
17	3.549	2.802	2.315	2.009	1.717	1.521
18	1.183	1.014	0.887	0.761	0.626	.507
19	2.129	1.836	1.638	1.479	1.331	1.253
20	1.868	1.638	1.479	1.331	1.183	.887

TABLE 44 THICKNESS OF CONCENTRATION BOUNDARY LAYER (mm x 10^2 AS A FUNCTION OF IMPELLER SPEED FOR THE DIFFERENT ELECTRODES

Impeller Diameter: 3.6cm
Liquid Depth: 13cm
Shaft Angle: 1.092 gm/cm^3
Viscosity of Solution: 1.55 x 10^{-2} gm/cm sec

Electrode No. \ Impeller Speed (RPM)	500	1000	1500	2000	2500	3000
1	0.3944	0.355	0.304	0.2878	0.2535	0.2265
2	0.1183	0.0887	0.071	0.05704	0.0507	0.4531
3	0.484	0.3803	0.3327	0.3042	0.2535	0.1936
4	0.0968	0.0812	0.07606	0.071	0.0626	0.0926
5	0.0665	0.05604	0.0532	0.0426	0.0394	0.03672
6	0.355	0.2662	0.2366	0.21297	0.2047	0.1936
7	0.484	0.355	0.3327	0.3042	0.2878	0.266
8	0.2218	0.1775	0.1521	0.1331	0.1253	0.1183
9	0.2048	0.1521	0.142	0.1183	0.1098	0.1065
10	0.2366	0.1775	0.1331	0.1183	0.1086	0.1065
11	0.3042	0.213	0.1775	0.15212	0.142	0.1365
13	0.463	0.3982	0.3042	0.2662	0.2366	0.1936
14	0.213	0.1331	0.1065	0.08874	0.0761	0.06655
16	0.4259	0.304	0.2535	0.2366	0.2265	0.1936
17	0.3944	0.2878	0.2366	0.213	0.1936	0.1638
18	0.1936	0.1521	0.142	0.1331	0.1253	0.1183
19	0.355	0.2662	0.2315	0.2129	0.1868	0.1638
20	0.3328	0.1775	0.142	0.1183	0.1121	0.1065

TABLE 45 THICKNESS OF CONCENTRATION BOUNDARY LAYER (mm x 10^2) AS A FUNCTION OF IMPELLER SPEED FOR THE DIFFERENT ELECTRODES

Impeller Diameter: 3.6cm
Liquid Depth: 16cm
Shaft Angle: -5^{o}
Density of Solution: 1.092 gm/cm^3
Viscosity of Solution: 1.55×10^{-2} gm/cm sec

Electrode No. / Impeller Speed (RPM)	500	1000	1500	2000	2500	3000
1	0.349	0.304	0.2958	0.2878	0.2535	0.21297
2	0.1183	0.0887	0.076	0.0665	0.0426	0.0394
3	0.394	0.3327	0.304	0.236	0.213	0.17748
4	0.0819	0.071	0.07006	0.0655	0.0608	0.06655
5	0.1183	0.1065	0.968	0.0926	0.0665	0.06264
6	0.288	0.2366	0.2218	0.1868	0.1638	0.15212
7	0.394	0.2878	0.2662	0.333	0.236	0.213
8	0.1936	0.1638	0.1521	0.142	0.1253	0.1065
9	0.366	0.1936	0.1775	0.148	0.1121	0.1065
10	0.142	0.1183	0.1121	0.1065	0.0968	0.07606
11	0.288	0.2366	0.213	0.1936	0.1038	0.1521
13	0.426	0.355	0.287	0.2366	0.213	0.1936
14	0.1775	0.1253	0.1183	0.1065	0.071	0.06264
16	0.3327	0.2878	0.28	0.2535	0.2265	0.1936
17	0.355	0.2535	0.236	0.213	0.1775	0.142
18	0.1183	0.1121	0.1183	0.1121	0.1065	0.0887
19	0.304	0.2366	0.213	0.1936	0.1775	0.1521
20	0.213	0.142	0.1253	0.1183	0.0968	0.0819

TABLE 46 THICKNESS OF THE CONCENTATION BOUNDARY LAYER (mm x 10^2) AS A FUNCTION OF IMPELLER SPEED OF THE DIFFERENT ELECTRODES

Impeller Diameter: 3.6cm
Liquid Depth: 20cm
Shaft Angle: -5^{o}
Density of Solution: 1.092 gm/cm^3
Viscosity of Solution: 1.55×10^{-2} gm/cm sec

Electrode No. \ Impeller Speed (RPM)	500	1000	1500	2000	2500	3000
1	4.840	4.096	3.440	2.878	2.366	1.936
2	1.775	1.521	1.253	0.666	0.533	0.426
3	4.630	3.550	3.043	2.597	2.366	1.836
4	1.183	1.065	0.968	0.819	0.761	0.710
5	1.183	1.065	0.926	0.819	0.761	0.687
6	3.950	2.535	2.048	1.589	1.521	1.331
7	5.071	3.435	2.802	2.315	2.130	1.936
8	2.662	2.130	1.775	1.638	1.521	1.224
9	2.366	2.009	1.868	1.775	1.638	1.183
10	0.9681	0.8874	0.819	0.761	0.666	0.592
11	3.043	2.662	2.266	2.130	1.868	1.521
13	4.840	4.260	3.550	3.043	2.662	2.130
14	1.775	1.521	1.331	1.183	1.065	0.887
16	4.260	3.550	2.878	2.662	2.535	2.366
17	4.260	3.550	2.662	2.130	1.936	1.638
18	1.420	1.331	1.121	1.014	0.926	0.710
19	1.878	2.662	2.366	2.266	2.130	1.775
20	2.266	2.048	1.718	1.253	1.183	0.968

TABLE 47 THICKNESS OF THE CONCENTRATION BOUNDARY LAYER (mm x 10^{2}) AS A FUNCTION OF IMPELLER SPEED FOR THE DIFFERENT ELECTRODES

Impeller Diameter: 3.6cm
Liquid Depth: 25cm
Shaft Angle: -5^{o}
Density of Solution: 1.092gm/cm^{3}
Viscosity of Solution: 1.55 x 10^{-2} gm/cm sec

Electrode No. \ Impeller Speed (RPM)	500	1000	1500	2000	2500	3000
1	1.183	1.014	0.887	0.710	0.887	0.626
2	1.383	1.253	0.968	0.819	0.560	0.507
3	4.260	3.803	3.043	2.662	2.265	2.05
4	1.065	0.887	0.761	0.626	0.532	0.463
5	1.121	0.968	0.852	0.761	0.710	0.645
6	2.878	2.366	2.130	1.638	1.521	1.331
7	4.630	3.803	3.043	2.662	2.265	1.936
8	2.366	2.048	1.717	1.521	1.419	1.224
9	2.130	1.936	1.589	1.479	1.298	1.183
10	0.887	0.761	0.666	0.592	0.560	0.507
11	3.227	2.662	2.366	2.088	1.868	1.717
13	3.803	3.328	2.802	2.535	2.265	2.050
14	1.936	1.420	1.253	1.183	1.014	0.852
16	3.550	2.958	2.662	2.218	2.048	1.868
17	3.328	2.802	2.476	2.048	1.868	1.638
18	1.331	1.253	1.121	1.014	0.968	0.852
19	2.420	2.048	1.836	1.521	1.253	1.121
20	1.718	1.521	1.331	1.157	1.065	0.926

TABLE 47A VELOCITY GRADIENT AS A FUNCTION OF LIQUID DEPTH FOR THE DIFFERENT ELECTRODES

Impeller Speed: 3000RPM
Impeller Diameter: 3.6cm
Shaft Angle: -5°
Density of Solution: 1.092 gm/cm^3
Viscosity of Solution: 1.55 x 10^{-2} gm/cm sec

Electrode No. \ Liquid Depth (cm)	10	13	16	19	22
1	2467.2	3331.15	4376.4	2467.2	5620.3
2	1214	1473.25	478.7	359.7	77.695
3	1214	2877.5	7895.7	3331.15	151.726
5	8772.7	7895.7	5620.3	9711.96	8772.7
6	98.78	123.35	184.15	123.34	184.15
7	123.34	98.78	123.3	77.7	123.35
8	151.726	184.15	184.15	184.15	359.7
9	123.45	123.34	151.73	98.8	151.726
10	986.76	1767.2	2667.1	2277.5	3331
11	359.7	546.99	790.2	721.53	359.7
13	18.22	26.65	37.34	23.02	32.777
14	0.3596	0.6215	0.7902	0.1215	1.473
16	32.777	77.695	44.96	23.02	32.777
17	151.726	303.4	416.38	359.7	44.962
18	9711.96	19735	23021	15422.2	44962.0
19	262.22	621.53	986.7	790.23	1214
20	123.345	262.22	359.7	184.15	986.76
21	6322.13	11786	19735	15422.2	23020.9

TABLE 48 CONCENTRATION BOUNDARY LAYER ($\delta c \times 10^2$mm) AS A FUNCTION OF IMPELLER DIAMETER FOR THE DIFFERENT ELECTRODES

Impeller Speed: 3000RPM
Liquid Depth: 11cm
Shaft Angle: -5°
Density of Solution: 1.077gm/cm^3
Viscosity of Solution: 1.484×10^{-2}gm/cm sec

Electrode No. \ Impeller Diameter cm	3.0	3.6	4.8	6.0	7.2
1	.394	.33	.313	.28	.266
2	3.04	2.66	2.13	1.64	1.42
3	3.55	2.66	2.13	1.77	1.64
6	1.77	1.33	.968	.819	.71
7	4.26	3.04	2.36	1.93	1.77
8	3.55	2.66	2.13	1.77	1.64
9	4.26	3.04	2.13	1.77	1.64
10	1.12	.88	.788	.57	.52
11	2.36	1.93	1.52	1.25	1.06
12	2.33	2.13	1.64	1.18	1.06
13	10.6	7.1	5.32	4.26	3.55
15	.88	.665	.443	.355	.343
16	4.26	3.55	3.04	2.36	2.13
17	1.77	1.52	1.25	1.01	.88
18	.355	.313	.28	.253	.236
19	4.26	3.55	3.04	2.66	2.36
20	1.25	1.066	.819	.71	.626
21	.33	.296	.266	.222	.204
22	1.18	.88	.665	.463	.394

TABLE 49 CONCENTRATION BOUNDARY LAYER (mm x 10^2) AS A FUNCTION OF SHAFT ANGLE FOR THE DIFFERENT ELECTRODES

Impeller Speed: 3000RPM
Impeller Diameter: 3.6cm
Liquid Depth: 11cm
Density of Solution: 1.077 gm/cm^3
Viscosity of Solution: 1.484×10^{-2} gm/cm sec

Electrode No. \ Shaft Angle (Degree)	-10^o	-5^o	0^o	$+5^o$	$+10^o$
1	0.313	0.266	0.287	0.253	0.355
2	2.13	1.12	1.25	1.12	1.77
3	1.77	1.06	1.18	1.25	2.13
6	2.13	1.77	2.13	1.42	2.13
7	1.77	1.42	1.52	1.77	1.930
8	0.968	1.01	1.18	1.18	1.42
9	1.06	1.18	1.25	1.42	1.42
10	0.507	0.463	0.56	0.532	0.532
11	1.33	1.330	2.13	2.36	2.13
12	0.88	1.120	1.18	0.819	1.06
13	2.13	2.130	2.36	3.55	2.36
15	0.443	0.409	0.367	0.463	0.355
16	1.93	2.130	1.33	1.64	2.13
17	1.06	0.626	0.968	0.819	0.313
19	0.819	0.880	0.852	1.06	1.06
20	0.597	0.710	0.88	0.819	0.969
21	0.355	0.296	0.304	0.253	0.266
22	0.665	0.532	0.532	0.443	0.56

TABLE 50 THICKNESS OF CONCENTRATION BOUNDARY LAYER ($mm \times 10^2$) AS A FUNCTION OF LIQUID DEPTH FOR THE DIFFERENT ELECTRODES

Impeller Speed: 3000RPM
Impeller Diameter: 3.6cm
Shaft Angle: -5^{o}
Density of Solution: 1.092 gm/cm^3
Viscosity of Solution: 1.55×10^{-2} gm/cm sec

Electrode No. \ Liquid Depth (cm)	10	13	16	19	22
1	.5605	.507	.463	.5605	.426
2	.7099	.6655	.968	1.065	1.775
3	.7099	.5325	.3803	.5071	1.42
5	.3627	.3805	.426	.355	.3627
6	1.6382	1.5212	1.3311	1.5212	1.331
7	1.5212	1.638	1.521	1.775	1.5212
8	1.42	1.331	1.331	1.331	1.065
9	1.5212	1.5212	1.42	1.638	1.42
10	.7606	.6264	.5461	.576	.5071
11	1.0648	.926	.8191	.887	1.065
13	2.878	2.535	2.2657	2.662	2.366
14	10.648	8.874	8.191	8.874	6.656
16	2.366	1.775	2.13	2.662	2.366
17	1.42	1.121	1.014	1.065	2.129
18	.355	0.2803	.2662	.3043	.213
19	1.183	.887	.7606	.8191	.710
20	1.5212	1.183	1.665	1.331	.7606
21	.4096	.333	.2802	.3043	.2662

TABLE 51 THICKNESS OF THE CONCENTRATION BOUNDARY LAYER (mm x 10^2) AS A FUNCTION OF DENSITY FOR THE DIFFERENT ELECTRODES

Impeller Speed: 3000RPM
Impeller Diameter: 3.6cm
Liquid Depth: 15cm
Shaft Angle: -5°

Electrode No.	Density (gm/cm^3)	1.051	1.150	1.215	1.245
	Viscosity (gm/cm sec)	0.0172	0.0178	0.0178	0.0181
1		1.638	1.331	1.065	.887
2		1.638	1.253	.968	.710
3		2.130	1.775	1.331	.968
4		.532	.484	.463	.409
6		.710	.626	.560	.532
7		.665	.592	.532	.484
8		.626	.560	.484	.444
9		.887	.710	.666	.626
10		.887	.710	.626	.532
11		.968	.710	.626	.507
13		.968	.710	.626	.507
14		.887	.666	.626	.592
16		2.13	1.936	1.775	1.638
17		1.638	1.331	1.253	.968
18		.887	0.666	.626	.592
19		.968	.710	.626	.507
20		,710	.626	.560	.532
21		1.183	.968	.761	.666
22		1.521	1.183	.887	.761

TABLE 52 THICKNESS OF THE CONCENTRATION BOUNDARY LAYER (mm x 10^2) AS A FUNCTION OF VISCOSITY FOR THE DIFFERENT ELECTRODES

Impeller Speed: 3000RPM
Impeller Diameter: 3.6cm
Liquid Depth: 15cm
Shaft Angle: -5^{o}

Electrode No.	Density (gm/cm^3)	1.049	1.051	1.052	1.055	1.058
	Viscosity (gm/cm sec)	0.01354	0.01723	0.02314	0.0422	0.0692
1		.710	.887	1.183	1.331	1.775
2		.789	.968	1.331	1.775	2.130
3		.852	1.183	2.130	2.130	2.662
4		.710	.887	1.183	1.331	1.521
5		.484	.592	.761	1.065	1.183
6		1.775	1.121	1.331	1.775	2.130
7		.592	.710	.887	1.331	1.521
8		1.638	1.936	2.130	2.662	2.662
9		.484	.592	.819	1.121	1.521
10		.645	.789	1.183	1.638	1.775
11		1.775	2.130	2.662	3.555	4.260
13		.761	.926	1.183	1.775	2.130
14		.592	.710	.887	1.331	1.521
16		.761	.968	1.183	1.521	1.775
17		1.638	1.936	2.366	3.043	3.550
18		1.775	2.130	2.662	3.550	3.550
19		.484	.592	.761	1.065	1.183
20		.424	.592	.819	1.183	1.331
21		.444	.592	.761	1.065	1.183
22		.355	.426	.592	.887	1.065

TABLE 53 THICKNESS OF THE VISCOUS SUB-LAYER AS A FUNCTION OF IMPELLER SPEED FOR THE DIFFERNT ELECTRODES

Impeller Diameter: 3.6cm
Liquid Depth: 10cm
Shaft Angle: -5^{o}
Density of Solution: $1.092 gm/cm^3$
Viscosity of Solution: 1.55×10^{-2} gm/cm sec

Electrode No. \ Impeller Speed	500	1000	1500	2000	2500	3000
1	0.77	0.643	0.5602	0.4	0.339	0.272
2	0.536	0.292	0.212	0.155	0.103	0.079
3	2.84	2.01	1.341	1.04	0.73	0.599
4	0.536	0.4	0.339	0.272	0.212	0.171
5	0.111	0.096	0.084	0.075	0.067	0.0548
6	1.584	1.111	0.838	0.599	0.503	0.439
7	2.513	1.912	1.517	1.241	0.888	0.77
8	1.241	0.73	0.502	0.483	0.368	0.314
9	0.676	0.536	0.40	0.339	0.272	0.1896
10	0.368	0.314	0.272	0.212	0.171	0.1417
11	1.340	0.888	0.676	0.514	0.439	0.339
13	2.67	1.912	1.517	1.196	0.888	0.676
14	0.599	0.439	0.339	0.254	0.189	0.1357
16	2.239	1.735	1.241	0.888	0.73	0.599
17	1.912	1.34	1.007	0.814	0.643	0.536
18	0.368	0.292	0.239	0.1896	0.1417	0.103
19	0.888	0.711	0.599	0.514	0.439	0.40
20	0.73	0.599	0.514	0.439	0.368	0.239

TABLE 54 THICKNESS OF THE VISCOUS SUB-LAYER (mm) AS A FUNCTION OF IMPELLER SPEED FOR THE DIFFERENT ELECTRODES

Impeller Diameter: 3.6cm
Liquid Depth: 13cm
Shaft Angle: -5^{o}
Density of Solution: 1.092 gm/cm^{3}
Viscosity of Solution: 1.55×10^{-2} gm/cm sec

Electrode No. \ Impeller Speed (RPM)	500	1000	1500	2000	2500	3000
1	2.24	1.912	1.517	1.396	1.154	0.975
2	0.368	0.239	0.171	0.12	0.103	0.0872
3	3.044	2.12	1.735	1.517	1.154	0.77
4	0.272	0.212	0.1896	0.171	0.142	0.2547
5	0.1552	0.12	0.111	0.075	0.0708	0.0636
6	1.912	1.242	1.041	0.888	0.838	0.77
7	3.044	1.912	1.735	1.517	1.396	1.242
8	0.944	0.676	0.536	0.439	0.4009	0.368
9	0.838	0.536	0.484	0.368	0.329	0.314
10	1.041	0.676	0.439	0.368	0.329	0.314
11	1.517	0.888	0.676	0.536	0.484	0.456
13	2.848	2.239	1.517	1.242	1.041	0.77
14	0.888	0.439	0.314	0.239	0.1896	0.155
16	2.513	1.517	1.154	1.04	0.975	0.77
17	2.239	1.396	1.04	0.888	0.77	0.5995
18	0.7702	0.5364	0.483	0.439	0.4009	0.368
19	1.912	1.242	1.007	0.888	0.73	0.5995
20	1.754	0.676	0.484	0.368	0.34	0.314

TABLE 55 THICKNESS OF THE VISCOUS SUB-LAYER (mm) AS A FUNCTION OF IMPELLER SPEED FOR THE DIFFERENT ELECTRODES

Impeller Diameter: 3.6cm
Liquid Depth: 16cm
Shaft Angle: -5^{o}
Density of Solution: 1.092 gm/cm^3
Viscosity of Solution: 1.55×10^{-2} gm/cm sec

Electrode No. \ Impeller Speed (RPM)	500	1000	1500	2000	2500	3000
1	2.2837	1.547	1.483	1.4236	1.1771	0.9062
2	0.3752	0.2437	0.1934	0.1583	0.081	0.0722
3	2.283	1.77	1.547	1.0614	0.9026	0.6894
4	0.2162	0.1744	0.171	0.1583	0.13829	0.1583
5	0.3752	0.3204	0.277	0.2598	0.1583	0.1445
6	1.4236	1.0614	0.9634	0.7445	0.6114	0.5471
7	2.284	1.4236	1.2666	1.77	1.0614	0.9062
8	0.7855	0.6114	0.547	0.4933	0.4088	0.3204
9	1.0614	0.7855	0.6894	0.5244	0.346	0.3204
10	0.4933	0.375	0.346	0.3204	0.2777	0.1934
11	1.423	1.0614	0.906	0.7855	0.6114	0.5471
13	2.563	1.9498	1.4236	1.0614	0.906	0.7855
14	0.6894	0.4088	0.3753	0.3204	0.1744	0.1445
16	1.77	1.4236	1.3677	1.1771	0.9943	0.7855
17	1.95	1.1771	1.0614	0.9062	0.6894	0.4933
18	0.375	0.346	0.3753	0.346	0.3204	0.2437
19	1.547	1.0614	0.9062	0.7855	0.6894	0.547
20	0.9062	0.4933	0.4088	0.375	0.2777	0.21616

TABLE 56 THICKNESS OF THE VISCOUS SUB-LAYER AS A FUNCTION OF IMPELLER SPEED FOR THE DIFFERNT ELECTRODE

Impeller Diameter: 3.6cm
Liquid Depth: 20cm
Shaft Angle: -5°
Density of Solution: 1.092gm/cm^3
Viscosity of Solution: 1.55 x 10^{-2} gm/cm sec

Electrode No \ Impeller Speed	500	1000	1500	2000	2500	3000
1	3.05	2.37	1.83	1.398	1.042	0.77
2	0.677	0.537	0.4	1.555	0.1112	0.079
3	2.85	1.915	1.52	1.198	1.042	0.771
4	0.368	0.3147	0.273	0.212	0.1899	0.171
5	0.368	0.3147	0.255	0.212	0.1889	0.163
6	2.24	1.156	0.839	0.574	0.537	0.439
7	3.27	1.823	1.34	1.008	0.89	0.77
8	1.244	0.89	0.677	0.6	0.537	0.387
9	1.042	0.815	0.732	0.677	0.60	0.368
10	0.272	0.239	0.212	1.90	0.155	0.130
11	1.52	1.244	0.977	0.89	0.731	0.561
13	3.05	0.484	1.915	1.52	1.24	0.89
14	0.677	0.537	0.439	0.368	0.315	0.239
16	2.517	1.915	1.398	1.244	1.156	1.042
17	2.517	1.915	1.244	0.89	0.77	0.629
18	0.484	0.44	0.399	0.292	0.255	0.171
19	1.398	1.24	1.04	0.97	0.89	0.677
20	0.977	0.839	0.644	0.402	0.368	0.276

TABLE 57 THICKNESS OF THE VISCOUS SUB-LAYER AS A FUNCTION OF IMPELLER SPEED FOR THE DIFFERENT ELECTRODES

Impeller Diameter: 3.6cm
Liquid Depth: 25cm
Shaft Angle: -5^{o}
Density of Solution: $1.092 gm/cm^{3}$
Viscosity of Solution: 1.55×10^{-2} gm/cm sec

Electrode No. \ Impeller Speed	500	1000	1500	2000	2500	3000
1	0.368	0.292	0.2392	0.171	0.239	0.1417
2	0.465	0.40	0.272	0.219	0.120	0.103
3	2.513	2.12	1.517	1.242	0.975	0.838
4	0.314	0.239	0.189	0.141	0.111	0.09
5	0.339	0.272	0.224	0.189	0.171	0.148
6	1.395	1.04	0.888	0.599	0.536	0.439
7	2.848	2.12	1.517	1.241	0.975	0.77
8	1.04	0.838	0.643	0.536	0.483	0.387
9	0.888	0.77	0.572	0.514	0.423	0.368
10	0.239	0.189	0.1552	0.130	0.1199	0.103
11	1.657	1.241	1.04	0.862	0.73	0.643
13	2.12	1.73	1.34	1.154	0.975	0.838
14	0.77	0.483	0.3995	0.368	0.292	0.225
16	1.912	1.45	1.241	0.944	0.838	0.73
17	1.735	1.34	1.114	0.837	0.73	0.599
18	0.439	0.4	0.339	0.292	0.272	0.225
19	1.076	0.838	0.711	0.536	0.40	0.339
20	0.643	0.536	0.439	0.356	0.314	0.254

TABLE 58 THICKNESS OF THE VISCOUS SUB-LAYER (mm) AS A FUNCTION OF IMPELLER DIAMETER FOR THE DIFFERENT ELECTRODES

Impeller Speed: 3000RPM
Liquid Depth: 11cm
Shaft Angle: -5^{o}
Density of Solution: 1.077 gm/cm^{3}
Viscosity of Solution: 1.484×10^{-2} gm/cm sec

Electrode No. \ Impeller Diameter (cm)	3.0	3.6	4.8	6.0	7.2
1	.0697	.054	.049	0417	.038
2	1.498	1.226	.875	.59	.478
3	1.88	1.226	.85	.666	.59
6	.666	.675	.269	.208	.168
7	2.478	1.498	1.025	.757	.666
8	1.88	1.226	.875	.666	.59
9	2.478	1.498	.875	.666	.59
10	.334	.236	1.197	1.23	.105
11	1.025	.757	.53	.395	.31
12	1.224	.375	.59	.362	.31
13	9.84	5.34	3.48	2.478	1.88
15	.236	.153	.083	.0596	.056
16	2.478	1.88	1.498	1.025	.875
17	.666	0.53	.395	.288	.236
18	.0596	.049	.0417	.036	.032
19	2.478	1.882	1.498	1.224	1.025
20	.395	.309	.208	.1685	.1397
21	.045	.045	.038	.0294	.026
22	.362	.236	.153	.0887	.0697

TABLE 59 THICKNESS OF THE VISCOUS SUB-LAYER (mm) AS A FUNCTION OF SHAFT ANGLE FOR THE DIFFERENT ELECTRODES

Impeller Speed: 3000RPM
Impeller Diameter: 3.6cm
Liquid Depth: 11cm
Density of Solution: 1.077gm/cm^3
Viscosity of Solution: 1.484 x 10^{-2} gm/cm sec

Electrode No. \ Shaft Angle (Degree)	-10^o	-5^o	0^o	$+5^o$	$+10^o$
1	0.049	0.038	0.0435	0.036	0.0596
2	0.875	0.334	0.395	0.334	0.666
3	0.666	0.31	0.362	0.395	0.875
6	0.875	0.666	.875	0.478	.875
7	0.666	0.478	.362	0.666	.757
8	0.269	0.288	.31	0.362	.478
9	0.310	0.362	0.395	0.478	0.478
10	0.1017	0.0887	0.118	0.109	.109
11	0.675	0.675	0.875	1.025	.875
12	0.236	0.334	0.362	0.208	.31
13	0.875	0.875	1.025	1.880	1.025
15	0.083	0.0738	0.0627	0.887	.0596
16	0.757	0.875	0.675	0.590	0.875
17	0.049	0.1397	0.269	0.208	0.049
19	0.208	0.236.	0.220	0.309	0.31
20	0.130	0.1685	0.236	0.208	.269
21	0.0596	0.045	0.0473	0.036	.038
22	0.153	0.109	0.109	0.083	.118

TABLE 60 THICKNESS OF THE VISCOUS SUB-LAYER (mm) AS A FUNCTION OF THE LIQUID DEPTH FOR THE DIFFERENT ELECTRODES

Impeller Speed: 3000RPM
Impeller Diameter: 3.6cm
Shaft Angle: -5^{o}
Density of Solution: 1.092 gm/cm^{3}
Viscosity of Solution: 1.55×10^{-2} gm/cm sec

Electrode No. \ Liquid Depth (cm)	10	13	16	19	22
1	.119	.1025	.0894	.119	.079
2	.1698	.154	2.7	.312	.671
3	.1698	.1103	.0666	.1025	.48
5	.0632	.066	.0789	.06	.0632
6	.5954	.533	.436	.533	.436
7	.533	.595	,533	.6712	.533
8	.48	.436	.436	.736	.312
9	.533	.532	.48	.5954	,48
10	.1883	.1407	.1145	.124	.1025
11	.312	.253	.2104	.237	.312
13	1.386	1.146	.968	1.233	1.033
14	9.866	.7504	6.655	7.504	4.874
16	1.033	.6712	.882	1.233	1.033
17	.78	.337	.29	.312	.882
18	.06	.042	.039	.0476	.028
19	.365	.237	.1883	.2105	.1698
20	.333	.365	.312	.436	.1883
21	.0744	.0545	.042	.0476	.039

TABLE 61 THICKNESS OF THE VISCOUS SUB-LAYER (mm) AS A FUNCTION OF DENSITY FOR THE DIFFERENT ELECTRODES

Impeller Speed: 3000RPM
Impeller Diameter: 3.6cm
Liquid Depth: 15cm
Shaft Angle: -5^{o}

Electrode No.	Density (gm/cm^3)	1.051	1.150	1.215	1.245
	Viscosity (gm/cm sec)	0.0172	0.0178	0.0176	0.0181
1		.560	.422	.312	.237
2		.560	.385	.271	.169
3		.831	.650	.436	.270
4		.104	.093	.089	.074
6		.159	.136	.119	.110
7		.145	.125	.110	.096
8		.132	.115	.096	.084
9		.223	.164	.154	.141
10		.223	.164	.141	.110
11		.255	.164	.141	.102
13		.255	.164	.141	.102
14		.223	1.149	1.141	.129
16		.831	.740	.672	.595
17		.560	.422	.398	.270
18		.223	.149	1.141	.129
19		.255	.164	.141	.102
20		.159	.136	.119	.110
21		.344	.262	.188	.154
22		.501	.354	.237	.188

TABLE 62 THICKNESS OF THE VISCOUS SUB-LAYER (mm) AS A FUNCTION OF VISCOSITY FOR THE DIFFERENT ELECTRODES

Impeller Speed: 3000RPM
Impeller Diameter: 3.6cm
Liquid Dpeth: 15cm
Shaft Angle: -5^{o}

Electrode No.	Density (gm/cm^3)	1.049	1.051	1.052	1.055	1.058
	Viscosity (gm/cm sec)	0.01354	0.01723	0.02314	0.0422	0.0692
1		.180	.223	.297	.263	.316
2		.211	.255	.354	.404	.416
3		.237	.344	.717	.531	.581
4		.180	.223	.297	.263	.251
5		.101	.122	.153	.188	.172
6		.713	.317	.354	.404	.416
7		.137	.160	.193	.263	.251
8		.632	.720	.717	.742	.581
9		.101	.122	.171	.203	.251
10		.156	.187	.297	.358	.316
11		.713	.831	1.002	1.143	1.17
13		.200	.238	.297	.404	.416
14		.137	.160	.193	.263	.251
16		.200	.255	.297	.321	.316
17		.632	.720	.840	.907	.894
18		.713	.831	1.002	1.143	.894
19		.101	.122	.153	.1878	.172
20		.0838	.122	.171	.220	.206
21		.089	.122	.153	.188	.172
22		.064	.074	.105	.143	.147

TABLE 63 CALIBRATION OF THE HOT-FILM ANEMOMETER

RUN NO: 1

Sample No.	Voltage (v)	Weight of water (gm)	Time (Sec)	Calculated Velocity mm/sec
1	2.48	1.7	100	.5368
2	2.76	3.7	50	2.336
3	2.98	15.9	50	10.041
4	3.22	22.1	50	13.957
5	3.46	56.8	50	35.871
6	3.83	32.8	20	51.785
7	4.11	113.0	50	71.363
8	4.24	59.5	20	93.94
9	4.35	74.5	20	117.623
10	4.48	104.2	20	164.514
11	4.63	71.1	10	224.509
12	4.90	80.8	10	255.139
13	5.05	96.5	10	304.714
14	5.11	128.8	10	466.707
15	5.18	71.9	5	454.072
16	5.20	142.5	10	449.967
17	5.30	76.1	5	480.596

TABLE 64 CALIBRATION OF THE HOT-FILM ANEMOMETER

RUN NO: 2

Sample No.	Voltage (v)	Weight of water (gm)	Time (Sec)	Calculated Velocity mm/sec
1	2.65	.3.5	100	1.105
2	2.85	10.1	100	3.189
3	3.06	10.6	50	6.694
4	3.37	43.7	100	13.799
5	3.61	69.9	100	22.072
6	3.79	47.9	50	30.250
7	4.04	22.7	20	35.839
8	4.12	81.8	50	51.659
9	4.32	112.9	50	71.300
10	4.45	131.9	50	83.299
11	4.53	63.7	20	100.571
12	4.65	70.9	20	111.939
13	4.90	91.2	20	143.989
14	5.09	64.5	10	203.669
15	5.29	75.8	10	239.35
16	5.54	90.1	10	284.505
17	5.73	124.5	10	393.1

TABLE 65 CALIBRATION OF THE HOT-FILM ANEMOMETER

RUN NO: 3, 4

Sample No	Voltage (v)	Weight of water (gm)	Time (Sec)	Calculated Velocity mm/sec
1	2.56	4.0	100	1.263
2	2.79	9.7	100	3.063
3	3.15	15.7	50	9.915
4	3.43	30.4	50	19.198
5	3.68	48.1	50	30.376
6	3.94	74.5	50	47.049
7	4.15	101.0	50	63.784
8	4.20	41.5	20	65.5215
9	4.32	131.6	50	83.1096
10	458	76.1	20	120.149
11	4.75	86.3	20	136.253
12	4.91	109.3	20	172.566
13	5.11	130.3	20	205.721
14	5.23	58.2	5	367.662
15	5.35	169.2	20	267.612
16	5.52	103.1	10	325.555
17	5.67	66.8	5	421.863

TABLE 66 CALIBRATED VELOCITY (cm/sec) AS A FUNCTION OF VOLTAGE FOR DIFFERENT PROBES

Voltage (v)	Run 1	Run 2	Run 3 & 4
2.90	0.8119	-	-
3.00	1.063	-	-
3.15	1.4914	-	1.3025
3.20	1.6517	-	-
3.30	2.006	-	1.5725
3.40	2.4145	-	1.796
3.45	2.6481	1.6761	1.9268
3.55	3.1582	1.8625	-
3.60	3.4989	-	2.4192
3.65	-	2.1106	2.6226
3.70	4.1077	2.2639	2.8485
3.80	-	2.6400	3.3741
3.85	5.2483	2.8668	3.6768
3.90	5.8014	3.1221	4.008
3.95	6.3146	3.4076	-
4.00	6.8815	3.7253	4.7623
4.05	-	4.0764	5.188
4.10	8.1496	4.463	4.646
4.15	8.8623	-	6.1398
4.20	-	5.3470	6.6692
4.25	10.4635	5.8472	7.2356
4.35	12.323	6.970	8.482
4.40	13.3605	7.5946	-
4.50	15.6693	-	10.6505
4.60	18.3204	10.5333	-
4.65	19.7956	11.3813	13.1915
4.75	23.0197	13.2762	15.0997
4.88	-	-	17.1824
5.05	-	19.8442	21.8774
5.10	-	21.1117	23.1616
5.15	40.7072	22.4247	-

Continued/...

TABLE 66 (Continued)

Voltage (v)	Run 1	Run 2	Run 3 & 4
5.25	46.6197	25.1855	27.278
5.35	-	28.121	-
5.50	64.2934	32.8358	-
5.60	-	36.174	38.374
5.75	-	-	43.7321

TABLE 67 HOT FILM VOLTAGE AS A FUNCTION OF IMPELLER SPEED AT DIFFERENT POSITIONS IN THE TANK

Impeller Diameter = 3.6cm
Shaft Angle = -5^{o}
Liquid Depth = 15cm

Position no \ Impeller speed (RPM)	500	1000	1500	2000	2500	3000
1	3.20	3.40	3.70	3.90	4.10	4.75
2	4.10	4.40	4.75	5.00	5.25	5.50
3	3.60	3.80	4.00	4.25	4.40	4.65
6	4.45	3.70	3.95	4.25	4.50	4.75
8	3.00	3.15	3.30	3.45	3.60	3.85
9	3.40	3.60	3.80	3.95	4.15	4.35
10	3.90	4.10	4.40	4.60	5.25	5.50
11	2.90	3.05	3.20	3.40	3.55	3.70

TABLE 68 VOLTAGE AS A FUNCTION OF IMPELLER DIAMETER AT DIFFERENT POSITIONS IN THE TANK

Impeller Speed = 3000RPM
Shaft Angle = -5^{o}
Liquid Depth = 15 cm

Position no \ Impeller diameter (cm)	3.0	3.6	4.8	6.0	7.2
1	3.40	3.65	4.10	4.35	3.65
2	4.00	4.20	3.65	5.00	6.00
3	3.10	3.35	3.65	3.50	4.10
6	3.65	3.80	4.00	4.15	4.35
8	3.15	3.45	3.80	4.00	4.10
9	3.90	4.05	4.80	5.60	6.00
10	4.60	4.80	5.20	5.65	5.75
11	3.15	3.35	3.50	4.05	4.20

TABLE 69 VOLTAGE AS A FUNCTION OF SHAFT ANGLE AT DIFFERENT POSITIONS IN THE TANK

Impeller Shaft = 3000RPM
Impeller Diameter = 3.6cm
Liquid Depth = 15cm

Position no \ Shaft angle (degree)	-10	-5	0	+5
1	4.05	4.50	5.30	5.05
2	5.10	5.60	5.60	5.30
3	4.20	4.75	4.50	4.75
6	5.25	5.25	5.20	5.10
8	4.75	5.10	5.00	4.75
9	5.00	4.50	4.10	4.10
10	4.75	5.10	5.25	4.85
11	4.85	5.60	5.25	5.10

TABLE 70 VOLTAGE AS A FUNCTION OF LIQUID DEPTH AT DIFFERENT POSITIONS IN THE TANK

Impeller Speed = 3000RPM
Impeller Diameter = 3.6cm
Shaft Angle = -5^{o}

Position no \ Liquid depth (cm)	10	12.5	15	19	22
1	5.15	5.25	5.10	4.65	4.75
2	5.60	5.45	5.50	4.90	4.75
3	5.25	5.35	5.50	4.75	4.35
6	5.60	5.45	5.50	4.90	4.75
8	4.00	4.35	5.45	5.25	4.65
9	4.55	4.40	4.35	4.25	4.20
10	5.35	5.25	5.15	5.10	5.05
11	4.10	3.80	3.70	3.85	4.00

TABLE 71 FRICTION VELOCITY (cm/sec) AS A FUNCTION OF IMPELLER SPEED AT DIFFERENT POSITIONS IN THE TANK

Impeller Diameter = 3.6cm
Shaft Angle = -5^{o}
Liquid Depth = 15cm

Position no \ Impeller speed (RPM)	500	1000	1500	2000	2500	3000
1	0.406	0.491	0.641	0.762	0.903	1.517
2	0.903	1.156	1.517	1.819	2.160	2.536
3	0.592	0.699	0.829	1.023	1.156	1.407
6	0.515	0.641	0.795	1.023	1.252	1.517
8	0.326	0.386	0.448	0.515	0.592	0.725
9	0.491	0.592	0.699	0.795	0.941	1.110
10	0.762	0.903	1.156	1.353	2.160	2.536
11	0.285	0.360	0.406	2.191	0.562	0.641

TABLE 72 FRICTION VELOCITY (cm/sec) AS A FUNCTION OF IMPELLER DIAMETER AT DIFFERENT POSITIONS IN THE TANK

Impeller Speed = 3000RPM
Liquid Depth = 15cm
Shaft Angle = -5^{o}

Position no \ Impeller diameter cm	3.0	3.6	4.8	6.0	7.2
1	0.433	0.512	0.751	0.921	1.149
2	0.690	0.817	1.149	1.437	2.310
3	0.349	0.409	0.512	0.633	0.751
6	0.512	0.581	0.690	0.784	0.921
8	0.361	0.439	0.581	0.690	0.751
9	0.633	0.720	1.270	1.959	2.310
10	0.492	1.269	1.608	2.003	2.091
11	0.361	0.410	0.633	0.720	0.817

TABLE 73 FRICTION VELOCITY (cm/sec) AS A FUNCTION OF SHAFT ANGLE AT DIFFERENT POSITIONS IN THE TANK

Impeller Speed = 3000RPM
Impeller Diameter = 3.6cm
Liquid Depth = 15cm

Position no \ Shaft angle (degree)	-10^{o}	-5^{o}	0^{o}	$+5^{o}$
1	0.720	1.032	1.695	1.479
2	1.522	1.959	1.959	1.695
3	0.816	1.229	1.032	1.229
6	1.652	1.652	1.608	1.522
8	1.229	1.522	1.437	1.229
9	1.437	1.032	0.751	0.7514
10	1.229	1.522	1.652	1.311
11	1.311	1.959	1.652	1.522

TABLE 74 FRICTION VELOCITY (cm/sec) AS A FUNCTION OF LIQUID DEPTH AT DIFFERENT POSITIONS IN THE TANK

Impeller Speed = 3000RPM
Impeller Diameter = 3.6cm
Shaft Angle = -5^{o}

Position no \ Liquid depth (cm)	10	12.5	15	19	22
1	2.019	1.587	1.453	1.253	1.517
2	1.902	1.767	2.536	1.277	1.149
3	1.587	1.677	2.536	1.149	1.110
6	1.902	1.767	2.536	1.277	1.149
8	0.610	1.110	1.767	1.587	1.067
9	0.986	0.871	1.110	0.764	0.731
10	1.677	1.587	2.019	1.453	1.409
11	0.668	0.514	0.641	0.535	0.610

TABLE 75 THICKNESS OF THE VISCOUS SUB-LAYER (mm) AS A FUNCTION OF THE IMPELLER SPEED AT DIFFERENT POSITIONS IN THE TANK

Impeller Diameter = 3.6cm
Liquid Depth = 15cm
Shaft Angle = -5^{o}

Position no \ Impeller speed (RPM)	500	1000	1500	2000	2500	3000
1	1.23	1.017	0.780	0.656	0.554	0.329
2	0.553	0.432	0.329	0.274	0.23	0.197
3	0.845	0.714	0.602	0.488	0.432	0.355
6	0.971	0.780	0.629	0.488	0.399	0.329
8	1.533	1.294	1.1165	0.971	0.845	0.690
9	1.017	0.845	0.715	0.629	0.531	0.450
10	0.656	0.554	0.432	0.369	0.23	0.197
11	1.755	1.388	1.23	1.017	0.889	0.780

TABLE 76 THICKNESS OF THE VISCOUS SUB-LAYER (mm) AS A FUNCTION OF IMPELLER DIAMETER AT DIFFERENT POSITIONS IN THE TANK

Impeller Speed = 3000RPM
Liquid Depth = 15cm
Shaft Angle = -5^{o}

Position no \ Impeller diameter (cm)	3.0	3.6	4.8	6.0	7.2
1	1.155	0.976	0.665	0.543	0.435
2	0.724	0.612	0.435	0.348	0.484
3	1.431	1.220	0.976	0.789	0.2164
6	0.976	0.860	0.724	0.638	0.543
8	1.385	1.139	0.860	0.724	0.665
9	0.789	0.694	0.394	0.255	0.2146
10	1.017	0.394	0.311	0.249	0.239
11	1.385	1.22	0.789	0.694	0.6123

TABLE 77 THICKNESS OF THE VISCOUS SUB-LAYER (mm) AS A FUNCTION OF SHAFT ANGLE AT DIFFERENT POSITIONS IN THE TANK

Impeller speed = 3000RPM
Impeller Diameter = 3.6cm
Liquid Depth = 15cm

Position no \ Shaft angle (degree)	-10	-5	0	+5
1	0.694	0.484	0.295	0.33
2.	0.328	0.255	0.255	0.295
3	0.6123	0.407	0.484	0.407
6	0.303	0.303	0.311	0.328
8	0.407	0.328	0.348	0.407
9	0.348	0.484	0.665	0.668
10	0.407	0.328	0.303	0.381
11	0.381	0.255	0.303	0.328

TABLE 78 THICKNESS OF THE VISCOUS SUB-LAYER (mm) AS A FUNCTION OF LIQUID DEPTH AT DIFFERENT POSITIONS IN THE TANK

Impeller speed = 3000RPM
Impeller diameter = 3.6cm
Shaft Angle = -5^{o}

Position no \ Liquid depth (cm)	10	12.5	15	19	22
1	0.247	0.315	0.344	0.355	0.329
2	0.263	0.283	0.197	0.391	0.435
3	0.315	0.298	0.197	0.435	0.450
6	0.263	0.283	0.197	0.391	0.435
8	0.819	0.450	0.283	0.315	0.468
9	0.506	0.573	0.45	0.653	0.684
10	0.298	0.315	0.247	0.344	0.355
11	0.748	0.973	0.780	0.933	0.819

TABLE 79 VELOCITY DISTRIBUTION (cm/sec) ALONG THE JET AXIS AS A FUNCTION OF IMPELLER SPEED

r/δ: 0.0
Impeller Diameter: 3.6cm
Kinematic Velocity: 1.37×10^{-2} cm^2/sec

Distance (cm) \ Impeller Speed (RPM)	500	1000	1500	2000	2500	3000
15	15.00	29.99	45.00	59.99	74.99	90.00
20	14.27	28.53	42.81	57.07	71.33	85.61
25	13.57	27.13	40.72	54.28	67.85	81.44
30	12.91	25.81	38.73	51.64	64.54	77.46
35	12.28	24.55	36.84	49.12	61.39	73.69
40	11.68	23.35	35.05	46.72	58.40	70.09
45	11.11	22.22	33.34	44.44	55.55	66.67
50	10.57	21.13	31.71	42.28	52.84	63.42
55	10.05	20.10	30.16	40.22	50.27	60.33
60	9.56	19.12	28.69	38.25	47.81	57.39
65	9.10	18.19	27.29	36.39	45.48	54.95
70	8.65	17.30	25.96	34.61	43.26	51.93
75	8.23	16.46	24.70	32.93	41.14	49.39
80	7.83	15.66	23.40	31.32	39.15	46.98
85	7.45	14.89	22.35	29.79	37.24	44.69
90	7.09	14.18	21.26	28.34	35.42	42.51
95	6.74	13.47	20.22	26.96	33.69	40.41
100	6.41	12.82	19.23	25.64	32.05	38.47
105	6.10	12.19	18.30	24.39	30.49	36.59
110	5.80	11.60	17.40	23.20	29.00	34.81
115	5.52	11.03	16.55	22.07	27.59	33.11
120	5.25	10.40	15.75	20.99	26.26	31.49

TABLE 80 VELOCITY DISTRIBUTION (cm/sec) ALONG THE JET AXIS AS A FUNCTION OF IMPELLER SPEED

r/δ: 0.2
Impeller Diameter: 3.6cm
Kinematic Viscosity: 1.37×10^{-2} cm^2/sec

Distance (cm) \ Impeller Speed (RPM)	500	1000	1500	2000	2500	3000
15	15.00	29.99	45.00	59.99	74.09	90.00
20	14.24	28.48	42.73	56.97	71.21	85.46
25	13.53	27.05	40.60	54.12	67.65	81.19
30	12.86	25.71	38.58	51.44	64.29	77.17
35	12.23	24.45	36.68	48.91	61.13	73.37
40	11.63	23.25	34.89	46.51	58.14	69.78
45	11.06	22.12	33.19	44.25	55.31	66.38
50	10.53	21.05	31.59	42.11	52.64	63.17
55	10.02	20.04	30.07	40.08	51.10	60.13
60	9.54	19.08	28.62	38.16	47.70	57.25
65	9.09	18.16	27.26	36.34	45.42	54.52
70	8.65	17.30	25.96	34.61	43.26	51.92
75	8.24	16.48	24.73	32.97	41.21	49.47
80	7.85	15.70	23.57	31.42	39.27	47.13
85	7.49	14.97	22.46	29.94	37.42	44.91
90	7.13	14.26	21.40	28.54	35.67	42.81
95	6.80	13.60	20.40	27.20	34.00	40.81
100	6.48	12.96	19.45	25.93	32.42	38.91
105	6.18	12.36	18.55	24.73	30.91	37.10
110	5.90	11.79	17.69	23.58	29.48	35.38
115	5.62	11.24	16.87	22.49	28.12	33.75
120	5.36	10.73	16.10	21.46	26.82	32.19

TABLE 81 VELOCITY DISTRIBUTION (cm/sec) ALONG THE JET AXIS AS A FUNCTION OF IMPELLER SPEED

r/ : 0.4
Impeller Diameter: 3.6cm
Kinematic Viscosity: 1.37×10^{-2} cm^2/sec

Distance (cm) \ Impeller Speed (RPM)	500	1000	1500	2000	2500	3000
15	15.00	29.99	45.00	59.99	74.99	90.00
20	14.18	28.35	42.54	56.72	70.89	85.08
25	13.43	26.84	40.28	53.71	67.13	80.57
30	12.73	25.46	38.20	50.93	63.66	76.40
35	12.09	24.17	36.28	48.36	60.45	72.55
40	11.50	22.98	34.49	45.98	57.47	68.98
45	10.94	21.87	32.82	43.76	54.70	65.65
50	10.42	20.84	31.27	41.69	52.11	62.45
55	9.94	19.87	29.81	39.75	49.68	59.63
60	9.48	18.96	28.45	37.93	47.41	56.90
65	9.06	18.10	27.17	36.22	45.27	54.34
70	8.65	17.30	25.96	34.61	43.26	51.92
75	8.24	16.54	24.83	33.10	41.37	49.65
80	7.92	15.83	23.75	31.67	39.58	47.51
85	7.58	15.15	22.74	30.32	37.89	45.48
90	7.26	14.51	21.78	29.04	36.30	43.56
95	6.96	13.91	20.87	27.83	34.78	41.75
100	6.67	13.34	20.01	26.08	33.35	40.02
105	6.40	12.79	19.20	25.59	31.99	38.39
110	6.14	12.28	18.42	24.56	30.70	36.84
115	5.89	11.79	17.69	23.58	29.47	35.37
120	5.66	11.32	16.99	22.65	28.30	33.97

TABLE 82 VELOCITY DISTRIBUTION (cm/sec) ALONG THE JET AXIS AS A FUNCTION OF IMPELLER SPEED

r/ δ: 0.6
Impeller Diameter: 3.6cm
Kinematic Viscosity: 1.37×10^{-2} cm²/sec

Distance (cm) \ Impeller Speed (RPM)	500	1000	1500	2000	2500	3000
15	15.00	29.99	45.00	59.99	74.99	90.00
20	14.09	28.18	42.28	56.37	70.46	84.57
25	13.29	26.56	39.86	53.14	66.43	79.73
30	12.56	25.12	37.69	50.25	62.81	75.38
35	11.91	23.81	35.73	47.63	59.54	71.45
40	11.31	22.62	33.95	45.26	56.57	67.90
45	10.77	21.54	32.32	43.10	53.87	64.65
50	10.28	20.55	30.84	41.12	51.39	61.68
55	9.82	19.64	29.47	39.29	49.11	58.95
60	9.40	18.80	28.21	37.61	47.01	56.43
65	9.01	18.02	27.05	36.02	45.07	54.09
70	8.65	17.30	25.96	34.61	43.26	51.92
75	8.32	16.63	24.95	33.26	41.58	49.90
80	8.00	16.00	24.01	32.00	40.00	48.01
85	7.71	15.41	23.12	30.82	38.53	46.24
90	7.43	14.85	22.29	29.71	37.14	44.58
95	7.17	14.33	21.51	28.67	35.84	43.01
100	6.92	13.84	20.77	27.69	34.61	41.53
105	6.69	13.37	20.07	26.76	33.44	40.14
110	6.47	12.93	19.41	25.87	32.34	38.81
115	6.26	12.52	18.78	25.04	31.30	37.56
120	6.06	12.12	18.19	24.25	30.30	36.37

TABLE 83 VELOCITY DISTRIBUTION (cm/sec) ALONG THE JET AXIS AS A FUNCTION OF IMPELLER SPEED

r/ δ: 0.8
Impeller Diameter: 3.6cm
Kinematic Viscosity: 1.37×10^{-2} cm^2/sec

Distance (cm) \ Impeller Speed (RPM)	500	1000	1500	2000	2500	3000
15	15.00	29.99	45.00	59.99	74.99	90.00
20	14.00	28.00	42.01	56.01	70.01	84.02
25	13.14	26.27	39.41	52.55	65.68	78.83
30	12.38	24.75	37.14	49.52	61.90	74.29
35	11.71	23.42	35.14	46.85	58.56	70.29
40	11.12	22.24	33.37	44.49	55.61	66.74
45	10.60	21.19	31.79	42.39	52.98	63.59
50	10.13	20.25	30.38	40.51	50.63	60.77
55	9.70	19.40	29.11	38.81	48.51	58.22
60	9.32	18.63	27.96	37.28	46.60	55.92
65	8.97	17.94	26.92	35.88	44.85	53.83
70	8.65	17.30	25.96	34.61	43.26	51.92
75	8.36	16.71	25.08	33.44	41.80	50.17
80	8.09	16.18	24.27	32.36	40.45	48.52
85	7.84	15.68	23.53	31.36	39.20	47.01
90	7.61	15.21	22.83	30.44	38.04	55.66
95	7.39	14.78	22.18	29.57	36.96	43.36
100	7.19	14.37	21.57	28.76	35.94	43.16
105	7.00	13.99	21.00	27.99	34.99	41.99
110	6.82	13.63	20.46	27.27	34.09	40.91
115	6.65	13.29	19.95	26.59	33.24	39.89
120	6.49	12.97	19.46	25.95	32.43	38.93

TABLE 84 VELOCITY DISTRIBUTION (cm/sec) ALONG THE JET AXIS AS A FUNCTION OF IMPELLER SPEED

r/ δ: 1.0
Impeller Diameter: 3.6cm
Kinematic Viscosity: 1.37×10^{-2} cm²/ sec

Distance (cm) \ Impeller Speed (RPM)	500	1000	1500	2000	2500	3000
15	15.00	29.99	45.00	59.99	74.99	90.00
20	13.92	27.84	41.77	55.69	69.61	83.54
25	13.01	26.00	39.02	52.02	65.03	78.04
30	12.22	24.43	36.66	48.88	61.10	73.33
35	11.54	23.08	34.63	46.17	57.71	69.26
40	10.95	21.90	32.87	43.82	54.77	65.73
45	10.44	20.88	31.33	41.77	52.21	62.66
50	9.99	19.98	29.98	39.97	49.96	59.96
55	9.60	19.19	28.79	38.39	47.98	57.59
60	9.25	18.49	27.74	36.98	46.23	55.48
65	8.93	17.86	26.80	35.73	44.66	53.60
70	8.65	17.30	25.96	34.61	43.26	51.92
75	8.40	16.79	25.20	33.60	41.99	50.40
80	8.17	16.33	24.51	32.68	40.84	49.02
85	7.96	15.91	23.88	31.84	39.80	47.76
90	7.77	15.53	23.30	31.07	38.83	46.61
95	7.59	15.17	22.70	30.36	37.94	45.54
100	7.42	14.84	22.28	29.70	37.12	44.55
105	7.27	14.54	21.81	29.08	36.35	43.63
110	7.13	14.25	21.38	28.50	35.63	42.76
115	6.99	13.98	20.97	27.96	34.95	41.94
120	6.86	13.72	20.59	27.44	34.30	41.17

TABLE 85 VELOCITY DISTRIBUTION (cm/sec) ALONG THE JET AXIS AS A FUNCTION OF IMPELLER DIAMETER

r/ δ: 0.0
Impeller Speed: 3000RPM
Kinematic Velocity: $1.37 \times 10^{-2} cm^2/sec$

Distance (cm) \ Impeller Diameter (cm)	3.0	3.6	4.8	6.0	7.2
15	75.00	90.00	120.00	150.00	180.00
20	71.34	85.61	114.15	142.68	171.22
25	67.86	81.44	108.58	135.73	162.87
30	64.55	77.46	103.28	129.11	154.93
35	61.40	73.69	98.25	122.81	147.37
40	58.41	70.09	93.46	116.82	140.18
45	55.56	66.67	88.90	111.12	133.35
50	52.85	63.42	84.56	105.70	126.84
55	50.27	60.33	80.44	100.55	120.66
60	47.82	57.39	76.52	95.64	114.77
65	45.49	54.95	72.78	90.98	109.18
70	43.27	51.93	69.23	86.54	103.85
75	41.16	49.39	65.86	82.32	98.79
80	39.15	46.98	62.65	78.31	93.97
85	37.24	44.69	59.59	74.49	89.39
90	35.43	42.51	56.68	70.85	85.03
95	33.70	40.41	53.92	67.40	80.88
100	32.06	38.47	51.29	64.11	76.93
105	30.49	36.59	48.79	60.99	73.18
110	29.01	34.81	46.41	58.01	69.61
115	27.59	33.11	44.15	55.18	66.22
120	26.25	31.49	41.99	52.49	62.99

TABLE 86 VELOCITY DISTRIBUTION (cm/sec) ALONG THE JET AXIS AS A FUNCTION OF IMPELLER DIAMETER

r/ δ: 0.2
Impeller speed: 3000RPM
Kinematic Viscosity: $1.37 \times 10^{-2} cm^2/sec$

Distance (cm) \ Impeller Diameter (cm)	3.0	3.6	4.8	6.0	7.2
15	75.00	90.00	120.00	150.00	180.00
20	71.22	85.46	113.95	142.44	170.92
25	67.66	81.19	108.25	135.32	162.38
30	64.30	77.17	102.89	128.61	154.33
35	61.14	73.37	97.82	122.28	146.73
40	58.15	69.78	93.04	116.30	139.56
45	55.32	66.38	88.51	110.64	132.77
50	52.64	63.17	84.23	105.29	126.35
55	50.11	60.13	80.18	100.22	120.26
60	47.71	57.25	76.33	95.42	114.50
65	45.43	54.52	72.69	90.86	109.03
70	43.27	51.92	69.23	86.54	103.85
75	41.22	49.47	65.95	82.44	98.93
80	39.28	47.13	62.84	78.55	94.26
85	37.43	44.91	59.88	74.86	89.83
90	35.67	42.81	57.08	71.35	85.62
95	34.01	40.81	54.41	68.01	81.61
100	32.42	38.91	51.87	64.84	77.81
105	30.91	37.10	49.46	61.83	74.20
110	29.48	35.38	47.17	58.97	70.76
115	28.12	33.75	44.99	56.24	67.49
120	26.83	32.19	42.92	53.65	64.38

TABLE 87 VELOCITY DISTRIBUTION (cm/sec) ALONG THE JET AXIS AS A FUNCTION OF IMPELLER DIAMETER

r/ δ: 0.4.
Impeller Speed: 3000RPM
Kinematic Viscosity: 1.37×10^{-2} cm²/sec

Distance (cm) \ Impeller Diameter (cm)	3.0	3.6	4.8	6.0	7.2
15	75.00	90.00	120.00	150.00	180.00
20	70.90	85.08	113.44	141.80	170.16
25	67.14	80.57	107.42	134.28	161.13
30	63.67	76.40	101.87	127.34	152.81
35	60.46	72.55	96.74	120.92	145.11
40	57.48	68.98	91.97	114.96	137.95
45	54.70	65.65	87.53	109.41	131.29
50	52.11	62.54	83.38	104.23	125.07
55	49.69	59.63	79.50	99.38	119.25
60	47.42	56.90	75.87	94.83	113.80
65	45.28	54.34	72.45	90.56	108.67
70	43.27	51.92	69.23	86.54	103.85
75	41.38	49.65	66.20	82.75	99.30
80	39.59	47.51	63.34	79.18	95.01
85	37.90	45.48	60.64	75.80	90.96
90	36.30	43.56	58.08	72.60	87.12
95	34.79	41.75	55.66	69.58	83.49
100	33.35	40.02	53.37	66.71	80.05
105	31.99	38.39	51.19	63.99	76.78
110	30.70	36.84	49.12	61.40	73.68
115	29.48	35.37	47.16	58.95	70.74
120	28.31	33.97	45.29	56.62	67.94

TABLE 88 VELOCITY DISTRIBUTION (cm/sec) ALONG THE JET AXIS AS A FUNCTION OF IMPELLER DIAMETER . . .

r/ δ: 0.6
Impeller Speed: 3000RPM
Kinematic Viscosity: $1.37 \times 10^{-2} cm^2/sec$

Distance (cm) \ Impeller Diameter (cm)	3.0	3.6	4.8	6.0	7.2
15	75.00	90.00	120.00	150.00	180.00
20	70.47	84.57	117.60	140.95	169.14
25	66.44	79.73	106.30	132.88	159.45
30	62.82	75.38	100.50	125.63	150.76
35	59.55	71.45	95.27	119.09	142.91
40	56.58	67.90	90.53	113.16	135.79
45	53.87	64.65	86.20	107.73	129.30
50	51.40	61.68	82.24	102.80	123.36
55	49.12	58.95	78.70	98.23	117.90
60	47.02	56.43	75.24	94.05	112.85
65	45.08	54.09	72.12	90.15	108.19
70	43.27	51.92	69.23	86.54	103.85
75	41.58	49.90	66.53	83.17	99.80
80	40.01	48.01	64.02	80.02	96.02
85	38.53	46.24	61.65	77.02	92.48
90	37.15	44.58	59.44	74.29	89.15
95	35.84	43.01	57.35	71.68	86.02
100	34.61	41.53	55.38	69.29	83.07
105	33.45	40.14	53.52	66.89	80.27
110	32.35	38.81	51.75	64.69	77.63
115	31.30	37.56	50.08	62.60	75.12
120	30.31	36.37	48.49	60.62	72.74

TABLE 89 VELOCITY DISTRIBUTION (cm/sec) ALONG THE JET AXIS AS A FUNCTION OF IMPELLER DIAMETER

r/ δ: 0.8
Impeller Speed: 3000RPM
Kinematic Viscosity: 1.37×10^{-2} cm²/sec

Distance (cm) \ Impeller Diameter (cm)	3.0	3.6	4.8	6.0	7.2
15	75.00	90.00	120.00	150.00	180.00
20	70.02	84.02	112.30	140.06	168.05
25	65.69	78.83	105.11	131.38	157.66
30	61.90	74.29	99.05	123.81	148.57
35	58.57	70.29	93.72	117.14	140.57
40	55.62	66.74	88.99	111.24	133.49
45	52.99	63.59	84.79	105.99	127.18
50	50.64	60.77	81.02	101.28	121.53
55	48.52	58.22	77.63	97.04	116.45
60	46.60	55.92	74.57	93.21	111.85
65	44.86	53.83	71.78	89.72	107.67
70	43.27	51.92	69.23	86.54	103.84
75	41.81	50.17	66.89	83.61	100.34
80	40.46	48.52	64.73	80.92	97.10
85	39.21	47.01	62.73	78.42	94.10
90	38.65	55.66	60.88	76.10	91.32
95	36.96	43.36	59.14	73.93	88.72
100	35.95	43.14	57.52	71.90	86.28
105	35.00	41.99	55.99	69.99	83.99
110	34.10	40.91	54.55	68.19	81.83
115	33.24	39.89	53.19	66.49	79.79
120	32.44	38.93	51.90	64.87	77.85

TABLE 90 VELOCITY DISTRIBUTION (cm/sec) ALONG THE JET AXIS AS A FUNCTION OF IMPELLER DIAMETER

r/δ : 1.00
Imeplller Speed: 3000RPM
Kinematic Viscosity: $1.37 \times 10^{-2} cm^2/sec$

Distance (cm) \ Impeller Diameter (cm)	3.0	3.6	4.8	6.0	7.2
15	75.00	90.00	120.00	150.00	180.00
20	69.62	83.54	111.39	139.24	167.09
25	65.04	78.04	104.06	130.07	156.09
30	61.11	73.33	97.77	122.21	146.65
35	57.72	69.26	92.35	115.43	138.52
40	54.78	65.73	87.65	109.56	131.47
45	52.22	62.66	83.55	104.43	125.32
50	49.97	59.96	79.95	99.94	119.93
55	47.99	57.59	76.79	95.98	115.18
60	46.23	55.48	73.98	92.47	110.97
65	44.67	53.60	71.47	89.34	107.21
70	43.27	51.92	69.23	86.54	103.84
75	42.00	50.40	67.20	84.00	100.80
80	40.85	49.02	65.36	81.70	98.05
85	39.80	47.76	36.68	79.61	95.53
90	38.84	46.61	62.14	77.68	93.22
95	37.95	45.54	60.72	75.90	91.08
100	37.13	44.55	59.40	74.25	89.10
105	36.36	43.63	58.17	72.71	87.25
110	35.63	42.76	57.01	71.27	85.52
115	34.95	41.94	55.92	69.90	83.88
120	34.31	41.17	54.89	68.62	82.34

TABLE 91 SHEAR STRESS (gm/cm sec ^{2}) ALONG THE JET AS A FUNCTION OF IMPELLER SPEED

Impeller Diameter: 3.6cm
Kinematic Viscosity: 1.37×10^{-2} cm^{2}/sec

Distance (cm) \ Impeller Speed (RPM)	500	1000	1500	2000	2500	3000
5	1.061	2.998	5.510	8.483	11.855	15.586
10	0.750	2.120	3.896	5.998	8.383	11.021
15	0.611	1.726	3.174	4.887	6.828	8.998
20	0.487	1.395	2.529	3.893	5.440	7.207
25	0.402	1.147	2.086	3.212	4.489	5.909
30	0.339	0.968	1.765	2.717	3.796	4.998
35	0.293	0.834	1.521	2.341	3.273	4.307
40	0.256	0.728	1.332	2.050	2.864	3.768
45	0.227	0.645	1.180	1.816	2.538	3.339
50	0.203	0.577	1.056	1.626	2.273	2.990
55	0.184	0.522	0.954	1.470	2.054	2.702
60	0.167	0.475	0.869	1.338	1.871	2.460
65	0.153	0.435	0.797	1.227	1.716	2.256
70	0.142	0.401	0.736	1.133	1.583	2.081
75	0.1313	0.372	0.682	1.050	1.467	1.930
80	0.1223	0.346	0.636	0.989	1.367	1.798
85	0.114	0.324	0.595	0.916	1.279	1.683
90	0.108	0.304	0.558	0.859	1.201	1.579
95	0.101	0.287	0.526	0.810	1.132	1.488
100	0.096	0.271	0.497	0.765	1.069	1.406
105	0.091	0.257	0.471	0.725	1.013	1.332
110	0.086	0.244	0.447	0.688	0.962	1.265
115	0.082	0.232	0.425	0.655	0.915	1.203
120	0.078	0.221	0.406	0.621	0.873	1.147

TABLE 92 SHEAR STRESS (gm/cm sec^2) ALONG THE JET AS A FUNCTION OF IMPELLER DIAMETER

Impeller Speed: 3000RPM
Kinematic Viscosity: 1.37×10^{-2} cm^2/sec

Distance (cm) \ Impeller Diameter (cm)	3.0	3.6	4.8	6.0	7.2
5	11.855	15.586	23.992	33.538	44.088
10	8.383	11.021	16.969	23.714	31.174
15	6.828	8.998	13.825	19.322	25.399
20	5.440	7.207	11.014	15.388	20.234
25	4.489	5.909	9.087	12.704	16.696
30	3.796	4.998	7.687	10.742	14.119
35	3.273	4.307	6.626	9.256	12.172
40	2.864	3.768	5.798	8.098	10.652
45	2.538	3.339	5.138	7.178	9.439
50	2.273	2.990	4.600	6.427	8.453
55	2.054	2.702	4.158	5.813	7.639
60	1.871	2.460	3.787	5.294	6.958
65	1.716	2.256	3.473	4.851	6.380
70	1.583	2.081	3.204	4.475	5.886
75	1.467	1.930	2.972	4.152	5.458
80	1.367	1.798	2.768	3.853	5.086
85	1.279	1.683	2.589	3.606	4.758
90	1.201	1.579	2.432	3.388	4.468
95	1.132	1.488	2.291	3.192	4.209
100	1.069	1.406	2.177	3.015	3.977
105	1.013	1.332	2.051	2.858	3.768
110	0.962	1.265	1.947	2.716	3.578
115	0.915	1.203	1.855	2.583	3.404
120	0.873	1.147	1.768	2.463	3.246

TABLE 93 FRICTION VELOCITY (cm/sec) ALONG THE JET AS A FUNCTION OF IMPELLER SPEED

Impeller Diameter: 3.6cm
Kinematic Viscosity: 1.37×10^{-2} cm^2/sec

Distance (cm) \ Impeller Speed (RPM)	500	1000	1500	2000	2500	3000
5	0.991	1.667	2.260	2.804	3.314	3.800
10	0.834	1.402	1.900	2.357	2.787	3.196
15	0.753	1.265	1.715	2.128	2.518	2.888
20	0.672	1.137	1.531	1.899	2.246	2.584
25	0.610	1.031	1.391	1.725	2.039	2.340
30	0.561	0.947	1.279	1.587	1.876	2.152
35	0.521	0.879	1.187	1.473	1.742	1.998
40	0.487	0.822	1.111	1.378	1.629	1.869
45	0.458	0.773	1.046	1.297	1.534	1.759
50	0.434	0.732	0.989	1.228	1.451	1.665
55	0.413	0.695	0.941	1.167	1.379	1.583
60	0.394	0.663	0.898	1.114	1.317	1.510
65	0.377	0.635	0.860	1.067	1.261	1.446
70	0.362	0.610	0.826	1.024	1.211	1.389
75	0.349	0.587	0.795	0.987	1.166	1.337
80	0.337	0.567	0.767	0.952	1.126	1.291
85	0.326	0.548	0.742	0.921	1.089	1.249
90	0.316	0.531	0.719	0.893	1.055	1.210
95	0.306	0.515	0.698	0.866	1.024	1.174
100	0.297	0.501	0.678	0.842	0.996	1.142
105	0.290	0.488	0.661	0.819	0.969	1.111
110	0.283	0.475	0.644	0.798	0.944	1.083
115	0.276	0.463	0.628	0.779	0.921	1.056
120	0.269	0.453	0.613	0.761	0.899	1.031

TABLE 94 FRICTION VELOCITY (cm/sec) ALONG THE JET AS A FUNCTION OF IMPELLE DIAMETER

Impeller Speed: 3000RPM
Kinematic Viscosity: 1.37×10^{-2} cm^2/sec

Distance (cm) \ Impeller Diameter (cm	3.0	3.6	4.8	6.0	7.2
5	3.314	3.800	4.716	5.575	6.392
10	2.787	3.196	3.966	4.688	5.371
15	2.518	2.888	3.579	4.232	4.852
20	2.246	2.584	3.195	3.776	4.331
25	2.039	2.340	2.902	3.431	3.934
30	1.876	2.152	2.669	3.155	3.618
35	1.742	1.998	2.478	2.929	3.359
40	1.629	1.869	2.318	2.740	3.142
45	1.534	1.759	2.182	2.579	2.958
50	1.451	1.665	2.065	2.441	2.799
55	1.379	1.583	1.963	2.321	2.661
60	1.317	1.510	1.874	2.215	2.539
65	1.261	1.449	1.794	2.120	2.432
70	1.211	1.389	1.723	2.037	2.336
75	1.166	1.337	1.659	1.962	2.249
80	1.126	1.291	1.602	1.889	2.171
85	1.089	1.249	1.549	1.828	2.100
90	1.055	1.210	1.501	1.772	2.035
95	1.024	1.174	1.457	1.720	1.975
100	0.996	1.142	1.421	1.672	1.920
105	0.969	1.111	1.379	1.627	1.869
110	0.944	1.083	1.344	1.587	1.821
115	0.921	1.056	1.311	1.547	1.776
120	0.899	1.031	1.280	1.511	1.734

TABLE 95 THICKNESS OF THE VISCOUS SUB-LAYER (mm) ALONG THE JET AXIS AS A FUNCTION OF IMPELLER SPEED

r/δ : 1.00
Impeller Diameter: 3.6cm
Kinematic Viscosity: 1.37×10^{-2} cm^2/sec

Distance (cm) \ Impeller Speed (RPM)	500	1000	1500	2000	2500	3000
5	0.6909	0.4109	0.3031	0.2443	0.2067	0.1802
10	0.8216	0.4886	0.3605	0.2906	0.2457	0.2143
15	0.9102	0.5414	0.3993	0.3218	0.2723	0.2372
20	1.0200	0.6024	0.4474	0.3606	0.3051	0.2651
25	1.1256	0.6643	0.4926	0.3970	0.3358	0.2927
30	1.2209	0.7230	0.5356	0.4317	0.3652	0.3183
35	1.3152	0.7793	0.5768	0.4650	0.3933	0.3429
40	1.406	0.8335	0.6166	0.4970	0.4205	0.3665
45	1.4935	0.8858	0.6551	0.5280	0.4466	0.3894
50	1.5782	0.9363	0.6922	0.5580	0.4720	0.4115
55	1.6597	0.9852	0.7282	0.5869	0.4965	0.4329
60	1.7390	1.0325	0.7630	0.6150	0.5202	0.4536
65	1.8166	1.0785	0.7968	0.6422	0.5432	0.4737
70	1.8913	1.1230	0.8296	0.6686	0.5656	0.4933
75	1.9636	1.1665	0.8614	0.6943	0.5873	0.5121
80	2.0342	1.2086	0.8924	0.7192	0.6085	0.5306
85	2.1032	1.2496	0.9226	0.7436	0.6290	0.5485
90	2.1700	1.2895	0.9522	0.7673	0.6492	0.5661
95	2.2360	1.3288	0.9809	0.7906	0.6688	0.5833
100	2.3012	1.3671	1.0093	0.8133	0.6880	0.6000
105	2.3635	1.4043	1.0368	0.8356	0.7069	0.6166
110	2.4248	1.4412	1.0639	0.8576	0.7256	0.6327
115	2.4862	1.4774	1.0907	0.8791	0.7437	0.6486
120	2.5467	1.5133	1.1169	0.9005	0.7616	0.6643

TABLE 96 THICKNESS OF THE VISCOUS SUB-LAYER (mm) ALONG THE JET AXIS AS A FUNCTION OF IMPELLER DIAMETERS

r/δ : 1.00
Impeller Speed: 3000RPM
Kinematic Viscosity: 1.37×10^{-2} cm²/sec

Distance (m) \ Impeller Diameter (cm)	3.0	3.6	4.8	6.0	7.2
5	0.2067	0.1802	0.1453	0.1228	0.1071
10	0.2457	0.2143	0.1727	0.1461	0.1274
15	0.2723	0.2372	0.1914	0.1619	0.1412
20	0.3051	0.2651	0.2144	0.1814	0.1582
25	0.3358	0.2927	0.2360	0.1996	0.1741
30	0.3652	0.3183	0.2566	0.2171	0.1894
35	0.3933	0.3428	0.2764	0.2339	0.2040
40	0.4205	0.3665	0.2955	0.2500	0.2180
45	0.4466	0.3894	0.3139	0.2656	0.2316
50	0.4720	.4115	0.3317	0.2806	0.2447
55	0.4965	0.4329	0.3489	0.2951	0.2575
60	0.5202	0.4536	0.3656	0.3092	0.2698
65	0.5432	0.4737	0.3818	0.3231	0.2817
70	0.5656	0.4933	0.3975	0.3363	0.2933
75	0.5873	0.5121	0.4128	0.3492	0.3046
80	0.6085	0.5306	0.4276	0.3625	0.3155
85	0.6290	0.5486	0.4421	0.3747	0.3262
90	0.6491	0.5661	0.4562	0.3865	0.3366
95	0.6688	0.5832	0.4700	0.3982	0.3468
100	0.6880	0.600	0.4822	0.4098	0.3568
105	0.7069	0.6166	0.4968	0.4209	0.3666
110	0.7256	0.6327	0.5099	0.4317	0.3762
115	0.7437	0.6486	0.5225	0.4427	0.3856
120	0.7616	0.6643	0.5351	0.4534	0.3950

TABLE 97 EFFECT OF IMPELLER SPEED ON THE LAYER

Impeller Speed (RPM)	Electro-chemical Thickness (mm)	Hot-film anemometer THickness (mm)
500	0.995	1.07
1000	0.708	0.88
1500	0.624	0.72
2000	0.553	0.61
2500	0.433	0.51
3000	0.349	0.41

Average deviation : 13%

TABLE 98 EFFECT OF DIAMETER ON THE VISCOUS SUB-LAYER

Impeller Diameter cm	Electro-chemical Thickness (mm)	Hot-film anemometer Thickness (mm)
3.0	0.924	1.11
3.6	0.707	0.89
4.8	0.479	0.65
6.0	0.4003	0.53
7.2	0.369	0.43

Average deviation : 20%

TABLE 99 EFFECT OF SHAFT ANGLE ON THE THICKNESS

Shaft Angle (degrees)	Electro-chemical Thickness (mm)	Hot-film anemometer Thickness (mm)
-10	0.336	0.43
-5	0.278	0.355
0	0.294	0.37
+5	0.326	0.395
+10	0.385	0.41

Average deviation : 17%

TABLE 100 EFFECT OF LIQUID DEPTH ON THE THICKNESS

Liquid Depth (cm)	Electro-chemical Thickness (mm)	Hot-film anemometer Thickness (mm)
10	0.264	0.43
13	0.387	0.435
16	0.339	0.33
20	0.372	0.475
25	0.316	0.49

Average deviation : 21%

TABLE 101 THICKNESS OF THE VISCOUS SUB-LAYER ESTIMATED FROM THE MATHEMATICAL MODEL FOR THE MODEL TANK

Z	$\frac{Z}{D}$	δv
10	0.08333	0.2143
15	0.125	0.2372
20	0.1666	0.2651
30	0.25	0.3183
40	0.333	0.3665
50	0.41666	0.4115
60	0.50	0.4536
70	0.5833	0.4933
80	0.666	0.5306
90	0.75	0.5661
100	9.833	0.600
110	0.9166	0.6327
120	1.00	0.6643

TABLE 102 THICKNESS OF THE VISCOUS SUB-LAYER ESTIMATED FROM THE MATHEMATICAL MODEL FOR THE FULL-SCALE TANK

Z	$\frac{Z}{D}$	δv
1	.01266	4.55
6	.07595	5.273
11	..13924	5.8584
16	..2025	6.282
21	.2658	6.64
26	.329	6.951
31	.3924	7.226
36	.4557	7.47
41	.5189	7.698
46	.5823	7.906
51	.64556	8.10
56	.70886	8.278
61	.77215	8.446
66	.83544	8.606
71	.8987	8.756

Continued/..

TABLE 102 (Continued)

Z	$\frac{Z}{D}$	δ_V
76	..962	8.898
79	1.00	8.994

TABLE A2.1 VISCOSITY AND DENSITY AS A FUNCTION OF PERCENTAGE OF NaCl ONLY

% Nacl	Density (gm/cm^3)	$\mu \times 10^2$ (gm/cm sec)	$\gamma \times 10^2$ (cm^2/sec)
0.0	1.076	1.4827	1.378
0.5	1.081	1.527	1.413
1.0	1.086	1.5388	1.417
1.5	1.091	1.554	1.425
2.0	1.092	1.566	1.429
2.5	1.101	1.585	1.440
3.0	1.106	1.601	1.448
3.5	1.111	1.6187	1.457
4.0	1.116	1.637	1.467
5.0	1.126	1.6833	1.495
6.0	1.136	1.7096	1.505
7.0	1.146	1.739	1.518
8.0	1.156	1.805	1.562
10.0	1.176	1.891	1.608
12.0	1.196	2.008	1.679
14.0	1.216	2.097	1.725
16.0	1.236	2.215	1.792
18.0	1.256	2.365	1.883
20.0	1.276	2.535	1.987
22.0	1.296	2.605	2.01

TABLE A2.2 VISCOSITY AND DENSITY OF SOLUTION AS A FUNCTION OF PERCENTAGLE OF ETHANOL AND NaCl

% NaCl	% Ethanol	Density (gm/cm^3)	$\mu \times 10^2$ (gm/cm sec)	$\gamma \times 10^2$ (cm^2/sec)
0.0	0.0	1.079	1.4868	1.378
0.0	10.0	1.0467	1.9856	1.897
0.0	15.0	1.0331	2.2439	2.172
0.0	20.0	1.0209	2.5165	2.465
0.0	25.0	1.0098	2.6456	2.620
0.0	30.0	0.9998	2.8614	2.862
0.0	35.0	0.9904	2.9543	2.983
5.0	5.0	1.1089	1.9117	1.724
5.0	10.0	1.091	2.1634	1.983
5.0	15.0	1.0751	2.4093	2.241
5.0	20.0	1.0608	2.7432	2.586
5.0	25.0	1.0478	2.8898	2.758
5.0	30.0	1.036	3.0365	2.931
10.0	5.0	1.1559	2.092	1.81
10.0	10.0	1.1355	2.388	2.103
10.0	15.0	1.1171	2.6386	2.362
10.0	20.0	1.1007	2.8464	2.586
10.0	25.0	1.0858	3.0326	2.793
15.0	15.0	1.1592	2.9583	2.552
20.0	5.0	1.250	2.715	2.172
20.0	10.0	1.2242	2.9552	2.414

TABLE A2.3 VISCOSITY OF SOLUTION AS A FUNCTION OF PERCENTAGE OF ETHANOL AND NaCl

Density Change within 7% only

% NaCl	% Ethanol	Density (gm/cm^3)	$\mu \times 10^2$ (gm/cm sec)
0.0	10.0	1.0467	1.9856
0.0	15.0	1.0331	2.2439
0.0	20.0	1.0209	2.5165
0.0	25.0	1.0098	2.6456
5.0	15.0	1.0751	2.4093
5.0	20.0	1.0608	2.7432
5.0	25.0	1.0478	2.758
5.0	30.0	1.036	3.0365
10.0	25.0	1.0858	3.0326

TABLE A2.4 DENSITY OF SOLUTION AS A FUNCTION OF PERCENTAGE OF ETHANOL AND NaCl

Viscosity change within 1.7%

% NaCl	% Ethanol	$\mu \times 10^2$ (gm/cm sec)	Density (gm/cm^3)
0.0	35.0	2.9543	0.9904
5.0	27.0	2.940	1.041
10.0	22.0	2.905	1.095
15.0	15.0	2.958	1.159
20.0	10.0	2.955	1.224

TABLE A2.5 VISCOSITY OF SOLUTION AS A FUNCTION OF PERCENTAGE OF GUM ARABIC

Density change within 10%

% Gum Arabic	Density (gm/cm^3)	$\mu \times 10^2$ (gm/cm sec)	$\gamma \times 10^2$ cm^2/sec
0.0	1.079	1.4868	1.378
0.5	1.084	1.529	1.4107
1.0	1.089	1.6139	1.482
2.0	1.099	1.766	1.607
3.0	1.109	2.000	1.8036
4.0	1.119	2.118	1.893
5.0	1.129	2.258	2.000
7.0	1.149	3.139	2.732
10.0	1.179	3.579	3.036
12.0	1.199	5.438	4.536

TABLE A2.6 VISCOSITY OF THE SOLUTION AS A FUNCTION OF PERCENTAGE OF POLYETHYLENE OXIDE

Density change within 0.95%

% polyethylene oxide	Density (gm/cm^3)	$\mu \times 10^2$ (gm/cm sec)	$\gamma \times 10^2$ (cm^2/sec)
0.0	1.045	1.139	1.09
0.25	1.0475	3.104	2.963
0.50	1.05	7.206	6.863
0.75	1.0525	12.43	11.81
1.00	1.055	14.833	14.06

TABLE A2.7 DENSITY OF THE SOLUTION AS A FUNCTION OF PERCENTAGE OF NaOH and NaCl

NaOH Molarity M	% NaCl	Density (gm/cm^3)	$\mu \times 10^2$ (gm/cm sec)	$\gamma \times 10^2$ (cm^2/sec)
1.0	0.0	1.045	1.139	1.09
1.0	5.0	1.095	1.293	1.181
1.0	10.0	1.145	1.436	1.254
1.0	15.0	1.195	1.607	1.345
1.0	20.0	1.245	1.813	1.456
1.5	0.0	1.065	1.246	1.172
1.5	5.0	1.115	1.388	1.245
1.5	10.0	1.165	1.556	1.336
1.5	15.0	1.215	1.755	1.445
1.5	20.0	1.265	1.954	1.545
2.0	0.0	1.085	1.495	1.378
2.0	5.0	1.135	1.697	1.495
2.0	10.0	1.185	1.905	1.608
2.0	15.0	1.235	2.173	1.76
2.0	20.0	1.285	2.553	1.987
2.5	0.0	1.105	1.597	1.445
2.5	5.0	1.155	1.826	1.581
2.5	10.0	1.205	2.103	1.745
2.5	15.0	1.255	2.396	1.909
2.5	20.0	1.305	Insoluble	
3.0	0.0	1.125	2.696	1.863
3.0	5.0	1.175	2.403	2.045
3.0	10.0	1.225	2.873	2.345
3.0	15.0	I N S O L U B L E		

TABLE A2.8 DENSITY OF THE SOLUTION AS A FUNCTION OF PERCENTAGE OF NaCl AND CONCENTRATION OF NaOH

Viscosity change within 3%

NaOH (M)	% NaCl	Density (gm/cm^3)	$\mu \times 10^2$ (gm/cm sec)	$\gamma \times 10^2$ (cm^2/sec)
1.0	0.0	1.046	1.782	1.704
2.7	0.0	1.113	1.780	1.61
2.5	4.5	1.150	1.781	1.551
1.5	15.0	1.215	1.755	1.445
1.0	20.0	1.245	1.813	1.456

NOTATIONS

A	Area of Electrode
C	Constant
C_A	Concentration of Solution
C_b	Concentration of Bulk
C_i	Concentration of Interface
D	Diffusivity Coefficient
D_r	Drag Coefficient
E	Eddy Viscosity
E_ψ	Eddy Diffusivity of Potential Field
E_D	Eddy Diffusivity of Mass
F	Farady number
I	Electrical current
K, K_1	Con stants
K', K'	Impeller Constants
K	Mass Transfer Coefficient
$\overline{K}$	Average Mass Transfer Coefficient
K'	Fluctuation in the Mass Transfer Coefficint
$\overline{K}_\alpha$	Average Mass Transfer Coefficinet for Fully Developed Flow
L	Length of Mass Transfer Section
M	Momentum
N	Impeller Speed
N_A	Rate of Mass Transfer
N_{Gr}	Grashof Number

N_{Re}	Reynolds Number
N_{Sc}	Schmidt Number
N_{Sh}	Nusselt Number
P_i	Power Consumed
P_Z	Pressure Gradient in the Z direction
P_ϕ	Pressure Gradient in the ϕ direction
P_r	Pressure Gradient in the r direction
Q	Flow rate
Q_o	Flow rate through nozzle
Q_{prop}	Flow rate at a propeller
R	Gas Constant
R_1	Probe hot resistance
R_{Tot}	Probe resistance at 20^oC
R_{20}	Sensor resistance at 20^oC
S	Velocity Gradient
T	Tank Diameter
T_e	Temperature
T_{eo}	Ambient Temperature
T_{es}	Selected Sensor Temperature
T	Period of the Sub-layer Build-up
T^+	Dimensionless $T=U^* \frac{T}{\gamma}$
V	Average Velocity
V_B	Turbulent Velocity Outside the Sub-layer
V_B^+	Dimensonless V_B
V_{max}	Maximum Velocity

V_s	Settling Velocity
V_Z	Z Velocity Component at the Edge of the Jet
V_ϕ	ϕ Velocity Component at the Edge of the Jet
V_r	r Velocity Component at the Edge of the Jet
V^+	Dimensionless $V = \frac{V}{U*}$
U*	Friction Velocity
W	Blade Width
Y	Linear Dimension
Y^+	Dimensionless $Y = Y\frac{U*}{\gamma}$
Z,ϕ,r	Cylindrical Coordinates
Z_L	Liquid Depth
a_{20}	Temperature Coefficient of Sensor at 20^oC
c	Concentration
d	Impeller Diameter
d_o	Jet Diameter
d_e	Electrode Diameter
d_p	Particle Diameter
f	Velocity Function
g	Gravity Acceleration
l	Linear dimension
m	Constant
n	Electrone Number
q	Pumping Capacity
t	Time
$\hat{v}_z, \hat{v}_\phi, \hat{v}_r$	Fluctuations in the z, ,r Velocity Components.

Greek Letters

α	Shaft Angle
Θ	Mixing Time
ρ	Density of Solution
ρ_s	Density of Solids
μ	Viscosity of Solution
γ	Kinematic Velocity
Ψ	Potential Field
δ	Jet Width
δ_1	Displacement Thickness
δ_2	Momentum Thickness
δ_c	Concentration Boundary Layer Thickness
$\delta(x)$	Boundary Layer Thickness
δ_v	Viscous Sub-layer Thickness
τ	Shear Stress
τ_w	Wall Shear Stress

Subscript

o	Jet
e	Electrode
+	Dimensionless
∞	Fully Developed Flow
prop	Propeller
tur	Turbine
Turb	Turbulent
w	Wall
z, ϕ, r	Direction

REFERENCES

1. VONKEN, R.M., British Chem.Eng., 10, 12, Part 1 (1965)

2. UHL, V.W. and GRAY, J.B., "Mixing - Theory and Practice" Volume 1, Academic Press, (1966)

3. FOSSETTE, H.,,Inst.Chem.Engrs., 29, 321, (1951)

4. RUSHTON, J.H. Petroleum Refiner, 33,101, (1954)

5. KRAMERS, H., BARRS, G.H., and KNOLL, W.H., Chem.Eng. Science, 2, 35, (1953)

6. HOLMES, D.B., VONCKEN, R.M., and DEKKER, J.A., Chem.Eng. Science, 19, 209, (1964)

7. BIGGS, R.D., A.I.Ch.E. Journal, 5, 636, (1963)

8. NORWOOD, K.W., and METZNER, A.B., A.I.Ch.E. Journal, 6, 432, (1960)

9. YUGE, K., and O'SHIMA, E., J. of Chem.Eng. of Japan, 8, 151, (1975)

10. DOYLE, K., "Mixing in Large Tanks", Ph.D. Thesis, Aston University, (1974)

11. FOX, E.A., and GEX V.E., A.I.Ch.E. Journal, 2, 539 (1956)

12. VAN DE VUSSE, J.G., Chem.Eng. Science, 4, 178 (1955)

13. GLUZ, M.D. and PAVLUSHEMKON, I.S., Zh.Priki.Khim., 39, 2719 (1966)

14. RUSHTON, J.H. MACK, D.E., and EVERETT, J.H., Trans.Am. Inst.Chem.Engrs., 42, 44, (1946)

15. SACKS, J.P. and RUSHTON, J.H., Chem.Eng. Prog; ,50 597, (1954)

16. METZNER, A.B., and TAYLOR, J.S., A.I.Ch.E. Journal 6, 109, (1960)

17. NAGATA, S., YAMAMOTO, K., and UJIHARA, M., Mem.Fac.Eng. Kyoto University, 20, 336, (1958)

18. NAGATA, S., YAMAMOTA, K., HASIMOTO, K., and NARUSE, Y., Kyoto University, 21, 260, (1959)

19. RUSHTON, J.H., and OLDSHUE, J.Y., Chem.Eng. Progress, 49, 161, Part 1, (1953)

20. NAGATA, S., Mem.Fac.Eng., Kyoto University, 22, 68, (1960)

21, HOLMES, D.B., VONCKEN, R.M., and DEKKER, J.A., Chem.Eng. Science, 19, 201, (1964).

22. NEWITT, D.M., SHIPP, G.C., and BLACK. C.R., Trans.Inst.. Chem.Engrs., 29, 278, (1951)

23. REAVELL, B.N. Trans.Inst.Chem.Engrs., 29, 301, (1951)

24. LIN., C.S., DENTON, E.B., GASKILL, H.S., and PUTNAM, G.L., Ind & Eng.Chem., 43, 2136 (1951)

25. SUTTON, F., "Volumentric Analysis", Blakiston and Co., Philadelphis (1935)

26. EISENBERG.,M.E., TOBIAS, C.W., and WILKE, C.R., J. Electrochem. Soc., 101, 306 (1954)

27. MACKLEY, N.V., Ph.D. Thesis, Aston University (1973)

28. KOLTHOFF, I.M., and PEARSON, Ind.Eng.Chem., 3, 381, (1931)

29. SUTEY, A.M., and KNUDSEN, J.G., I&EC Fundamentals, 6, 132, (1967)

30. WILKE, C.R., EISENBERG, M., TOBIAS, C.W., J.Electrochim. Soc., 100, 513, (1953)

31. WILKE, C.R., TOBIAS, C.W., and EISENBERG, M., Chem.Eng. Prog., 49, 663, (1953)

32. WAGNER, C., J.Electrochim.Soc., 95, 161 (1949)

33. FONAD, M.G., and IBL, N., Electrochim. acta, 3, 233, (1960)

34. BOHM, V., IBL, N., and FREI, A.M., Electrochim. acta, 11, 421, (1966)

35. FENCH, E.J. and TOBIAS, C.W., Electrochim, acta, 2, 331, (1960)

36. SCHUTZ, G., Inter. J. Heat Mass Transfer, 6, 873 (1963)

37. BAZAN, J.C., and ARVIA, A.J., Electrochim, acta, 9, 667 (1964)

38. IBID, Electochim acta, 10, 1025, (1965)

39. LIN, C.S., MOULTON, R.W., and PUTNAM, G.L., Ind.Eng.Chem. 45, 636 (1953)

40. DEISSLER, R.G., NACA Report Note No. 1210, (1955)

41. SHAW, P.V., and HANRATTY, T.J, A.I.Ch.E. Journal 10, 475, (1964)

42. HUBBARD, D.W., and LIGHTFOOT, E.N., Ind.Eng.Chem. Fundamentals, 5, 370, (1966)

43. CHILTON, T.H., anc COLBURN, A.P., Ind.Eng.Chem., 26, 1183, (1934)

44. ROSS, T.K., and WRAGG, A.A., Electrochim. acta, 10, 1093 (1965)

45. FRIEND, W.K., and METZNER, A.B., A.I.Ch.E. Journal 4, 393, (1958)

46. SHAW, P.V., REISS, L.P., and HANRATTY, T.J., A.I.Ch.E. Journal 9, 362, (1963)

47. MIZUSHINA, T., Advances in Heat Transfer 7, 87 (1971

48. HARRIOTT, P., and HAMILTON, R.M., Chem.Eng.Sci, 20, 1073 (1965)

49. SON, J.S., and HANRATTY, T.J., A.I.Ch.E. Journal, 13, 689 (1967)

50. MIZUSHINA, T., ITO, R., OGINO, F., and MURAMOTO, H., Mem.Fac.Eng., Kyoto University, 31, 169, (1969)

51. DIMOPOULOS, G.H., and HANRATTY, T.J., J. Fluid Mech, 33, 303, (1968)

52. MIZUSHINA, T., ITO, R., HIRAOKA, S., IBUSUKI, A., and SAKAGUCHI, I., J.Chem.Eng. of Japan, 2, 89, (1969)

53. MITCHELL, J.E., and HANRATTY, T.J., J. Fluid Mech. 26, 199, (1966)

54. REISS, L.P., and HANRATTY, T.J., A.I.Ch.E. Journal, 9, 154, (1963)

55. LAUFER, J., NACA, Tech. Note No. 1053, (1951)

56. IBID, , NACA, Rep. No., 1247 (1955)

57. KLEBANOFF, P.S., NACA, Tech. Note No. 3187 (1954)

58. IBID NACA, Rep. No. 1247 (1954)

59. SIRKAR, K.K., and HANRATTY, T.J., J. Fluid Mech., 44, 589, (1970)

60. IBID, I & EC Fundementals, 8, 189 (1969)

61. IBID, J. Fluid Mech., 44, 605, (1970)

62. PRANDTL, L., NACA Tech.Mem. No. 720 (1933)

63. VON KARMAN, Th., Nach.Ges.Wiss. gottingery 58 (1930)

64. HIGBIE, R., Trans. A.I.Ch.E., 31, 365, (1935)

65. DANCKWERTS, P.V., Ind.Eng.Chem., 43, 1450 (1951)

66. HARRIOTT, P., Chem.Eng.Sci., 17, 149 (1962)

67. TOOR, H.J. and MARCHELLO, L.M., A.I.Ch.E.J., 4, 97 (1958)

68. LIN, C.C., "Turbulent Flow and Heat Transfer" (1959)

69. LEVICH, V.G., "Physicochemical Hydrodynamics", Prentice-Hall, Inc. CANADA, (1962)

70. BELOV, A., GORSHKOV, KOMAROV, V.S., and TERPIGOREV, V.S., Inter.Chem.Eng., 13, 443, (1973)

71. TAYLOR, G.I., Brit.Aero.Res.Comm., R & M No. 272, 423 (1916)

72. DEISSLER, R.G., NACA, Techn. Note No. 3145 (1954)

73. RANNIE, W.D., J.Aero.Sci., 23, 485, (1956)

74. REICHDERT, H., Z. Angew. Math.Mech., 20, 297, (1940).

75. VAN DRIEST, E.R., J.Aero.Sci., 23, 1007, (1956)

76. SPALDING, D.B., J. Applied Mechanics, Trans.ASME., 28, 455, (1961)

77. HANRATTY, T.J., A.I.Ch.E. Journal 2, 359 (1956)

78. DANCKWERTS, P.V., Ind.Eng.Chem., 43, 1460, (1951)

79. EINSTEIN, H.A., and LI, H., J.Eng.Mech. Division, preceedings of the ASCE, Paper No., 945 (1956)

80. SACKMANN, L.A., and HETTLER, J.P., Compt. Rend, 251, , 2874, (1960)

81. MEEK, R.L., and BAER, A.D., A.I.Ch.E. Journal, 16, 841 (1970)

82. SCHLICHTING, H., "Boundary Layer Theory", McGraw-Hill, New York, (1960)

83. POPOVICH, A.T., and HUMMEL, R.L., Chem.Eng.Sci., 22 21, (1967)

84. KLINE, S.J., and RUNSTADLER, P.W., Trans. ASME, J. of Applied Mechanics, 26, Series, E, No. 2, 166, (1959)

85. TOWNSEND, A.A., "The Structure of Turbulent Shear Flow" Cambridge University Press (1956)

86. LANFER, J. NACA, Report No. 1174 (1954)

87. SHIGEMITSU, Y., J. of the Physical Society of Japan, 12, 183, (1957)

88. EINSTEIN, H.A., and LI, H., Preceedings of the Heat Transfer and Fluid Mechanics Institute, Stanford University (1955)

89. COLES, D., J. Aero.Sci., 24, 495, (1957)

90. CLAUSER, F.H., J. Aero,Sci., 21, 91, (1954)

91. BLACK, T.J., Preceedings of the Heat Transfer and Fluid Mechanics Institute, Stanford University 366, (1966)

92. CORINO, E.R., and BORADKEY, R.S., J. Fluid Mech., 37, 1, (1969)

93. KLINE, S.J., REYNOLDS, W.C., SCHRAUB, F.A., and RUNSTADLER, P.W., J. Fluid Mech., 30, 741, (1967)

94. NEEDERMAN, R.M., Chem.Eng.Sci., 16, 113, 1961)

95. KIM, H.T., KLINE, S.J. and REYNOLDS, W.C., J.Fluid Mech., 50, 133, (1971)

96. FAGE, A., and TOWNEND, H.C.H., Roy.Soc., London, 135A, 656, (1932)

97. TAYLOR, G.I., Roy.Soc. London, 135A, 678 (1932)

98. POPOVICH, A.T., and HUMMEL, R.L., A.I.Ch.E., Journal, 13, 855, (1967)

99. REICHARDT, H., Z.A.M.M., 20, 297, (1940)

100. HETTLER, J.P., MUNTZER, P., and SCRIRENER, O., Compt.Rend. 258, 4201 (1964)

101. ECHELMANN, H., and REICHARDTS, H., Symposium on Turbulence in Liquids, University of Missouri - Rotla, 144, (1971)

102. BAKEWELL, H.P., Ph.D. Thesis, Pennsylvania State University (1966)

103. GUPTA, A.K., Ph.D. Thesis, University of Southern California, Los Angeles (1970)

104. THOMAS, L.C., and GREEN, H.L., Symposium on Turbulence in Liquids, University of Missouri - Rolla, 394, (1973)

105. STERNBER, J., J.Fluid Mech., 13, 241, (1963)

106. NAGATA, S., NISHIKAWA, M., INONE, A., and OKAMOTO, Y., J. of Chem.Eng. of Japan, 8, 243, (1975)

107. ARMISTEAD, R.A., and KEYES, J.J., J. Heat Transfer ASME, Trans., 90, 13, (1968)

108. DAVIES, J.T., "Turbulence Phenomena", Academic Press, New York and London (1972)

109. HINZE, O., "Turbulence", McGraw-Hill, New York (1959)

110. RASMUSSEN, C.G., DISA Information, No. 5, DISA Elektronic A/S, Denmark, (1967)

111. KANEVCO, G., and OKA, S., DISA Information, No. 15, DISA Elektronic A/S, Denmark (1971)

112. BEARMAN, P.W., DISA Information, No. 15, DISA Elektronic A/S, Denmark (1971)

113. DISA Probe Manual, DISA Elektronic A/S, Denmark (1973)

114. DELAHAY, P., "New Instrumental Methods in electrochemistry", p.217, Interscience, New York, (1954)

115. DISA 55M10 Instruction Manual, DISA Elektronic A/S, Denmark, (1971)

116. COULSON, J.M., and RICHARDSON, J.F, "Chemical Engineering", Volume 2, Pergamon Press, London (1968).